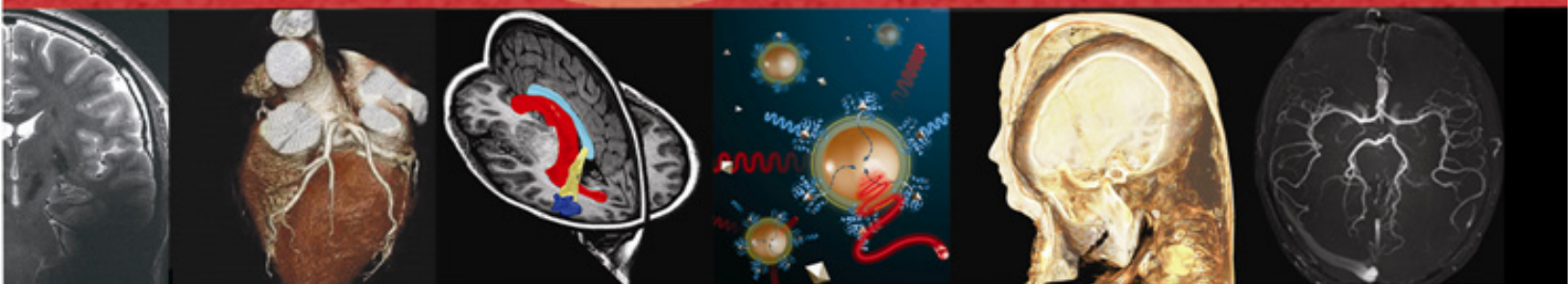


# RICHARD M. LUCAS CENTER FOR IMAGING

## Annual Report 2007

YEARS ON THE LEADING EDGE

Stanford University School of Medicine  
Department of Radiology





# STANFORD

## UNIVERSITY MEDICAL CENTER

Hospital & Clinics • School of Medicine

**GARY M. GLAZER, M.D.**  
*Emma Pfeiffer Merner Professor  
in the Medical Sciences  
Professor and Chairman  
Department of Radiology*

Fifteen years is a very short period of time in the evolution of academic institutions. I am not certain what Don Sr. and the Lucas matriarch "Go-Go" (Mary Lucas) expected us to achieve at the Lucas Center by its 15<sup>th</sup> birthday. What I can report is that the achievements of our faculty and students have become very well known and that the term "Lucas Center" is synonymous with excellence and innovation in imaging throughout the world.

The span of 15 years is an eternity in rapidly moving scientific disciplines such as imaging. To be on the leading edge of imaging during this time period, we have expanded well beyond our initial dreams. As those of you who have been closely associated with us over time know, the name of our newly constructed building in 1992 was the "Richard M. Lucas Center for Magnetic Resonance Spectroscopy and Imaging." By 2007, the building had been renamed the "Richard M. Lucas Center for Imaging" to reflect its broader scope.


Remaining unchanged is the fact that we are bound together by our focus on imaging. We believe that the field of imaging will be enduring because it provides an unparalleled approach for humans to understand complexity. In this post-genomic era with an explosion of data and information, imaging provides a vital means to understand very complicated and interconnected biological systems.

To develop serious efforts at the leading edge of imaging science has required us to rapidly expand. Two scientists, Gary Glover and Norbert Pelc, started the Lucas Center, and today, we have 20 full-time researchers forming the core of Center programs. Their scientific lineage has expanded from the initial roots in physics and electrical engineering to include clinical medicine, molecular biology, chemistry, materials science, computer science, mathematics, and bioinformatics. Research in 1992 was dominantly focused on whole organisms, and today, spans from that size to the tiny worlds of cells and molecules. Research in 1992 was dominated by achieving greater clarity in imaging structure, and today, functional imaging comprises a substantial body of our work. In 1992, there were two students at the Lucas Center, and today, they number over 100.

We will continue to build better tools for imaging structure and function, and this should lead to better understandings of health and disease. This year, we embarked on a process to define a few high impact areas of focus to add to our existing work because of huge opportunities to use our methods to make a large impact in medicine and biology. The areas of focus we are embarking on include the following:

Early Detection of Disease  
Imaging of the Aging Brain  
Innovations in Image-Guided Interventions

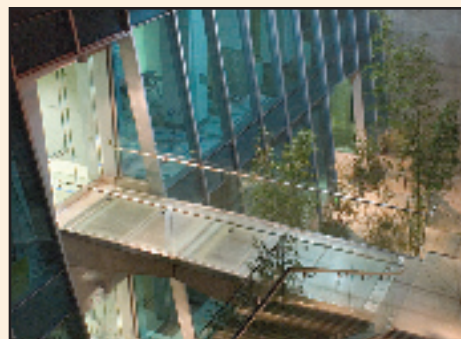
I offer my deepest thanks to the Lucas Family for their support that has enabled us to dream big dreams and has assisted us in finding ways to realize them.



Gary M. Glazer, MD  
Professor and Chairman

# LUCAS ANNUAL REPORT

YEARS ON THE CUTTING EDGE





# EXCELLENCE IN ARCHITECTURE

---

AWARDED BY THE AIA SAN FRANCISCO FOR THE  
RICHARD M. LUCAS CENTER EXPANSION, STANFORD UNIVERSITY

## 2007 DESIGN HONOR AWARD Excellence in Architecture Award



The following quotation is taken from the Campus Guide, Stanford University: An Architectural Tour, by Richard Joncas, David Neuman, and Paul Turner.

“This is a remarkable facility, despite being nearly entirely underground. It fulfills the program requirements of the Department of Radiological Sciences, as well as completes a vital portion of the medical center region plan by contributing carefully designed site improvements at grade level. It also helps to resolve pedestrian access issues created by the original building’s loading and drop-off areas interface. An eye-catching lightwell with giant bamboo plantings delves into this three-story deep structure. The relationship of the interior spaces to the lightwell and to passersby at grade create a novel, yet essential relationship to the general campus itself, especially the nearby Center for Clinical Sciences Research. This project is a true integration of site planning, landscape, and architecture at its highest (and physically lowest) level.”



# ACKNOWLEDGEMENTS

---

With the 2007 LUCAS REPORT we take the time to reflect on the past 15 years of progress made possible by the generosity of the Richard M. Lucas Foundation and their continued support of the Richard M. Lucas Center for Imaging at Stanford University Department of Radiology.

## SPECIAL THANK YOU TO

THE RICHARD M. LUCAS FOUNDATION

and

THE NATIONAL INSTITUTES OF HEALTH

NCRR P41 RR09784

NCI P50 CA114747

NCI U54 CA119367

Acronyms used in text:

AIA=American Institute of Architects  
AMI=Academy of Molecular Imaging  
ACNP=American College of Nuclear Physicians  
CAD=computer-aided detection  
CAMRT=Center for Advanced Magnetic Resonance Technology  
CCNE=Center for Cancer Nanotechnology Excellence  
CE=contrast-enhanced MRI  
CIRM=California Institute for Regenerative Medicine  
CMUT=capacitive micromachined ultrasonic transducers  
CT=computed tomography  
DOD=Department of Defense  
DTI=diffusion tensor imaging  
DWI=diffusion-weighted MRI  
EE=electrical engineering  
EEG=electroencephalography  
EPI=echo-planar imaging  
FROC=free-response operator characteristic  
GE=General Electric  
GEHC= General Electric Health Care  
HIFU=high-intensity focused ultrasound  
HRT=hormone replacement therapy  
IC=integrated circuit  
ICA=independent component analysis  
ICBP=Integrative Cancer Biology Program  
ICMIC=In Vivo Cellular and Molecular Imaging Center at Stanford

IEEE=Institute of Electrical and Electronics Engineers  
IEEE MIC=IEEE Medical Imaging Conference  
IGCT=inverse-geometry CT  
ISMRM=International Society of Magnetic Resonance in Medicine  
IUGR=intrauterine growth retardation  
MIPS=Molecular Imaging Program at Stanford  
MR=magnetic resonance  
MT=magnetization transfer  
NCRR=National Center for Research Resources  
NIH=National Institutes of Health  
NMR=nuclear magnetic resonance  
PET=positron emission tomography  
PR=projection reconstruction  
RF=radiofrequency pulses  
RNA=ribonucleic acid  
RSL=Radiological Sciences Laboratory  
RSNA=Radiological Society of North America  
SCBT=Society of Computed Body Tomography  
SMI=Society for Molecular Imaging  
SMIS=Stanford Molecular Imaging Scholars (SMIS)  
SNM=Society of Nuclear Medicine  
SPECT=single photon emission computed tomography  
SPIE=International Society for Optical Engineering  
TE=echo time

Editor/Production-Susan Kopiwoda  
Design/Layout-Janice Wolfe  
Photography-Mark Rieszenberger  
Archiving/Data Import-Gale Evans  
Printing-Lahlouh Press

# LUCAS ANNUAL REPORT 2007

## Table of Contents

Chairman's Letter.....	i
Lucas Annual Report.....	iii
Acknowledgements.....	v
Acronym list.....	vi
Table of Contents .....	vii
Collaborators.....	viii
Stanford Radiology Centers of Excellence.....	ix
Overview: Radiological Sciences Laboratory and Center for Advanced MR Technology (RSL & CAMRT) .....	1
Overview: Molecular Imaging Program at Stanford (MIPS) .....	3
Overview: Strategic Research Development and Sponsored Research.....	6
Sponsored Research.....	7
1993 and 2007 Group Photo of the Radiology Research Faculty, Staff and Students.....	12
Radiology Scientific Research Personnel, Students, and Visitors .....	14
Awards and Honors .....	16
Group Summaries .....	19
RSL Group Updates .....	20
<i>Functional Imaging-Technology Development (Glover)</i> .....	20
<i>Functional "Microvascular" Neuroimaging (Bammer/Moseley)</i> .....	21
<i>Magnetic In Vivo Spectroscopy and Multinuclear Imaging (Spielman)</i> .....	22
<i>Body MR Imaging (Hargreaves)</i> .....	23
<i>Interventional and Open MRI (Butts Pauly)</i> .....	23
<i>X-Ray Guidance of Interventional Procedures (Fahrig)</i> .....	24
<i>Inverse Geometry CT and Conventional CT (Pelc)</i> .....	24
<i>Image Display and Analysis (Napel)</i> .....	25
<i>Imaging Bioinformatics (Paik)</i> .....	25
<i>Mathematical and Computational Modeling of Cancer (MCMC) (Plevritis)</i> .....	26
<i>Proteomics, Biomarkers, and Nanoparticle Platforms for Imaging Therapeutics (Guccione)</i> .....	26
MIPS Group Updates .....	27
<i>Multimodality Molecular Imaging Lab (Gambhir)</i> .....	27
<i>Cellular and Molecular Imaging Lab (Rao)</i> .....	27
<i>Molecular Imaging Instrumentation Lab (Levin)</i> .....	28
<i>Molecular Imaging Probe Lab (Chen)</i> .....	28
<i>Cardiovascular Molecular Imaging Lab (Wu)</i> .....	29
<i>Clinical Molecular Imaging Research (Quon)</i> .....	29
<i>Molecular Imaging of Musculoskeletal Illnesses (Biswal)</i> .....	30
Education and Training.....	33
<i>Postgraduate Education</i> .....	33
<i>Advanced Techniques for Cancer Imaging and Detection (T32)</i> .....	34
<i>Stanford Molecular Imaging Scholars (R25)</i> .....	35
<i>In Vivo Cellular and Molecular Imaging (P50)</i> .....	35
<i>Lucas Center MR Training and Support</i> .....	36
Research Facilities .....	37
<i>Outpatient Imaging Center</i> .....	39
<i>3D Medical Imaging Lab</i> .....	40
<i>Experimental Animal Model Care</i> .....	41
<i>Small Animal Imaging Center (SCi3)</i> .....	42
<i>Cyclotron Suite Update</i> .....	43
<i>Lucas Center MR Systems 1.5T, 3T, and 7T Whole Body Magnets</i> .....	44
Abstracts .....	48
Publications and Presentations.....	145



## Collaborating Stanford Departments

We work with almost three hundred faculty, postdoctoral fellows, students, and research staff from across the University and wish to thank you all for the friendly, productive collaborations that we enjoy all year long. Stanford departments with whom we have long-standing research projects include the following:

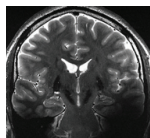
Anesthesia	Nephrology
Applied Physics	Neurobiology
Bioengineering	Neurology
Cancer Biology	Neurosurgery
Cardiovascular Medicine	OB/GYN
Chemistry	Orthopedics/Orthopedic Surgery
Computer Sciences	Pediatrics/Neonatology
Electrical Engineering	Psychiatry
ENT	Psychology
Functional Restoration	Radiation Therapy
Infectious Diseases	Stanford Center for Biomedical Ethics
Materials Science	Stroke Center
Mechanical Engineering	Surgery
Medical Informatics	Urology
Medicine/Oncology	Vascular Surgery

## Collaborators Outside of Stanford

We also enjoy many collaborations with foundations, agencies, institutions, and industry for whose support we are indeed thankful. We look forward to continued success in these collaborative endeavors as well.

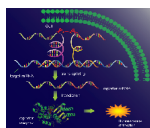
Alza Corporation	Medimmune Inc.
Amgen	Mellennium Pharmaceuticals
Brown University	NexRay
Cedars Sinai, Los Angeles	Nova R&D Inc.
Chiron Corporation	Palo Alto Veterans Administration
Colorado State University–Boulder	Pfizer
The Canary Foundation	Prostrate Cancer Foundation
Dana Farber Cancer Institute	Riken, Saitama, Japan
Diadexus	RMD Inc.
Endius	Sidney Frank Foundation
Ethicon	Siemens Medical Systems
FeRx, Inc.	Smith Kettlewell Eye Institute
Fred Hutchinson Cancer Research Center	SRI International
GE Medical Systems	University of California, Berkeley
Genentech	University of California, Davis
Glaxo Smith Kline	University of California, Irvine
Intel	University of California, Los Angeles
Intronn Inc.	University of California, San Francisco
The Richard M. Lucas Cancer Foundation	University of California, San Diego
Mag Design and Engineering	University of Texas, Austin
MediCorp Health System	Varian Medical Systems

## Stanford Radiology Centers of Excellence



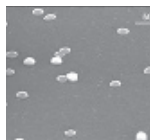
### THE CENTER FOR ADVANCED MAGNETIC RESONANCE TECHNOLOGY (CAMRT)

Established in 1995 and directed by Gary Glover, PhD, the Center for Advanced Magnetic Resonance Technology (CAMRT) supports excellence in biomedical magnetic resonance imaging. Over the years, the CAMRT has served as an important imaging resource for at least 14 departments and more than 30 faculty from other departments and has provided the original structure for the development of the Richard M. Lucas Center for Imaging.



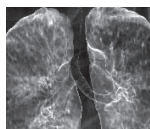
### THE IN VIVO CELLULAR AND MOLECULAR IMAGING CENTER AT STANFORD (ICMIC)

The ICMIC, directed by Sam Gambhir, MD, PhD, brings together more than 50 faculty from 21 different departments, including Radiology, across the Stanford campus. As only one of eight in vivo cellular and molecular imaging centers (ICMIC) in the country, the ICMIC studies disease by connecting preclinical models with clinical management through advances in multimodality molecular imaging. This molecular imaging program benefits from the highly regarded infrastructure provided by the CAMRT and RSL in the Richard M. Lucas Center for Imaging.



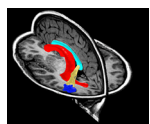
### THE CENTER FOR CANCER NANOTECHNOLOGY EXCELLENCE-FOCUSED ON THERAPY RESPONSE (CCNE-TR)

Stanford Radiology also has been identified as one of eight institutions in the nation to receive NIH support to develop a major nanotechnology center: the Center for Cancer Nanotechnology Excellence Focused on Therapy Response (CCNE-TR). This new center, directed by Sam Gambhir, MD, PhD, will include scientists from Stanford and from six other sites across the country. The goal of this center is to use nanotechnology for the benefit of cancer patient management. The CCNE greatly expands our collaborative efforts, and we now work with an additional 35 faculty in more than 20 departments here at Stanford and across the country.



### THE CENTER FOR CANCER EARLY DETECTION

The Stanford Department of Radiology and the Canary Foundation have united to support research in early cancer detection to establish the Center for Cancer Early Detection, which has recently received a National Cancer Institute designation. Headed by Sanjiv Sam Gambhir, MD, PhD, professor of radiology as well as bioengineering and director of the Molecular Imaging Program at Stanford (MIPS), the Center will advance molecular diagnostics by emphasizing molecular imaging to detect disease at its earliest and most treatable stage.



### THE AGING BRAIN AND COGNITIVE DISORDERS

We are pleased to announce the Center for the Aging Brain and Cognitive Disorders, a new collaboration among the Radiology, Neurology, Psychiatry, and Psychology Departments at Stanford. Supported by generous funding from the Richard M. Lucas Foundation, this new collaboration forms a multidisciplinary center-of-excellence focused on the aging brain, Alzheimer's disease, dementias, neurodegenerative disease, psychiatric disorders, and screening for preclinical cognitive decline. We will investigate and develop new diagnostic tools and therapies to care for patients with cognitive disorders..





# OVERVIEWS

15 YEARS ON THE CUTTING EDGE





# RSL OVERVIEW

## RADIOLOGICAL SCIENCES LABORATORY AND THE CENTER FOR ADVANCED MR TECHNOLOGY (CAMRT)

Gary H. Glover, PhD • Director, Radiological Sciences Laboratory

The Lucas Center is home to the Radiological Sciences Laboratory (RSL), which is a section of the Radiology Department. In conjunction with the Electrical Engineering Department, the RSL is host to the Center for Advanced MR Technology, an NIH-funded National Research Resource. Its state-of-the-art imaging facilities support the research of the RSL and the entire Radiology Department as well as hundreds of on-campus and extramural researchers. The Center continues to be an exciting and lively nexus for fundamental imaging research.

### THE RADIOLOGICAL SCIENCES LABORATORY

The RSL is comprised of 12 faculty and approximately 50 graduate and postdoctoral students, 30 scientific staff, and 7 administrative assistants, as well as the Lucas Center/RSL Administrative Services Manager, Donna Cronister.

The faculty serve in a wide variety of advisory roles for government and foundation agencies, such as the NIH, and in policy-making positions for international scientific societies such as the ISMRM and RSNA. A number of our faculty, scientific staff, and students have garnered prestigious awards for their exceptional research achievements. Some of the Lab's honors of the past year are noted here with great pleasure.

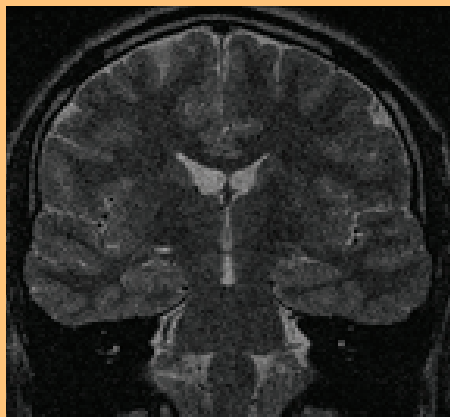
Roland Bammer's student, Thomas Hope, was chosen

by the RSNA to receive the Trainee Research Prize for his research project "Time-Resolved 3-D Quantitative Flow MRI of Intracranial Vessels: Comparative Evaluation at 1.5T and 3.0T in Combination with Parallel Imaging."

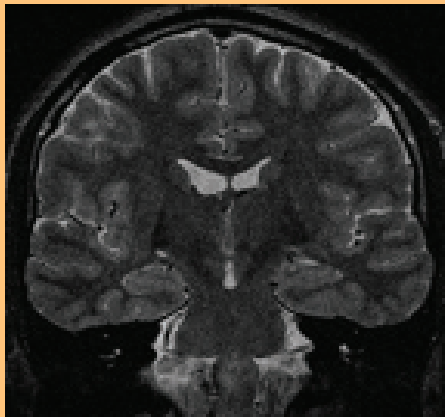
Brian Hargreaves' grant proposal to the California Breast Cancer Research Program received the top score out of 103 applications. His graduate student, Wenmiao Lu, received second place for the Best Poster in the pulse sequence category at the ISMRM Annual Meeting in Berlin, Germany.

Mike Moseley was elected to an honorary life-time membership in the Society of Magnetic Resonance Technologists. His postdoctoral student, Chunlei Liu, received a K99-R00 grant from the NIH. These prestigious grants are highly competitive and intended to assist in the transition from postdoctoral student to junior faculty member.

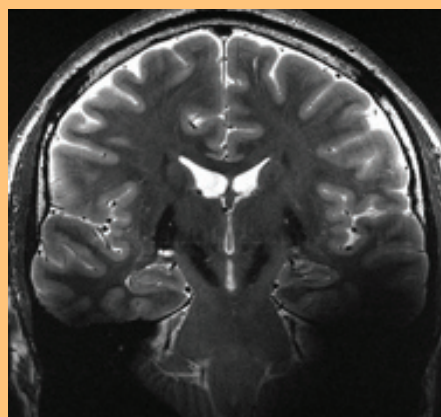
Kim Butts Pauly continues to serve on the ISMRM Board of Trustees, an elected position that demonstrates peer recognition of her contributions to science. She is now the chair of the Annual Meeting Program Committee, the most prestigious committee of the Society. In this role, she has overall responsibility for meeting planning. She also was invited to serve on the editorial board of the *Journal of Magnetic Resonance Imaging*.



1.5T (352 microns x 352 microns x 2mm)  
+62.5 kHz, 6.5 min



3.0T (176 microns x 352 microns x 2mm)  
+62.5 kHz, 6.5 min



7.0T (176 microns x 352 microns x 2mm)  
+62.5 kHz, 6.5 min



Norbert Pelc's students and advisees have fared well: the SCBT/MR in-training award was given to David Tran at the Annual Scientific Meeting of SCBT/MR, Orlando. Sam Mazin's poster at the SPIE meeting was recognized with the Cum Laude Award. Only one poster within the "Physics of Medical Imaging" conference can receive this award each year.

Dan Spielman's MD/PhD student, Yakir Levin, was honored: Yakir was the recipient of an Achievement Rewards for College Scientists (ARCS) Award. The ARCS Foundation provides scholarships to academically outstanding United States citizens studying to complete their degrees in science, medicine, and engineering, thereby contributing to the worldwide advancement of science and technology.

Gary Glover was invited to serve on the Advisory Council of the National Institutes of Biomedical Imaging and Bioengineering, after six years of service as a special advisor to the institute director. His graduate student, Catie Chang, received an NIH Fellowship Award through the Biocomputation Program.

Several RSL students received their PhDs this year, including Yakir Levin, Sam Mazin, Yanle Hu, and Priti Balchandani. Congratulations to all who make the RSL an exciting environment in which to conduct research.

### The National Center for Advanced MR Technology at Stanford (CAMRT)

The CAMRT is now in its thirteenth year of operation as a Research Resource, sponsored by a grant from the NIH's National Center for Research Resources. Outstanding

progress has been made in all six of the core technology development areas, including reconstruction methods (Dwight Nishimura, Electrical Engineering Department, core director); imaging of brain activation (Gary Glover, core director and PI); diffusion and perfusion weighted imaging methods (Mike Moseley, core director); imaging of cardiovascular structure and function (Norbert Pelc, core director and CAMRT co-PI); spectroscopic imaging development (Dan Spielman, core director); and interventional MRI technique development (Kim Butts Pauly, core director). Much of this exciting research is chronicled in the scientific reports that follow.

### LUCAS CENTER FACILITIES

The Center's major expansion has provided a wonderful addition to the Department, and we are grateful to the Lucas Foundation for the support. The 7T magnet has been generating exciting images and much research is under way with this unique system. It was recently upgraded with new front-end RF components.

Renovation of the animal magnet lab for installation of a second 3T magnet was completed in the summer of 2007. The new magnet is in place, but the delivery of the electronics was delayed by the vendor (GE) until the end of the year. This new system will have advanced capabilities, and its design was a collaboration between RSL and GE.

The new "micro-Signa" 7T animal-sized magnet has been installed under the direction of Mike Moseley in the Clark Center's Small Animal Imaging Facility. It is undergoing final testing and should be operational in the early fall period.



The Richard M. Lucas Center for Magnetic Resonance Spectroscopy and Imaging, 1992.

## MIPS OVERVIEW

## MOLECULAR IMAGING PROGRAM AT STANFORD

Sanjiv Sam Gambhir, MD, PhD • Director, MIPS

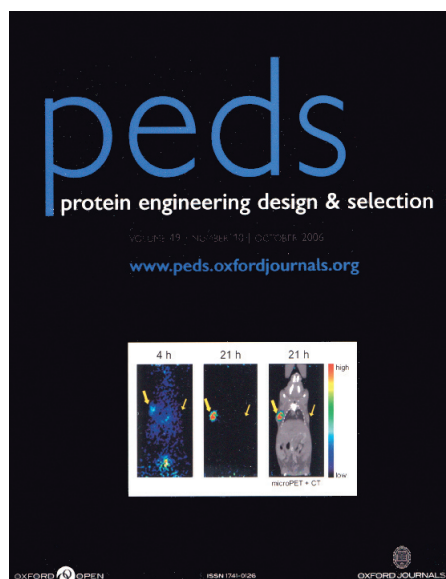
The Molecular Imaging Program at Stanford (MIPS) (<http://mips.stanford.edu>) continues to experience significant growth this year. The faculty have received several new grants from the NIH and several other agencies. We are now in the third year of the NCI-funded In Vivo Cellular and Molecular Imaging Center (ICMIC) P50 grant. We are in the second year of the NCI Center for Cancer Nanotechnology Excellence-Focused on Therapy Response (CCNE-TR) U54 grant. We are also in the second year of the NIH R25T training grant, Stanford Molecular Imaging Scholars (SMIS), to train the next generation of cancer molecular imaging scholars. In addition, all labs continue to grow with many new students and outstanding research staff joining the program.

We were also funded by the Canary Foundation to develop a new center for early cancer detection (\$7.5 million) in addition to funds provided by the Department of Radiology to help develop such a strategic center. We are convinced that more investments are needed in the earlier detection of all disease, including cancer. The ability to detect disease earlier will allow much better potential for cure. This center will work on novel in vitro diagnostics (e.g., using patient blood samples) as well as new imaging strategies with high sensitivity to detect very low burden disease. It is hoped that in the next three to five years Stanford can become a leader in the important field of early cancer detection.

We also continue to grow our industrial partnerships with key leaders in the molecular imaging community. Several projects to develop new imaging agents/strategies are underway with General Electric Global Research, General Electric Healthcare, as well as Bayer-Schering. It is likely that additional industrial partners will enter into collaborative research relationships over the next several years. These will be key to helping to translate discoveries at Stanford to the patient bedside.

We continue to have several seminar series on campus to help educate scientists about molecular imaging. The

molecular imaging seminar series ([http://mips.stanford.edu/public/mi\\_seminar.adp](http://mips.stanford.edu/public/mi_seminar.adp)) is now in its fourth year and has a large collection of videos of speakers from the last few years available on line. This year, we also initiated student presentations from different MIPS labs. Last year, we started a new nanobiotechnology seminar series ([http://mips.stanford.edu/public/nanobiotech\\_seminar.adp](http://mips.stanford.edu/public/nanobiotech_seminar.adp)), which focuses on new applications of nanotechnology to cancer. Several speakers from around the country have already presented in the series, and all lectures are available on-line.



## BISWAL LAB (MOLECULAR IMAGING OF MUSCULOSKELETAL ILLNESSES)

The Biswal lab is interested in using multimodality molecular imaging techniques to study musculoskeletal inflammation and pain. In addition to collaboration with a number of MIPS research groups, the Biswal lab has formed productive collaborative relationships with Dr. David Yeoman's group focusing on pain research; Dr. Stuart Goodman's group studying prosthetic-induced osteolysis; and Dr. Blankenberg's group studying the role of Annexin V in pain.

## CHEN LAB (MOLECULAR IMAGING PROBE LABORATORY)

Some of the molecular imaging probes developed in this lab, which exhibit great tumor targeting efficacy and favorable in vivo kinetics, are now in either late stage preclinical testing or are being translated into the clinic for initial testing in humans. Of note are imaging agents for PET targeted against integrins and the vascular endothelial growth factor receptor (VEGFR).

Dr. Weibo Cai was awarded the Benedict Cassen Postdoctoral Fellowship from the Society of Nuclear Medicine. Drs. Zibo Li and Qizhen Cao were awarded the Dean's Fellowship. Dr. Ha-Young Lee was awarded the Korean Research Foundation (KRF) Scholarship. Drs. Weibo Cai and Zibo Li were awarded 1st and 2nd Place Young Professionals Committee Best Basic Science



Awards, respectively, for the 2007 Annual Convention of the Society of Nuclear Medicine in Washington, DC. Numerous travel awards were also received by the Chen group to attend AMI and SMI annual conferences.

#### GAMBHIR LAB (MULTIMODALITY MOLECULAR IMAGING LAB)

The Gambhir lab continues to develop multimodality strategies for molecular imaging. This year we have developed several new strategies for Raman Spectroscopy using nanoparticles, photoacoustics using smart probes, and targeted microbubbles for ultrasound. These are in addition to assays being developed for PET, optical bioluminescence, and fluorescence. Efforts in the early detection of cancer are also growing in the lab.

Our lab received numerous honors this year. Dr. Gambhir co-hosted the Nobel Symposium entitled “Watching Life through Molecular Imaging” in Stockholm, Sweden. This event, which brought together the leading scientists in the field, served to educate the Nobel Committee with respect to the growing importance of molecular imaging.

Dr. Gambhir was elected to the American Institute for Medical and Biomedical Engineering (AIMBE) as a fellow.

Dr. Gambhir was awarded the Aunt Minnie Most Influential Radiology Researcher Award in 2006. This award, presented at the RSNA meeting, recognizes Dr. Gambhir as a leader in the field of Radiology.

Adam de la Zerda, a graduate student, and three students from the Stanford Graduate School of Business won 1st prize in the Bay Area Entrepreneurship Contest for their idea regarding a new medical device for wound closure using short pulsed lasers.

Ricky Tong, a medical student in the lab, received an

RSNA research grant to develop transgenic mouse models for reporter gene imaging. He also received a research fellowship from the SNM.

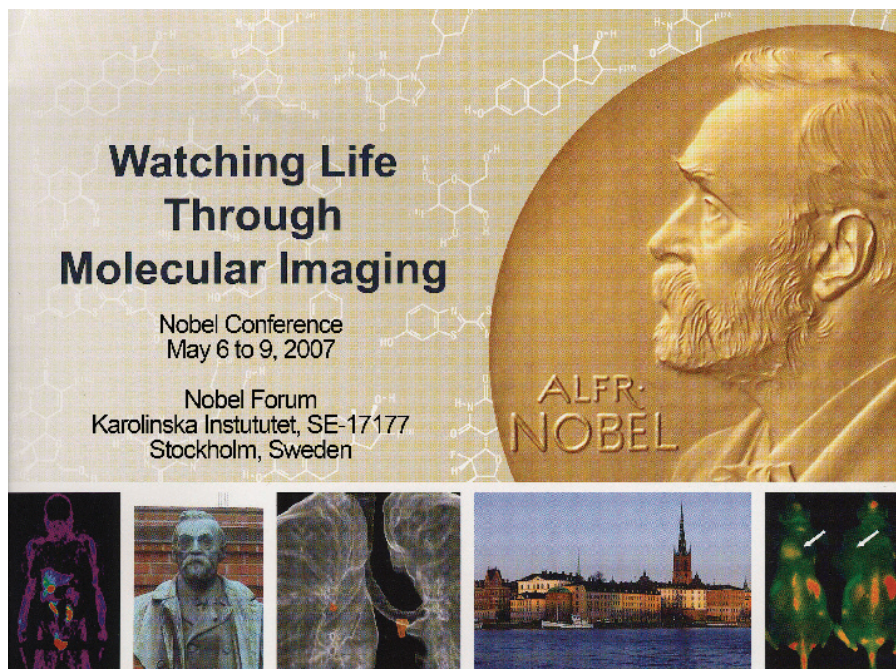
Dr. Juergen Willmann, a visiting physician-scientist in the lab, received a fellowship from the Swiss Foundation for Medical-Biological grants (SSMBS).

Dr. Amelie Lutz, a visiting physician-scientist in the lab,

received the Swiss National Science Foundation Scholarship.

Dr. Bryan Smith, a post-doc in the lab, and an NIH R25 trainee, received the Dean's Fellowship award.

Work from the lab was featured on the covers of the journals *Protein Design Engineering and Selection* as well as *Trends in*



#### Molecular Medicine.

#### LEVIN LAB (MOLECULAR IMAGING INSTRUMENTATION LABORATORY)

The lab's research interests involve the development of novel instrumentation and software algorithms for in vivo imaging of molecular signals in humans and small laboratory animals. These new cameras efficiently image radiation emissions in the form of positrons, annihilation photons, gamma rays, and light from molecular probes developed to target molecular signals from deep within the tissue of living subjects. The goals of the instrumentation projects are to push the sensitivity and spatial, spectral, and/or temporal resolutions as far as physically possible.

Frances Lau, Peter Olcott, Angela K. Foudray, and Guillem Pratx all received several travel awards. Frances Lau received the prestigious Bio-X Graduate Fellowship Award.

Peter Olcott received the top student presentation at IEEE MIC 2006.



### RAO LAB (CELLULAR AND MOLECULAR IMAGING LAB)

The Rao lab works at the interface of biology and chemistry, combining synthetic and physical organic chemistry and molecular biology with imaging techniques like fluorescence microscopy and whole-body fluorescence/bioluminescence imaging to develop novel imaging probes and methods to image biology in living subjects.

Dr. Jianghong Rao was selected by the Human Frontier Science Program as the 2007 Young Investigator.

Dr. Gayatri Gowrishankar was awarded the Cancer Biology Program Postdoctoral Fellowship.

### WU LAB (CARDIOVASCULAR MOLECULAR IMAGING)

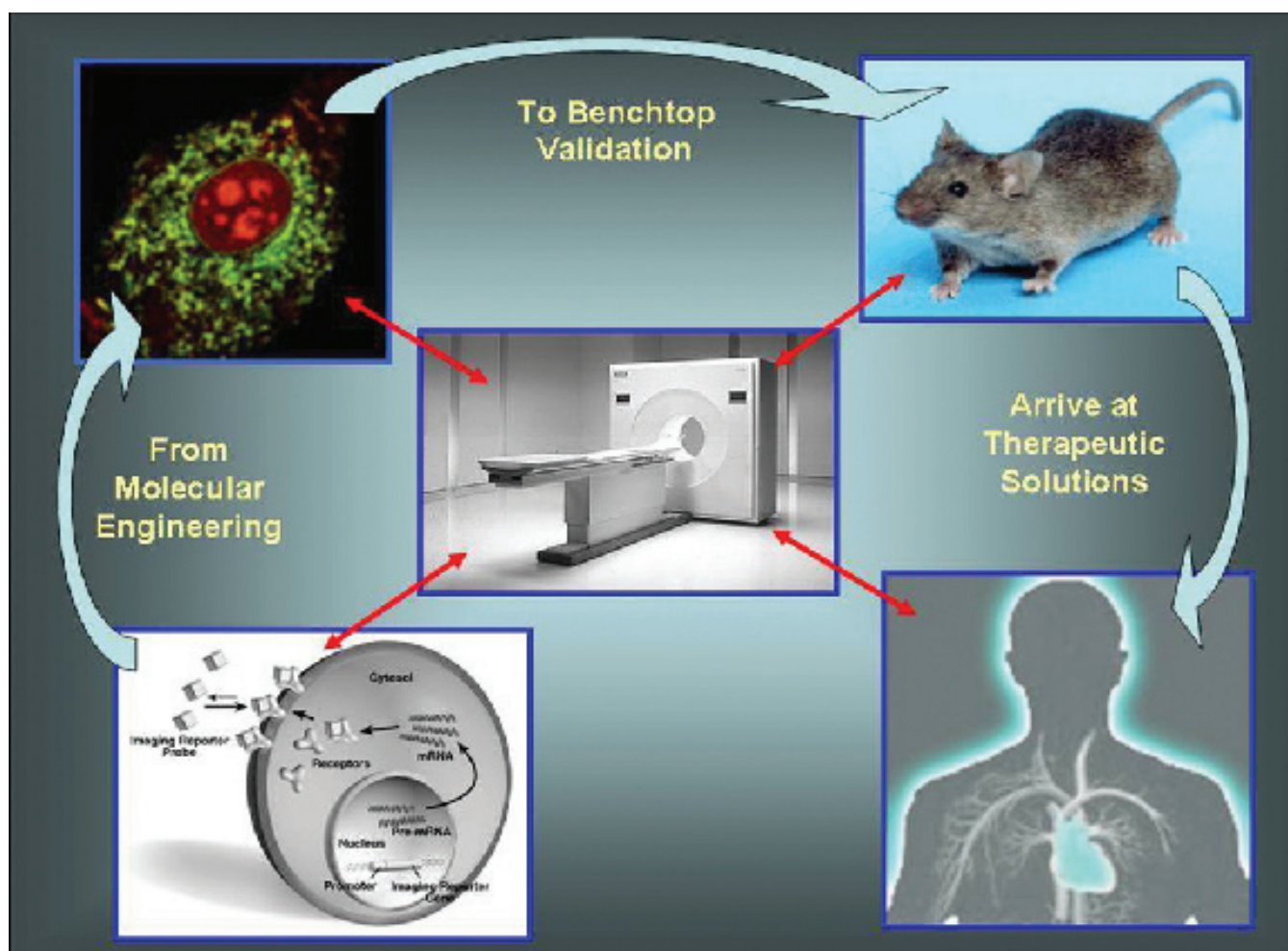
The cardiovascular molecular imaging lab is a multi-disciplinary team that combines expertise in molecular and cell biology, cardiovascular physiology, and molecular imaging. To better understand stem cell biology in

vivo, we use novel molecular markers that enable us to follow the fate of transplanted stem cells noninvasively. These include monitoring survival, proliferation, and differentiation as related to embryonic stem cells and bone marrow stem cells. The highly sensitive imaging devices we use include bioluminescence, fluorescence, positron emission tomography, and magnetic resonance scanners.

One of our research papers was selected as the best basic science paper in the journal *Circulation* for the year 2006 (Cao F, Lin S, Xie X, Ray P, Patel M, Zhang X, Drukker M, Dylla SJ, Connolly AJ, Chen X, Weissman IL, Gambhir SS, Wu JC. In vivo visualization of embryonic stem cell survival, proliferation, and migration after cardiac delivery. *Circulation*. 2006 Feb 21;113(7):1005-14.).

Kitch Wilson, MD received a three-year Bio-X Graduate Student Fellowship Award.

Mei Huang, PhD received a two-year American Heart Association Postdoctoral Fellowship Award.



## RESEARCH OVERVIEW

## STRATEGIC RESEARCH DEVELOPMENT

Norbert Pelc, ScD • Associate Chair for Research

## LUCAS CENTER EARLY DAYS VS. TODAY

We have come a long way since 1992 when the newly established Richard M. Lucas Center for Magnetic Resonance Spectroscopy and Imaging and the fledgling Radiological Sciences Lab (RSL) began making medical imaging history. The imaging pioneers who comprised our faculty in those early days could not have imagined how successful the Lucas Center and RSL would become. Faculty in the early RSL group were trained in physics, NMR, and electrical engineering with MRI, MRS, and CT as their primary foci. Following the 2005 expansion of the Lucas Center, the Center's name was changed to the Richard M. Lucas Center for Imaging to represent the expansion of our imaging-related interests over the years.

Today, fifteen faculty scientists with backgrounds representing a broad array of disciplines that include biomedical engineering, electrical engineering, materials science, physics, mathematics, chemistry, biology, computer science, bioinformatics, and molecular imaging are located in the Lucas Center. Other research faculty, who are members of the Lucas Center family but not housed in the Lucas Center due to space, bring our research faculty number to twenty.

With the increase in research faculty from three in 1992 to eighteen in 2007, there has been an explosion in the number of trainees, scientific staff, and administrative staff who support the varied research projects that are carried out in the Lucas Center and related labs. Figure 1 shows our population growth since 1992. While our faculty has more than quadrupled, most of our population growth is due to an increase in the number of graduate students and postdoctoral trainees. In 1992, we had two postdoctoral

trainees, while today there are more than one-hundred students working in the Lucas Center. Many scientists who trained at the Lucas Center now populate academic centers around the world, providing a testament to the impact of the Richard M. Lucas Center for Imaging well beyond the Stanford campus.

## RESEARCH FUNDING HISTORY

For the second year in a row, Stanford Radiology ranks as the third highest NIH-funded radiology department among medical schools across the nation. We have

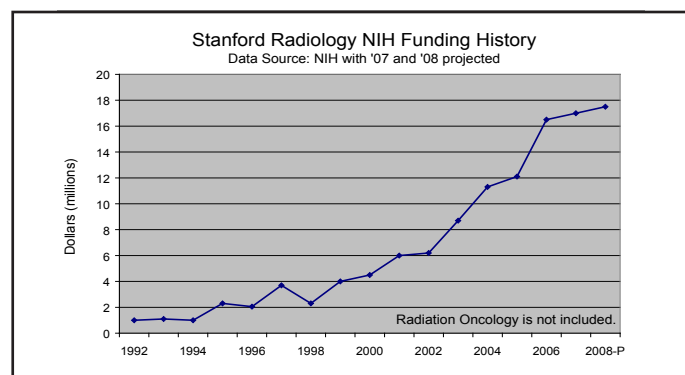


Figure 2. Shows the change in NIH funding from 1992 to 2006 with '07 and '08 projected.

achieved this ranking with less than half the number of faculty of any other NIH-ranked radiology department. Figure 2 shows how far we have come in research funding since 1992 when we had four funded projects. Today, our faculty and scientists lead more than 35 NIH projects and a total of nearly 100 projects sponsored by NIH, DOD, the State of California, industry, clinical trials, and various foundations.

Since the 2004-2005 fiscal year, the NIH budget has been flat at \$28B and has not kept up with the increasing number of investigators, applications, or inflation. In spite of this negative climate, our faculty have been able to sustain programs and have even acquired new funding for novel programs.

This year, we are pleased to report that five new NIH programs have been or will be funded shortly. We have also acquired new funding from CIRM, the American Heart Association, the Society of Nuclear Medicine, and the RSNA, as well as renewed funding for two long-stand-

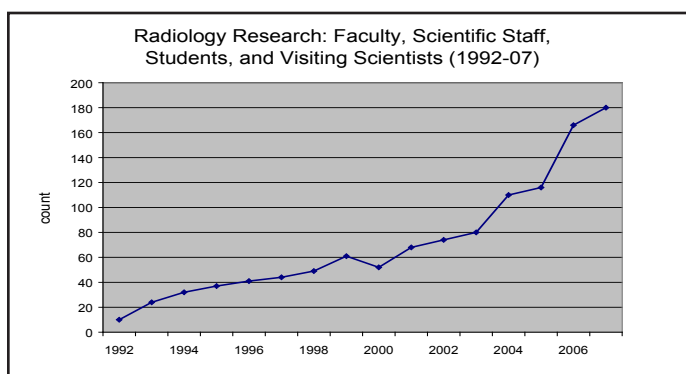


Figure 1. Shows the population growth of the research personnel in the Stanford Radiology Department from 1992 to 2007.

ing NIH projects. Since 2000, we have increased our proposals from 25 in 2000 to 85 this year, with an average request of approximately \$1M per proposal (Figure 3). Because of our outstanding faculty, postdocs, students, and staff, combined with a tenacious level of proposal activity, we have enjoyed yet another banner year for 2007.

*The following pages list active Radiology projects during 2007. An asterisk (\*) indicates a newly funded program. Double asterisks (\*\*) indicate long-standing programs that have successfully undergone competing renewals.*

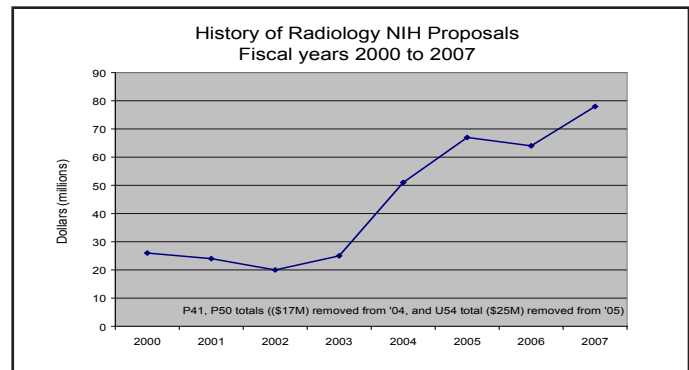


Figure 3. Shows an increase in proposed dollars of more than 100% since FY 2000.

## NIH Supported Research

PI	AGENCY	TITLE
Roland Bammer, PhD	NIH/NIBIB-R01	**Improving SENSE MRI for Spiral and Echo-Planar Imaging
Roland Bammer, PhD	NIH/NIBIB-R21	*Real-Time MRI Motion Correction System
Chris Beaulieu, MD, PhD	NIH/NCI-R01	Three-Dimensional CT Colonography
Francis Blankenburg, MD	NIH/NIBIB-R01	Imaging Apoptosis In Vivo with Technetium 99m Annexin
Kim Butts Pauly, PhD	NIH/NCI-R01	MR-Image Guided Focused Ultrasound for Treatment of Liver and Renal Cancer
Kim Butts Pauly, PhD	NIH/NCI-R01	iMRI Methods for Cancer Diagnosis and Treatment
Kim Butts Pauly, PhD	NIH/NCI-R21	Improved Open MRI for Image-Guided Breast Procedure
Xiaoyuan Chen, PhD	NIH/NCI-R21	Imaging AVD-3 Integrin Expression
Xiaoyuan Chen, PhD	NIH/NCI-R21	*Quantum Dots for NIR Fluorescence Imaging of Tumor Angiogenesis
Xiaoyuan Chen, PhD	NIH/NCI-R01	*Radiolabeled RGD Peptides for Breast Cancer Imaging and Therapy
Bruce Daniel, MD	NIH/NCI-R01	Techniques for MRI-Guided Cryosurgery of Prostate Cancer
Rebecca Fahrig, PhD	NIH/NIBIB-R01	Improved C-Arm CT for Interventional Procedures
Sam Gambhir, MD, PhD	NIH/NCI-U54	Center of Cancer Nanotechnology Excellence Focused on Therapy Response (CCNE-TR)
Sam Gambhir, MD, PhD	NIH/NCI-P50	In Vivo Cellular and Molecular Imaging Center at Stanford (ICMIC)
Sam Gambhir, MD, PhD	NIH/NCI-R25	Stanford Molecular Imaging Scholars (SMIS)
Sam Gambhir, MD, PhD	NIH/NCI-R01	Reporter Imaging of Protein-Protein Interactions
Sam Gambhir, MD, PhD	NIH/NHLBI-R01	Multimodality Imaging of Cell Mediated Gene Transfer
Gary M Glazer, MD	NIH/NCI-T32	**Advanced Techniques for Cancer Imaging
Gary H Glover, PhD	NIH/NCRR-P41	Center for Advanced Magnetic Resonance Technology at Stanford (CAMRT)
Garry Gold, MD	NIH/NIBIB-R01	Rapid MRI for Evaluation of Osteoarthritis
Garry Gold, MD	NIH/NIBIB-R01	Real-Time MRI-3D Modeling: Development and Application to Patellofemoral Pain
Craig Levin, PhD	NIH/NCI-R01	*Enhancing Molecular Cancer Imaging with Cadmium Zinc Telluride PET
Craig Levin, PhD	NIH/NCI-R01	Advanced PET System Dedicated to Breast Cancer Imaging
Craig Levin, PhD	NIH/NCI-R13	Workshop on the Nuclear Radiology of Breast Cancer
Craig Levin, PhD	NIH/NIBIB-R33	New Scintillation Light Detection Concepts for PET
Chunlei Liu, PhD	NIH/NIBIB-K99	High Resolution Diffusion-Weighted MRI at 300-Micron Level
Michael Moseley, PhD	NIH/NINDS-R01	Improved PWI Methodology in Acute Clinical Stroke
Sandy Napel, PhD	NIH/NHLBI-R01	Efficient Implementation of 3D Vascular Image Data
Norbert Pelc, ScD	NIH/NIBIB-R01	Inverse Geometry CT for Dose-Efficient Volumetric Imaging
Laura Pisani, PhD	NIH/NIBIB-F32	Fetal Functional Magnetic Resonance Imaging
Sylvia Plevritis, PhD	NIH/NCI-U56	Computational Modeling of Cancer Biology
Sylvia Plevritis, PhD	NIH/NCI-R01	Breast Cancer Trend Analysis Using Stochastic Simulation
Sylvia Plevritis, PhD	NIH/NCI-R01	Cost-Effectiveness Analysis of Lung Cancer Screening

## NIH Supported Research (continued)

PI	AGENCY	TITLE
Geoffrey Rubin, MD	NIH/NCI-R01	Improving Radiologist Detection of Lung Nodules with CAD
F. Graham Sommer, MD	NIH-NCI	Precise MRI-Directed Sonic Ablation of Prostate Cancer
Dan Spielman, PhD	NIH-NCI	Magnetic Resonance Spectroscopic Neoplasm Imaging
Joseph Wu, MD, PhD	NIH-NHLBI	*Biological Insights into Dynamics of Stem Cell Differentiation & Misbehavior
Joseph Wu, MD, PhD	NIH-NHLBI	Molecular Imaging of Cardiac Cell Transplantation
Joseph Wu, MD, PhD	NIH-NHLBI	*Nanostructuring and Molecular Imaging of Engineered Cardiovascular Tissues
Francis Blankenburg, MD	NIH-sub (UWash)	Membrane Binding and Imaging Applications of Annexins
Rebecca Fahrig, PhD	NIH-sub (ICMIC)	ICMIC Developmental Project #4
Rebecca Fahrig, PhD	NIH-sub (Sbrook)	Low Cost Digital X-Ray Detectors Using Liquid Crystals
Rebecca Fahrig, PhD	NIH-sub (UHN)	Image Science for the New X-Ray: Taking NEQ to Task
Sam Gambhir, MD, PhD	NIH-sub (UCLA)	*Multimodal Qdot Probes to Bioimage Cells and Tumors in Small Animals
Gary H. Glover, PhD	NIH-sub (UC Irvine)	Functional Imaging Research in Schizophrenia Testbed
Garry Gold, MD	NIH-sub (UCSF)	Data Coordinating Center for Osteoarthritis Initiative
Robert Herfkens, MD	NIH-sub (Surg)	Aortic Structure, Biology and Strain in Human AAA
Craig Levin, PhD	NIH-sub (ICMIC)	Small Animal Imaging Resource (SAIR) for ICMIC at Stanford
Dirk Mayer, PhD	NIH-sub (Scripps)	Effects of Acute Alcohol Exposure on Rat Brain Metabolites Detected by MRS
Sandy Napel, PhD	NIH-sub (BioE)	SIMBIOS - Physics-Base Simulation of Biological Structures
Sylvia Plevritis, PhD	NIH-sub (CCNE)	Center of Cancer Nanotechnology Excellence Focused on Therapy Response-CCNE-TR
Dan Spielman, PhD	NIH-sub (SRI)	In Vivo Diffusion and Spectroscopic Brain Imaging in Alcoholism

## Other Government Supported Research

Xiaoyuan Chen, PhD	DOD	Molecular Imaging of Ovarian Carcinoma Angiogenesis
Xiaoyuan Chen, PhD	DOD	VEGF-Iron Oxide Conjugate for Dual MR & PET Imaging of Breast Cancer Angiogenesis
Xiaoyuan Chen, PhD	DOD	Imaging Primary Prostate Cancer and Bone Metastasis
Xiaoyuan Chen, PhD	DOD	Alpha-v Integrin Targeted PET Imaging of Breast Cancer Angiogenesis and Low-Dose Metronomic Anti-Angiogenic Chemotherapy Efficacy
Xiaoyuan Chen, PhD	DOD	*MSC as Targeted-Delivery Vehicle in Breast Cancer
Brian Hargreaves, PhD	CBCRP	*Multinuclear MRI of Breast Tumors
Craig Levin, PhD	UCOP	New Technology to Enhance PET in Breast Cancer Management
Rebecca Rakow-Penner, BS	DOD	Improving Breast Cancer MRI
Jianghong Rao, PhD	DOD	Ribozyme-Mediated Imaging of p53 Expression in Breast Tumor Cells
Jianghong Rao, PhD	DOD	Bioluminescent Nanosensors for Multiplex Imaging of MMPs
Joseph Wu, MD, PhD	CIRM	*In Vivo Imaging of Human ESC Derivatives and Tumorigenicity

## Stanford University Supported Research

Terry Desser, MD	Stanford-Wallenberg	Learning Radiology in Simulated Environments
Huy Do, MD	Stanford-OTL	A Novel Non-Invasive Device for Occluding Cerebral Aneurysms
Garry Gold, MD	Stanford-VPUE	Testing 3D FSE MRI as a Clinical Tool in the Diagnosis and Treatment of OA
Garry Gold, MD	Stanford-Wallenberg	Learning Radiology in Simulated Environments
Robert Herfkens, MD	Stanford-OTL	His-Solution Encoder for Diagnostic Radiological Imaging
Sandy Napel, PhD	BioX	Novel Transducer Array and Software for Automated Detection of Asymptomatic Carotid Artery Stenosis



## Foundation Supported Research

PI	AGENCY	TITLE
Weibo Cai, PhD	SNM	*PET Imaging and Therapy Targeting Tumor Angiogenesis
Weibo Cai, PhD	AHA	Cellular Therapy for the Ischemic Myocardium: In Vivo Characterization of Biology and Physiology
Ian Chen, PhD	AHA	Multimodality Imaging of Cardiac Therapy
Hyung Chun, PhD	SNM	*Integration of Imaging and Genomics for Characterization of Cardiac Stem Cell therapy
Sam Gambhir, MD, PhD	Beckman-ITRP	Integrated Optical Bio-Sensors & Fluorescent Molecular Imaging Probes to Continuously Monitor Stem Cells in Living Subjects
Sam Gambhir, MD, PhD	Doris Duke Foundation	Molecular Imaging of Cancer with a Voltage Sensor
Sam Gambhir, MD, PhD	Susan G. Komen Foundation	Imaging the Efficacy of Heat Shock Protein 90 Inhibitors in Human Breast Cancers
Samira Guccione, PhD	Goldhirsh Foundation	Vascular Targeted Therapeutics for Treatment and Imaging Diffuse Glioma
Jianghong Rao, PhD	Human Frontier Science	*Imaging mRNA in Synaptic Plasticity
Jianghong Rao, PhD	Burroughs Wellcome	Career Award at the Scientific Interface
Geoffrey Rubin, MD	RSNA	Fellowship in Cardiovascular Imaging
Humberto Wong, MD	RSNA	*Fellowship in Cardiovascular Imaging
Joseph Wu, MD, PhD	ACCF	Multi-Modality Imaging of Cardiac Stem Cell
Joseph Wu, MD, PhD	AHA	*In Vivo Tracking of Stem Cells in the Ischemic Myocardium
Joseph Wu, MD, PhD	Burroughs Wellcome	*Molecular and Cellular Mechanisms of Cardiac Regeneration
Joseph Wu, MD, PhD	ASNC	Integration of Molecular Imaging and Genomics for Advancing Cardiac Stem Cell Therapy

## Industry Supported Research

Xiaoyuan Chen, PhD	Med Immune, Inc	In Vivo Imaging at Stanford
Terry Desser, MD	Berlex Labs	*Simulation-Based Medical Training Exercise in Management of Contrast Media Adverse Reactions for Residents
Rebecca Fahrig, PhD	Siemens Medical Solutions	Gated 3D DynaCT for Cardiac Applications
Rebecca Fahrig, PhD	Varian Associates	Correction Approaches for Amorphous Silicon Detector Non-Idealities
Sam Gambhir, MD, PhD	Alza Corporation	Delivery of Labeled FHBG to Animal Brain
Sam Gambhir, MD, PhD	GE Healthcare	Multimodality Molecular Pre-Clinical Imaging
Sam Gambhir, MD, PhD	Schering AG	Collaborative Research Agreement: PET Imaging of Breast Cancer Using Fructose Analogues
Sam Gambhir, MD, PhD	Genentech	PET Imaging of Lymphoma Patients Using Radiolabeled Rituximab
Gary M. Glazer, MD	GE Healthcare	Destination Digital Agreement
Garry Gold, MD	GlaxoSmithKline	Sodium MRI at 3T for Drug Discovery
Rusty Hofmann, MD	Cook Incorporated	Study of IVC Filter Retrieval Using the Gunther Tulip Vena Cava Filter
Debra Ikeda, MD	ART, Inc.	*Efficacy Study of the SoftScan Optical Breast Imaging System
Debra Ikeda, MD	U-Systems	3-D Full Field Breast Ultrasound: Development, Testing, and Application to Breast Cancer Diagnosis
Craig Levin, PhD	GE Healthcare	*Combined PET MR System
Michael Marks, MD	Diversified Diagnostic	Xenon-CT Imaging to Measure Cerebral Blood Flow (CBF)
Michael Marks, MD	Micrus Corporation	Safety and Efficacy of Cerecyte Polymer Filled Coil in Intracranial Aneurysms
Sandy Napel, PhD	Siemens Corp. Research	Interventional Room of the Future



## Industry Supported Research (continued)

Norbert Pelc, ScD	GE Healthcare	Inverse Geometry CT
Andrew Quon, MD	Genentech	*Avastin/[18f]-5fluorouracil PET/CT Imaging Feasibility Project
Geoffrey Rubin, MD	Cook Medical	*Zenith TX2 Thoracic TAA Endovascular Graft
Daniel Sze, MD, PhD	Cook Incorporated	Zilver Vascular Stent in the Femoral Popliteal Artery
Daniel Sze, MD, PhD	Cook Incorporated	Zilver Vascular Stent in the Iliac Arteries
Daniel Sze, MD, PhD	WL Gore & Associates	Use of the GORE TAG Thoracic Endoprosthesis in Descending TAA Requiring Surgical Repair
Daniel Sze, MD, PhD	WL Gore & Associates	Evaluation of the GORE TAG Thoracic Endoprosthesis for Treatment of the Descending Thoracic Aorta
Daniel Sze, MD, PhD	WL Gore & Associates	Evaluation of the GORE TAG Thoracic Endoprosthesis for Treatment of Descending Thoracic Aneurysms
Daniel Sze, MD, PhD	WL Gore & Associates	Evaluation of the Thoracic EXCLUDER Endoprosthesis for Descending Thoracic Aortic Diseases
Daniel Sze, MD, PhD	WL Gore & Associates	Use of the Bifurcated EXCLUDER to Treat Infrarenal Abdominal Aortic Aneurysms (AAA)
Daniel Sze, MD, PhD	WL Gore & Associates	Modified Bifurcated EXCLUDER Endoprosthesis to Treat Infrarenal AAAs
Joseph Wu, MD, PhD	Pfizer Pharmaceuticals	The Role of Statins in Cardiac Stem Cells



# RESEARCH PERSONNEL

15 YEARS ON THE CUTTING EDGE



Song Lai • Gerry Naaman • Atsushi Takahashi • Yudong Zhu • Tom Brosnan • Paul Himlet • Grant Stevens • Roger Shiffrin  
 • Rico Galvez • Sandy Napel • Yi Fen Yun • Smadar Shiffman • Donna Cronister • Lynn Nagie • Suzie Spielman • Michelle  
 Christierson • Jill Fredrickson • Sara McAfee • Diane Howard • Anne Sawyer • Judy Illes • Lorie Pelc • Bruce Daniel •  
 Bob Herfkens • Garry Glazer • Joanne Murphy • Kim Butts • Gary Gover • Rasool Khadem • Dan Spielman • Norbert Pelc  
 • Marc Alley • Maria Drangova • Richard M. Lucas Center for Imaging, Stanford University School of Medicine • Richard M. Lucas  
 Center for Imaging, Stanford University School of Medicine • Richard M. Lucas Center for Imaging, Stanford University School of  
 Medicine • Richard M. Lucas Center for Imaging, Stanford University School of Medicine • Richard M. Lucas Center for Imaging,  
 Stanford University School of Medicine • Richard M. Lucas Center for Imaging, Stanford University School of Medicine • Richard M.  
 Lucas Center for Imaging, Stanford University School of Medicine • Richard M. Lucas Center for Imaging, Stanford University School of  
 Medicine • Richard M. Lucas Center for Imaging, Stanford University School of Medicine • Richard M. Lucas Center for Imaging,  
 Stanford University School of Medicine • vRichard M. Lucas Center for Imaging, Stanford University School of Medicine • Richard  
 M. Lucas Center for Imaging, Stanford University School of Medicine • Richard M. Lucas Center for Imaging, Stanford University School  
 of Medicine • Richard M. Lucas Center for Imaging, Stanford University School of Medicine • Richard M. Lucas Center for Imaging,  
 Stanford University School of Medicine • Richard M. Lucas Center for Imaging, Stanford University School of Medicine • Richard M.  
 Lucas Center for Imaging, Stanford University School of Medicine • Richard M. Lucas Center for Imaging, Stanford University School of



1994



Roland Bammer, PhD • Sandip Biswal, MD • Kim Butts Pauly, PhD • Xiaoyuan (Shawn) Chen, PhD • Zehn • Cheng, PhD • Rebecca Fahrig, PhD • Sam Gambhir, MD, PhD • Gary M Glazer, MD • Gary H Glover, PhD • Samira Guccione, PhD • Brian Hargreaves, PhD • Robert J Herfkens, MD • Craig Levin, PhD • Michael E Moseley, PhD • Sandy Napel, PhD • David Paik, PhD • Norbert J Pelc, ScD • Sylvia K Plevritis, PhD • Andy Quon, MD • Jianghong Rao, PhD • Daniel M Spielman, PhD • Joseph Wu, MD, PhD • Greg Zaharchuk, MD, PhD • Mary Bobel, MBA • Maggie Bos • Michelle Christerson • Bonita Crabbe • Donna Cronister • Debra Frank • Elizabeth Gill • Sofia Gonzales, MS • Sondra Horn • Mandeep Kaur • Susan Kopiwoda, MS, MPH • Marlys Lesene • Donna Niernberger • Sharon Pollio • Kala Raman • John Reuling • Lanzie Rivera • Julie Ruiz, PhD • David Russel • Monique Schareck, MHA • Susan Singh • Betsey Sowder • Susie Spielman • Lakeesha Winston • Wei Xiong • Scientific Staff • Marcus Alley, PhD • Neal Bangerter, PhD • Wendy Baumgardner, RVT, LATg • Rhona Berganos, BS • Thomas Brosnan, PhD • Zhen Cheng, PhD • Danye Cheng • Frederick Chin, PhD • Garry Chinn, PhD • David Clayton, PhD • Abhijit De, PhD • David Dick, PhD • Aihua Fu, PhD • Arundhuti Ganguly, PhD • Andrew Gentles, PhD • Lina He, PhD • Pam Hertz • Jung-Jin (Jason) Hsu, PhD • William Johnsen • Anitha Jununtula • Seungbum Koo • Keshni Kumar, CRT • Andy Lamb • Malika Larabi, PhD • Jelena Levi, PhD • Andreas Loening, PhD • Dirk Mayer, PhD • Mohammed • Namavari, PhD • Rexford • Newbould, PhD • Linda Novello, RT • Laura Pierce, MPA, RT • Paulmurgan Ramasamy, PhD • Pritha Ray, PhD • Viola Rieke, PhD • Sandra Rodriguez, RT (R)(MR) • Jarrett Rosenberg, PhD • Ruminder Samra, RT • Anne Marie Sawyer, BS, RT (R) • Greig Scott, PhD • Bronislava Sigal, PhD • Stefan Skare, PhD • Marc Sofilos, RT • Muru Subbarayan, PhD • Ron Watkins • Shahriar Yaghoubi, PhD • Yishan Yang • Marowan • Zakhour, MD • Lei • Zhu, MS • Stephanie • Bailey, PhD • Weibo • Cai, PhD • Feng • Cao, PhD • Qizhen • Cao, PhD • Carmel • Chan, PhD • Kai • Chen, PhD • Ted • Chu, PhD • Nga-Wai • (Tiffany) Chung, PhD • Anca Dragulescu • Andrasi • Byard • Edwards, MD, PhD • Frank Cochran, PhD • Hua Fan-Minogue, PhD • Gayatri • Gowrishankar, PhD • Mei Huang, PhD • Andrei Iagaru, MD • Shay Keren, PhD • Richard Kimura, PhD • Allison Kurian, MD, MS • Ha-Young Lee, PhD • Sheen-Woo Lee, MD • 2007 • Zi-bo Li, PhD • Zongjn Li, PhD • Hin-Tsu Jill Lin, PhD • Chunlei Liu, PhD • Amelie Lutz, MD • Gang Niu, PhD • Jinha Park, MD, PhD • Maxim Pashkevich, PhD • Hao, Peng, PhD • Laura Pisani, PhD • Jennifer Prescher, PhD • Hongjun Ren • Cesar Rodriguez, MD • Babak Shahbaba, PhD • Bryan Smith, PhD • Matus Straka, PhD • Rutger-Jan • Swijnenburg, PhD • Maurice Van den Bosch, MD • Arne Vandenbroucke, PhD • Hui Wang, PhD • Sen Wang, PhD • Yingbing Wang, PhD • Juergen Willmann, MD • Yun Wu, PhD • Zuyong Xia, PhD • Fei Xiao, PhD • Xiaoyan Xie, PhD • Yun Xing, PhD • Hequan Yao, PhD • Christina Zavaleta, PhD • Yan Zhang, PhD • Jingying Sarah Zhang, PhD • Graduate Students • Arpit Aggarwall, MS • Murat Aksoy, MS • Jongduk Baek, MS • Priti • Balchandani, PhD • Christopher Caires • Ian Chen, MD/PhD • Jean Chen, MS • Adam de la Zerda, BSc • Kristi Granlund, MS • Meng Gu, MS • Misung Han, MS • Andrew Holbrook, MS • Yanle Hu, PhD • Caroline Jordan, MS • Sonal Josan, MS • Elena Kaye, MS • Frances Lau • Christine Law, MS • Yakir Levin, PhD • Calvin Lew, MS • Pasheel Lillaney, MS • Ray Lin, MS • Susan Shu-An Lin, MS • Wenmiao Lu, MS • Sam Mazin, PhD • Peter Olcott, PhD • Guillem Pratx, PhD • Rebecca Rakow-Penner, BS • Julia Rasooly • Debashis Sahoo, MS • Heiko Schmiedeskamp, MS • Anthony Sherbondy, MS • Jared Starman, MS • Ernesto Staroswiecki • Moriah Thomason, MS • Ricky Tong, MS • Emily Tsai, BS • Chardonnay Vance, MS • Kitch Daniel Wilson • Jung Ho Won, MS • Serena Wong • Yao-Hung Yang, MS • David Yerushalmi, MS • Sung-Won Yoon, MS • Ryan Youland • Jian Zheng, MS • Visiting Researchers and Scholars • Maximilan Haeberlin, PhD • Joachim Hornegger, PhD • Sun Kim, PhD • Kopenigg Daniel, PhD • Minkyung So, PhD • Zhengming Xiong, MD, PhD • Xianzhong Zhang, PhD • Manish Patel, M.S. • Zachary Walls, M.S. • Richard M. Lucas Center for Imaging, Stanford University School of Medicine • Richard M. Lucas Center for Imaging, Stanford University School

## Lucas Family Now...



2007

MS • Ha-Young Lee, PhD • Sheen-Woo Lee, MD • 2007 • Zi-bo Li, PhD • Zongjn Li, PhD • Hin-Tsu Jill Lin, PhD • Chunlei Liu, PhD • Amelie Lutz, MD • Gang Niu, PhD • Jinha Park, MD, PhD • Maxim Pashkevich, PhD • Hao, Peng, PhD • Laura Pisani, PhD • Jennifer Prescher, PhD • Hongjun Ren • Cesar Rodriguez, MD • Babak Shahbaba, PhD • Bryan Smith, PhD • Matus Straka, PhD • Rutger-Jan • Swijnenburg, PhD • Maurice Van den Bosch, MD • Arne Vandenbroucke, PhD • Hui Wang, PhD • Sen Wang, PhD • Yingbing Wang, PhD • Juergen Willmann, MD • Yun Wu, PhD • Zuyong Xia, PhD • Fei Xiao, PhD • Xiaoyan Xie, PhD • Yun Xing, PhD • Hequan Yao, PhD • Christina Zavaleta, PhD • Yan Zhang, PhD • Jingying Sarah Zhang, PhD • Graduate Students • Arpit Aggarwall, MS • Murat Aksoy, MS • Jongduk Baek, MS • Priti • Balchandani, PhD • Christopher Caires • Ian Chen, MD/PhD • Jean Chen, MS • Adam de la Zerda, BSc • Kristi Granlund, MS • Meng Gu, MS • Misung Han, MS • Andrew Holbrook, MS • Yanle Hu, PhD • Caroline Jordan, MS • Sonal Josan, MS • Elena Kaye, MS • Frances Lau • Christine Law, MS • Yakir Levin, PhD • Calvin Lew, MS • Pasheel Lillaney, MS • Ray Lin, MS • Susan Shu-An Lin, MS • Wenmiao Lu, MS • Sam Mazin, PhD • Peter Olcott, PhD • Guillem Pratx, PhD • Rebecca Rakow-Penner, BS • Julia Rasooly • Debashis Sahoo, MS • Heiko Schmiedeskamp, MS • Anthony Sherbondy, MS • Jared Starman, MS • Ernesto Staroswiecki • Moriah Thomason, MS • Ricky Tong, MS • Emily Tsai, BS • Chardonnay Vance, MS • Kitch Daniel Wilson • Jung Ho Won, MS • Serena Wong • Yao-Hung Yang, MS • David Yerushalmi, MS • Sung-Won Yoon, MS • Ryan Youland • Jian Zheng, MS • Visiting Researchers and Scholars • Maximilan Haeberlin, PhD • Joachim Hornegger, PhD • Sun Kim, PhD • Kopenigg Daniel, PhD • Minkyung So, PhD • Zhengming Xiong, MD, PhD • Xianzhong Zhang, PhD • Manish Patel, M.S. • Zachary Walls, M.S. • Richard M. Lucas Center for Imaging, Stanford University School of Medicine • Richard M. Lucas Center for Imaging, Stanford University School

# RADIOLOGY SCIENTIFIC RESEARCH PERSONNEL

## FACULTY AND STAFF

### FACULTY

Roland Bammer, PhD  
 Sandip Biswal, MD  
 Kim Butts Pauly, PhD  
 Xiaoyuan (Shawn) Chen, PhD  
 Zehn Cheng, PhD  
 Rebecca Fahrig, PhD  
 Sam Gambhir, MD, PhD  
 Gary M. Glazer, MD  
 Gary H. Glover, PhD  
 Samira Guccione, PhD  
 Brian Hargreaves, PhD  
 Robert J. Herfkens, MD  
 Craig Levin, PhD  
 Michael E. Moseley, PhD  
 Sandy Napel, PhD  
 David Paik, PhD  
 Norbert J. Pelc, ScD  
 Sylvia K. Plevritis, PhD  
 Andy Quon, MD  
 Jianghong Rao, PhD  
 Daniel M. Spielman, PhD  
 Joseph Wu, MD, PhD  
 Greg Zaharchuk, MD, PhD

### ADMINISTRATIVE AND SUPPORT STAFF

Mary Bobel, MBA  
 Maggie Bos  
 Michelle Christerson  
 Bonita Crabbe  
 Donna Cronister  
 Debra Frank  
 Elizabeth Gill  
 Sofia Gonzales, MS  
 Sondra Horn  
 Mandeep Kaur  
 Susan Kopiwoda, MS, MPH  
 Marlys Lesene  
 Donna Niernberger  
 Sharon Pollio  
 Kala Raman  
 John Reuling  
 Lanzie Rivera  
 Julie Ruiz, PhD

David Russel  
 Monique Schareck, MHA  
 Susan Singh  
 Betsey Sowder  
 Susie Spielman  
 Lakeesha Winston  
 Wei Xiong

### SCIENTIFIC STAFF

Marcus Alley, PhD  
 Neal Bangerter, PhD  
 Wendy Baumgardner, RVT, LATg  
 Rhona Berganos, BS  
 Thomas Brosnan, PhD  
 Zhen Cheng, PhD  
 Danye Cheng  
 Frederick Chin, PhD  
 Garry Chinn, PhD  
 David Clayton, PhD  
 Abhijit De, PhD  
 David Dick, PhD  
 Aihua Fu, PhD  
 Arundhuti Ganguly, PhD  
 Andrew Gentles, PhD  
 Lina He, PhD  
 Pam Hertz  
 Jung-Jin (Jason) Hsu, PhD  
 William Johnsen  
 Anitha Jununtula  
 Seungbum Koo  
 Keshni Kumar, CRT  
 Andy Lamb  
 Malika Larabi, PhD  
 Jelena Levi, PhD  
 Andreas Loening, PhD  
 Dirk Mayer, PhD  
 Mohammed Namavari, PhD  
 Rexford Newbould, PhD  
 Linda Novello, RT  
 Laura Pierce, MPA, RT  
 Paulmurgan Ramasamy, PhD  
 Pritha Ray, PhD  
 Viola Rieke, PhD  
 Sandra Rodriguez, RT (R)(MR)

Jarrett Rosenberg, PhD  
 Ruminder Samra, RT  
 Anne Marie Sawyer, BS, RT  
 (R)(MR)  
 Greig Scott, PhD  
 Bronislava Sigal, PhD  
 Stefan Skare, PhD  
 Marc Sofilos, RT  
 Muru Subbarayan, PhD  
 Ron Watkins  
 Shahriar Yaghoubi, PhD  
 Yishan Yang, PhD  
 Marowan Zakhour, MD  
 Lei Zhu, MS



# RADIOLOGY SCIENTIFIC RESEARCH PERSONNEL

## STUDENTS AND VISITORS

### POSTDOCTORAL FELLOWS

Stephanie Bailey, PhD  
 Weibo Cai, PhD  
 Feng Cao, PhD  
 Qizhen Cao, PhD  
 Carmel Chan, PhD  
 Kai Chen, PhD  
 Ted Chu, PhD  
 Nga-Wai (Tiffany) Chung, PhD  
 Anca Dragulescu-Andrasi  
 Byard Edwards, MD, PhD  
 Frank Cochran, PhD  
 Hua Fan-Minogue, PhD  
 Gayatri Gowrishankar, PhD  
 Mei Huang, PhD  
 Andrei Iagaru, MD  
 Shay Keren, PhD  
 Richard Kimura, PhD  
 Allison Kurian, MD, MS  
 Ha-Young Lee, PhD  
 Sheen-Woo Lee, MD  
 Zibo Li, PhD  
 Zongjin Li, PhD  
 Hin-Tsu Jill Lin, PhD  
 Chunlei Liu, PhD  
 Amelie Lutz, MD  
 Gang Niu, PhD  
 Jinha Park, MD, PhD  
 Maxim Pashkevich, PhD  
 Hao Peng, PhD  
 Laura Pisani, PhD  
 Jennifer Prescher, PhD  
 Hongjun Ren  
 Cesar Rodriguez, MD  
 Babak Shahbaba, PhD  
 Bryan Smith, PhD  
 Matus Straka, PhD  
 Rutger-Jan Swijnenburg, PhD  
 Maurice Van den Bosch, MD  
 Arne Vandenbroucke, PhD  
 Hui Wang, PhD  
 Sen Wang, PhD  
 Yingbing Wang, PhD  
 Juergen Willmann, MD

Yun Wu, PhD  
 Zuyong Xia, PhD  
 Fei Xiao, PhD  
 Xiaoyan Xie, PhD  
 Yun Xing, PhD  
 Hequan Yao, PhD  
 Christina Zavaleta, PhD  
 Yan Zhang, PhD  
 Jingying Sarah Zhang, PhD

### GRADUATE STUDENTS

Arpit Aggarwall, MS  
 Murat Aksoy, MS  
 Jongduk Baek, MS  
 Priti Balchandani, PhD  
 Christopher Caires  
 Ian Chen, MD, PhD  
 Jean Chen, MS  
 Jing Chen, MS  
 Adam de la Zerda, BSc  
 Angela Foudray, MS  
 Kristi Granlund, MS  
 Meng Gu, MS  
 Misung Han, MS  
 Andrew Holbrook, MS  
 Thomas Hope, BS  
 Yanle Hu, PhD  
 Caroline Jordan, MS  
 Sonal Josan, MS  
 Elena Kaye, MS  
 Frances Lau  
 Christine Law, MS  
 Yakir Levin, PhD  
 Calvin Lew, MS  
 Pasheel Lillaney, MS  
 Ray Lin, MS  
 Susan Shu-An Lin, MS  
 Wenmiao Lu, MS  
 Sam Mazin, PhD  
 Peter Olcott, PhD  
 Guillem Pratx, PhD  
 Rebecca Rakow-Penner, BS  
 Julia Rasooly  
 Debashis Sahoo, MS

Heiko Schmiedeskamp, MS  
 Anthony Sherbondy, MS  
 Jared Starman, MS  
 Ernesto Staroswiecki  
 Moriah Thomason, MS  
 Ricky Tong, MS  
 Emily Tsai, BS  
 Chardonnay Vance, MS  
 Kitch Daniel Wilson  
 Jung Ho Won, MS  
 Serena Wong  
 Yao-Hung Yang, MS  
 David Yerushalmi, MS  
 Sung-Won Yoon, MS  
 Ryan Youland  
 Jian Zheng, MS

### VISITING RESEARCHERS AND SCHOLARS

Maximilian Haeberlin, PhD  
 Joachim Hornegger, PhD  
 Sun Kim, PhD  
 Kopenigg Daniel, PhD  
 Min-kyung So, PhD  
 Zhengming Xiong, MD, PhD  
 Xianzhong Zhang, PhD  
 Manish Patel, MS  
 Zachary Walls, MS



## AWARDS AND HONORS

Recipient	Award
PRITI BALCHANDANI, MS	2007 ISMRM Student Stipend Award.
PAT BASU, MD, MBA	AMA Excellence in Medicine Award (Pfizer Humanities Initiative).
CHRIS BEAULIEU, MD, PhD	Cum Laude Award for outstanding paper from the SCBT/MRI, "Isotropic MRI with 3D-FSE-XETA (Extended Echo Train Acquisition)," (Gold GE, Busse RF, Stevens K, Han E, Brau AC, Beatty P, Beaulieu CF).
SANDIP BISWAL, MD	AMI Top Scientific Abstract Award for "Simultaneous Non-Invasive Imaging of Estrogen Receptor Ligand Induced Homodimerization and Gene Transactivation in Living Mice," (Padmanabhan P, Ramasamy P, Gambhir SS, Biswal S).
WEIBO CAI, PhD	Benedict Cassen Postdoctoral Fellowship from the Society of Nuclear Medicine.
WEIBO CAI, PhD	2007 SNM Young Professionals Best Basic Science Award: "Quantitative RadioimmunoPET of EphA2 Expression in Xenograft-Bearing Mice."
FENG CAO, PhD	2006 Circulation Best Basic Science Paper Award for "In Vivo Visualization of Embryonic Stem Cell Survival, Proliferation, and Migration after Cardiac Delivery."
ADAM DE LA ZERDA, BSc	1st prize in the Bay Area Entrepreneurship Contest for Laser Seal idea.
MELISSA ENRIQUEZ, MD	2007 Norman Blank Award for outstanding Radiology medical student.
DOMINIK FLEISCHMANN, MD	2006 Hounsfield Award for best scientific paper, SBCT.
SAM GAMBHIR, MD, PhD	AIMBE--Elected as a Fellow of the American Institute for Medical and Biological Engineering.
SAM GAMBHIR, MD, PhD	ACNP/SNM Best Essay Award for "F18 PET/CT Evaluation of Response to Therapy in Lymphoma: When Is the Optimal Time for the First Re-Evaluation Scan?"
SAM GAMBHIR, MD, PhD	2006 Aunt Minnie Award given for the Most Influential Radiology Researcher of 2006.
SAM GAMBHIR, MD, PhD	Co-host of the Nobel Symposium, "Watching Life through Molecular Imaging," along with Dr. Ringertz from May 6 to 9, 2007 at the Karolinska Institute in Stockholm, Sweden.
GARY M. GLAZER, MD	Honorary membership to the German Radiological Society, 2007.
GARY M. GLAZER, MD	Honorary membership to the Japanese Radiological Society, 2007.
GARRY E. GOLD, MD	2006 Lauterbur Award from the SCBT/MR: "Patellofemoral Pain: Analysis with Upright Real-Time MRI and 3D Finite Element Modeling."
GARRY E. GOLD, MD	2007 Cum Laude Award for outstanding paper from SBCT/MR: "Isotropic MRI with 3D-FSE-XETA (Extended Echo Train Acquisition)" (Gold GE, Busse RF, Stevens KJ, Han E, Brau AC, Beatty PJ, Beaulieu CF).
LUKE HIGGINS, PhD	Society of Interventional Radiology (SIR) Foundation Medical Student Research Grant.
PEI-LIN HSIUNG, PhD	American Cancer Society-Canary Foundation Postdoctoral Fellowship: "Development of Peptide Reagents for In Vivo Detection of Dysplasia in the Colon."

## AWARDS AND HONORS

### Recipient

MEI HUANG, PhD

HA-YOUNG LEE, PhD

YAKIR LEVIN, PhD

ZIBO LI, PhD

SAM MAZIN, PhD

IAIN ROSS McDUGALL, MD, PhD

JOSEPH MCGINLEY, MD, PhD

MATILDE NINO-MURCIA, MD

NORBERT PELC, ScD

SYLVIA PLEVritis, PhD

ANDREW QUON, MD

JIANGHONG RAO, PhD

HANS RINGERTZ, MD, PhD

EUN KYOUNG RYU, PhD

RICKY TONG, PhD

RICKY TONG, PhD

DAVID N. TRAN, BS

JOSEPH WU, MD, PhD

### Award

American Heart Association (AHA) Postdoctoral Fellowship Grant for 2007 to 2009.

Korean Research Foundation (KRF) Scholarship.

2006-07 ARCS Award (Achievement Rewards for College Scientists).

2007 SNM Best Basic Science Award.

Society of Photo-Optical Instrumentation Engineers (SPIE) Cum Laude Award for "A Fast 3D Reconstruction Algorithm for Inverse-Geometry CT Based on an Exact PET Rebinning Algorithm."

Distinguished Scientist Award from the Western Region of the Society of Nuclear Medicine, October 2006.

Participant in the Siemens Outstanding Academic Research (SOAR) Award Program: Awards for Excellence in Cardiac CT.

Received the 2006 Inspirational Immigrant Professional of the Year (IIPY) Award from Upwardly Global at the Commonwealth Club of California in San Francisco.

Elected to the College of Fellows of the American Institute for Medical and Biological Engineering (AIMBE) for his contributions to our field as a scientist, engineer, educator, and mentor for over three decades.

Honorable Mention for study on the cost-effectiveness of breast MRI (Plevritis et al, *JAMA* 2006 May 24;295(20):2374-84), which was highly cited in a landmark decision by the American Cancer Society.

Best Image and Article of the Year for paper entitled "'Flying Through' and 'Flying Around' a PET/CT Scan: Pilot Study and Development of 3D Integrated 18F-FDG PET/CT for Virtual Bronchoscopy and Colonoscopy" (Quon A, Napel S, Gambhir SS, Beaulieu C). Awarded by Society of Nuclear Medicine (SNM).

Named 2007 Young Investigator by the Human Frontier Science Program.

Named president-elect of the International Society of Radiology (ISR) at the 2006 International Congress of Radiology (ICR).

2007 Dean's Fellowship Award.

Chinese American Medical Society Fellowship, 2007.

2007 SNM Fellowship for a transgenic mouse with the ubiquitous expression of a triple-fusion reporter protein.

SBCT/MR in Training Award for "Promises and Limitations of Dual-Energy CT in Lower Extremity CT Angiography" (Tran DN, Roos J, Straka M, Sandner D, Razavi H, Chang M, Pelc N, Napel S, Fleischmann D).

Circulation Best Basic Science Paper for "In Vivo Visualization of Embryonic Stem Cell Survival, Proliferation, and Migration after Cardiac Delivery" (Cao F, Lin S, Xie X, Ray P, Patel M, Zhang X, Drukker M, Dylla SJ, Connolly AJ, Chen X, Weissman IL, Gambhir SS, Wu JC).



# RESEARCH GROUP UPDATES

15 YEARS ON THE CUTTING EDGE





## RSL GROUP UPDATES

## MAGNETIC RESONANCE RESEARCH

## Neuroimaging Functional Imaging–Technology Development

GARY GLOVER, PHD

The functional MRI group continues to develop new methods for the acquisition of functional imaging data. Projects include the development of alternative fMRI contrast methods, real-time biofeedback for training brains, 3D fMRI acquisitions, and the calibration of fMRI using breath holding measurements. In addition, we continue to play an active role in the NCRR-funded FIRST BIRN schizophrenia test bed project, with Gary Glover as the chair of the calibration working group. The following are a few of the highlights; see abstracts for further details.

Christine Law has been studying the use of a new method for speeding up fMRI acquisitions, using spiral parallel imaging. The technique uses conventional two-shot spiral acquisitions and a novel method of reconstruction in which the sensitivity maps are generated from every other, fully sampled acquisition. This self-calibration approach provides an initially unexpected benefit in that the signal-to-noise ratio is improved by virtue

of thermal noise cross correlation between the sense maps and the reconstructed images. The technique will be most beneficial for high-resolution scans, where the readout time is reduced and the thermal noise tends to be dominant.

The real-time fMRI projects include collaborations with Sean Mackey (director of the Stanford Pain Center, Anesthesiology); Allan Reiss (director of the Center for Interdisciplinary Brain Sciences Research, Psychiatry); Ian Gotlib, (director of the Mood and Anxiety Disorders Lab, Psychology); and Brian Knutson, Psychology. Experiments in the areas of pain, depression, learning disorders, and addiction are ongoing, and the results suggest that subjects can learn to modulate brain areas associated with these disorders using imaging-guided feedback.

Graduate student Yanle Hu has largely concluded his study of high resolution 3D spiral fMRI acquisitions. Results show that 3D methods have advantages in these high-resolution applications but not for low-resolution scanning because of the properties of the physiological noise. Previous studies showed mixed results because the noise contributions were not understood. His methods are being applied by several groups interested in the visual cortex. Yanle recently defended his thesis and will be taking

a position at the University of Texas at Austin this fall.

Jung Jiin (Jason) Hsu, a postdoctoral scholar, has developed a rapid T1 mapping method with which functional contrast has been obtained. This is yet another method of fMRI that shows promise in reducing the deleterious signal dropout problem in the frontal regions of the brain. He is extending this work to

develop quantitative ways of mapping brain oxygenation for tumor and stroke imaging, and he is collaborating with radiologist Greg Zaharchuk.

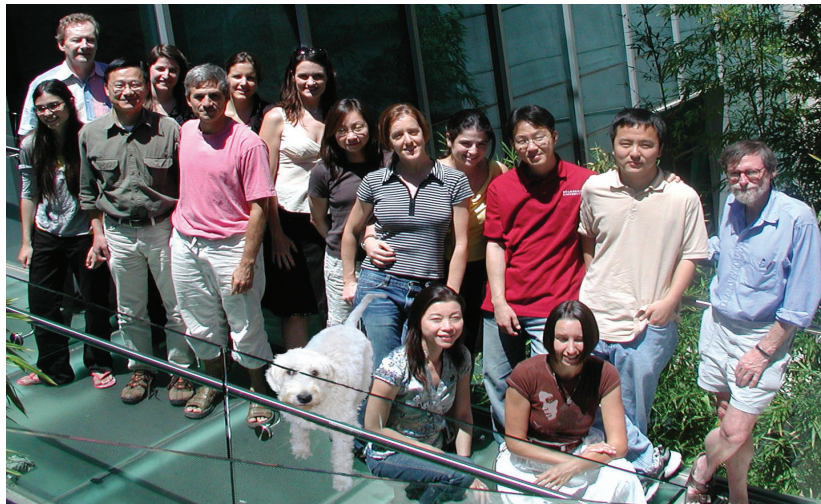
Chardonay Vance is a graduate student at UC Berkeley and Stanford, and she is studying aging processes as well as the biochemistry of placental membranes. Using measurements of NMR relaxation times and other parameters in vitro and in vivo, she is developing a new understanding of the various transport mechanisms in the placenta in health and IUGR.

Rebecca Rakow-Penner, a graduate student in biophysics and a third-year medical student, is

examining the use of functional methods to characterize breast cancer. She recently passed her medical board, and is returning to a more active research role.

Moriah Thomason Caires received her PhD during the year and is now serving as a postdoctoral student under Ian Gotlib and Gary Glover. We have concluded an experiment investigating the use of behavioral feedback to enhance the precision of the breath holding for fMRI calibration and found good utility to the new method. We now have a publication from this research in press in *Neuroimage*.

Catherine (Catie) Chang, an electrical engineering student interested in fMRI/EEG acquisitions, has been investigating denoising methods to allow the concurrent use of the two modalities. She has recently undertaken a new project investigating the dynamics of brain intrinsic networks. She has found evidence that the hemodynamic delays between various network nodes can be large enough to cause confounds in the interpretation of results, which is an issue that has been completely ignored to date by the brain imaging community. She is also interested in the processing of real-time fMRI signals for biofeedback, using ICA and support vector machines as state classifiers.



*This is my wonderful group as of July 2007—my colleagues and my friends, whom I love with my heart. I am privileged to be challenged by and to learn from them. fMRI group: Back (l-r standing), Catie Chang, Paul Mazaika, Jung-Jiin Hsu, Allyson Rosen, Philippe Goldin, Joelle Barral, Moriah Thomason Caires, Christine Law, Laura Pisani, Rebecca Rakow-Penner, Jongho Lee, Yanle Hu, Gary Glover. Front (l-r, kneeling), Fumiko Hoeft, Chardonay Vance. The furry dude is Tosca Caires. Not shown, Jin Hyung Lee and Sean Mackey.*

## FUNCTIONAL "MICROVASCULAR" NEUROIMAGING

ROLAND BAMMER, PhD, AND MICHAEL MOSELEY, PhD

State-of-the-art advances in magnetic resonance imaging (MRI) continue to improve adult and pediatric neuroimaging. Using functional MRI, we can now map and measure brain tissue water diffusion rates and direction, the perfusion of blood, and the brain's response to many functional activation tasks (such as vascular responses to mild reversible stresses) in a large number of diseases.

During the past year, we continued to make significant progress in developing functional imaging technologies in several key areas. These included diffusion and perfusion techniques for the imaging of acute stroke and for the imaging of white matter structure and integrity. We began to use the new 7 tesla MRI scanner to improve higher-resolution tools of high-field and high-speed MRI, focusing on disease processes in "brain attacks" (cerebral stroke) in both adults and in children using diffusion MRI (DWI), tissue perfusion mapping (PWI), as well as the new field of mapping the brain connectivity, DTI. By responding to the needs of our collaborators and colleagues here at Stanford and worldwide, we have found that diffusion and perfusion techniques have significantly advanced far beyond the experimental arena into everyday, routine clinical applications in a wide variety of fields where they are being actively and effectively used in numerous self-initiated and collaborative studies.

Major strides have been made migrating research acquisition and reconstruction methods to our hospital systems with *quasi* product performance to facilitate clinical studies. Moreover, considerable improvements in image quality have been achieved for DTI at 3T. In the next year, we are eager to move these methods from workbench to bedside. With two clinical 3T MRIs on the horizon, we will further advance our MR imaging tools and sharpen our focus on the critical clinical issues in the coming year with new experimental and clinical MR methods to predict eventual brain injury; to detect diffuse abnormalities in the brain occult to conventional imaging; to further map how the brain and spine are "wired"; to understand the complex physiological stresses and changes that the brain experiences during ischemia and other pathologic processes; and to extend these tools to better evaluate evolving therapies. A recent research effort is focused on real-time motion correction of MRI scans with a special focus on children. This prospective approach is a major paradigm change and might help to reduce the sedation needed during the imaging of children.

Over the last few years, we were lucky to assemble a critical mass of highly qualified and remarkably creative researchers who are well sought-after in their field. Their unique expertise and industriousness have allowed us to design highly innovative methods that significantly strengthened the quality of both diffusion-weighted and perfusion-weighted MRI.

Roland Bammer is an established faculty member at the Lucas Center where he serves as an assistant professor of radiology and imaging physicist for pediatric radiology. He has created several key collaborations with the Departments of Neurology and Pediatrics and has already initiated an active pediatric DTI program on the Lucile Packard Children's Hospital MRI scanner. Roland is an expert in parallel imaging with a special focus on

applying this method to diffusion and perfusion imaging. He was a recent visiting professor at Bosphorus University, Istanbul, Turkey, and he is also a university docent at the University of Graz, Austria. Roland has two funded peer-reviewed grants from the NIH. He directs one multi-center trial, and has been named as "key personnel" on ten others. During the last year, Roland served as reviewer on several NIH study sections and is a member on the editorial board of *Magnetic Resonance in Medicine*.



*Functional Microvascular Neuroimaging group: Left row (front to back), Roland Bammer; Chunlei Liu, Murat Aksoy, Daniel Kopeinigg, Matus Straka. Middle row (front to back), Samantha Holdsworth, Maximillian Haeberlin, Michael Moseley, Rexford Newbould. Right row (front to back), Lanzie Rivera, Heiko Schmiedeskamp, Kian Zhang, Stefan Skare.*

Mike Moseley is the past president of the International Society of Magnetic Resonance in Medicine (ISMRM) and has had two key grants funded recently, including an NCRR grant for a \$2M experimental GE 7T MRI scanner. Mike is a leading expert and pioneer of stroke imaging. He also sits on different NIH study sections.

The neuroimaging team remains involved in white matter tensor "fiber-tracking" neuroimaging projects as well as building collaborative programs. Jean-Marc Olivot has started working with Mike this year as a postdoctoral fellow. Jean-Marc is a stroke neurologist and is focusing on a comparative evaluation of Xenon-enhanced CT perfusion and MR perfusion. Jian Zhang is a third-year graduate student actively involved in 3D volume spiral imaging for diffusion applications. Chunlei Liu is a first-year postdoctoral scholar who has received a highly-regarded K99 award from the NIH on high-field applications of DWI. Murat Aksoy is a fourth-year graduate student working with Roland on the exciting applications in fiber tractography and on motion correction projects. Rexford Newbould is a research associate with a background in IC design and is currently involved in MR



post-processing perfusion data and real-time motion correction with Roland. Lanzie Rivera is our administrative associate. Stefan Skare is a research associate and visiting scholar from Sweden working with Roland. Stefan is focused on multi-shot MR sequences for high-resolution diffusion in the presence of patient motion.

Over the last year, our group has expanded greatly. Samantha Holdsworth from New Zealand has joined our lab. Together with Roland and Stefan, she is working on high-resolution diffusion sequences at 3T. Matus Straka, from the Vienna General Hospital (Austria) and the Computer Graphics Department of the University of Vienna, is focused on parallel computing issues for image reconstruction and quantitative parameter mapping. Heiko Schmiedeskamp, a graduate student from the ETH in Zurich, joined us as a visiting researcher and tested a promising new multi-echo sequence for functional MRI. Heiko was successfully

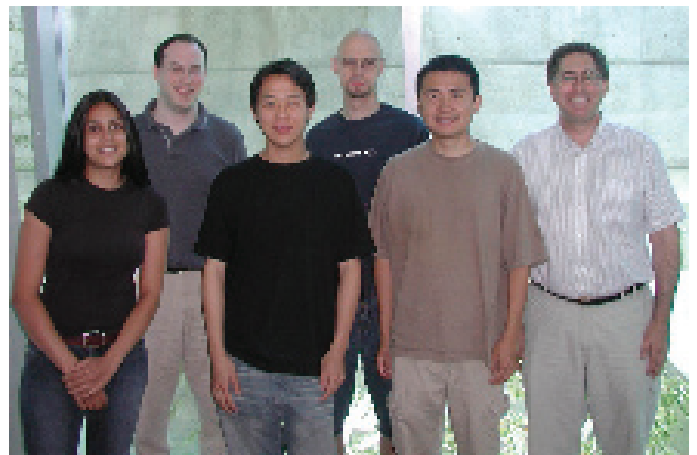
admitted to the Stanford Bioengineering PhD Program and will stay for a couple more years in our lab. During the last year, Anders Nordell, from the Karolinska Institute in Stockholm, Sweden, has been working with us on selected topics of echo-planar imaging. Anders will continue working with us remotely as Stefan's first graduate student in Stockholm. His clever work on EPI ghost correction led to significantly accelerated image reconstruction times. Daniel Kopeinigg is another visiting researcher who works with Roland, Marcus Alley, and Dominik Fleischmann on contrast-enhanced angiography with a special focus on improving contrast injection profiles to achieve desired enhancement profiles in the arterial system. Recently, Maximilian Haerberlin has joined us as a visiting researcher from the ETH in Zurich. Max has started working on a reconstruction algorithm for highly undersampled MR data to improve temporal resolution.



## IN VIVO SPECTROSCOPY AND MULTINUCLEAR IMAGING

DANIEL SPIELMAN, PhD

We have continued our research in the development of novel magnetic resonance spectroscopy (MRS) and spectroscopic imaging (MRSI) techniques. Areas of particular focus include optimized techniques for ultrahigh field (7T) proton spectroscopy of the brain and hyperpolarized  $^{13}\text{C}$  imaging and spectroscopy. Hyperpolarized  $^{13}\text{C}$  is an exciting new technology capable of directly probing key metabolic pathways by providing several orders of magnitude of increased signal than previously available from  $^{13}\text{C}$ -labeled compounds injected into the body. A new polarizer for this program has been installed as part of a collaborative agreement among SRI International, GE Healthcare, and the Stanford Department of Radiology. Our initial studies are focused on small rodent animal models.



*MR Spectroscopy group: (l-r), Priti Balchandani, Yakir Levin, Calvin Lew, Dirk Mayer, Meng Gu, Dan Spielman.*

## BODY MR IMAGING

BRIAN A. HARGREAVES, PhD

Our body MR imaging group addresses applications of MRI to clinical body imaging. Our research includes abdominal imaging, cardiovascular imaging, breast imaging, and musculoskeletal imaging, collaborating with numerous clinical faculty, engineering faculty, and GE's Applied Sciences Laboratory.

Wenmiao Lu has developed some highly-efficient and robust methods to separate water and fat in MR images. This is of critical importance for breath-held scanning, where scan times currently limit the spatial resolution that can be achieved in 3D images. Misung Han has implemented parallel imaging techniques to significantly increase frame rates in dynamic contrast-enhanced breast imaging to diagnose and classify breast tumors. Her techniques have been used on over 100 patients already. Anthony Faranesh, who recently moved to the NIH, has developed tools to analyze contrast kinetics for cancer imaging, which will soon become a routine part of patient protocols. Reduced sodium levels are an important indicator of cartilage degeneration. Ernesto Staroswiecki and Neal Bangerter have produced some



*Body MR Imaging group: Back row (l-r), Kristin Granlund, Neal Bangerter, Wenmiao Lu, Misung Han, Caroline Jordan, Philip Vuong, Anderson Nnewiwe. Front row (l-r), Brian Hargreaves, Marlys LeSene, Ernesto Staroswiecki, Marcus Alley.*

of the highest-quality 3D sodium MR images of cartilage at 3.0T and 7.0T, in collaboration with Dr. Garry Gold. They have also begun testing sodium imaging for cancer assessment in the breast, leading to recent funding from the California Breast Cancer Research Program. Kristin Granlund has worked on off-resonance correction methods and is now developing new non-contrast methods to assess perfusion.

We also have collaborations with Dr. Bruce Daniel in breast MRI research. As described above, one of our major achievements is the integration

of a fully-bilateral breast imaging protocol, which is now the standard patient protocol at the Hospital. Simultaneous bilateral breast imaging will mean that most patients will only have to have a single MR exam, rather than the current multi-exam procedure. Finally, we continue to support the imaging components of numerous biomechanics projects in collaboration with Drs. Thomas Andriacchi and Nicholas Giori. These projects have a common goal of investigating the origins of osteoarthritis for which MRI is an important diagnostic tool.

## INTERVENTIONAL AND OPEN MRI

KIM BUTTS PAULY, PhD

Our interventional MRI group is developing several MR-guided thermal therapy interventions in order to increase treatment options for prostate, breast, and liver cancers. In the area of MR-guided cryoablation of the prostate, we have been developing improved methods for imaging frozen tissue. The work here has

centered on developing improved imaging methods for ultrashort TE imaging, including eddy current compensated PR sequences and composite half RF pulses. Additionally, we are investigating the imaging appearance of previously frozen tissue on MT, DWI, and CE MRI and correlating these results to histology, both acutely and as the thermal lesion evolves over time. In the area of MR-guided ultrasound ablation of the prostate, we have been working with collaborators at UCSF to develop a transurethral delivery system, combined with our improved MR imaging



*Interventional and Open MRI group: (l-r), Andrew Holbrook, Viola Rieke, Ron Watkins, Serena Wong, Sonal Josan, Kim Butts Pauly, Jing Chen, Elena Kaye.*

methods. MT, DWI, and CE MRI are also providing assessment of the tissue after ultrasound ablation. For the MR-guided focused ultrasound ablation of the liver, we are developing a handheld system in collaboration with GE, where the focal point is tracked in real-time. With collaborators in electrical engineering, we are investigating the applicability of CMUTs

to therapeutic applications. We have shown that CMUTs can be operated continuously at durations and power levels consistent with HIFU. For this project, we are also developing rapid MR thermometry methods suitable for monitoring liver ablations. Future work for our group includes working with the InSightec focused ultrasound system, which was installed on the 3T system at the Lucas Center in February. This system is FDA approved for fibroid ablation and is in clinical trials in several other applications.



## ADVANCED X-RAY TECHNIQUES

## X-RAY GUIDANCE OF INTERVENTIONAL PROCEDURES

REBECCA FAHRIG, PhD

Our group leader, Dr. Fahrig, continues to conduct research on the X-ray guidance of interventional procedures and X-ray system development in both the Axiom Lab (C-arm CT system development) and the Advanced X-Ray Imaging Lab (table-top cone beam CT system and X-ray/MR system development). We are also improving the image quality of C-arm CT images by developing new methods to correct for the lag in digital flat panels (see abstract by Starman) and to correct for scatter in volumetric X-ray CT (see abstract by Zhu). Our NIH R-21 investigative grant was recently funded and will allow the transition of our new scatter correction technique from the bench into the clinic.

We have continued to improve the automatic analysis of stents in the superficial femoral artery (see abstract by Ganguly and Keck) by acquiring images of in vivo stents with the patient placed in different positions to determine how stents deform under stress.



*X-Ray Guidance of Interventional Procedures group: Back row (l-r), Prasheel Lillaney, Jared Starman, Sungwon Yoon. Front row (l-r), Erin Girard-Hughes, Rebecca Fahrig, Marlys LeSene, Arun Ganguly.*

This work is possible due to the very high resolution of C-arm CT images and the flexibility of the open “C-arm” geometry of the acquisition system hardware. Our investigation of 3D imaging during radiofrequency ablation of atrial fibrillation in the cardiac interventional suite continues (see abstract by Girard), and our first volunteer trial in patients prior to treatment is underway. Our image optimization work is funded by the NIH and also benefits from close collaboration with the AX Division of Siemens Medical Solutions and with Varian Medical Systems. The cardiac C-arm CT work is a project sponsored by Siemens Medical Solutions, AX Division.

Our group’s research in new reconstruction approaches for CT acquisitions has expanded to include the application of level sets to the reconstruction of sparse data sets, with potential application in cardiac and lung imaging (see abstract by Yoon). We continue to develop our X-ray/MR project as we expand the availability of truly integrated XMR by placing a fluoroscopy system directly adjacent to a 1.5T closed-bore magnet (see abstract by Lillaney).

## INVERSE GEOMETRY CT AND CONVENTIONAL CT

NORBERT PELC, SCD

Led by Dr. Pelc, our group is researching the technology and applications of computed tomography (CT). An important group focus is aimed at understanding the basic limitations in current systems and, when physically possible, the development of solutions to effectively address these issues. Our main project in recent years has been the development of an advanced CT platform that uses an inverted imaging geometry and is therefore called inverse-geometry CT (IGCT).

Our long-term aim is to push the limits in CT performance and to aid in the development of new applications. Currently, our main project is to develop a system that can image an arbitrarily thick section of anatomy (e.g., an entire organ) in a single, fast rotation while producing uncompromised image quality and outstanding dose efficiency. The specific approach we are pursuing employs an inverse geometry with one critical aspect: a distributed X-ray source whose length is comparable to the thickness of the section being imaged. This approach presents many opportunities, and we have already demonstrated excellent spatial resolution and complete freedom from cone-beam artifacts, which can plague scientists using conventional systems when they try to image a thick region in a single scan. One major achievement this past year was the awarding of an NIH grant that is funding the development of the first full-size IGCT system, a project in close col-



*Inverse Geometry CT group: Back row (l-r), Jongduk Baek, Adam Wang, Yao Xie, Sam Mazin. Front row (l-r), Arun Ganguly, Norbert Pelc.*

laboration with GE Global Research Center.

IGCT also presents a number of problems in the image reconstruction step. We have continued to develop computationally efficient reconstruction methods, and we have demonstrated a technique that is both accurate and much faster than previous methods (see abstract by Mazin). One challenge in IGCT systems is related to the lack of a “reference detector” to monitor variations in the source output. We developed a technique that “bootstraps” reference channel information from the edge of the field of view inwards (see abstract by Baek). We also studied a class of reconstruction methods that are more tolerant than the con-

ventional filtered-back projection technique to truncated projection data. The low efficiency of X-ray sources is a significant challenge in all X-ray systems. We are conducting theoretical studies to understand the effect of design choices in the X-ray source on available X-ray intensity (see abstract by Ganguly). All CT systems (and many other medical imaging systems) can run into bottlenecks due to the need to transmit large amounts of raw data rapidly. We are studying data compression methods to alleviate these problems (see abstracts by Wang and Xie). Finally, we congratulate Sam Mazin on completing his PhD degree. We are lucky that he is staying in the lab as a postdoctoral fellow.

## IMAGE ANALYSIS, BIOINFORMATICS, SYSTEMS BIOLOGY, AND PROTEOMICS

## IMAGE DISPLAY AND ANALYSIS

SANDY NAPEL, PhD, CHRISTOPHER F. BEAULIEU, MD, PhD, DOMINIK FLEISCHMANN, MD, ANDREW QUON, MD, GEOFFREY RUBIN, MD

Our group addresses the field of image analysis, focusing on volumetric visualization, structure segmentation, quantitative analysis, and computer-aided detection of lesions. We believe the future of radiology will benefit from the continuously increasing “computations/dollar” in computing technology, as we continue to refine and evaluate these techniques and apply them and their derivatives to new areas. As the following examples illustrate, our advances have impacted many technical and clinical areas at Stanford: the suppression of bones and vascular calcifications from CT images acquired by newer “dual-energy” scanners (see abstract by Tran) to simplify the assessment of vascular disease; the determination of likely neuronal connections in the brain, as well as likely fiber distributions in the muscles, using MR images (see abstracts by Sherbondy) for understanding human anatomy and patient-specific conditions; the development of computer-aided methods for the detection of lung cancer (see abstracts by Roos and Yi) and colon cancer (see abstract by Sundaram); the automated generation of



*Image Display and Analysis group: Back row (l-r), Tejas Rakshe, Markus Kukuk, Ushah Kiran Kommi Reddi, Joong Ho (Johann) Won, Gennadiy Chuyeshov, David Tran. Front row (l-r), Jessica Faruque, Sandy Napel, Chin A. Yi. Hanging on wall, Padmavathi Sundaram, Anthony Sherbondy, Bhargav Raman.*

curved-planar images through blood vessels (see abstracts by Roos and Rakshe) for the simplified assessment of vascular disease; the development of methods for real-time stereo visualization of a guidewire in the context of a 3D volume (see abstracts by Kukuk and Chuyeshov) for more precise interventional therapeutic procedures; and the automated computation of peak-flow velocity using a novel ultrasound transducer (see abstract by Faruque) for reproducible determinations of carotid stenosis. Our group is highly collaborative, working with many Radiology

department investigators (including Chris Beaulieu, Dominik Fleischmann, Rusty Hofmann, Brooke Jeffrey, Justus Roos, Geoff Rubin) as well as many other Stanford faculty (including Scott Delp, bioengineering; Pierre Khuri-Yakub, electrical engineering; Brian Wandell, psychology). Based on our work, twelve new manuscripts have been accepted for publication, and eleven presentations were given at international meetings.

## IMAGING BIOINFORMATICS

DAVID PAIK, PhD

Our research lab is devoted to using computational methods for the analysis and modeling of imaging data with an emphasis on pre-clinical imaging and linking these to other non-imaging data sources. While the tremendous advances made in imaging physics provide ever clearer pictures, it is not the images themselves but, rather, the information extracted from these images that is paramount. We are developing analytic methods and models for small animal imaging that are a close, but not exact, analog to that of clinical imaging.

Our laboratory collaborates with several other groups and laboratories on both preclinical and clinical imaging projects. The collaboration with Dean Felsher's laboratory on characterizing oncogene-induced tumorigenesis has been quite successful. We continue to develop an image analysis pipeline to bring automation and objectivity to the analysis of a large number of time-varying 3D microCT datasets of the transgenic mice used in this experiment. Additionally, we have developed a model that infers aspects of tumor growth signaling from the imaging-derived growth kinetics. This model has been used to generate the first quantitative evidence to support the differential signal attenuation hypothesis put forth by Sharma et al. in 2006. Our laboratory is also working on a new col-



*Imaging Bioinformatics group: Back row (l-r), Jiantao Pu, David Paik, Arpit Aggarwal. Front row (l-r), Shradha Budhiraja, Jill Lin. Not shown, Guanglei Xiong (former rotation student), Florian Schmitzberger (new student).*

laboration with Alejandro Sweet-Cordero's laboratory on the characterization of tumor response to chemotherapy in a mouse model.

On the clinical side, our laboratory has also furthered work toward a clinical lung cancer computer-aided diagnosis system developed with the labs of Sandy Napel and Geoff Rubin. The first version of the overall CAD algorithm has now been fixed, and we are proceeding with a larger-scale clinical evaluation. The proper statistical evaluation of CAD-like methods has been problematic ever since these methods were first proposed. Current free-response ROC models lack the rigor of ROC methods. Our latest

work has proposed a novel statistical framework for FROC analysis that overcomes previous limitations and will dramatically improve statistical inference on this type of data.

Our other work involves running the quantitation and visualization resource for the ICMIC@Stanford program. Additionally, our lab, along with the labs of Sylvia Plevritis and Samira Guccione, has been leading efforts within the cancer nanotechnology community to form a framework for nanobioinformatics that will enable cancer researchers to have grid-enabled access to a multitude of cancer nanotechnology data and knowledge sources.

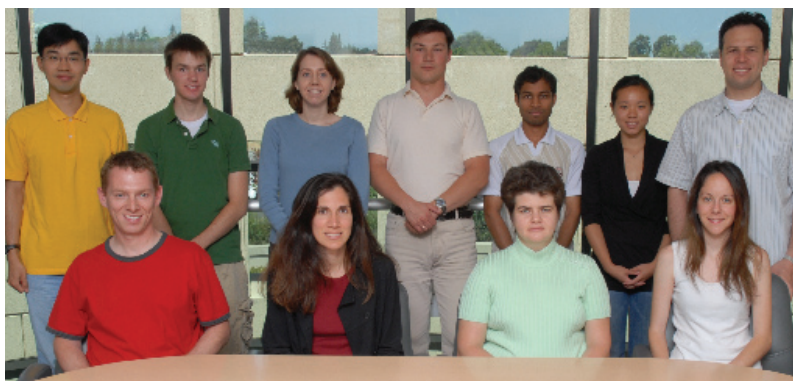


## MATHEMATICAL AND COMPUTATIONAL MODELING OF CANCER (MCMC) GROUP

SYLVIA PLEVritis, PhD

Our research program provides new insights into clinical cancer progression by integrating data from genomic, proteomic, pathological, imaging, and patient outcomes studies using novel mathematical and computational models. Our core research produces models of the natural history of cancer that describe the probabilistic behavior of tumor growth and metastatic spread. We apply these models to address important health policy questions, such as What impact has screening mammography had on breast cancer mortality in the U.S.? What impact has HRT had on the sensitivity of mammography and changes in breast cancer incidence trends in the U.S.? What are the expected outcomes for individuals at high risk for cancer who choose screening over prophylactic interventions? What impact could CT screening for lung cancer have on reducing lung cancer mortality and overall mortality? While these applied areas of our research are diverse, they are fundamentally similar from a mathematical perspective, thus the breadth of our research demonstrates the power of modeling.

We also analyze cancer progression at the molecular level by



*Mathematical and Computational Modeling of Cancer group: Back row (l-r), Ray Lin, Ryan Youland, Allison Kurian, Maksim Pashkevich, Debashis Sahoo, Emily Tsai, Babak Shahbaba. Front Row (l-r), Andrew Gentles, Sylvia Plevritis, Bronislava Sigal, Stephanie Bailey.*

developing and utilizing mathematical and computational models to understand how the “molecular circuitry” of cancer cells and their microenvironment are fundamentally different than that of normal cells. One of our major research goals is to analyze global gene and protein expression data to understand the transformation of lymphoma from low-grade to high-grade disease. Here, we provide molecular biologists with molecular targets that may eradicate low-grade

disease before it progresses. We are also analyzing “-omics” data to identify markers predictive of the treatment response in prostate cancer. The goal of this work is to provide molecular biologists with novel markers for monitoring cancer patients. Both of these programs embrace a “systems biology approach” to the study of cancer biology by having computational researchers working side-by-side with biological experimentalists. We believe that computational models are a critical tool in developing a multi-scale understanding of cancer progression and, ultimately, will help to identify optimal approaches to eradicate the cancer burden.

## PROTEOMICS, BIOMARKERS, AND NANOPARTICLE PLATFORMS FOR IMAGING THERAPEUTICS

SAMIRA GUCCIONE

The completion of the initial draft of the human genome and the rapid growth in high throughput assays, has opened a new era in translational research in medicine. The focus of our laboratory is translational research leading to agents for clinical use in detection, diagnosis, treatment, monitoring, and prognosis of clinical pathologies. We take a comprehensive approach in the design of agents that can span the “bench to bedside” timeline efficiently with our primary focus on the development of novel agents for cancer.

The research in our laboratory uses high throughput genomic and proteomic analysis on clinical pediatric and adult tissue samples to identify molecular targets. Ligands that bind these molecular targets are used to develop molecular imaging and therapeutic agents. We have developed a nanoparticle-based platform for attaching these ligands, thus creating targeted imaging and/or therapeutic agents. These targeted nanoparticles are first tested in vitro and used in in-vivo animal models, as molecular imaging probes. We have developed multimodality probes for MRI, gamma, fluorescent, and CT imaging. Visualization and quantitative evaluation of these targeted nanoparticles in vivo through molecular imaging, will provide in-



*Proteomics group: (l-r), Yi-Shan Yang, Christopher Caires, Samira Guccione, Regina Bower, Steven Choi.*

formation on the bio-distribution and accumulation of probes at the site of interest. Subsequently, we design therapeutic approaches including the delivery of targeted chemo or radioactive agents, or non-viral-based genes for gene therapy. Specifically, we have developed therapeutic and imaging agent targeting tumor vessels. In addition, we have successfully synthesized drug delivery agents controlled by external energy sources such as ultrasound. This is a powerful new approach that uses molecular imaging for identifying patients that will respond to treatment prior to choosing the best treatment regimen. We have successfully used this approach to image tumor vasculature in models of primary brain tumors, melanoma, and metastatic colon cancer to the liver and lung. A modified form of these nanoparticles was then successfully used for an antiangiogenic therapeutic approach to the tumor vasculature. We are currently performing toxicity studies as the preclinical requirement for clinical trials. Other research areas include tissue engineering applications in revascularization to enhance wound healing and vascularly compromised tissue; localized drug delivery systems; and biomarker development.



# MIPS GROUP UPDATES

## MULTIMODALITY MOLECULAR IMAGING LAB

SAM GAMBHIR, MD, PhD

We are developing imaging assays to monitor fundamental cellular events in living subjects. We are actively investigating technologies such as micro-positron emission tomography (micro-PET); bioluminescence optical imaging with a charge coupled-device (CCD) camera; fluorescence optical imaging; micro-computerized axial tomography (microCAT); photoacoustics; and Raman spectroscopy in small animal models. Our goals are to marry fundamental advances in molecular/cell biology with those in biomedical imaging to advance the field of molecular imaging. We have a particular focus on can-

cer biology. We have developed several reporter genes/reporter probes compatible with all of the above imaging modalities. These reporter genes are being used in cell trafficking models, gene therapy models, as well as in transgenic models for studying cancer biology. Assays to interrogate cells for mRNA levels, cell surface antigens, protein-protein interactions, protein phosphorylation, and intramolecular folding are also under active development. We are also extending many of these approaches for human clinical applications. In particular we have done the first cell trafficking imaging studies with PET in humans this year.

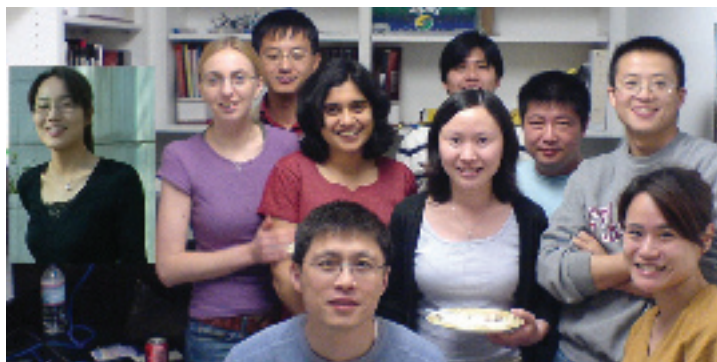


*Multimodality Molecular Imaging Lab group: Back row (l-r), Robert Teed, Sunil Bodapati, Carmel Chan, Carsten Neilsen, Adam de la Zerda, Bryan Smith, Zac Walls, Abhijit De. Middle row (l-r): Shay Keren, Jinha Park, Juergen Willmann, Amelie Lutz, Shuan Snyder, Frank Cochran, David Yerushalmi, Cristina Zavaleta, Julia Rasooly, Zhen Cheng, Bonita Crabbe, Manish Patel. Front row (l-r), Shahriar Yaghoubi, Paul Ramasamy, Elizabeth Gill, Sanjiv Sam Gambhir, Mohammad Namavari, Pritha Ray*

## CELLULAR AND MOLECULAR IMAGING LAB

JIANGHONG RAO

The Rao lab works at the interface of biology and chemistry, combining synthetic and physical organic chemistry and molecular biology with imaging techniques, like fluorescence microscopy and whole-body fluorescence/bioluminescence imaging, to develop novel imaging probes and methods to image biology in living subjects. A typical project evolves from the hands of the chemist, who synthesizes the probes, to the hands of the biologist, who proceeds to test the probes in cells and/or living animals. As part of the NCI-funded Center for Cancer Nanotechnology Excellence, a large part of our work involves the development of nanosensors for the imaging and detection of tumor cells through the use of self-illuminating quantum dots, which operate based on the principle of bioluminescence resonance energy transfer (BRET). This novel nanodetection and imaging sys-



*Cellular and Molecular Imaging Lab group: (l-r), Min-kyung So, Anca Dragulescu-Andrasi, Fei Xiao, Gayatri Gowrishankar, Yun Xing, Zuyong Xia, Hongjun Ren, Hequan Yao. Front: Jianghong Rao, Tiffany Chung*

tem promises the multiplex and highly sensitive detection and imaging of cancer biomarkers. The second area in which we are interested involves developing tools to visualize RNA localization through the use of RNA aptamers. Our understanding of RNA biology would greatly benefit from an imaging study of RNA in living subjects. We have successfully developed a ribozyme-mediated imaging system to enable the visualization of specific RNA in living cells and living animals. Last, we are interested

in imaging infectious diseases in vivo. One of the diseases we are currently working on is tuberculosis. Since a bacterial enzyme beta-lactamase is expressed by *M. tuberculosis*, we are developing probes to image beta-lactamase with both optical detection and positron emission tomography.

## MOLECULAR IMAGING INSTRUMENTATION LAB

CRAIG LEVIN

Our research interests are to advance instrumentation and algorithms for the in vivo imaging of certain molecular signatures associated with disease. These new “cameras” image photon emissions from molecular probes designed to target specific molecular processes associated with disease in cells located deep within the tissues of living subjects. The goals of the instrumentation projects are to advance the photon detection efficiency and spatial, spectral, and temporal resolutions. The algorithmic goals are to understand the physical system comprising the subject tissues, photon transport, and camera, and to realize the best available reconstructed image quality and quantitative accuracy. The work involves the design, development, and testing of novel position sensitive photon



*Molecular Imaging Instrumentation Lab: Back row (l-r), Frances Lau, Donna Niernberger, Hao Peng, Arne Vandenbroucke, Peter Olcott. Front row (l-r), Garry Chinn, Orr Keshet, Craig Levin, Angela Foudray.*

sensors and systems; low-noise readout electronics; data acquisition; modeling; computer graphics; tomographic image reconstruction; image processing; and data/image analysis. The final step in our research involves incorporating these innovations into practical imaging devices. The goal of this research is to introduce new imaging tools to advance studies of molecular mechanisms and treatments of disease within living subjects. The research is supported by grants from

the National Cancer Institute, National Institute of Biomedical Imaging and Bioengineering, the California Breast Cancer Research Program, GE Medical Systems, the Stanford Bio-X Program, and NVIDIA Corporation.

## MOLECULAR IMAGING PROBE LAB

XIAOYUAN (SHAWN) CHEN

Our group is interested in developing and validating novel molecular imaging probes (monoclonal antibodies, minibodies, proteins, peptides, and peptidomimetics) for the visualization and quantification of molecular targets that are aberrantly expressed during tumor growth, angiogenesis, and metastasis. We are trying to combine both anatomical (microMRI and microCT) and molecular (microPET, microSPECT, and NIR fluorescence) imaging techniques to pinpoint molecular and functional information related to tumor growth and dissemination and to monitor specific molecular therapeutic efficacy. We are currently working closely with two important angiogenesis targets: integrin  $\alpha(v)\beta(3)$  and vascular endothelial growth factor receptor subtype-2 (VEGFR-2). Integrins expressed on endothelial cells modulate cell migration and survival during angiogenesis. Integrins expressed on carcinoma cells potentiate metastasis by facilitating invasion and movement across blood vessels. In several malignancies, tumor expression of integrin  $\alpha(v)\beta(3)$  correlates well with tumor progression. VEGF is a key regulator of tumor angiogenesis and is the most potent endothelial cell mitogen. Binding of VEGF to its receptor on the endo-



*Molecular Imaging Probe Lab group: Front row (l-r), Kai Chen, Zibo Li, Weibo Cai, Gang Niu, Xiaoyuan (Shawn) Chen. Back row (l-r), Qizhen Cao, Zhanhong Wu, Ha-Young Lee, Lina He, Hui Wang.*

thelial cell membrane stimulates the VEGF signaling pathway. VEGFR-2 (KDR/Flk-1) is the primary VEGF receptor on endothelial cells. Specific projects include multimodality (e.g., PET, SPECT, optical) imaging of tumor angiogenesis in vivo as well as tumor vessel specific delivery of gene, chemo, and radiotherapeutics.

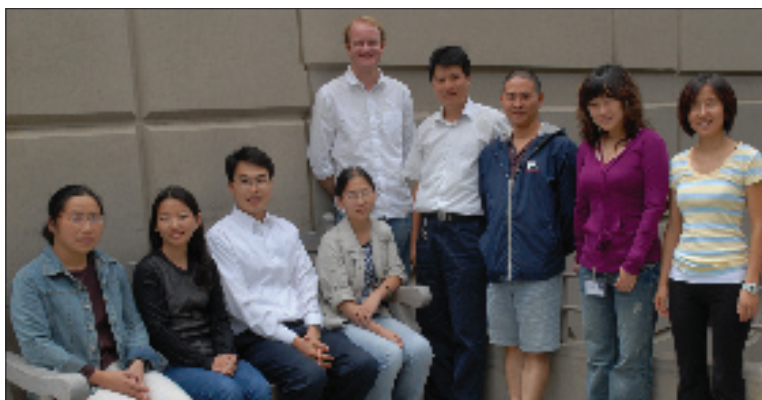
Our research efforts are currently supported by both the federal government (NIH and DOD) and industry (MedImmune, Inc.). Dr. Weibo Cai was awarded the Benedict Cassen Postdoctoral Fellowship from the Society of Nuclear Medicine. Drs. Zibo Li and Qizhen Cao received Dean's Fellowships. Dr. Ha-Young Lee was awarded a Korean Research Foundation (KRF) Scholarship. Drs. Weibo Cai and Zibo Li won 1st and 2nd place, respectively, in the Young Professionals Committee Best Basic Science Awards competition for the 2007 Annual Convention of the Society of Nuclear Medicine in Washington, DC. Chen group members also received numerous travel awards to attend the AMI and SMI annual conferences. Overall, we are proud to say that the year 2007 has been very busy and productive.



## CARDIOVASCULAR MOLECULAR IMAGING LAB

JOSEPH WU

Ischemic heart disease is the number one cause of morbidity and mortality in the United States. Repeated ischemic insults can lead to congestive heart failure, which is the leading cause of hospital admissions for people aged 65 years and over. With the advent of the human genome project, cardiovascular diseases will likely be targeted at the basic cellular and molecular levels. The cardiovascular molecular imaging lab is a multidisciplinary team that combines expertise in molecular and cell biology, cardiovascular physiology, and molecular imaging. To better understand stem cell biology in vivo, we use novel molecular markers that enable us to follow the fate of transplanted stem cells noninvasively. These include monitoring survival, proliferation, and differentiation as related



*Cardiovascular Molecular Imaging group: (l-r), Mei Huang, Feng Cao, Joseph Wu, Xiaoyan Xie, Kitch Wilson, Zongjin Li, Fangjun Jia, Jin Yu, Sarah Zhang.*

profiling of stem cell markers as well as optimizing cardiac gene therapy protocols. The eventual goal is to establish molecular imaging as a platform for translational research in cellular and gene therapies for ischemic heart disease in the 21<sup>st</sup> century.

to embryonic stem cells and bone marrow stem cells. The highly sensitive imaging devices we use include bioluminescence, fluorescence, positron emission tomography, and magnetic resonance scanners. We are actively engaged in studying the differentiation of human embryonic stem cells into endothelial and cardiac cells, which will have important applications for regenerative medicine applications in the future. Our lab also works on gene expression

## CLINICAL MOLECULAR IMAGING RESEARCH

ANDY QUON

Our group is focused on applying emerging molecular imaging techniques into clinical practice. Recent projects have included the development of 3D volume rendered PET/CT acquisition and processing techniques for virtual colonography and bronchoscopy and the description of the importance of a truly integrated interpretation of PET and CT for bone metastases.

Currently, the group has been working on developing tools for integrated PET/CT computer-aided diagnosis (PET/CT CAD). The design philosophy is to evaluate both the PET and CT data using an integrated algorithm for both modalities



*Clinical Molecular Imaging Research group: (l-r), Maurice Zissen, Hedieh Eslamy, Andrew Quon, Larry McNutt. Not shown, Andrei Iagaru, Edward (Ted) Graves.*

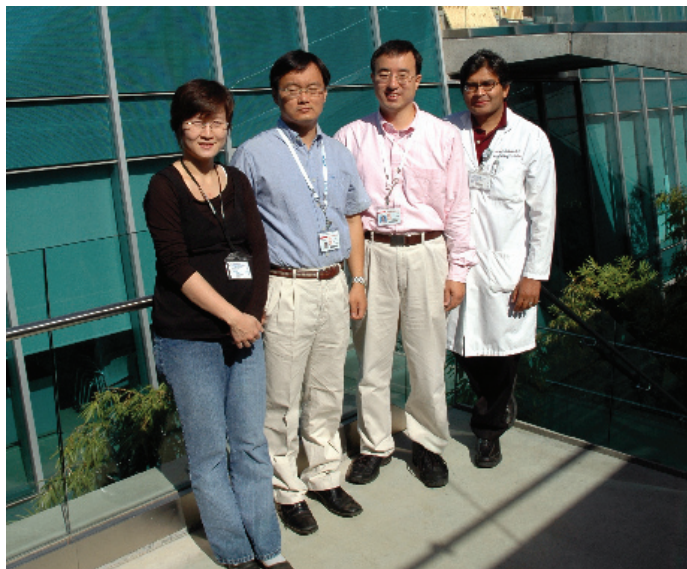
applications; and to evaluate the potential of 18F-FLT for evaluating GI malignancies.

to provide the greatest accuracy. Additionally, the group is studying alternative PET radiotracers such as 18F-5FU (a radiolabelled form of the chemotherapy agent 5FU); 18F-NaF (a tracer specialized for bone imaging); and 18F-FLT (a cellular proliferation surrogate). Using these tracers, the goals of the group are to elucidate the effects of angiogenesis inhibitors on chemotherapy uptake in tumors; to evaluate PET/CT for imaging the skeleton in both oncological and non-oncological



## MOLECULAR IMAGING OF MUSCULOSKELETAL ILLNESSES

SANDIP BISWAL



*Molecular Imaging of Musculoskeletal Illnesses group: (l-r), Sheen-Woo Lee, Tae Joo Jeon, Sang Hoo Lee, Sandip Biswal.*

Dr. Sandip Biswal, MD, and members of the lab, Sheen-Woo Lee, MD; Tae Joo Joon, MD PhD; Sang Hoon Lee, MD; Deepak Behera, MD; Andrew Tye; Shin Kamaya, BS; Harpreet Singh, BS; Brian Kim, MD; Bao Do, MD, are interested in using multimodality molecular imaging techniques to study musculoskeletal inflammation and pain. Dr. Sheen-Woo Lee, Mr. Kamaya, and Dr. Behera have employed manganese-enhanced magnetic resonance imaging (MEMRI) to study spinal cord activation in models of neuropathic and inflammatory pain. They have also been studying the effects of analgesics on MEMRI patterns. Dr. Do, Dr. Kim, Mr. Dhatt, and Mr. Tye continue to make significant inroads in understanding glucose metabolism in the human and animal spinal cord using 18F-FDG PET-CT. Furthermore, in addition to a number of MIPS research groups, our lab has formed productive collaborative relationships with Dr. David Yeoman's group focusing on pain research; Dr. Stuart Goodman's group studying prosthetic-induced osteolysis; and Dr. Blankenberg's group studying the role of Annexin V in pain. In the past year, we have been fortunate to present our work at a number of scientific meetings including RSNA, SNM, AMI, and SMI.



*This unique lightcourt, with two floors of treated glass, brings daylight to two floors of below ground workspace in the Lucas Center for Imaging.*



# EDUCATION & TRAINING

YEARS ON THE CUTTING EDGE





# EDUCATION AND TRAINING

## POSTGRADUATE TRAINING

Stanford's Continuing Medical Education (CME) program offers exceptional courses in state-of-the-art medical imaging and continues to be the leading radiology CME effort in the country. Our goal is to provide up-to-date clinical and research information at the highest possible levels, commensurate with Stanford's standards of excellence.

We present current, comprehensive, and relevant content to radiologists and technologists globally. Our registrants learn the latest imaging techniques and how to optimize medical imaging in all subspecialties of radiology and in all major modalities. Our programs are presented as symposia, workshops, panels, enduring materials, and unique live demonstrations to ensure participants are able to improve their knowledge, skills, and the clinical outcomes for their patients.

In FY 2007, we welcomed over 3,600 registrants to 16 courses and distributed DVDs with CME courses covering CT, breast imaging, and PET/CT. The Department's distinguished faculty serve as course directors and speakers for each program,

and guest faculty from leading academic institutions worldwide are invited to complement our roster of presenters. Our International Symposium on Multidetector Row CT (MDCT), now in its ninth year, is one of our most successful programs with 950 registrants. The meeting has been groundbreaking as a new model for education in radiology.

We are also proud of the partnerships we have formed with many distinguished organizations and institutions. We have just completed our first joint conference in Shanghai, China. This program included 300 radiologists from throughout the region and was developed in partnership with the Chinese Radiological Society. Other meetings on our calendar are co-hosted by strategic partners in Japan and Europe. These efforts enable us to provide education to radiology communities around the world and to establish important linkages with imaging scientists in leading Chinese, Japanese, and European universities.

### STANFORD RADIOLOGY COURSES—2007

COURSES	DIRECTOR (JOINT SPONSORS)	LOCATION
Venous Disease	Hofmann	Carmel
Breast MRI	Ikeda/Daniel	Las Vegas
Clinical High Field MRI	Atlas/Glover/Herfkens	Las Vegas
Current Concepts—MRI	Pelc/Spielman	Monterey
Small Animal Imaging	Levin	Stanford
Diagnostic Imaging	Sommer	Vail
PET/CT & Molec Img	Gambhir/Quon	Las Vegas
CVIR	Sze	Squaw
MR—Neuro/MSK	Atlas/Beaulieu	Las Vegas
Diagnostic Imaging	Glazer (Keio, Tokyo, Osaka Universities)	Hawaii
Breast Imaging	Ikeda	Las Vegas
MDCT	Rubin	San Francisco
State-of-the-Art Imaging	Glazer (Universities of Munich, Rotterdam, and Sloan Kettering)	Dubrovnik, Croatia
State-of-the-Art Imaging	Moseley (Japanese Society for Radiological Technology)	Stanford
Venous Disease	Hofmann	Hawaii
Multislice CT	Glazer (Chinese Radiological Society)	Shanghai, China

## NCI TRAINING PROGRAM—ADVANCED TECHNIQUES FOR CANCER IMAGING AND DETECTION (T32)

PI, GARY GLAZER, MD—PROGRAM MANAGER, DONNA CRONISTER

The Department of Radiology at Stanford University offers qualified individuals a unique research opportunity through our Advanced Techniques for Cancer Imaging and Detection Program, which began its 15th year of training on February 1, 2007. The goal of our program is to provide MD and PhD research fellows with training in cancer-related imaging research. Fellows have the opportunity to work with our world-renowned faculty who are committed to sharing their knowledge and mentoring the future leaders in radiology. Our program allows basic scientists in medical imaging (PhD) and clinical scientists (MD post-residency) to collaborate in an unparalleled environment that combines medical imaging sciences, clinical sciences, a strong cancer focus, and an institutional commitment to training academic radiologists and basic scientists in imaging science.

A specific aim of our training program is to position our trainees for a career in academic radiology. To date, we have graduated 24 trainees from our program. Eighteen of the post-doctoral fellows who have completed the program are actively performing research as faculty or academic staff in major universities. Our trainees continue to be extremely productive, and we often collaborate with them in their new positions both locally and throughout the country. We recently received the great news that our program has been awarded another five years of support. We are grateful to the National Institutes of Health for its recognition of the strength and success of our training program.

The following table presents a history of NCI fellows who have graduated from this T32 program, which is supported by NIH/NCI T32 CA09695.

NCI FELLOW	GRADUATED	MENTOR	CURRENT POSITION	INSTITUTION
John Strang, MD	1995	Herfkens	Assistant Professor	Univ of Rochester, Rochester, NY
Susan Lemieux, PhD	1996	Glover	Assistant Professor	Diagnostic Imaging Western Virginia Univ, Morgantown, WV
Ian Chen, MD	1996	Li	Radiologist	Southwest Washington Medical Center, Vancouver, WA
Yi-Fen Yen, PhD	1997	Glover	Research Scientist	GE Advanced Health Care
Garry Gold, MD	1997	Macovski	Associate Professor	Radiology, Stanford Univ, Stanford, CA
Bruce Daniel, MD	1997	Herfkens	Associate Professor	Radiology, Stanford Univ, Stanford, CA
Roger Shifrin, MD	1998	Pelc & Herfkens	Assistant Professor	Univ of Florida
Esther Yuh, PhD	1998	Li & Napel	Clinical Fellow	Radiology (Neuroradiology) UCSF, San Francisco, CA
Steven Heiss, MD	1999	Li	Radiologist	Radiology Imaging Associates, Denver, CO
Martin Blum, MD	2000	Jeffrey	Researcher	PET/Nuclear Medicine, Palo Alto VA
Curtis Coulam, MD	2001	Sommer	Radiologist	Gem State Radiology Group, Boise, ID
Lawrence Chow, MD	2002	Sommer	Assistant Professor	Univ of Oregon, Eugene, OR
Yishan Yang, PhD	2002	Bednarski	Research Associate	Radiology, Stanford Univ, Stanford, CA
Samira Guccione, PhD	2002	Bednarski	Assistant Professor	Radiology, Stanford Univ, Stanford, CA
Charles Liu, MD	2003	Herfkens & Sommer	Radiologist	La Jolla Radiology, La Jolla, CA
Susan Hobbs, MD, PhD	2003	Bednarski	Resident	Univ of Minnesota
Karl Vigen, PhD	2003	Butts Pauly	Research Scientist	Univ of Wisconsin-Madison, Madison, WS
Laura Pisani, PhD	2004	Glover	Postdoctoral Fellow	Radiology, Stanford Univ, Stanford, CA
Jon Levin, MD	2004	Herfkens & Sommer	Radiologist	St. Luke's Medical Center & Clinic, Minneapolis, MN
Daniel Margolis, MD	2005	Jeffrey	Assistant Professor	Department of Radiology, UCLA, Los Angeles, CA
Daniel Ennis, PhD	2006	Pelc	Postdoctoral Fellow	Stanford Univ (leaving for Univ of Washington, Seattle, WA)
Michael McDonald, PhD	2007	Guccione	Research Scientist	NIH, Washington, DC
Anthony Faranesh, PhD	2007	Pelc & Hargreaves	Research Scientist	NIH, Washington, DC
Lewis Shin, MD	2007	Herfkens	Assistant Professor	Radiology, Stanford Univ, Stanford, CA



## NCI TRAINING PROGRAM—STANFORD MOLECULAR IMAGING SCHOLARS (R25)

PI, SAM GAMBHIR, MD, PhD—PROGRAM MANAGER, SOFIA GONZALES, MS

The Stanford Molecular Imaging Scholars (SMIS) program is a diverse training program bringing together more than 13 departments, predominantly from the Stanford Schools of Medicine and Engineering. Oncologic molecular imaging is a rapidly growing area within molecular imaging, which combines the disciplines of chemistry, cell/molecular biology, molecular pharmacology, bioengineering, imaging sciences, and clinical medicine to advance cancer research, diagnosis, and management. The goals of SMIS are to train postdoctoral fellows by providing mentorship through a diverse group of over 40 basic

science and clinical faculty mentors representing eight program areas; by incorporating formal courses in molecular imaging, molecular pharmacology, cancer biology, cancer immunology, virology, and gene therapy; and by including a clinical component such as hematology/oncology rounds. Our first year of training began in September, 2006. Six fellows have been recruited to the program. Four fellows are now in their second year of training. The following list summarizes where our new trainees are in the program.

*The R25 program is supported by NIH/NCI R25 CA118681.*

NCI FELLOW	YEAR(S)	MENTOR
Ted Chu, PhD	2007 (1 <sup>st</sup> year)	Calvin Kuo, MD
Hua Fan-Minogue, MD, PhD	2007 (1 <sup>st</sup> year)	Sam Gambhir, MD, PhD
Richard Kimura, PhD	2006 (2 <sup>nd</sup> year)	Jennifer Cochran, PhD
Jill Lin, PhD	2006 (2 <sup>nd</sup> year)	David Paik, PhD
Jennifer Prescher, PhD	2006 (2 <sup>nd</sup> year)	Christopher Contag, PhD
Bryan Smith, PhD	2006 (2 <sup>nd</sup> year)	Sam Gambhir, MD

## IN VIVO CELLULAR AND MOLECULAR IMAGING (P50)

PI, SAM GAMBHIR, M.D., PH.D.—PROGRAM MANAGER, BILLIE ROBLES

The vision of the “In Vivo Cellular and Molecular Imaging Center at Stanford” (ICMIC@Stanford) is to bring together researchers from various disciplines to form synergistic teams that will make significant advances in the use of multimodality molecular imaging strategies for better linking pre-clinical models of cancer with the clinical management of cancer. The career development component of this P50 is designed to be as flexible as possible to attract highly qualified candidates with the passion and ability to make an impact on cancer research that will benefit patient care in terms of diagnosis, therapy, and monitoring. This overarching theme will guide the process of candidate selection and lead to successfully trained individuals who will be capable

of leading their own independent research teams in the field of molecular imaging cancer research. As we enter the second year of the ICMIC@Stanford, we have a total of four trainees in the program. Selected candidates attend various educational activities in the Molecular Imaging Program at Stanford (MIPS) and work to bridge activities between a minimum of two laboratories. The candidates invited to join the ICMIC@Stanford Program are expected to be well trained in basic science or in imaging science and to have the energy and drive to impact the growing field of molecular imaging cancer research.

*The P50 program is supported by NIH/NCI P50CA114747.*

NCI P50 TRAINEE	YEAR(S) OF TRAINING	MENTOR
Sheen-Woo Lee, MD	2005	Sandip Biswal, MD
Frank Cochran, PhD	2005-08	Jennifer Cochran, PhD
Erhan Yenilmez, PhD	2006-07	Hongjie Dai, PhD
Mike Helms, PhD	2007-08	Chris Contag, PhD



## LUCAS CENTER MR TRAINING AND SUPPORT: 1.5T, 3T, &amp; 7T WHOLE BODY MAGNETS

ANNE MARIE SAWYER, BS, RT(R)(MR); ROMI SAMRA, RT(R); SANDRA RODRIGUEZ, RT(R)(MR)

## SAFETY TRAINING AND SYSTEM OPERATION INSTRUCTION 2006-2007

Safety training and system instruction have been provided to 112 new researchers conducting experimental MR studies at the Lucas Center over the last 12 months. Magnet safety training is provided twice a month and is an annual requirement for all researchers assisting or conducting studies on any of the magnet systems at the Lucas Center. A magnet safety refresher course will be provided to over 200 researchers this coming fall. This ensures that all users and assistants are qualified to operate the system and satisfies Lucas Center and University requirements for safety. System and safety support is provided to the researchers 7 days a week, 24 hours a day to ensure that research endeavors are successful, valuable data is generated, and, above all, to ensure the facilities are safe for researchers, human subjects, and the MR system and its components (Image 1).



Image 1. Chris Cheng, PhD, and Gilwoo Choi, MS, (collaboration of Radiology, Mechanical Engineering, and Vascular Surgery) prepare a subject for imaging of the femoral arteries with a new MR-safe (MR-conditional at 1.5T) device that simulates weight-bearing on a human subject laying in the supine position (Ben Krasnow, Mag Design & Engineering, MagConcept.com).

Magnet safety is an ongoing concern as the MR environment can be a potentially lethal setting without continuing education and persevering support.

The research environment generates many new, yet prototype, designs in RF imaging coils; imaging accessories; and monitoring and response devices, such as button boxes, eye trackers, and electroencephalogram (EEG) recorders, and sensory devices (Image 2). Evaluation of these new devices is ongoing to ensure that neither the image data, the safety of the human subject, nor the integrity of the MR system is compromised by the presence of these devices in the magnet room, in the bore of the magnet, or in the presence of an RF coil.

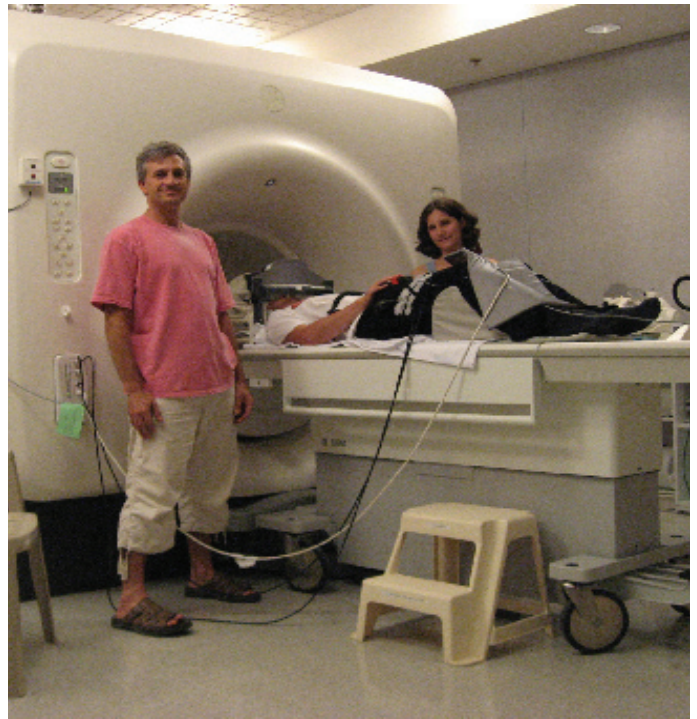
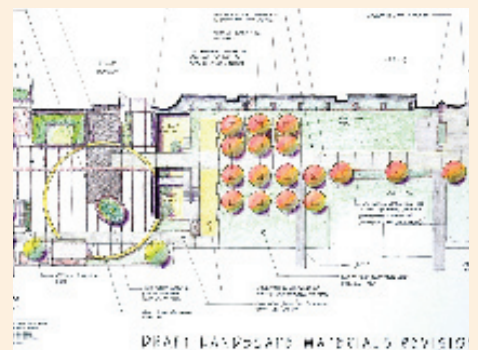


Image 2. Philippe Goldin, PhD, and Tali Manber, MA, from the Department of Psychology prepare a subject for a functional MRI of the brain at the Lucas 3.0T MR system using physiologic monitoring, galvanic skin response monitoring, button response boxes, and video-projected images.

# FACILITIES

YEARS ON THE CUTTING EDGE







# FACILITIES UPDATES

## OUTPATIENT IMAGING

Volney Van Dalsem, MD • Director

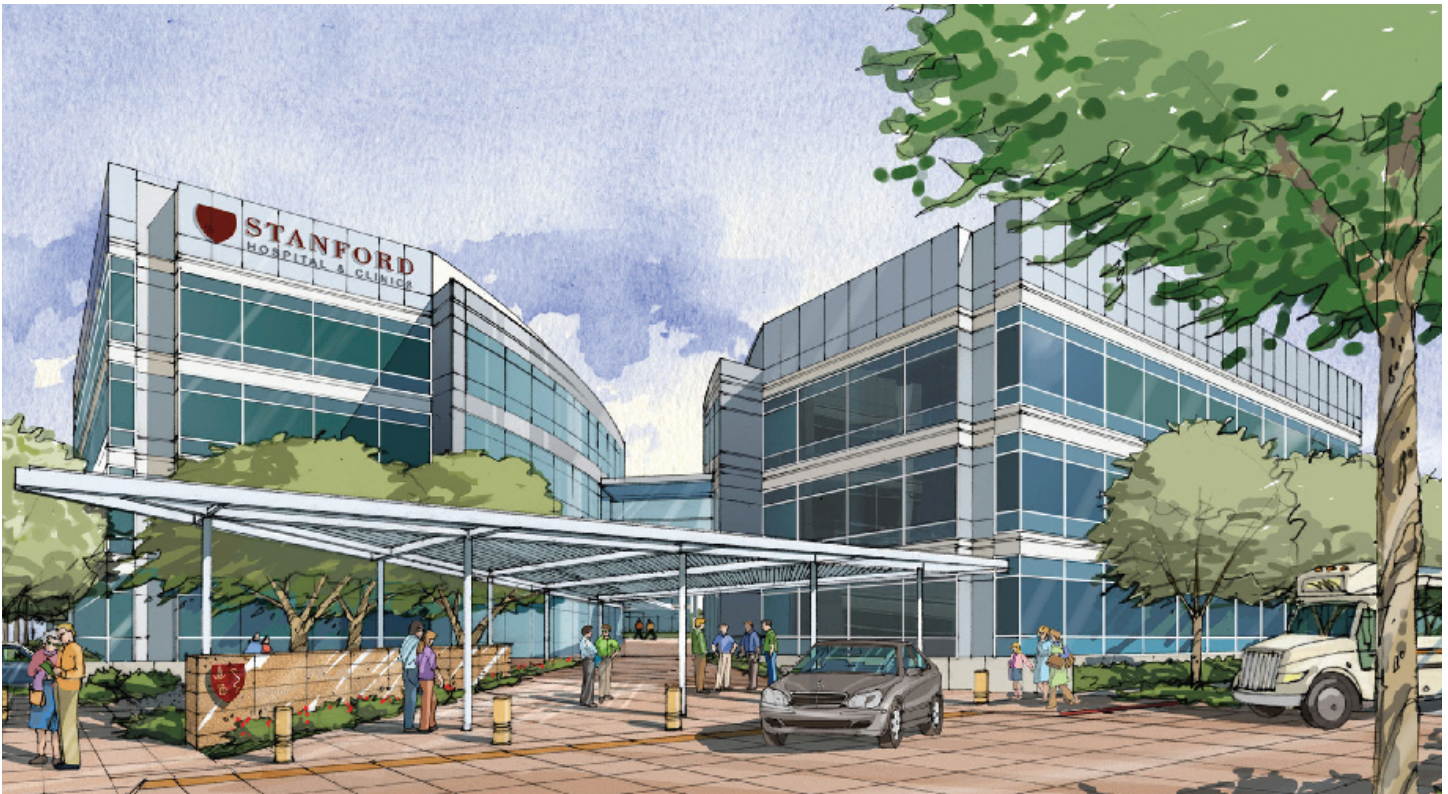
Our Department is in the midst of a major expansion with two new projects underway: an outpatient imaging center in Palo Alto and Stanford Hospital's "North Campus" outpatient facility. The opening of these centers will double our current capacity and transform our radiology clinical care by extending our outpatient imaging services and ensuring the availability of leading-edge technology.

The Palo Alto complex is scheduled to open in June of 2008 as a combined clinical and research center and will have two CT and two 3T MRI scanners. A significant goal for our Palo Alto facility is to create a unique, patient-centered environment with the highest standards of service, ultimately providing direct communication between the healthcare professional and patient about the results of imaging studies.

We are pleased to welcome Dr. Volney Van Dalsem as the director of outpatient imaging for the imaging center in Palo

Alto. Dr. Van Dalsem comes to us from El Camino Hospital where he served for 27 years, 11 of those as medical director. He is also the current president of the California Radiological Society. Because of Dr. Van Dalsem's exceptional clinical skills, local knowledge, and administrative expertise, we look forward to the leadership he will provide to our unique, new efforts in outpatient imaging.

The North Campus facility is scheduled to open by December of 2008 and will house one CT and two MR scanners. Future plans include increasing the number of modalities to three CT and three MR scanners as well as adding two radiography/fluoroscopy (R/F) systems and one ultrasound machine. The expansion of our facilities not only enables our Department to offer world-renowned programs but also to house one of the world's largest centers for imaging located on a university campus.



## 3D Medical Imaging Lab

LAURA PIERCE • Lab Manager

The Stanford 3D medical imaging laboratory began its second decade of service to the Stanford Medical community this year. The 3D laboratory continues to be guided by the mission of developing and applying innovative techniques for efficient analysis and display of medical imaging data through interdisciplinary collaboration. Our clinical goal is to deliver 3D imaging advances as rapidly as possible following validation to the Stanford and worldwide healthcare communities for the swift and accurate diagnosis and treatment of disease. Our educational goal is to disseminate knowledge and duplicate our 3D services at other institutions by providing training for local and international physicians and technologists in the latest developments in 3D imaging.

### PROGRESS

**Clinical:** Over the past year, the 3D laboratory has continued its operations simultaneously in two locations: the first floor of the Lucas Center as well as the third floor of the James H. Clark Center, a building dedicated to interdisciplinary science. Our average monthly 3D volume has increased to approximately 780 examinations, and we have processed over 48,000 examinations, for nearly every clinical department at the Stanford Medical Center since our inception in 1996. The majority of our referrals come from vascular surgery, cardiothoracic surgery,

demand for 3D imaging as well as 3D management training, the 3D lab sponsors visiting radiologists and technologists through our 3D clinical fellowship program. This past year, we hosted 30 visitors from a combination of local, national, and international hospitals and medical centers. Our international visitors traveled from New Zealand, Singapore, England, and Israel.

### INFRASTRUCTURE

3D imaging technologists include: Laura Pierce, 3D lab manager; Marc Sofilos; Linda Novello; Keshni Kumar; and William Johnsen. Our technologists offer not only expertise in 3D imaging, but also experience in CT and MRI scanning techniques as well. We also employ administrative assistants Lakeesha Winston and Debra Frank, and a database administrator, Kala Raman. The research arm of the lab retains an annual average of 12 engineering graduate students and postdoctoral scholars as well as 2 clinical MD researchers. Both 3D lab locations include a central area table that invites professional collaboration (see image 1). The lab encompasses a total of 13 advanced 3D workstations for processing clinical cases and for research and development. We also have three servers, which provide remote 3D rendering to the Stanford medical community, and two research and development servers for image and data storage. Two remote PACS workstations allow access to all Stanford



Image 1. The Lucas and Clark Center 3D laboratories. Images courtesy of Mark Riesenberger.

gastroenterology, cardiology, urology, reconstructive surgery, orthopedics, and neurosurgery.

**Education:** The 3D lab is attended by a rotation of Stanford Radiology fellows, residents, and medical students who acquire skills in 3D interpretation as part of their medical training. Our 3D imaging technologists also train Stanford researchers from engineering and medical departments for acquiring 3D images and data for research projects involving all kinds of images, including video microscopy, electron microscopy, and multimodality small animal imagers. In response to external

medical imaging and reporting. The lab also houses a variety of PCs and printers for software development and support.

We continue our excellent relationships with corporate developers of 3D workstations (e.g., GE Healthcare, Siemens Medical Solutions, TeraRecon, and Vital Images) who site their hardware and software in the 3D lab in anticipation of our feedback. These relationships ensure that we maintain the most advanced multi-dimensional analytical technologies available. Future clinical applications under investigation include automatic bone removal from CT datasets, automatic pre-processing of



patient examinations to improve efficiency, and improvements to graphical user interfaces for simplicity and ease of use of clinical 3D software.

To facilitate the bridge between innovation and other clinical use of technology, we also serve as an imaging core lab for medical device developers. These companies use our expertise to evaluate their current and future products in anticipation of FDA approval. Present industrial projects include the evaluation of data from pulmonary vein ablation procedures (to treat atrial fibrillation), as well as thoracic stent-graft deployment (for the treatment of thoracic aortic aneurysms).

## CONCLUSION

The 3D Medical Imaging Lab continues to function as an international leader in clinical care, teaching, and research in medical imaging analysis. The confluence of talented, medical and engineering expertise as well as the most up-to-date equipment has been a consistent source of innovative developments in diagnostic and treatment planning approaches.

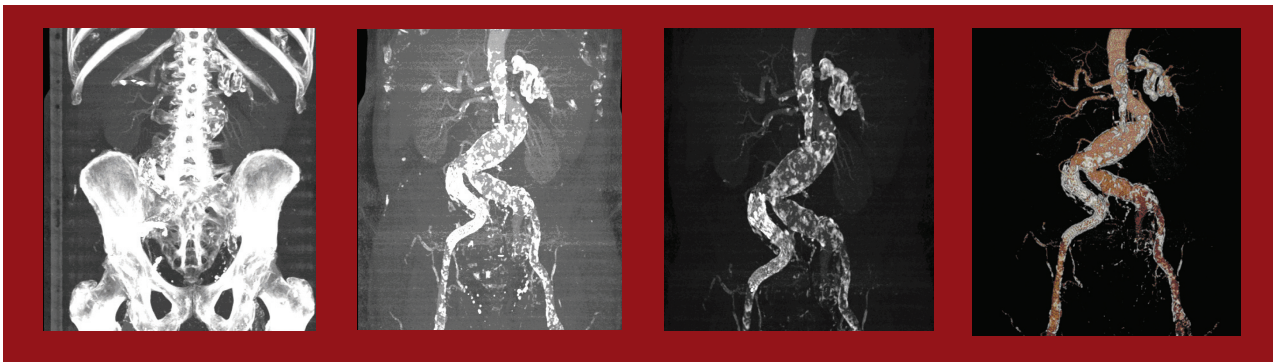


*Image: Example of CT abdomen/pelvis angiogram initially edited with automatic bone removal tool, and completed by 3D user assistance. Images acquired on GE Advantage Windows workstation.*

## EXPERIMENTAL ANIMAL MODEL CARE FACILITY

WENDY BAUMGARDNER, RVT, LATG

Animal studies at the Lucas Center enhance both our treatment and diagnostic abilities. In our continuing efforts to provide support to the Radiology investigative staff, we are entrusted with the responsibility of overseeing all animal protocols within our Department and all other departments carrying on work at the Lucas Center. Two experienced California licensed veterinary nurses (RVTs), with over 38 years in the field, attend all animal studies, always making the health and welfare of the animals their most important priority. Diligent care is taken during all procedures involving animal subjects. They are treated with the utmost respect and professional care; the amount of compassion we show to each animal is considered equal to the amount of compassion we give to our patients in our human studies. All personnel working with animals under approved Institutional Animal Care and Use Committee (IACUC) protocols have attended "required" seminars from the University's Department of Comparative Medicine. Further, specifically tailored, one-on-one training for more advanced techniques is taught by Wendy, here, at the Lucas Center.

We realize that living subjects are needed to advance our knowledge, and we ensure that the proper respect for life is part of all protocols. Work at the Lucas Center improves and develops new invasive and non-invasive procedures that use magnetic

resonance imaging, fluoroscopy, focused ultrasound, and computed tomography to guide them. Clinical studies currently being done involve the study of alcoholism; stroke; liver and prostate cancers; neuroimaging of the brain; and stent/graft implantation. The techniques currently being explored at the Lucas Center all contribute to more efficient and effective medical treatment for illness and disease.



*Wendy Baumgardner prepares the surgical suite for a day-long procedure.*

## SMALL ANIMAL IMAGING CENTER (SCi3)

TIM DOYLE, PHD

This year the Stanford Center for Innovation in In Vivo Imaging (SCi3) finally received the long-awaited 7 tesla small animal MRI system. After the MR suite was renovated over the start of the year, the magnet was delivered in June. Varian is currently preparing the system to be energized; after this is completed, GEHC will finish the installation and facilitate the magnet testing and set up with Signa clinical software interface. We are hopeful that we can do our first “live” scan and make the system available to users in the fourth quarter. We are also

in response to the heavy demand experienced on the other three systems in place. The new system provides the same bioluminescence capability of the existing systems but also provides spectral and tomographic fluorescence imaging capabilities.

The core has just finished its second year as a University-shared resource, and we are continuing to operate within our budgets while still providing access to all the modalities at rates that should not prevent users from performing the experiments they need to perform. Stanford was awarded Cancer Center status earlier this year, with the imaging facility as one of the highest rated cores, and this will further aid the financial support to users by supporting salary overheads as well as by providing imaging rate discounts to Cancer Center members.

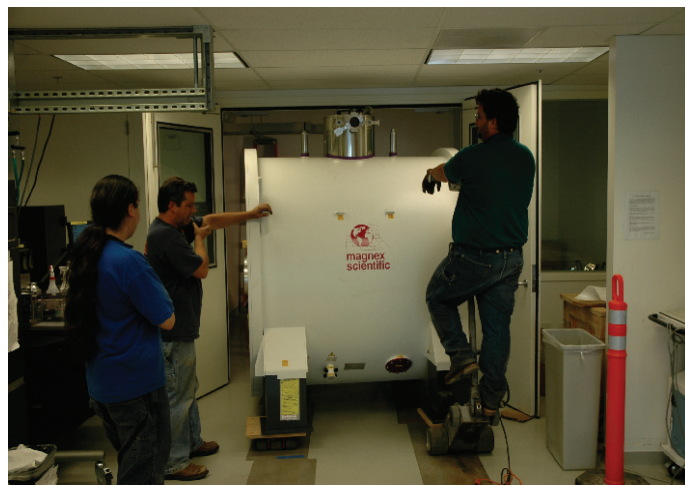
The annual small animal imaging workshop is now preparing for its third year. During last year’s workshop, we expanded the scientific presentations to cover a whole day and included some modality overview talks by Stanford faculty. We are now preparing for our third workshop that will occur November 7-10; the whole event will be hosted in the Clark Center, and the talks will be open to registered Stanford students and faculty.



*Tim Doyle and Nissim Benhamo (GEHC) watch as the new 7T magnet is lowered into the basement of the Clark Center.*

actively searching for a new facility staff scientist who will oversee the running of the magnet, along with the other modalities. Shay Keren, who has been working as a postdoctoral fellow in Dr. Sam Gambhir’s lab and who has been an integral part of the imaging core, will be returning to Israel in 2008. Consequently, we hope that the new full-time scientist will assume Shay’s duties in the core, in addition to running the MRI.

At the start of the year, the latest bioluminescence imaging system available from Caliper Life Sciences (Xenogen) was delivered. This bioluminescence imaging system was purchased



*The 7T magnet is moved through the small animal imaging facility into the newly renovated MRI suite. Ephraim Delgadillo (Varian Inc, left) watches the riggers move the magnet into the MR suite.*



## CYCLOTRON SUITE UPDATE

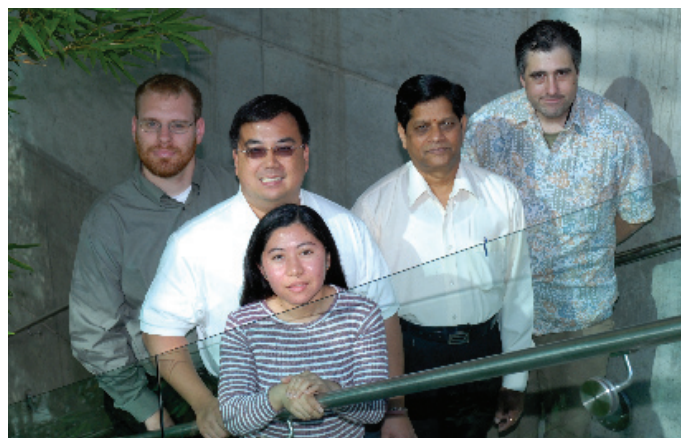
FREDERICK CHIN, PhD AND DAVID DICK, PhD

The capabilities of the Cyclotron Suite as well as the production of radiotracers continued to increase over the past year. Several exciting compounds, both novel and known, are now being produced in the Cyclotron Suite and used for both animal and human imaging in order to better understand, diagnose, and stage disease. In addition to the novel radiotracer work done by the Chen and Gambhir groups, the staff of the Cyclotron Suite has implemented the synthesis of many radiotracers for use by clinicians and researchers.

Fluorine-18 labeled fluorodeoxyglucose (FDG) is produced daily for use at the Stanford Hospital. Over the past year, standard operating procedures were written and good manufacturing practices were implemented for the synthesis of Nitrogen-13 labeled ammonia and Fluorine-18 labeled sodium fluoride. Nitrogen-13 ammonia is used to assess myocardial perfusion. The half-life of Nitrogen-13 is only 9.96 minutes, so a new batch of ammonia is made for each imaging session and rushed to the clinic without delay to minimize the amount lost due to radioactive decay. Fluorine-18 sodium fluoride is used to image bones and joints. Its uses include looking for skeletal abnormalities and the detection of bone metastases. The synthesis and quality control for each radiopharmaceutical was validated and clinical research studies have begun.

GE TRACERlab FX-FN modules #1 and #2 continue to carry out the syntheses of many 18F-labeled radiotracers and labeling agents for Stanford and other collaborative research including pharma. In addition, the final installation of the TRACERlab

FX-C Pro and FX-FE modules have enabled us to perform C-11 and electrophilic F-18 radiochemistries. Our group will continue to grow with the addition of a new PhD-level radiochemist in the fall of 2007. The planned acquisition of a two-reactor automated radiosynthesis module, single-mode microwave apparatus, and multiple-plate radioTLC scanner will complement the increasing demand of more radiochemists (i.e., students, faculty, and our staff) using our facility. In the near future, additional PET radiotracers will become available to meet the increasing needs for performing preclinical ( $[^{11}\text{C}]\text{NMSP}$  and  $[^{18}\text{F}]\text{SPA-RQ}$ ) and clinical ( $[^{11}\text{C}]\text{PIB}$  and  $[^{18}\text{F}]\text{FU}$ ) research studies with PET.



Cyclotron Suite group: (l-r), David Dick, Frederick Chin, Murugesan Subbarayan, Andrew Lamb. Front: Rhona Berganos.

The following table summarizes a list of radiolabeled compounds that are made in the research radiochemistry lab excluding other research compounds protected under current confidentiality agreements.

TRACER	USE	APPLICATION
$[^{11}\text{C}]\text{NMSP}$	Imaging dopamine-2 receptors (D2R)	Monitoring D2R-related neurological disorders
$[^{11}\text{C}]\text{PIB}$	Imaging $\alpha\beta\delta$ amyloid in brain	Monitoring progression of Alzheimer disease in brain
$[^{18}\text{F}]\text{fluoroalkyne}$	Labeling agent used with "Click Chemistry"	Novel method for radiolabeling peptides
$[^{18}\text{F}]\text{Fluoro-BG-137}$	Imaging $\delta$ -opioid receptor	Imaging the process of chronic pain
$[^{18}\text{F}]\text{FAZA}$	Hypoxia imaging agent	Evaluating clinically relevant hypoxia-directed cancer therapies
$[^{18}\text{F}]\text{fluorobenzaldehyde}$	Prosthetic labeling group	1) Radiolabeling peptides for potential clinical use 2) Radiolabeled affibody for imaging of NER2neu
$[^{18}\text{F}]\text{fluorobenzoic acid}$	Prosthetic labeling group	Radiolabeling peptides for potential clinical use
$[^{18}\text{F}]\text{FDF}$	Imaging fructose metabolism and pentose pathway	Imaging fructose metabolism and the pentose pathway
$[^{18}\text{F}]\text{FEAU}$	Imaging substrates expressing mutant HSV1-sr39tk	1) Monitoring gene therapies targeting cancer 2) Monitoring cell therapies
$[^{18}\text{F}]\text{FHBG}$	Imaging agent for tumors expressing HSV1-tk	Monitoring various cancer therapies
$[^{18}\text{F}]\text{FLT}$	Imaging agent for tumor cell proliferation	Monitoring various cancer therapies
$^{18}\text{F}$ -labeled RGD peptides	$\alpha\beta_3$ integrin imaging agent	Imaging tumor integrin expression
$[^{18}\text{F}]\text{SFB}$	Prosthetic labeling group	Radiolabeling peptides for clinical use

## LUCAS CENTER MR SYSTEMS 1.5T, 3.0T AND 7.0T WHOLE BODY MAGNETS

ANNE MARIE SAWYER, ROMI SAMRA, SANDRA RODRIGUEAZ, KRISTI L. ARRUZA

The 1.5 tesla (image 1), 3.0 tesla, and 7.0 tesla (image 2) GE Healthcare MR systems are currently operating at 12.0 M5 systems revision; a maximum slew rate of 150 millitesla per meter per second; and maximum gradient amplitudes of 50 millitesla per meter (1.5T) and 40 millitesla per meter (3.0T and 7.0T). The hardware currently allows the use of 8-channel phased array coils at 1.5T and 16-channel phased array coils at 3.0T and 7.0T.



Image 1. Romi Samra and Sandra Rodriguez, MR research technologists at the 1.5T MR system, prepare a human subject for an examination of the abdomen.



Image 2. The 7.0T whole-body MR system at the Richard M. Lucas Center for Imaging utilizes 16-channel receiver hardware (GE Healthcare, Milwaukee, Wisconsin, USA).

A second 3.0T GE Healthcare MR system was recently installed at the Lucas Center (images 3 and 4).



Image 3. A new short-bore 3.0T magnet is delivered to the Richard M. Lucas Center for Imaging.



Image 4. The new 3.0T magnet is lifted over the Richard M. Lucas Center for Imaging.



New radiofrequency (RF) coils at the Lucas Center include an 8-channel phased array knee coil at 3.0T (GE Healthcare, Milwaukee, WI, USA) (images 5 and 6) and a 16-channel phased array head coil at 7.0T (Nova Medical, Inc., Wilmington, MA, USA) (images 7, 8, and 9).



Image 5. The new 3.0T 8-channel knee coil at the Richard M. Lucas Center for Imaging (GE Healthcare, Milwaukee, WI, USA).

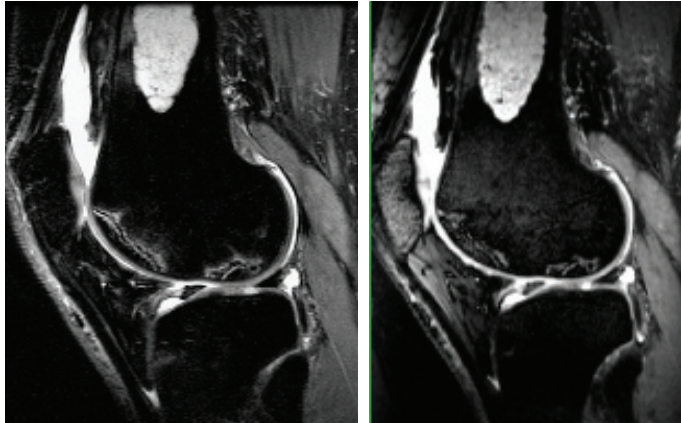


Image 6. Image comparison at 3.0T of a sagittal 2D FSE-xl scan using 2.5 mm slice thickness (l) to a 3D XETA scan using 0.6 mm slice thickness (r) acquired in the coronal plane and reformatted to a sagittal image.

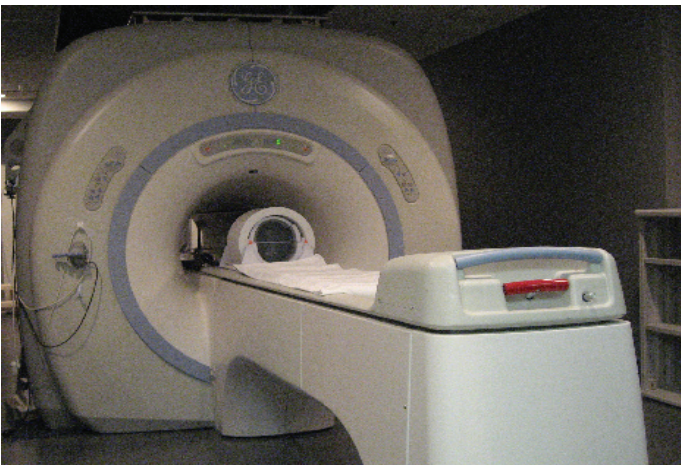


Image 7. The new 16-channel head coil at the 7.0T MR system at the Richard M. Lucas Center for Imaging.

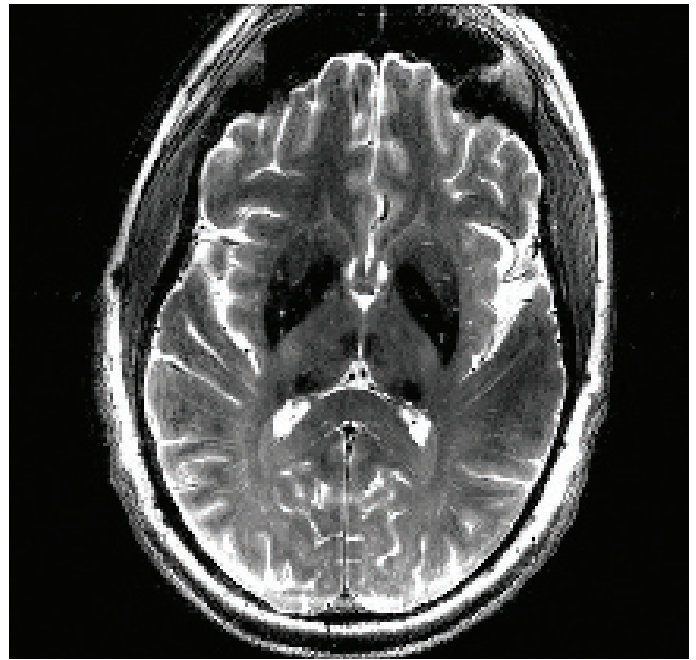


Image 8. Image comparison at 3.0T of a sagittal 2D FSE-xl scan using 2.5 mm slice thickness (l) to a 3D XETA scan using 0.6 mm slice thickness (r) acquired in the coronal plane and reformatted to a sagittal image

Daily support in MR system operation and screening and safety is provided to all researchers including faculty, postdoctoral fellows, graduate students, and visiting scholars in the Lucas Center and Department of Radiology; researchers from other University departments such as Psychology, Psychiatry, Neurology, Neurosurgery, and Nephrology; and service center users from outside of the University.

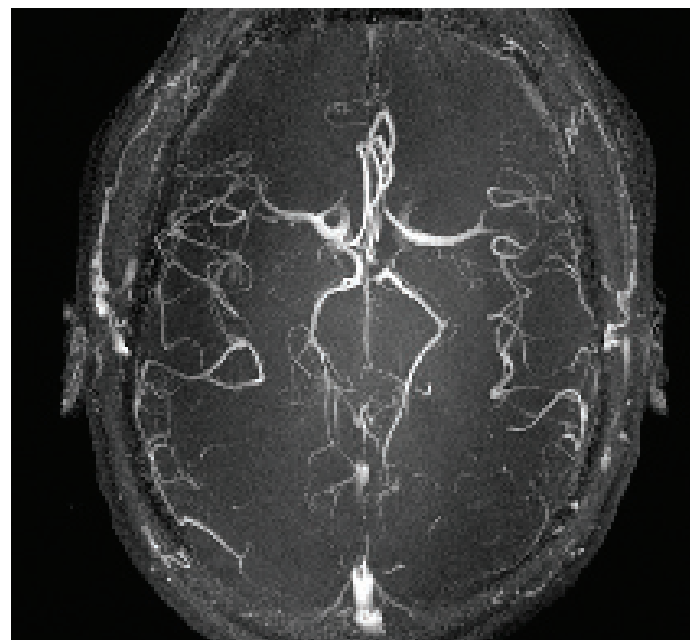


Image 9. An axial 3D time-of-flight image acquired with the new 16-channel head coil at the 7.0T (Nova Medical, Inc., Boston, MA, USA).





# ABSTRACTS

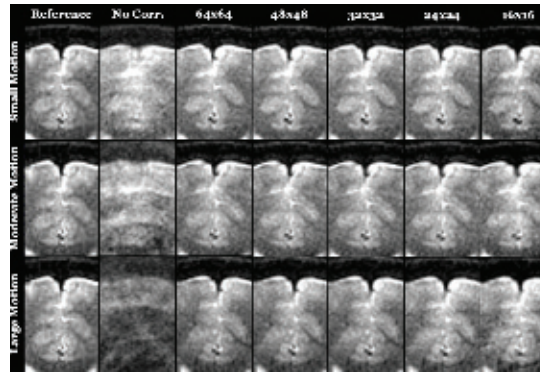
YEARS ON THE CUTTING EDGE



## The Effect of Navigator Resolution on Registration Accuracy in Rigid Head Motion Correction

MURAT AKSOY, CHUNLEI LIU, MIKE MOSELEY, ROLAND BAMMER, DEPARTMENT OF RADIOLOGY

Motion correction schemes in MR often make use of a navigator image for detecting the amount of motion. However, a trade-off exists between the resolution of this navigator and the minimum TE that can be accomplished. It is necessary to choose the navigator resolution large enough so that the registration routine used for detecting the motion parameters is accurate. On the other hand, the readout length for the navigator resolution has to be as small as possible to allow short TE values. It has been shown that subpixel registration is possible using low resolution navigator images. In this study, we examined the effect of navigator resolution on registration accuracy using a parallel-imaging based rigid head motion correction scheme that we developed in-house. Our novel motion correction algorithm uses a spiral in & out readout to detect and eliminate rigid head motion. The spiral in part is used to get a low resolution navigator image for each interleaf and the spiral out part makes up one interleaf of the final high resolution image. The navigator images are used to obtain relative rotation and translation between interleaves. Translational motion is corrected by applying a linear phase to k-space data. Rotational motion is corrected by counter-rotating the k-space



The results of motion correction with our SENSE-based motion correction algorithm for different navigator resolutions are shown

trajectories. This causes undersampling in k-space. An Augmented SENSE reconstruction is used to compensate for this undersampling and to get the final motion-corrected image. In order to assess the impact of navigator resolution on the final image quality, both computer simulations and in vivo studies were performed. For computer simulations, using linear analysis,  $\Delta x_{\text{measured}}$  vs  $\Delta x_{\text{real}}$ ,  $\Delta y_{\text{measured}}$  vs  $\Delta y_{\text{real}}$  and  $\Delta \phi_{\text{measured}}$  vs  $\Delta \phi_{\text{real}}$  graphs were obtained and the correlation coefficient and the linear fit error were used as a measure for the performance of our algorithm. For the in-vivo studies, the correlation coefficient between the motion corrected and reference images were used as a

measure. In this study, accurate and reproducible subpixel registration was possible for images at all resolution levels. In-vivo studies showed that navigator images as small as 32x32 provide adequate image quality. No substantial improvement in image quality could be made above 32x32.

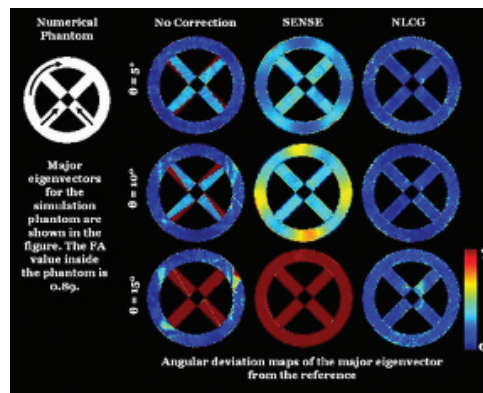
### REFERENCES/FUNDING SOURCE

This work was supported in part by the NIH (1R01EB002711), the Center for Advanced MR Technology at Stanford, P41RR09784, Lucas Foundation, and Oak Foundation.

## Rigid Head Motion Correction for DTI Using Non-Linear Conjugate Gradient

MURAT AKSOY, CHUNLEI LIU, ROLAND BAMMER, Department of Radiology

In multi-shot sequences, rigid body motion can be normally corrected by acquiring a low resolution navigator images to estimate the amount of rotation and translation for each interleaf. However, for a multi-shot diffusion-weighted imaging (DWI) acquisition, simply correcting the rotation and translation of the image itself may not be sufficient. Patient motion does not only affect image registration from shot to shot, but it also changes the diffusion encoding gradients. As a result, each interleaf will have a different diffusion weighting due to the altered gradient direction with respect to patient frame of reference. In this case, it is not feasible to reconstruct the diffusion-weighted images directly. We propose to use a non-linear reconstruction algorithm to estimate diffusion tensors instead of reconstructing the images. In this study, we investigate the use of Non-Linear Conjugate Gradient Algorithm (NLCG) for rigid head motion correction in DTI. In our motion correction algorithm, we used a spin-echo sequence with a spiral in & out readout. In this sequence, the spiral in part was used to get a low resolution navigator image for each interleaf and the spiral out part makes up one interleaf of the final high resolution image. The low resolution navigator images were used for three purposes : 1) Determination of rotation and translation between interleaves 2) Determination of coil sensitivities 3)



Results of computer simulations using SENSE and NLCG. The error resulting from uncorrected diffusion encoding direction in SENSE is eliminated by the application of NLCG.

Detection and elimination of interleaves that are highly corrupted by intra-scan motion. To illustrate the performance of our method, both computer simulations and in-vivo studies were carried out. Reconstructions were obtained with 1) Conventional gridding 2) Phase correction (SENSE) 3) Phase & motion correction (SENSE) 4) Phase & motion & diffusion encoding direction correction (NLCG). Image quality was assessed using point-by-point dot product maps between reference and reconstructed images. Computer simulations showed decreased error in the case of NLCG compared to SENSE. Some improvements were also observed in in-vivo studies. A limitation of our algorithm is its sensitivity to inconsistent data such as noise, artifacts resulting from misregistration and inaccurate estimation of coil sensitivities. This limitation can be alleviated up to a certain degree using preconditioning and regularization.

misregistration and inaccurate estimation of coil sensitivities. This limitation can be alleviated up to a certain degree using preconditioning and regularization.

### REFERENCES/FUNDING SOURCE

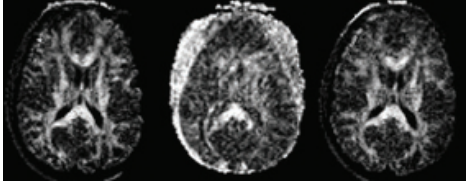
This work was supported in part by the NIH (1R01EB002711), the Center for Advanced MR Technology at Stanford, P41RR09784, Lucas Foundation, and Oak Foundation.



## Tensor Estimation for DTI Using Non-Linear Conjugate Gradient

MURAT AKSOY, CHUNLEI LIU, ROLAND BAMMER, DEPARTMENT OF RADIOLOGY

Reconstruction of diffusion tensors from multi-shot & multi-coil diffusion tensor imaging data is generally a two step procedure, 1) reconstruction of individual diffusion weighted images using non-linear phase correction and SENSE reconstruction, 2) estimation of tensors from the diffusion weighted images using multivariate regression. However, in the case of rotational motion between the shots, each interleaf experiences a different



*In-vivo results showing the FA maps reconstructed with NLCG. The FA map reconstructed using NLCG in case of no subject motion (left) demonstrates the successful visualization of white matter pathways. In the presence of motion, the FA map reconstructed with SENSE and without motion correction (middle) shows significant motion artifacts compared to the motion-corrected image using NLCG (right).*

encounters a different diffusion encoding. This makes it impossible to reconstruct each diffusion weighted image individually. In this study, we propose a single-step tensor estimation scheme that uses a non-linear conjugate gradient (NLCG)

algorithm to overcome this problem. For a multi-shot & multi-coil DTI acquisition, the k-space signal is given by:

$$d_{\gamma,\delta}(k_{\kappa,\xi}) \approx 1/n_p \sum \exp\{jk_{\kappa,\xi}r_p\} s_{\gamma,\xi}(r_p) \exp\{-\sum b_{\delta,\xi} D(r_p)\} m(r_p)$$

where  $\gamma$  stands for the coil number,  $\delta$  for diffusion weighting direction number,  $\xi$  for interleaf number,  $\kappa$  for k-space point and  $\rho$  for image space point.  $m(r_p)$  is the non-diffusion weighted image. Because of the

random nonlinear phase and altered sensitivity exposure due to motion, each interleaf is assigned a different set of modified coil sensitivity profiles. For such a situation, the diffusion encoding ( $b\delta,\xi$ ) has to be different for each interleaf as well. In particular, when there is rotational motion,  $b_{\delta,\xi}$  is given by  $b_{\delta,\xi} = R_{\delta,\xi} b_{\delta} R_{\delta,\xi}^T$ , where  $R_{\delta,\xi}$  is the rotation matrix of  $\xi^{\text{th}}$  interleaf with respect to a template. The aim of the NLCG algorithm is to find the  $D(r_p)$  that minimizes a cost function  $f$  given by:

$$f = \|d_{\gamma,\delta}(k_{\kappa,\xi}) - 1/n_p \sum \exp\{jk_{\kappa,\xi}r_p\} s_{\gamma,\xi}(r_p) \exp\{-\sum b_{\delta,\xi} D(r_p)\} m(r_p)\|^2$$

To find the  $D(r_p)$  that minimizes this cost function, we employed the NLCG algorithm using Polak-Ribiere and Newton-Raphson line search [4]. In order to use this algorithm efficiently, we need the first derivative and an approximation to the second derivative of the cost function given above with respect to the tensor elements  $D(r_p)$ :

$$df/dD(r_{p1}) = 1/n_p \sum_{\gamma,\delta,\xi} 2b_{\delta,\xi} \text{Re}\{DWI_{\gamma,\delta,\xi}(r_{p1})^* FT1\{d_{\gamma,\delta}(k_{\kappa,\xi}) - FT2\{DWI_{\gamma,\delta,\xi}(r_{p1})\}\}\}$$

$$d^2f/dD(r_{p1})^2 = \sum_{\gamma,\delta,\xi} 2n_{\kappa} [b_{\delta,\xi}]^2 / n_p^2 |DWI_{\gamma,\delta,\xi}(r_{p1})|^2 - [b_{\delta,\xi}] df/dD(r_{p1}) DWI_{\gamma,\delta,\xi}(r_p) = s_{\gamma,\xi}(r_p) \exp\{-\sum b_{\delta,\xi} D(r_p)\} m(r_p)$$

In-vivo studies showed that successful visualization of white matter pathways is possible using NLCG. The method performs similar to the conventional two step tensor estimation when there is no motion.

### REFERENCES/FUNDING SOURCE

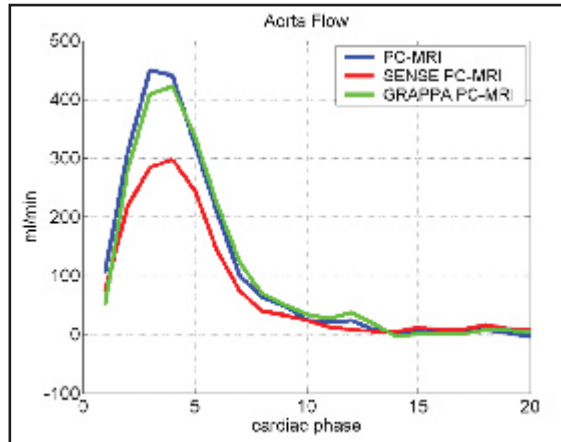
M Aksoy, C Liu, R Bammer "Tensor Estimation for DTI Using Non-Linear Conjugate Gradient" ISMRM-ESMRMB, May, 2007. NIH 1R01EB002711, the CAMRT P41RR09784, Lucas Foundation and Oak Foundation.

## Autocalibrated Phase-Contrast Imaging

CALVIN LEW<sup>1</sup>, MARC ALLEY<sup>2</sup>, DAN SPIELMAN<sup>2</sup>, ROLAND BAMMER<sup>2</sup>, FRANDICS CHAN<sup>2</sup>,  
DEPARTMENTS OF <sup>1</sup>ELECTRICAL ENGINEERING AND <sup>2</sup>RADIOLOGY

In phase-contrast MRI (PC-MRI), the full field of view is commonly aliased in order to maximize the spatial resolution. It has been reported that SENSE may pose as a problem in correctly unaliasing the tissue due to coil sensitivity maps that do not match that of the aliased tissue in the full field of view. The reconstructed images will have artifacts that may compromise the accuracy of a flow experiment. However, autocalibration sequences do not have this problem.

We apply an autocalibrating sequence to PC-MRI for both aortic and pulmonary flow. We reconstruct the data using the GRAPPA method and then compare our measurements with SENSE. Data was acquired with 5 normal volunteers using conventional PC-MRI, SENSE PC-MRI, and autocalibrated PC-MRI. Reduction factor of 2 was used for the undersampling. For autocalibrated PC-MRI, 32 central fully-sampled phase encodes (ACS) were acquired. Volunteers were scanned on a 1.5T TwinSpeed MRI Scanner (GE Medical Systems, Waukesha, WI) Flow from the aorta and pulmonary artery was measured. Bland-Altman analysis was used.



*The flow curve of the aorta shows that the SENSE acquisition deviated from the reference and GRAPPA reconstruction.*

The mean differences for aorta flow between PC-MRI and SENSE PC-MRI is -500 mL/min, while for pulmonary artery flow, it is -500 mL/min. The mean differences for aorta flow between PC-MRI and GRAPPA is 50 mL/min. The mean differences for pulmonary artery flow between PC-MRI and GRAPPA is -300 mL/min.

Measured flow from a GRAPPA reconstruction shows closer agreement to flow from conventional PC-MRI than that from SENSE PC-MRI. The aortic flow measurements seemed to benefit more from GRAPPA than the pulmonary artery flow measurements because the aliased signal is stronger in the aorta cases. A clinical application of the autocalibrating PC-MRI sequence would be the

natural extension of this work. A smaller number of central phase-encodes can be used to further reduce scan time. An investigation into finding this limit for aorta and pulmonary artery scans may be beneficial.

### FUNDING SOURCE

GE Medical Systems, Center for Advanced MR Technology at Stanford P41RR09784, R01EB002711, the Whitaker Foundation, and the Lucas Foundation. This work is supported by NIH RR09784 and the Richard M. Lucas Foundation.

## Parallel Imaging Reconstruction for Arbitrary Trajectories with k-Space Sparse Matrix (kSPA)

CHUNLEI LIU, ROLAND BAMMER, MICHAEL E. MOSELEY  
LUCAS IMAGING CENTER, DEPARTMENT OF RADIOLOGY

Despite the recent advances of several parallel imaging algorithms, it remains a challenge in many applications to rapidly and reliably reconstruct an image from partially acquired non-Cartesian k-space data. Such applications include, for example, 3D imaging, functional MRI (fMRI), perfusion-weighted imaging and diffusion tensor imaging (DTI), where a large number of images have to be reconstructed. In this abstract, we propose a systematic non-iterative reconstruction algorithm termed kSPA that suits arbitrary sampling patterns. The kSPA algorithm computes a sparse approximate inverse that can be applied repetitively to

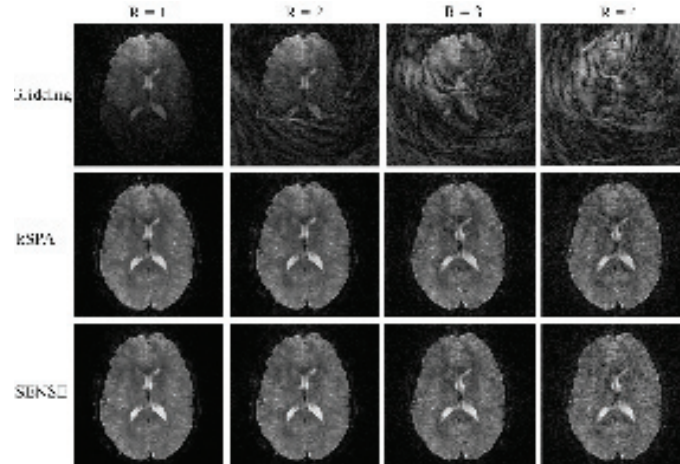


Figure 1. Shows examples of kSPA reconstructed in vivo spiral brain images with various reduction factors.

reconstruct all subsequent images. This algorithm is demonstrated using both simulated and in vivo data, and the resulting image quality is shown to be comparable to that of the iterative SENSE algorithm. In addition, the image reconstruction time can be reduced approximately by a factor of 100 for every thousand images. This algorithm, therefore, is particularly useful for the aforementioned applications.

Examples of kSPA reconstructed in vivo spiral brain images with various reduction factors are shown in figure 1. We have started to apply this technique for fMRI, DTI, and spectroscopy.

## Fast Parallel Spiral Chemical Shift Imaging at 3 Tesla Using Iterative SENSE Reconstruction

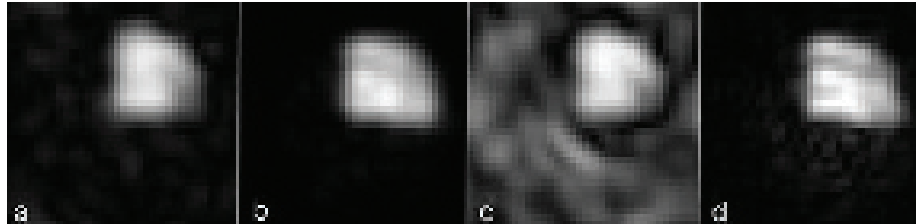
D. MAYER, D.M. SPIELMAN, R. BAMMER  
DEPARTMENT OF RADIOLOGY, STANFORD UNIVERSITY

**Introduction**  
Spiral chemical shift imaging (CSI) reduces the scan time of a CSI experiment by acquiring the time domain data while playing out spiral gradient waveforms along two spatial dimensions.

This achieves the simultaneous encoding of both spatial and spectral information and theoretically permits the acquisition of a complete 2D CSI data set with a single excitation. However, for most applications, limitations on maximum gradient strength and slew rate usually make multiple excitations necessary in which either the start of the data acquisition is shifted (spectral interleaves) or the spiral k-space trajectories are rotated (spatial interleaves). Gradient limitations are even more a problem at higher field strength because of the increased dispersion of the chemical shift. While parallel imaging techniques are commonly used even in non-Cartesian imaging to speed up the acquisition, so far, they have been only applied to CSI using conventional phase encoding and echo planar spectroscopic imaging. Therefore, the aim of this work was to reduce the minimum total measurement time ( $T_{min}$ ) of spiral CSI by using an iterative sensitivity encoding (SENSE) reconstruction algorithm.

**Method** A spiral CSI sequence with point resolved spectroscopy (PRESS) volume pre-selection was used with  $TE = 144$  ms. The spiral gradient waveforms were designed for 4 spatial interleaves with a FOV of  $24 \times 24$  cm<sup>2</sup> for a  $16 \times 16$  matrix and a spectral width of 1202 Hz. To simulate accelerated data acquisition, the data set was subsampled by using only every  $R^{\text{th}}$  interleaf ( $R = 1, 2, 4$ ).

After apodization and FFT in the spectral dimension, reconstruction in the two spatial dimensions was accomplished by a variant of



Metabolic images of NAA: (a)  $R = 1$ , SoS (b)  $R = 1$ , SENSE, (c)  $R = 2$ , SoS, and (d)  $R = 2$ , SENSE.

iterative SENSE reconstruction using the conjugate gradient method and a transfer function approach. Alternatively, a sum of squares (SoS) reconstruction was accomplished by setting

all coil sensitivity information to “1”. Using  $n_{it} = 1$ , this is similar to gridding reconstruction without correcting for coil sensitivity variation.

**Results** Using the PRESS volume pre-selection, the top, right sector of the sphere containing a solution of various brain metabolites. Results Metabolic images of NAA reconstructed with  $R=1$  and  $R=2$  for both SoS and SENSE are shown in Fig. 1.

Subtle differences in relative image intensities between Fig. 2a and 2b are due to normalization with coil sensitivities. Due to insufficient k-space sampling, the image reconstructed with  $R=2$  and SoS (Fig. 1c) is severely aliased. Considering that only half of the data were used for the image reconstructed with  $R=2$  and SENSE (Fig. 1d), the image is comparable to the one reconstructed with  $R=1$  and SoS (1b). Minimum spatial aliasing artifacts were observed.

**Conclusion** The presented data demonstrate the feasibility of reducing  $T_{min}$  of fast spiral CSI by using iterative SENSE reconstruction. The reduction in the number of spatial interleaves is beneficial when extending CSI to incorporate multiple frequency dimensions.

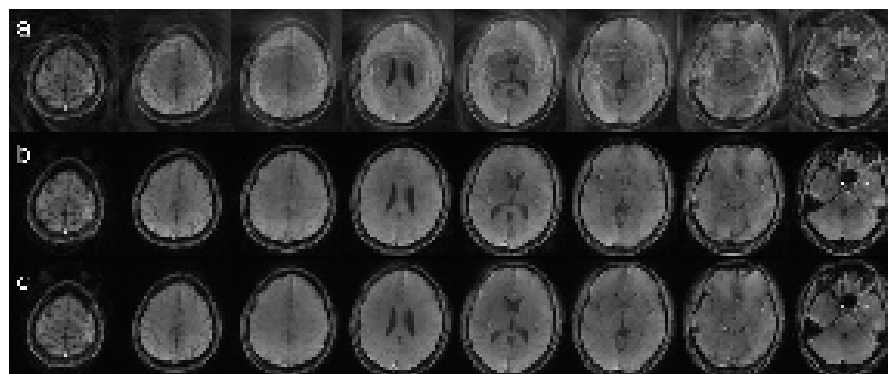
### REFERENCES/FUNDING SOURCE

NIH grants RR09784, AA12388, AA13521, and RO1 EB002711.  
Fast Parallel Spiral Chemical Shift Imaging at 3T Using Iterative SENSE Reconstruction (Proceedings ISMRM 2007)

## kSPA for 3D Parallel Imaging Reconstruction

CHUNLEI LIU, MICHAEL E. MOSELEY, DEPARTMENT OF RADIOLOGY, RICHARD M. LUCAS IMAGING CENTER

Although 3D parallel imaging is conceptually a simple extension of 2D parallel imaging, its application has been far less common than its 2D counterpart due to various technical difficulties (1). In particular, more development is required for generic algorithms that can be applied to arbitrary 3D sampling trajectories. In principle, the iterative conjugate gradient SENSE algorithm still applies in the 3D case (2). However, the computational load and memory requirement render it impractical. Here, we present a novel 3D kSPA (k-space SPArse matrix) parallel imaging technique that works on general non-Cartesian trajectories. The kSPA algorithm computes a sparse approximate inverse of the k-space encoding matrix. Using this inverse matrix, the Fourier transform of an image can be reconstructed through a matrix-vector product. This technique is dem-



A representative set of images from a 128x128x32 volume reconstructed by: (a) gridding and sum-of-squares reconstruction; (b) kSPA; (c) reference images without undersampling.

onstrated using a multi-shot 3D stack-of-spiral sequence. Excellent image quality is demonstrated with a reduction factor of 2.

Examples of kSPA reconstructed in vivo spiral brain images with various reduction factors are shown in figure 1. We have started to apply this technique for fMRI, DTI, and spectroscopy.

### REFERENCES/FUNDING SOURCE

Proceedings of 15th ISMRM, Berlin 2007, abstract #147.  
NIH-1R01NS35959, NIH-1R01EB002771, Lucas Foundation, NCRR P41RR09784, NIH-1K99NS057943-01.

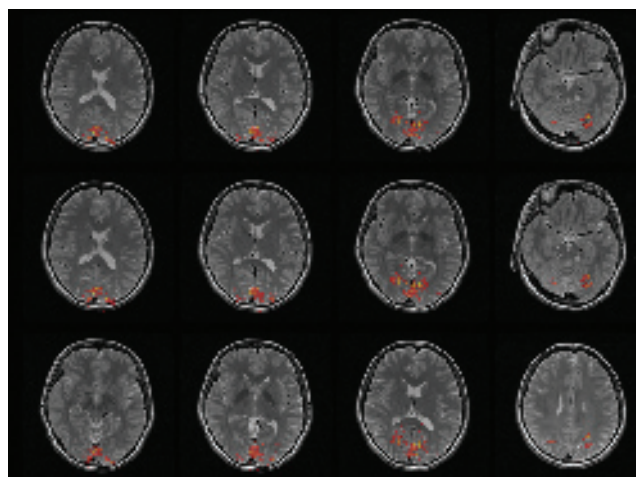
## kSPA for High Spatial and High Temporal Resolution 3D fMRI.

CHUNLEI LIU<sup>1</sup>, YANLE HU<sup>1,2</sup>, JINGJING LU<sup>3</sup>, GARY H. GLOVER<sup>1</sup>, MICHAEL E. MOSELEY<sup>1</sup>

DEPARTMENTS OF <sup>1</sup>RADIOLOGY (RICHARD M. LUCAS IMAGING CENTER) AND <sup>2</sup>PHYSICS, STANFORD UNIVERSITY.

<sup>3</sup>DEPARTMENT OF RADIOLOGY, PEKING UNION MEDICAL COLLEGE HOSPITAL, BEIJING, P.R. CHINA

Parallel imaging techniques have been applied in functional MRI (fMRI) to improve spatial and temporal resolution. However, its application has so far been hampered by reduced signal-to-noise ratio (SNR) and extensively prolonged image reconstruction time, especially for non-Cartesian sampling trajectories. In this abstract, we introduce a novel 3D kSPA (k-space SPArse matrix) parallel imaging technique with volumetric acquisition to alleviate these two problems. kSPA is a fast reconstruction algorithm that is particularly suited for repetitive image reconstruction where thousands of images are acquired in a single scan. The kSPA algorithm computes a sparse approximate inverse that can be applied repetitively to reconstruct all subsequent images. By combining kSPA with 3D fMRI, we can trade



Comparison of activation maps for 4 typical slices out of a total 32 slices. (a) kSPA reconstruction with  $R = 2$ , half of the frames were used for correlation; (b) kSPA reconstruction with  $R = 2$ , all frames were used for correlation; (c) normal gridding reconstruction. kSPA results in comparable activation maps but increases the temporal resolution.  $p < 0.001$  in all cases.

the SNR gain from 3D acquisition for higher spatial or temporal resolution, and less geometric distortion and signal drop-off. In vivo 3D kSPA fMRI is demonstrated with a stack-of-spiral 3D gradient echo sequence using a typical contrast-reversing checkerboard visual stimulus. The kSPA reconstruction results in an improved temporal resolution without compromising the activation volume.

Examples of 3D kSPA fMRI with visual activation are shown in figure 1.

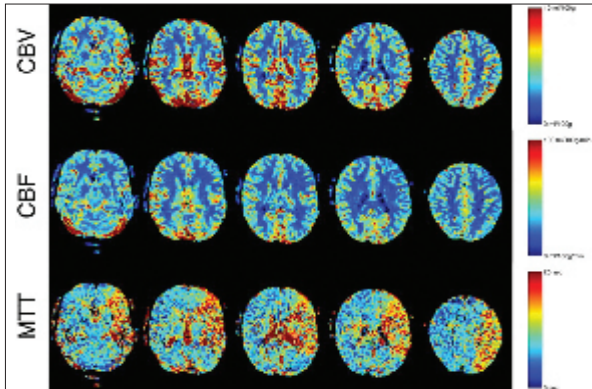
### REFERENCES/FUNDING SOURCE

Proceedings of 15th ISMRM, Berlin 2007, abstract #1946. Funded by the Lucas Foundation and NIH 1R01NS35959, NIH 1R01EB002771, NCRR P41RR09784, and NIH 1K99NS057943-01.



## Perfusion Mapping with Multiecho Multishot Parallel Imaging EPI

REXFORD D. NEWBOULD<sup>1</sup>, STEFAN T. SKARE<sup>1</sup>, THIES H. JOCHIMSEN<sup>3</sup>, MARCUS T. ALLEY<sup>1</sup>, MICHAEL E. MOSELEY<sup>1</sup>,  
GREGORY W. ALBERS<sup>2</sup>, ROLAND BAMMER, DEPARTMENTS OF <sup>1</sup>RADIOLOGY, <sup>2</sup>NEUROLOGY, AND <sup>3</sup>PSYCHOLOGY



Hemodynamic maps from a 62-year-old male admitted for headaches and right-sided weakness, calculated using a PERMEATE scan. Significantly reduced blood flow can be seen in the vascular territory of the left MCA.

Dynamic susceptibility contrast (DSC)-based perfusion-weighted imaging (PWI) can visualize cerebrovascular hemodynamics. Therefore, it may be an important asset to determine tissue-at-risk in acute stroke patients. When used with diffusion-weighted imaging (DWI), it can help to triage patients who would potentially benefit from IV tPA treatment or mechanical thrombectomy. In DSC imaging, an exogenous paramagnetic tracer (e.g., Gd-DTPA or Dy-DTPA) is rapidly injected into the venous system and its passage is tracked through concentration-related  $T_2^*$  changes in the cerebral vascular bed.

Echo-planar imaging (EPI) is the standard technique for dynamic susceptibility-contrast (DSC) perfusion MRI. However, EPI suffers from well-known geometric distortions, which can be reduced by increasing the k-space phase velocity. Moreover, the long echo times (TEs) used in DSC lead to signal saturation of the arterial input signal, and hence to severe quantitation errors in the hemodynamic information. Here, through the use of interleaved shot acquisition and parallel imaging (PI), rapid volumetric EPI is performed using pseudo-single-shot (ss)EPI with the effective  $T_2^*$  blur and susceptibility distortions of a multishot EPI sequence. The reduced readout lengths permit multiple echoes to be acquired with temporal resolution and spatial coverage similar to those obtained with a single-echo method. Multiecho readouts allow for unbiased  $R_2^*$  mapping to avoid incorrect estimation of tracer concentration due to signal saturation or  $T_1$  shortening effects. Multiecho perfusion measurement also mitigates the signal-to-noise ratio (SNR) reduction that results from utilizing PI. Results from both volunteers and clinical stroke patients are presented. This acquisition scheme can aid most rapid time-series acquisitions. The use of this method for DSC addresses the problem of signal saturation and  $T_1$  contamination while it improves image quality, and is a logical step toward better quantitative MR PWI.

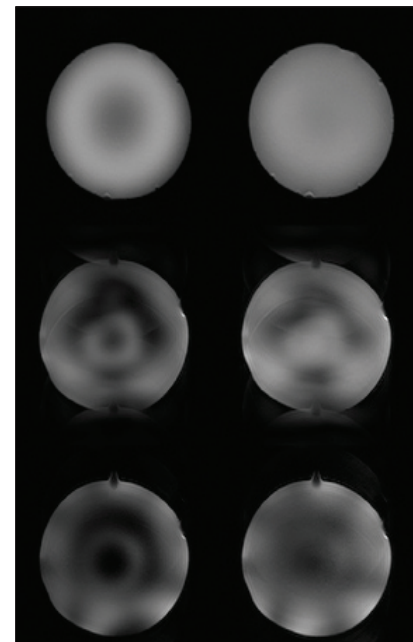
### REFERENCES/FUNDING SOURCE

Magnetic Resonance in Medicine, Volume 58, Issue 1, 2007. Pages: 70-81  
Lucas Foundation, Oak Foundation, National Institutes of Health; Grant Number: 1R01EB002771,  
Center of Advanced MR Technology at Stanford; Grant Number: P41RR09784.

## Adiabatic Refocusing Pulses in 3T and 7T Diffusion Imaging

S SKARE, P BALCHANDANI, RD NEWBOULD, R BAMMER, RADIOLOGICAL SCIENCES LABORATORY, DEPARTMENTS OF RADIOLOGY

The two traditional 3.2 ms long sinc refocusing pulses in a diffusion-weighted single-shot EPI sequence were optionally replaced by two slice selective truncated hyperbolic secant pulses (4) of 10 ms in length. Here, the two adiabatic  $180^\circ$  pulses cancel their quadratic phase across the slice and yield a linear spin phase at the time when a spin echo is formed. The addition of the two adiabatic pulses led to an increased TE of  $\sim 13$  ms. For the excitation, a standard spectral spatial (SPSP)  $90^\circ$  pulse was used, which has the fat saturation properties needed for EPI. In our first attempt towards B1 insensitivity, we have not modified the SPSP  $90^\circ$  as no good fat-suppressed slice-selective adiabatic excitation alternative currently exists. Experiments were performed on phantoms at 3T and 7T GE whole body systems equipped with 40 mT/m gradients. The standard transmit/receive head coil was used on the 3T scanner and a volume/8-channel dual mode transmit/receive head coil was used in both modes on the 7T scanner. Image parameters were as follows: FOV = 24 cm, slice thickness = 4 mm, b-value 1000 s/mm<sup>2</sup>, and 3 interleaves (to keep the phantom somewhat round). When the 8-channel coil was used, the inter-shot ghosting in the data was avoided by means of GRAPPA reconstruction of each shot. However, this has no impact on the transmit B1-related intensity variations.



$b=0$  s/mm<sup>2</sup> images without (left) and with (right) the use of adiabatic refocusing pulses. At 3T, the signal variations are almost eliminated. At 7T, the situation is substantially improved, while some residual variations remain due to the increased sensitivity of the non-adiabatic  $90^\circ$  excitation.

### REFERENCES/FUNDING SOURCE

ISMRM Berlin 2007. pp. 1493. This work was supported in part by the NIH (1R01EB002711), the Center for Advanced MR Technology at Stanford (P41RR09784), Lucas Foundation, and Oak Foundation.

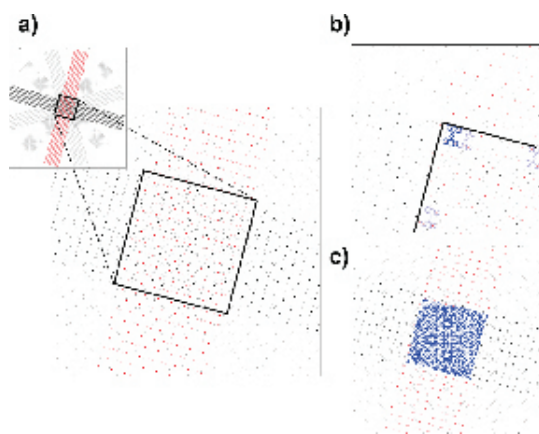
## GRAPPA Estimations from Undersampled Propeller Trajectories

S SKARE, RD NEWBOULD, R BAMMER

DEPARTMENT OF RADIOLOGY, RADIOLOGICAL SCIENCES LABORATORY

GRAPPA weights are typically estimated using a fully sampled central region of k-space. These weights are then used to synthesize the outer parts of k-space. Parallel imaging (PI) techniques such as GRAPPA are of great advantage for sequences using propeller shaped readouts. For example, the echo spacing is long in PROPELLER (1) due to the RF refocused echoes. With PI, however, the readout time becomes R times shorter for a given blade width - which reduces the T2-blurring, SAR, and increases the number of slices/TR. Recently we proposed a new EPI-based propeller readout design with the readout direction along the short-axis of the blade ("Short-Axis readout Propeller EPI" or "SAP-EPI") in order to reduce the geometric distortions associated with EPI (2). We have also presented the SAP-EPI in combination with GRAPPA using R=3 and R=4 (3), in which it was shown to reduce the geometric distortions by an order of magnitude compared to standard EPI. The purpose of this study was to explore the possibility of extracting the GRAPPA weight information by capitalizing on the excessively sampled center of k-space, which is well sampled even though each blade itself is undersampled by a factor of R.

To calculate the GRAPPA weights on a per-blade basis, two strategies were investigated:



GRAPPA estimation in the intersection between undersampled propeller blades. The two alternative approaches tested in this work are shown in b) and c). (In b) label the RO and PE direction and for which blade direction you are determining the weights).

1) Two orthogonal blades to form a Cartesian grid at the center of k-space. The intersecting area is not fully sampled, but samples are bound to a Cartesian grid. The GRAPPA kernel is here shifted over the entire intersecting area by R increments of  $k_x$  and  $k_y$ , rather than single increments along  $k_x$  and  $k_y$ , as is typically performed during the weight determination phase. For an R of 3 one ends up with 9 times less locations to train the data making the system less over-determined. For that reason, one has to resort to small GRAPPA kernels, e.g. two source lines and three  $k_x$  (read) locations.

2) The inclusion of all blade data in the central region will provide sufficiently dense k-space coverage (blue dots in Fig. 1c) that for each blade, data can be gridded to Cartesian k-space locations. This intersecting central area will allow the estimation

of GRAPPA weights using the conventional 2D sliding scheme of the GRAPPA kernel. This reconstruction requires extra computation due to the gridding of blade data around the origin of k-space for each blade (with up to  $N_{RO}^2/R \times N_{blades}$  k-space samples for each blade).

### REFERENCES/FUNDING SOURCE

This work was supported by NIH 1R01EB002711, the CAMRT P41RR09784, Lucas Foundation, and Oak Foundation. Presented PGRAPPA estimations using undersampled propeller trajectories", at ISMRM, 2007.

## Mood and Gender Effects on Amygdalar Activation in Pediatric Bipolar Disorder

NANCY E. ADLEMAN<sup>1,2</sup>, ASYA KARCHENSKIY<sup>1</sup>, MEGHAN E. HOWE<sup>1</sup>, AMY S. GARRETT<sup>1</sup>, ALLAN L. REISS<sup>1</sup>, KIKI D. CHANG<sup>1</sup>

<sup>1</sup>DEPARTMENT OF CHILD & ADOLESCENT PSYCHIATRY AND <sup>2</sup>PROGRAM IN NEUROSCIENCES

A previous study by our laboratory failed to find a difference between children with bipolar disorder (BD) and healthy controls in amygdala activation in response to emotionally valenced stimuli taken from the International Affective Pictures Scale. However, studies have demonstrated that the amygdala does respond to such emotionally valenced stimuli. Also, research suggests that both activation in, and structure of, the amygdala may be abnormal in children with BD. In order to further explore amygdalar activation in pediatric BD, we employed an amygdalar region of interest (ROI) analysis to a larger sample of children and adolescents with BD. Several studies have suggested that amygdalar activity may be moderated by degree of severity of mood symptoms. We hypothesized that mood state would influence amygdalar activation levels in our population, and that the diverse mood symptoms observed in our cohort might mask any group differences in activation in this region.

Subjects were 25 children and adolescents (19 males, 6 females) diagnosed with BD and 20 healthy controls (15 males, 5 females). There were no significant differences between the bipolar and control groups or between genders with regards to percent of voxels activated in either amygdala ROI in response to negative images compared to neutral images. However, it was evident that there was an interaction between amount of depressive symptomatology, as measured by the

CDRS, and gender influencing amygdalar activation for the BD group. There was a significant positive correlation between CDRS score and percent activation in both amygdalae for female BD subjects. However, for male BD subjects, an inverse correlation existed between CDRS score and percent activation in the right amygdala, but not in the left.

In accordance with our hypothesis, we found a relationship between activation in the amygdala and mood state, specifically degree of depression. A surprising finding was that the relationship between degree of depression and amygdalar activation differed between male and female subjects, in some cases these correlations were directly opposite. This is the largest pediatric BD cohort in an analysis of this kind, and it highlights the potential confound gender may play in mood disorder studies of adolescents. These data suggest a potential site for mood-related treatment for bipolar disorder, and that boys and girls with bipolar disorder may have different mechanisms of amygdalar activity during mood episodes, potentially requiring different treatment approaches according to gender.

### REFERENCES/FUNDING SOURCE

The authors gratefully acknowledge the support of this research by the NIMH MH046640, NARSAD, the Klingenstein Third Generation Foundation, and the Hahn Family.

## Continuous 2D GRAPPA Kernel for Propeller Trajectories

S SKARE, RD NEWBOULD, R BAMMER

RADIOLOGICAL SCIENCES LABORATORY, DEPARTMENT OF RADIOLOGY

Building on the ideas from our earlier work on spatial modeling of 1D GRAPPA kernels in hybrid space (5), we have now used a similar continuous representation of the GRAPPA weights using a 2D GRAPPA kernel in k-space with the continuous representation being the angle of the blades. The weight estimation for blade 1, in which the relation between ACS line  $i$  for coil  $j$ ,  $y_{ij}$ , and the surrounding acquired lines (all coils), contained in a matrix  $\mathbf{A}$ , is given by, where  $\mathbf{w}_{ij,1}$  is an  $(N_{\text{coils}} \times N_{\text{ky}} \times N_{\text{kx}}) \times 1$  vector representation of the GRAPPA kernel, and  $N_{\text{ky}}$  and  $N_{\text{kx}}$  are the number of rows and columns involved in the GRAPPA kernel. In our setting  $\mathbf{w}_{ij}$  is of size  $(8 \times 2 \times 3) \times 1$ . We can now estimate the GRAPPA weights for all  $N$  blades at once by:

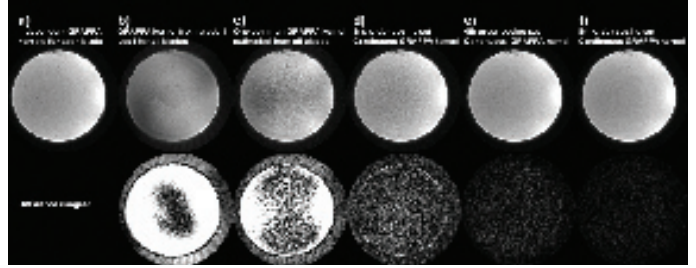
$$\mathbf{y}_{\text{big}} = \begin{bmatrix} y_{ij,1} \\ \vdots \\ y_{ij,N} \end{bmatrix} = \begin{bmatrix} \mathbf{A}_1 & 0 & 0 & 0 \\ 0 & \mathbf{A}_2 & 0 & 0 \\ 0 & 0 & 0 & 0 \\ 0 & 0 & 0 & \mathbf{A}_N \end{bmatrix} \begin{bmatrix} \mathbf{w}_{ij,1} \\ \vdots \\ \mathbf{w}_{ij,N} \end{bmatrix} = \mathbf{A}_{\text{big}} \text{vec}(\mathbf{W}_{ij}) \quad [1]$$

where  $\mathbf{W}$  is a matrix of size  $(N_{\text{coils}} \times N_{\text{ky}} \times N_{\text{kx}}) \times N$  and the “vec” operator unravels the matrix  $\mathbf{W}$  into a single column. To reduce the total number of independent unknowns in  $\mathbf{W}$  and to make the GRAPPA kernel a continuous function over the blade angles,  $\mathbf{W}$  is constrained by a cosine basis set  $\mathbf{C}$  of size  $N \times N_{\text{order}}$  across the columns of  $\mathbf{W}$ :  $\mathbf{w} = (\mathbf{CH})^T$ . Given the basis set  $\mathbf{C}$ ,  $\mathbf{W}$  (and hence the GRAPPA coefficients for all blades) is solely determined by the unknown elements of  $\mathbf{H}$ , which is arbitrary

smaller than  $\mathbf{W}$ . The elements of  $\mathbf{H}$  are estimated from the k-space data  $\mathbf{A}_{\text{big}}$  and  $\mathbf{y}_{\text{big}}$  via:

$$\mathbf{y}_{\text{big}} = \mathbf{A}_{\text{big}} \text{vec}(\mathbf{H}^T \mathbf{C}^T) = \mathbf{A}_{\text{big}} \underbrace{(\mathbf{C} \otimes \mathbf{I})}_{\mathbf{Q}} \underbrace{\text{vec}(\mathbf{H}^T)}_{\mathbf{h}} = (\mathbf{A}_{\text{big}} \mathbf{Q}) \mathbf{h} \Rightarrow \mathbf{h} = (\mathbf{A}_{\text{big}} \mathbf{Q})^+ \mathbf{y}_{\text{big}} \quad [2]$$

where “+” denotes the pseudo inverse and “ $\otimes$ ” the Kronecker product and we have used the following algebraic rule:  $\text{vec}(\mathbf{xy}) = \mathbf{Y}^T \mathbf{I}$ . Interestingly, the number of rows of  $\mathbf{C}$  may be different when estimating and applying  $\mathbf{h}$ . This allows e.g. the use of a sub-set of the final blades for the calibration. Exactly how many blades required for the estimation of  $\mathbf{h}$  depends on the 2D GRAPPA kernel size, number of coils used and the richness of the basis set.



Different GRAPPA kernels used to synthesize missing lines in 20 propeller blades, each undersampled by R-2. See above text for details. An 4th to 8th order cosine set seems to be enough to model the variations in GRAPPA coefficients over an 180° sweep.

REFERENCES/FUNDING SOURCE: Supported by NIH EY015000

## Major Speed-Up of Nyquist Ghost Correction in Ramp-Sampled EPI

A. NORDELL<sup>1,2</sup>, R. BAMMER<sup>1</sup>, AND S. SKARE<sup>1</sup> <sup>1</sup>LUCAS CENTER, STANFORD, PALO ALTO, CA, UNITED STATES,

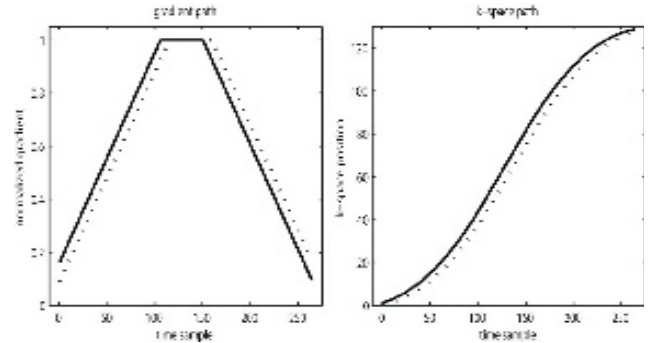
<sup>2</sup>DEPT OF CLINICAL NEURO SCIENCE, KAROLINSKA INSTITUTE, STOCKHOLM, SWEDEN

In echo planar imaging (EPI), even and odd k-space lines are acquired using positive and negative readout gradient lobes. Small undesired timing differences between these gradient waveforms will cause misalignments between odd and even echoes leading to FOV/2-ghosting (Nyquist ghosting). Further more in order to reduce echo spacing, which reduces image distortion, modern EPI acquires data on the attack and decay ramp of the readout gradient. In order to obtain Cartesian uniform sampling, gridding is needed. For minimum ghost levels, the linear gradient time delays that lead ultimately to ghosting are to be corrected before ramp sampling rather than afterwards, as the gradient time delay is constant for each sample prior to, but not after gridding. This, however, requires two additional computationally expensive non-power-of-two 1D-FFT's in the kx direction. For dynamic EPI acquisitions, this may cause prohibitively long delays in the image reconstruction time. In this work, we demonstrate that, by embedding a previously estimated phase correction in the ramp sampling correction, a major speed-up in EPI reconstruction can be achieved at identical FOV/2 ghost level.

By incorporating the FOV/2N ghost correction into the gridding portion of the ramp sampling reconstruction, simply by treating it as a gradient time delay when computing the underlying k-space trajectory, a major reduction in reconstruction time could be achieved (see fig. 4). Reconstruction time was approximately 5× faster in both cases (64×64 and 128×128 matrix), with ghost correction being 85% of the total reconstruction time in the conventional method, compared to a

25% in the new approach. Despite the faster reconstruction there was no change in ghost artifact removal and image quality.

This new reconstruction method is simple but has very important consequences for EPI reconstruction. Particularly, for increase in dynamic scan numbers the method has dramatic potential.



The estimated linear phase is translated into a gradient waveform delay (left dashed). Integration of the gradient waveform, gives the shifted k-space path (right dashed) used to construct the gridding kernel that corrects for both Nyquist ghosting and ramp sampling.

FUNDING

Karolinska University Hospital, Stockholm, Sweden  
Stiftelsen Frimurare, Stockholm, Sweden

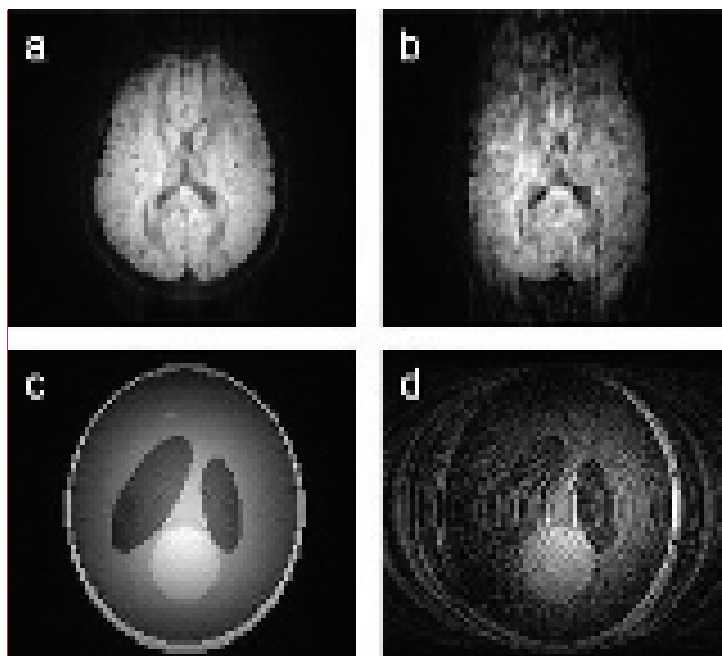


## 3D Self-Navigated Interleaved Spiral (3D-SNAILS) for DWI

JIAN ZHANG<sup>1,2</sup>, CHUNLEI LU<sup>1</sup>, MICHAEL MOSELEY<sup>1</sup>,  
Departments of <sup>1</sup>ELECTRICAL ENGINEERING; <sup>2</sup>RADIOLOGY

3D diffusion imaging offers some very desirable features such as isotropic resolution and higher signal-to-noise ratio. One of the major challenges for 3D diffusion imaging is the motion correction problem since a high resolution DWI/DTI acquisition inevitably requires multiple shots and long acquisition time. Self-Navigated InterLeaved Spiral (SNAILS) is an effective 2D diffusion imaging method in which motion-induced phase errors can be estimated and corrected by using variable-density (VD) spiral trajectories. Currently, there is a lack of effective 3D self-navigated DWI methods. Here, we present a novel 3D-SNAILS approach that is capable of estimating and correcting 3D linear and non-linear phase errors. Our preliminary results show that 3D SNAILS can provide effective 3D phase navigations and high quality 3D DWI volume scans.

In our method, the whole 3D k-space is fully sampled by a set of radial 2D planes with each one sampled by interleaved VD-spirals. To achieve 3D navigation, we modify the beginning part of each interleaved spiral by applying a short continuous and oscillating z-gradient along the perpendicular direction (kz). This zigzagged or EPI-fashioned spiral segment will fully sample a small cylindrical volume at k-space origin. As a result, the overall kxy trajectory is still a variable-density spiral with its beginning part very slowly sam-



3D reconstruction results of simulated DWI data by using 3D-SNAILS. (a) and (c) were reconstructed with phase error estimation and subtraction. (b) and (d) show the corresponding slices reconstructed by direct 3D griddings.

pled and remaining part regularly sampled (slew-rate limited).

A two-stage gridding approach is used for our reconstruction to avoid the massive 3D weighting density computation. First, in-plane samples are gridded to its corresponding “radial k-space Cartesian plane”. Afterwards, each radial plane is gridded into the true 3D k-space Cartesian grids. Analogous to 2D SNAILS, the navigator of each interleaved spiral is used to estimate the phase errors. Finally, the motion corrected reconstruction can be done by either applying direct phase subtractions or conjugate-gradient iterations. The reconstruction results are shown in the figure.

3D-SNAILS will be an effective technique for studying tractography since it images diffusion weighted volumes with isotropic resolution and high SNR. In most applications, a reduction of scan time can be achieved via undersampling of the outer k-space. According to our results, the total number of interleaves can be reduced by up to 50% without introducing non-tolerable aliasing.

REFERENCE/FUNDING SOURCE  
Lucas Foundation, NCCRR P41 RR09784.

## Neural Correlates of Inhibitory Deficits in Depression

JUTTA JOORMANN, J. PAUL HAMILTON, AND IAN H. GOTLIB  
DEPARTMENT OF PSYCHOLOGY

**Background:** Depression is a widely diagnosed and highly debilitating disorder. Recurrent and often unintentional and uncontrollable negative thoughts are a hallmark feature of depressive episodes. Not only are these ruminative thoughts a debilitating symptom of depression, but they have also been associated with vulnerability to the onset of depression, the recurrence of depressive episodes, and the maintenance of negative affect. It is still unclear, however, why some people are especially prone to ruminate. Difficulties in executive functions in working memory, specifically inhibitory deficits, in depression have been proposed as an important underlying mechanism of rumination. In the present study, we used a modified Sternberg task to investigate neural correlates of the ability to remove irrelevant negative material from working memory in depressed and nondepressed participants.

**Methods and Results:** 5 participants meeting criteria for Major Depressive Disorder (MDD) and 5 age and sex-matched healthy control participants have been run in this study so far. fMRI was used to measure neural activation during the presentation of a cue that indicat-

ed that negative, positive, or neutral material should be expelled from working memory. Comparisons of trials in which the participants were instructed to expel negative material with trials in which participants were instructed to expel positive or neutral material indicate differences between depressed and nondepressed participants in activation in DLPFC during expel instructions. In addition, compared with their nondepressed counterparts, depressed participants exhibited greater activation in the amygdala and ACC when they were required to expel negative compared to neutral material.

**Conclusions:** These findings support the formulation that depression is associated with inhibitory deficits in the processing of emotional material. Moreover, the present study extends this postulation by implicating the DLPFC, amygdala, and ACC in depression-associated exhibit difficulties removing irrelevant negative material from working memory.

FUNDING SOURCE  
NIMH Grant MH59259 to Ian H. Gotlib.

## 3D Spiral Technique for High Resolution fMRI

YANLE HU<sup>1, 2</sup>, GARY H. GLOVER<sup>2</sup>  
DEPARTMENTS OF <sup>1</sup>PHYSICS AND <sup>2</sup>RADIOLOGY

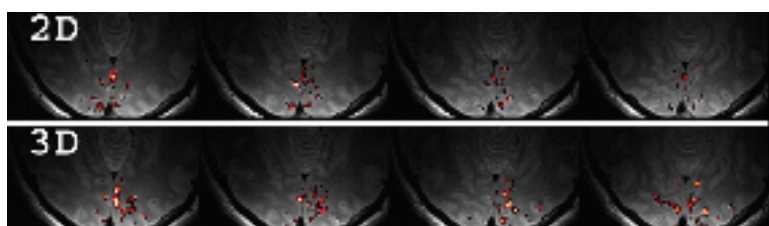
The main limitations for high resolution BOLD fMRI are low signal to noise ratio (SNR) and long volume scan time. Here our efforts were focused on improving the SNR of high resolution fMRI scans by switching to 3D acquisition methods. Compared to 2D multi-slice methods, 3D stack-of-spiral methods in general can improve SNR performance due to volume excitation. In this work, the SNR ratio of the 3D method over the 2D method was calculated based on a model in which thermal noise dominates physiological noise. This is valid for high resolution scanning. Comparison of high resolution fMRI studies using 3D and 2D methods confirmed our calculation.

All experiments were performed on a 3T whole body scanner (Signa, rev 12M4, General Electric Medical Systems, Milwaukee, WI) with a 3in surface coil. Two functional scans using 2D multi-slice and 3D stack-of-spiral sequences were performed for each volunteer. Each scan lasted 4 minutes and 54 seconds. A contrast-reversing (3 Hz) checkerboard visual stimulus was used.  $T_s$  was set to be 90ms. 32-1mm slices were collected with TE of 30ms, an in-plane

FOV of 14cm×14cm and a matrix size of 128×128. The nominal voxel size was 1mm×1.1mm×1.1mm. The flip angle was 83° and 21° for 2D and 3D methods respectively. Functional maps were overlaid on the  $T_2$ -weighted anatomic images.

The average SFNR of gray matter from each volunteer were measured. An average 20% improvement was observed. The comparison

of activation maps from a representative subject are shown in Fig. 1. The advantage of the 3D method is qualitatively apparent. The total number of activated voxels and the corresponding average Z-scores were also obtained for each subject, with the average to be 407 and 2.798 for the 2D method and 841 and 2.877 for



Comparison of activation maps from one representative volunteer between 2D and 3D methods. The scale of P-value is [0.0005, 0.05].

the 3D method, respectively. Therefore, the 3D technique may be a useful alternative to the conventional 2D method for high resolution fMRI studies.

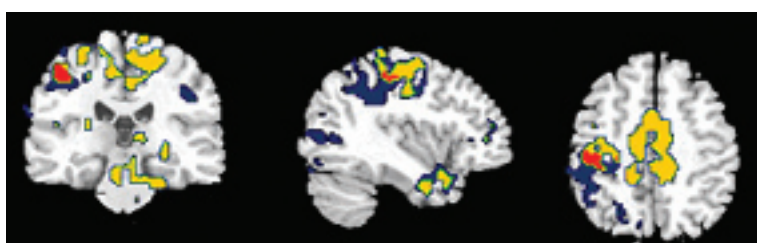
### REFERENCES/FUNDING SOURCE

3D spiral technique for high resolution fMRI, ISMRM, 2007, NIH RR09784

## Functional Magnetic Resonance Imaging of Pain Modulation by Cognitive Behavioral Strategies

JANE LAWRENCE<sup>1</sup>, FUMIKO HOEFT<sup>1</sup>, ETHAN GROVEMAN<sup>1</sup>, AXEL LUCCA<sup>1</sup>, CHRISTOPHER DECHARMS<sup>2</sup>, SEAN MACKEY<sup>1</sup>  
<sup>1</sup>DEPARTMENT OF ANESTHESIA, STANFORD UNIVERSITY SCHOOL OF MEDICINE, <sup>2</sup>OMNEURON, INC

Cognitive behavioral strategies (CBS) are used to help chronic pain patients control their level of pain. The goal of this study is to distinguish the neural correlates of two different cognitive strategies: external focus of attention and reappraisal. These techniques were selected as they involve distinct behaviors and so are hypothesized to recruit distinct neural networks. External focus of attention was expected to evoke activity in areas involved in executive function (e.g. prefrontal cortex). Reappraisal was anticipated to recruit limbic structures (e.g. amygdala, hippocampus). Both techniques are effective in reducing pain and so are anticipated to exert influences on common areas of the pain matrix. To date, the brain regions involved in pain modulation by different CBS have not been compared. Functional magnetic resonance imaging was performed at 3T in 7 chronic pain patients while told to increase and decrease their pain by 1) shifting attention to and from the affected area and 2) reappraising the sensation as pain or as another sensation (e.g. warmth). Data were analyzed using a general linear model contrasting Attention To vs. Attention Away [Attention], and contrasting Reappraising as Pain vs. Non-painful Sensation [Reappraisal] in SPM



( $p < 0.01$  corrected). Group analysis revealed activity restricted to cortical areas during external focus of attention (shown in blue). During reappraisal, activity was observed in the thalamus, amygdala, hippocampus, and several cortical regions (shown in yellow).

Both strategies evoked activity in one common area, the postcentral gyrus (shown in red). These results demonstrate that pain modulation can be achieved through various networks that involve distinct structures. Further work is needed to characterize these networks and establish methods of identifying the strongest networks within individuals. In turn this may lead to more effective and efficient training.

Figure 1. Group activity map ( $n=7$ ) of modulation of chronic pain using cognitive behavioral strategies. Areas of the brain recruited during external focus of attention are shown in blue, regions recruited during reappraisal are shown in yellow, and areas that were active during both strategies are shown in red.

### REFERENCES/FUNDING SOURCE

Poster presented at the 2007 Society for Neuroscience (SFN) conference. This research was supported by the NINDS, NIH P41 RR09784, and the Rosekrans Pain Research Endowment.

## Self Calibrated Spiral-In/Out for Parallel Imaging fMRI

CHRISTINE LAW<sup>1,2</sup>, CHUNLEI LIU<sup>1</sup>, ROLAND BAMMER<sup>1</sup>, GARY GLOVER<sup>1</sup>

DEPARTMENTS OF <sup>1</sup>RADIOLOGY AND <sup>2</sup>ELECTRICAL ENGINEERING

Image resolution in BOLD functional magnetic resonance imaging (fMRI) is limited by susceptibility-induced signal dropout and off-resonance artifacts. Although higher spatial resolution can be achieved with multi-shot sequences, increasing the number of shots reduces temporal resolution. We propose an auto-calibrated multi-shot interleaved spiral-in/out sequence in conjunction with parallel imaging to improve spatial resolution while maintaining the desired temporal resolution. Temporal resolution is maintained by reconstructing one frame of image using only partially acquired k-space data through the iterative SENSE algorithm. Sensitivity auto-calibration is achieved by combining consecutive frames of data to reconstruct a fully sampled image. Compared to the conventional one-shot technique, SENSE reconstruction improves image quality and significantly increases activation in areas of severe susceptibility artifacts.

Further, when sensitivity profiles are updated synchronously with

image acquisition, thermal noise is reduced in resulting images. This is accomplished by retaining thermal noise in sensitivity profiles; no spatial smoothing is performed. These noisy profiles actually provide a closer match to those required for thermal noise-free reconstruction than conventional sensitivity generations. Our proposed technique is especially applicable in acquiring high spatial resolution images where thermal noise dominates. With small voxel size, our technique reveals activation from visual stimulation when other sensitivity calculation techniques fail. With parallel imaging, fMRI sensitivity is preserved when using a voxel size such that physiological noise still dominates. Our technique will help fMRI detection when even higher spatial resolution is desired.

### REFERENCES/FUNDING SOURCE

Presented at ISMRM 2007.

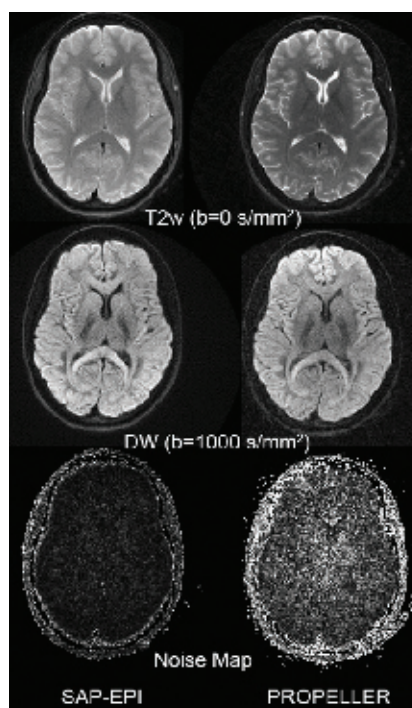
NIH RR09784, Lucas Foundation and GE Medical Systems.

## Benchmarking SAP-EPI and PROPELLER for Diffusion Imaging

SAMANTHA J. HOLDSWORTH, ROLAND BAMMER, REXFORD D. NEWBOULD, STEFAN SKARE

DEPARTMENT OF RADIOLOGY, RICHARD M. LUCAS IMAGING CENTER (RSL)

“Short-Axis readout Propeller EPI” (SAP-EPI) developed in-house has been proposed as a new variant for EPI-based PROPELLER. The short-axis readout uses a faster traversal of k-space and thus minimizes artifacts from off-resonant spins and T2\* decay. It has been shown that SAP-EPI is superior in image quality over its long-axis variant. Historically, DWI PROPELLER has been combined with FSE readouts because of FSE’s immunity to susceptibility distortions and eddy current effects. This is the only commercially available alternative to EPI for DWI, and has demonstrated increased geometrical and motion correction properties due to the RF refocusing pulses. Clinically, this has proven a great utility for the diagnostic work-up of lesions in the posterior fossa and brain stem, as well as in patients with surgical material or with hemorrhage. However, the requirement for large flip angle FSE trains in PROPELLER-FSE to combat violations of the CPMG condition as well as quite long scan times can pose difficulties in critically ill patients, and raise problems at higher magnetic field strengths where the specific absorption rate (SAR) issues and B1 inhomogeneities increase. In these situations, with the reduced distortions and minimum SAR of SAP-EPI in concert with the great motion insensitivity of the PROPELLER trajectory, SAP-EPI poses as an attractive alternative to FSE-based PROPELLER.



SAP-EPI (3 shots, 6 blades, blade width = 64, effective TE = 54 ms) and PROPELLER (ETL = 20, effective TE = 106 ms) T2w and DWI images, acquired at 1.5T, a resolution of 1x1x5 mm, and a TR of 5 s. The corresponding noise map for the DWI images are corrected for motion and normalized for scan time and the maximum number of achievable slices. Note: No distortion correction was necessary for the SAP-EPI data.

T2w and DWI PROPELLER and SAP-EPI human brain images are shown in the figure. Also shown are noise maps obtained by taking the relative standard deviation over the mean of two repeated scans. These maps have been normalized by multiplying with  $\sqrt{\text{scan time}}/(\text{slices/TR})$ , indicating that SAP-EPI has a substantial advantage over PROPELLER in terms of SNR/scan time efficiency. SAP-EPI allows a smaller minimum TE, smaller minimum TR, thus a shorter scan time can be achieved for a given number of slices. The use of dual blade SAP-EPI can further increase the scan time efficiency. For full brain coverage (21 slices), the scan time for PROPELLER is 2 mins per volume (TR = 6 s, ETL = 16), while the scan time for dual SAP-EPI is only 23 s per volume (3 shots, 3 dual-blades, blade width = 64, TR = 2.6 s). In addition, the average SAR for SAP-EPI is significantly lower than in PROPELLER (typically 0.1W/kg compared with 1.3W/kg). The results of this study demonstrate that SAP-EPI is a viable alternative to PROPELLER.

### REFERENCES/FUNDING

"Benchmarking SAP-EPI and PROPELLER for Diffusion Imaging", presented at ISMRM, 2007. Supported in part by NIH 1R01EB002711, the CAMRT P41RR09784, The Lucas Foundation, and Oak Foundation



## Effective Connectivity Changes Associated with Learned Control Over Neural Activity: A Granger Causality Study

JANE LAWRENCE<sup>1</sup>, AXEL LUCCA<sup>1</sup>, JARRED YOUNGER<sup>1</sup>, TAKEFUMI UENO<sup>1</sup>, KRISTEN LUTOMSKI<sup>3</sup>, SAXON MACLEOD<sup>3</sup>,  
FUMIKO HOEFT<sup>1</sup>, GARY GLOVER<sup>2</sup>, RAYMOND GAETA<sup>1</sup>, CHRISTOPHER DECHARMS<sup>3</sup>, SEAN MACKEY<sup>1</sup>  
DEPARTMENTS OF <sup>1</sup>ANESTHESIA AND <sup>2</sup>RADIOLOGY, STANFORD UNIVERSITY, <sup>3</sup>OMNEURON, INC

**Introduction:** Recent research has shown that individuals are able to modulate brain activity in specific areas using real-time functional magnetic resonance imaging (rtfMRI), to provide feedback of rostral anterior cingulate cortex (rACC) activity (1). While individuals have a demonstrated ability to gain volitional control over brain activity using this training technique, it is unknown what functional changes are associated with this learned ability. We employed a Granger Causality Mapping (GCM) algorithm to determine changes in the pain processing network associated with rtfMRI training (2). GCM analysis identifies the temporal relationship of active voxels in relation to a defined region of interest (ROI). We hypothesized that a shift in areas preceding rACC activity would predict those individuals who learn to control their rACC activity.

**Methods:** Real-time fMRI was performed in 8 chronic pain patients and 8 healthy controls with a GE 3T scanner, as previously described (1). Participants were trained to modulate activity in the rACC over several days. GCM analyses were performed with Brainvoyager QX (Brain Innovation, Maastricht, The Netherlands), using the rACC as the seed ROI. Networking was contrasted on the first training day and last training day.

**Results:** GCM analyses revealed a consistent pattern of activity across participants. Chronic pain patients demonstrated preceding prefrontal activity at the first training session. By the end of the training program, however, there was no relationship between prefrontal and rACC activity. Instead, insular activity reliably preceded rACC activity

(Figure 1). This change in brain regions showing directed influence over the rACC may reflect a shift from conscious to more automated control over brain modulation.

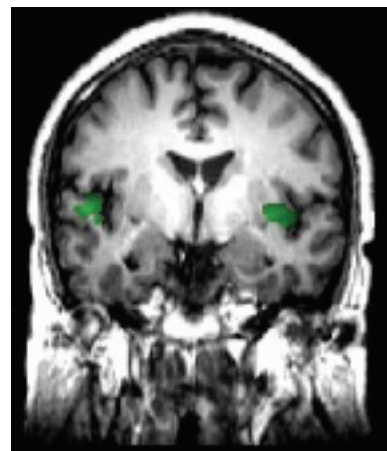


Figure 1. GCM demonstrating insular activation preceding rACC activity on the final day of rtfMRI-feedback training.

### REFERENCES/FUNDING SOURCE

Poster presented at the 2007 Organization for Human Brain Mapping Conference. Supported by NIH P41 RR 09784 and Rosekrans Pain Research Endowment.

## 5-HTTLPR Biases Default Mode Subgenual Cingulate Activity in Childhood

MORIAH E. THOMASON<sup>1,4</sup>, CATHERINE E. CHANG<sup>2</sup>, MICHAEL D. GREICIUS<sup>3</sup>, HANNAH S. KANG<sup>4</sup>,  
MEGGY W. WANG<sup>4</sup>, MELISSA L. HENRY<sup>4</sup>, GARY H. GLOVER<sup>1,5</sup>, IAN H. GOTLIB<sup>4</sup>  
DEPARTMENTS OF <sup>1</sup>NEUROSCIENCE, <sup>2</sup>ELECTRICAL ENGINEERING, <sup>3</sup>NEUROLOGY, <sup>4</sup>PSYCHOLOGY, <sup>5</sup>RADIOLOGY

**Introduction:** Converging evidence suggests that the serotonin system plays a central role in the pathophysiology of major depression. Recent studies have demonstrated that the short variant (S) in a functional variable repeat sequence polymorphism in the human serotonin transporter gene (SLC6A4) is associated with an increased depressogenic effect of stressful life events. One explanation for this effect is that this polymorphism is related to a persistent disruption in default mode network functional connectivity. **Materials and Methods:** To test this hypothesis we used functional magnetic resonance imaging (fMRI) to examine the effects of the serotonin transporter polymorphism on default mode functional connectivity in children. We predicted that genetic variations in the serotonin transporter gene would be associated with differences in resting-state activity within the default-mode network, primarily in prefrontal and cingulate cortices. We chose to assess

default mode activity in young children, who do not have a long history of exposure to stressors. Twenty healthy children between ages 9-14 were scanned at 3T during 6 minutes of undirected wakefulness, eyes closed. **Results:** Consistent with results of previous positron emission tomography and fMRI studies of depressed adults, S carriers showed greater subgenual cingulate activity during resting state than did long-variant (L) carriers. Moreover, there was a significant positive correlation between the magnitude of the subgenual cingulate BOLD response and scores on a measure of state anxiety. **Conclusion:** The results of this within-subject functional connectivity analysis indicate disrupted response across the default mode neural network in S allele carriers, which may explain, in part, the increased risk for depression in this group.

## Time-Variable Filtering Of Spiral Acquisitions For Outer Volume Suppression

L.J. PISANI, R. BAMMER, AND G. GLOVER, DEPARTMENT OF RADIOLOGY

While restricting the field of view (FOV) in MRI with Cartesian readouts is straightforward using anti-aliasing filter, slab selective excitation, and aliasing suppression techniques; that is not the case with time varying readout gradients ( $G(t)$ ). Aliasing patterns are particularly difficult to identify with a spiral k-space trajectory as compared to Cartesian readout. We reduce aliased signal by retrospectively applying an anti-aliasing filter to the raw data (length =  $N$  samples). During a spiral readout the net gradient field rotates about the origin with increasing amplitude. Band-pass filtering the signal spectrum can define a restricted FOV (rFOV) and suppress signal originating beyond it.

We Fourier transform an increasing extent of the raw data time-series ( $n = 1 \dots N$ ), and filter the resulting spectrum with the corresponding cutoff frequency ( $W_c(t)$ ) (Figure 1, plot).  $W_c(t)$  was determined according to:

$$W_c(t) = \gamma |G(t)| \text{ rFOV}$$

where gamma is the gyromagnetic ratio. The  $n$ th sample in the filtered spectrum was thereby calculated. The highest frequency in the filtered spectrum is calculated by filtering the spectrum of the entire initial time-series. The inverse transform of the filtered spectrum was calculated for the new time-series.

Figure 1 (right) demonstrates frequency filtering on a T2\*-weighted slice of a fetal brain. Above are initial data, and below is the filtered slice. The filter was set to suppress data outside of a 10 cm circular rFOV around the fetal brain (blue circle). The filtered slice demonstrates that the correction preferentially removes signal outside of the rFOV. In order to clearly demonstrate the filtering effect outside the desired region, we did not restrict the FOV. Features in the fetal brain such as the eye sockets are increasingly visible in the filtered images.

Outside the rFOV signal is removed but not completely eliminated, and within the rFOV desired signal is attenuated. For this method to be

implemented, original data must be acquired with a bandwidth (BW) at or above the temporal Nyquist frequency of the signal. Otherwise temporal aliasing will preclude successful filtering of the signal. That depends on the maximum gradient amplitude and the extent of the subject. However, the pass-band narrows as the gradient amplitude decreases and thus the speed in k-space is reduced. The results demonstrate a partial reduction in signal originating from outside the rFOV. To the best of our knowledge this approach has not been previously proposed.

Applying consistent projection reconstruction techniques to the filtered data further reduces aliasing artifacts.

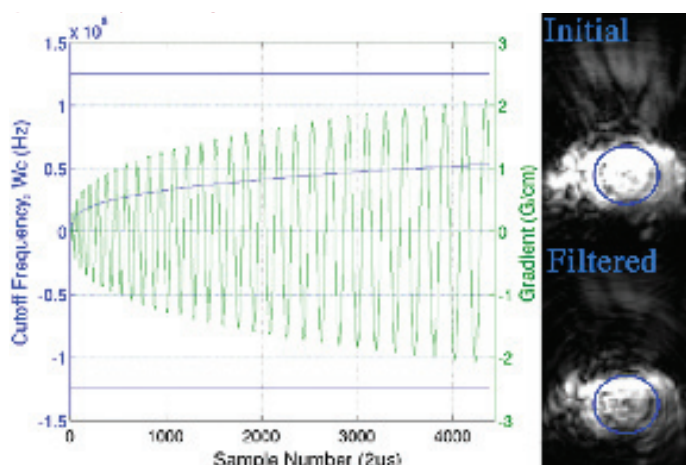


Figure 1 Cutoff frequency and gradient waveforms over a spiral readout.

ISMRM 15th Scientific Meeting Program, 2007.  
F32 EB005572-01A1.

## Processing of Motor, Tonic Pain, and Phasic Pain Signals in the Human Spinal Cord

DAENA WATCHA<sup>1</sup>, JUSTIN BROWN<sup>1</sup>, JOEL DARNAUER<sup>1</sup>, RITU SARIN<sup>1</sup>, GARY GLOVER<sup>2</sup>, SEAN MACKEY<sup>1</sup>  
DEPARTMENTS OF <sup>1</sup>ANESTHESIA AND <sup>2</sup>RADIOLOGY

The primary aim of this study was to compare and contrast fMRI spinal processing of nociceptive and motor signals in humans. We hypothesized that 1) the signal time course of the nociceptive and motor tasks would differ and 2) tonic pain and phasic pain would differ, as tonic pain activates both A-delta and C nociceptive fibers while phasic pain primarily activates A-delta fibers. Twelve volunteers consented to the study and were scanned in a 3T whole-body MRI system by GE, with an HD neurovascular array coil. Noxious stimuli were presented by a computer-controlled thermode placed in the thenar eminence of the hand. Tonic heat stimulus was a 48°C block. The phasic stimulus oscillated from 40°C to 48°C at 10°C/sec. Each subject participated in three, eight-minute blocks of functional scans: 1) thirty seconds of fist-clenching alternated with thirty seconds of rest, 2) thirty seconds of 48°C phasic stimulus alternated with thirty seconds of rest, and 3) thirty seconds of 48°C tonic stimulus alternated with thirty seconds of rest.

Preliminary data were analyzed in Brain Voyager at  $p=0.05$ . Because the hemodynamic response function (HRF) has not been well characterized in the spinal cord, we deconvolved a spinal HRF from the motor task and used that HRF for all analyses. Activity maps and signal time courses were generated from all three runs for each subject. In the fist-clenching task, activity was observed in the dorsal horn, corresponding to sensory input from the palm. During both tonic and phasic pain, there was activity in the spinal areas of C5-C7. Event-related averages (ERAs) for the fist-clenching task increased and plateaued. ERAs for phasic pain were slower to peak. As compared to the tonic task, the phasic task showed increased BOLD percent change. These results are in concordance with electrophysiological recordings of nociceptive fibers in animals.

### REFERENCES/FUNDING SOURCE

This research was supported by the NINDS, NIH P41 RR09784, and the Rosekrans Pain Research Endowment

## Improvements in Parallel Imaging Accelerated fMRI

H. SCHMIEDESKAMP<sup>1,2</sup>, R. D. NEWBOULD<sup>1</sup>, G. H. GLOVER<sup>1</sup>, K. P. PRUESSMANN<sup>2</sup>, R. BAMMER<sup>1</sup>

<sup>1</sup>DEPARTMENT OF RADIOLOGY, STANFORD UNIVERSITY, <sup>2</sup>INSTITUTE FOR BIOMEDICAL ENGINEERING, UNIVERSITY AND ETH ZURICH

Parallel imaging (PI) has shown great utility to counteract the issues of signal dropouts as well as image distortions in EPI by faster traversing through k-space. However, decreased SNR and SFNR (temporal SNR) prevented PI techniques from being broadly accepted in conjunction with fMRI. In this study, a multi-echo EPI acquisition technique using parallel imaging has been applied towards fMRI at 1.5T to compensate for the lower SNR and SFNR. Therefore, fMRI time series using PI reduction factors of 2 and 3 were acquired and compared to non-accelerated EPI scans.

A multi-shot, multi-echo gradient-echo EPI sequence named PERMEATE has been used for data acquisition on a 1.5T unit (gradients = 50mT/m and 150T/m/s). An 8-channel phased array head receiver coil was used for all measurements. PI reconstruction was performed using GRAPPA. Different echo images of a single signal excitation were combined using an approach for T2\*-weighted summation. A breath holding task was performed by the volunteer to stimulate functional activation in all areas of the brain. Therefore, a baseline period of 16.5s was followed by 3s breath-in and 16.5s of breath-holding. This cycle was repeated 8 times, beginning with baseline. The correlation of the stimulus response with a sinusoid function was calculated for fMRI analysis (threshold:  $r=0.3$ ).

By acquiring multiple echoes following a single excitation pulse, the lower SNR and SFNR in PI could be compensated for. The results at 1.5T showed that by the combination of three echoes and R=2, the average SFNR was 8% higher compared to non-accelerated single-echo EPI. In case of a four-echo acquisition with R=3, SFNR dropped by 1% on average over six subjects. In contrast, by considering only the echo image at TE≈50ms, SFNR decreased by 28% for R=2 and 47%

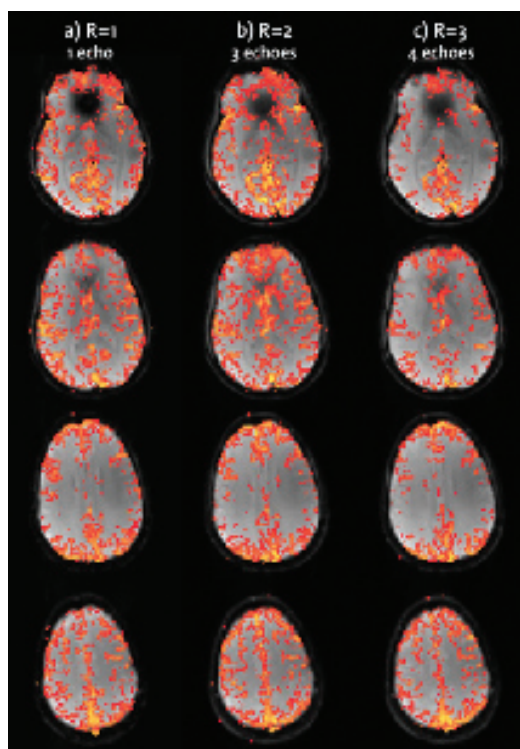


Figure: Breath-holding activation maps for different reduction factors

for R=3. Overall sensitivity to functional activation from the breath-holding task could be increased by 10% when PI with 3 echoes and R=2 was used compared to single-echo measurements with R=1. For R=3 and 4 echoes, the number of activated voxels was reduced by 12% (Fig.1). This is due to the higher geometry factor of the coil and the shorter total readout time for acquisitions with R=3. However, using the presented multi-echo pulse sequence, the level of functional activation could be increased if a PI reduction factor of 2 was used compared to non-accelerated scans. In addition, the quality of fMRI measurements improved for R=2, in particular in dropout regions where activation could be restored due to the acquisition of early-echo images. This together with reduced image distortions makes the presented method using a three-echo acquisition and a reduction factor of 2 favorable over conventional EPI for fMRI measurements in clinical applications, where accurate localization and good image quality is desirable and mostly 1.5T systems are available..

As fMRI analysis of humor progresses, examination of the role of specific brain regions can elucidate how the components of these networks interact and functionally connect, further revealing the neuroanatomical correlates of cognition, emotion, and sense of humor.

BOLD signal activation for funny-unfunny cartoons. Compared to males, females exhibit greater activation of the dorsolateral prefrontal cortex, as well as subcortical dopaminergic reward regions, including the nucleus accumbens.

### REFERENCES/FUNDING SOURCE

NIH 1R01EB002711, Center for Advanced MR Technology at Stanford, P41RR09784, Lucas Foundation

## High-resolution fMRI of the Medial Temporal Lobe During Delayed-Match-to-Sample

ROSANNA K. OLSEN<sup>1</sup>, ELIZABETH A. NICHOLS<sup>1</sup>, JANICE CHEN<sup>1</sup>, JOHN D. E. GABRIEL<sup>2</sup>, ANTHONY D. WAGNER<sup>1</sup>

<sup>1</sup>PSYCHOLOGY, STANFORD UNIV., STANFORD, CA. <sup>2</sup>BRAIN AND COGNITIVE SCIENCES, MIT, CAMBRIDGE, MA

The medial temporal lobe (MTL) is known to be critical for long-term memory for events and facts. However, recent functional neuroimaging and neuropsychological data using short-delay task paradigms have suggested that the MTL contributes to performance even after brief retention intervals. Moreover, single-unit data in rodents have demonstrated performance-related delay activity in the MTL in the context of delayed-non-match-to-sample tasks. In the current study, healthy adults were scanned using high-resolution functional MRI to explore the contributions of human MTL subregions to performance during a short-delay (30 s) delayed-match-to-sample task. On half of the trials, two faces were presented (1 s) followed by a 30-s delay, after which participants encountered a two-alternative forced choice probe (720 tri-

als). On the other half of trials, the delay period was 4 s. Accuracy on the 30-s trials was 72% correct. Initial fMRI results (n=11) revealed significant delay-period activity in subregions of the hippocampus (anterior hippocampus and CA2/3/DG), as well as in entorhinal cortex. Furthermore, a significant linear increase in delay-period activity over the course of the 30-s delay was observed in several subregions of the MTL (subiculum and parahippocampal cortex) extending into the fusiform gyrus. These results advance understanding of the MTL mechanisms supporting recognition memory across short and long delays.

### REFERENCES/FUNDING SOURCE

NIMH 1R01MH076932-01A1, NSF and NARSAD



# Distortion Reduction for Spiral-fMRI: Comparison of Iterative and Non-iterative Parallel Imaging Reconstruction Algorithms

H. SCHMIEDESKAMP<sup>1,2</sup>, L. J. PISANI<sup>1</sup>, C. LIU<sup>1</sup>, C. LAW<sup>1</sup>, K. P. PRUESSMANN<sup>2</sup>, G. H. GLOVER<sup>1</sup>, AND R. BAMMER<sup>1</sup>

<sup>1</sup>DEPARTMENT OF RADIOLOGY, STANFORD UNIVERSITY, <sup>2</sup>INSTITUTE FOR BIOMEDICAL ENGINEERING, UNIVERSITY AND ETH ZÜRICH

Single-shot spiral imaging is a very efficient technique to acquire dynamic data for fMRI experiments rapidly and has profound advantages over single-shot EPI as it distributes the burden over two gradient axes. Similar to EPI, spirals suffer from geometric image distortions, T2\*-related blurring, and signal dropout artifacts. Parallel imaging (PI) has shown great utility to counteract these issues by faster traversing through k-space at the cost of increased signal-to-noise ratio (SNR) and (in the case of non-Cartesian acquisitions) considerably increased reconstruction times. Specifically, CG SENSE has been proposed as a robust, iterative PI reconstruction method for spiral data. However, its iterative fashion has two potential shortcomings: 1) prohibitively long reconstruction time for time-series imaging; 2) unknown number of iterations required to reach the optimal convergence. A reconstruction that determines the unfolding parameters upfront and applies it successively to all dynamic phases would be more desirable. We have recently developed a non-iterative PI reconstruction method for arbitrary trajectories using k-space sparse matrices (kSPA), which affords much faster reconstructions of dynamic time series. In this study, we assessed 1) conventional and PI-accelerated single-shot, variable density (VD) spiral fMRI for image distortion; 2) CG SENSE and kSPA for differences in image quality and fMRI activation.

A T2\*-weighted VD spiral sequence was implemented on a 1.5T unit for performing the aforementioned comparisons. A combined auditory and visual stimulus with 8 on/off-cycles of 48 seconds each was presented to each subject. In addition, the volunteers were asked to perform a bilateral finger-tapping experiment during the 24 seconds long on-periods. For post-processing, the voxel-wise temporal signal curve was correlated with a sine wave. The total number of activated vox-

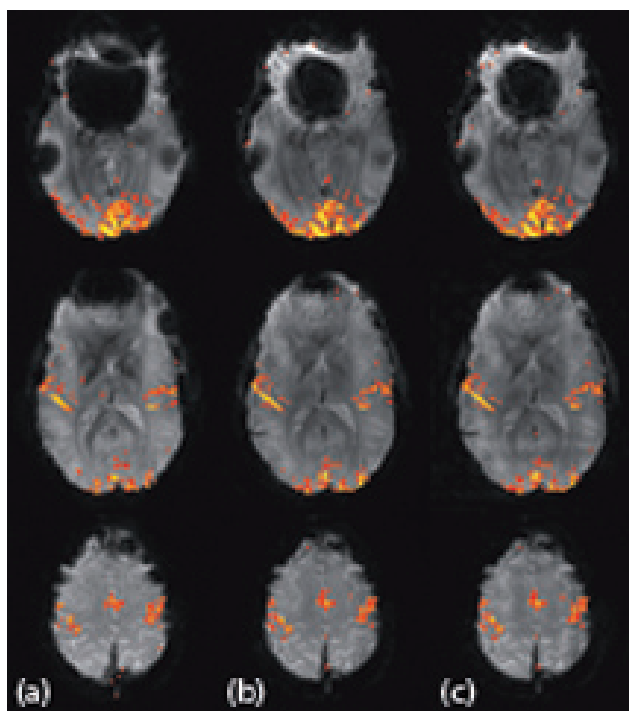


Fig. 1: Comparison of R=1 (a) to R=2 reconstructed using CG SENSE (b) and kSPA (c) for selected slices

els being above a linear correlation coefficient threshold of 0.35 were quantified and served as a metric for efficacy. The average SNR as well as the SFNR (temporal SNR) were determined for CG SENSE, kSPA as well as for the non-accelerated scan.

Considerable distortion reduction was achieved by using PI-accelerated VD spiral scans. Non-accelerated scans suffered from big signal dropouts, located mainly in frontal regions of the brain above the sinuses and near the auditory canals (Fig.1). As expected, the SNR and SFNR of the accelerated scans were less than that of conventional VD spirals. However, the distribution of activation patterns was very similar across all three methods. Despite kSPA's 5-6 times faster reconstruction speed than CG SENSE no significant differences in activated voxels and signal stability were found.

This study demonstrated improved image quality with PI-accelerated scans and that kSPA can be used for fMRI image reconstruction of parallel acquired data without the reconstruction time penalty of CG SENSE. Here, kSPA showed activation patterns similar to CG SENSE. Compared to non-accelerated spiral imaging, the parallel acquisitions demonstrated less blurred activation. In particular, the reduced T2\* blurring helps to better localize activation, whilst the faster readout allows a larger spatial frequency range to be covered at instances when the BOLD contrast is optimal.

## REFERENCES/FUNDING SOURCE

H. Schmiedeskamp et al., Proc. Intl. Soc. Mag. Reson. Med. 15 (2007), p 693.  
NIH 1R01EB002711, CAMRT P41RR09784, Lucas Foundation, August-Karolus Foundation of ETH Zurich, Stanford University Bio-X Program.

## Controlled Inspiration Depth Reduces Variance in Breath-Holding Induced BOLD Signal

MORIAH THOMASON<sup>1,3</sup>, GARY H. GLOVER<sup>2,3</sup>, FIRST BIRN<sup>4</sup>  
 DEPARTMENTS OF <sup>1</sup>PSYCHOLOGY, <sup>2</sup>RADIOLOGY, AND <sup>3</sup>NEUROSCIENCES PROGRAM  
 STANFORD UNIVERSITY AND <sup>4</sup>UNIVERSITY OF CALIFORNIA, IRVINE

**Introduction:** One of the primary methodological challenges facing fMRI is that the blood oxygen level dependent (BOLD) signal is only an indirect measure of neuronal activity, because it derives from neurovascular processes. There is concern that inferences regarding cerebral activation may be confounded by regional variation in brain vasculature, or alterations in the cerebral vascular system that are due to age- or disease-related changes. Recent studies used BOLD contrast scanning during short periods (~18s) of breath holding (BH) to measure hemodynamic response differences between different age groups (1, 2). Because BH is easy to implement and noninvasive, and the effects of BH are global and robust, this paradigm is applicable for routine use in research studies. Measurement of neural activity has been shown to be improved by calibrating for fMRI signal variance that results from intrinsic properties of the local vasculature (3). Thomason and colleagues used BH to derive a correction map for each individual, then applied voxel-wise hemodynamic correction to working memory scan data taken in the same session. In the present study we have performed further studies to extend the precision of this technique with the express goal of attaining an effective and routine hemodynamic calibration metric. **Materials and Methods:** Thirteen healthy adults (ages 24-64) performed six BH scans. Three versions of BH scans were run, twice each, and all included seven repetitions of alternat-

ing periods of breath-holding and self-paced breathing in 18-s blocks. Versions differed in whether or not participants received feedback on the depth to which they should inspire. The average of controlled-depth scans and the average of no- feedback scans were compared for more or less variance in (a) inspiration depth (a performance measure) and (b) BOLD signal. **Results:** BH-induced BOLD signal amplitude corresponded to depth of inspiration. Inspiration depth variation and BOLD signal variation were reduced with feedback that cued participants to the appropriate inspiration depth. Greater overall magnitude and extent was demonstrated in activation maps for scans with controlled feedback compared to the no-control scans. **Conclusion:** This study extends the precision of the BH method for obtaining rapid, global systemic BOLD calibration data. With the inclusion of inspiration depth feedback to the participants, the BH method is more robust to cross-trial and individual variance.

### REFERENCES/FUNDING SOURCE

Riecker, A. et al. *JCerebBloodFlowMetab* 2003, 23, (5), 565-73.  
 Thomason, M. E. et al. *Neuroimage* 2005, 25, (3), 824-37.  
 Thomason, M. E. et al. *HBM* 2007, 28, (1), 59-68.  
 P41 RR09784 and M01 RR000827

## Cognitive and Neural Basis of Memory in Older Aviators Genetically at Risk for Alzheimer's Disease

MAHEEN M. ADAMSON<sup>1,2</sup>, BEN HUTCHINSON<sup>3</sup>, ANTHONY WAGNER<sup>3</sup>, JOY L. TAYLOR<sup>1,2</sup>  
<sup>1</sup>DEPARTMENT OF VETERANS AFFAIRS AND SIERRA-PACIFIC MIRECC, PALO ALTO, CALIFORNIA,  
 DEPARTMENTS OF <sup>2</sup>PSYCHIATRY AND BEHAVIORAL SCIENCES AND <sup>3</sup>PSYCHOLOGY, STANFORD UNIVERSITY

The APOE  $\epsilon 4$  allele is a major genetic risk factor Alzheimer's Disease (AD). Furthermore, over 25% of the general population are  $\epsilon 4$  carriers. To enhance early identification of AD, studies are assessing the impact of  $\epsilon 4$  on memory in older nondemented carriers. The literature is inconsistent and few studies have examined the impact of APOE  $\epsilon 4$  in older professionals performing complex "real-world" tasks, such as flying an airplane. Our recent structural MRI study of 45 aviators found that  $\epsilon 4$  carriers had poorer memory performance when learning a word list (Rey AVLT). Interestingly, no  $\epsilon 4$ -related differences in hippocampal volume were observed. The fMRI study underway aims to shed light on the neural mechanisms associated with the poorer word list learning observed in  $\epsilon 4$  carriers. We have adapted the Rey AVLT to a visually presented format for fMRI. We predict that  $\epsilon 4$  carriers will show overall lower activation than non-carriers during memory encoding in MTL regions (specifically the hippocampus), prefrontal, parietal and anterior cingulate regions. We are also testing spatial navigational

memory, as navigation is crucial in aviation. Here, we are presenting a survey and route virtual reality task developed by Shelton and Gabrieli (2002; 2005). We will assess the extent to which  $\epsilon 4$  carriers with advanced FAA proficiency ratings show preserved activation during navigational memory encoding (APOE x Expertise interaction). Forty actively flying, FAA medically certified aviators with a range of proficiency ratings are being recruited for the study.

### REFERENCES/FUNDING SOURCE

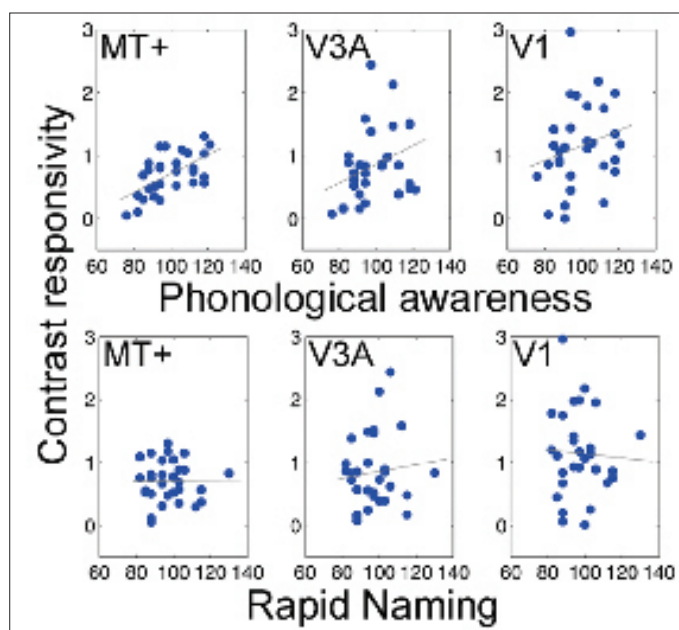
This work will be submitted to the International Neuropsychological Society Meeting, Hawaii, 2008. P30AG017824 (Taylor: Pilot Grant 4.1) and R01 AG021632-04S1 (Adamson: Diversity Supplement)

## Contrast Responsivity in MT+ Correlates with Phonological Awareness and Reading Measures in Children

MICHAL BEN-SHACHAR<sup>1,2</sup>, ROBERT F. DOUGHERTY<sup>1,2</sup>, GAYLE K. DEUTSCH<sup>1</sup> AND BRIAN A. WANDELL<sup>1,2</sup>

<sup>1</sup>STANFORD INSTITUTE FOR READING AND LEARNING; <sup>2</sup>PSYCHOLOGY DEPARTMENT, STANFORD UNIVERSITY

We tested the hypothesis that reading-related skills correlate with MT+ contrast responsivity in a group of 35 children. Previous neuroimaging studies in adults have demonstrated MT+ differences between small groups of poor readers and controls (Eden et al., 1996; Demb et al., 1997, 1998). In the current study we measured MT+ BOLD signals to moving gratings of different contrasts, and examined the relation between contrast responsivity and performance on a battery of standardized behavioral tests. We measured BOLD signals while 35 children (7-12y) performed a speed discrimination task on pairs of drifting gratings at 4 contrast levels (1, 2, 7, and 25% contrast). Stimuli were large (20°) low spatial frequency drifting sinusoidal gratings with a mean luminance of 86 cd/m<sup>2</sup>. Contrast was varied parametrically in a block design (12s blocks interleaved with fixation blocks). Twenty-six 2.5x2.5x3 mm axial slices were acquired (3T GE Signa, spiral acquisition) covering occipito-temporal cortex. We measured BOLD responses within MT+, V1 and V3A, defined anatomically and functionally by comparing responses to moving gratings with fixation. Contrast responsivity was calculated for each subject as the slope of a line fit through the BOLD log-contrast response function. There were robust responses to moving gratings in MT+, V1 and V3A. Contrast responsivity in MT+, but not V1, was highly correlated with phonological awareness (CTOPP; elision and blending standardized scores combined). Smaller correlations were found with two other reading scores: Basic Reading (WJ-III) and the Oral Reading Quotient (GORT4). These results demonstrate for the first time a significant correlation between MT+ contrast responsivity and phonological awareness in children. Phonological awareness is thought to be an essential skill for reading acquisition. The correlation between phonological awareness and MT+ signals suggests that MT+ deficits are not limited to a small subgroup of poor readers.



Each point in these scatter plots is a measurement from a single subject. The X-axis measures Phonological Awareness age standardized scores (top panels) or Rapid Naming standardized scores (bottom panels). The Y-axis measures the slope of a linear function through the mean BOLD contrast values plotted against log stimulus contrast. Slopes are averaged across hemispheres for each subject ( $N=30$ ) for each ROI. The three panels are measurements in three different cortical regions: MT+ (left panel), V3A (center) and V1 (right panel). Only the correlation between contrast responsivity and phonological awareness in MT+ is significant  $r = 0.597$  ( $r^2 = 0.36$ ,  $p < 0.0005$ ). Shown in gray are the regression lines fit to data points to minimize the mean square error.

### REFERENCES/FUNDING SOURCE

Ben-Shachar, M., Dougherty, R.F., Deutsch, G.K. and Wandell, B.A. Contrast Responsivity in MT+ Correlates with Phonological Awareness and Reading Measures in Children. In press, *Neuroimage* doi:10.1016/j.neuroimage.2007.05.060.P41 Supported by NIH grant R01 EY15000.



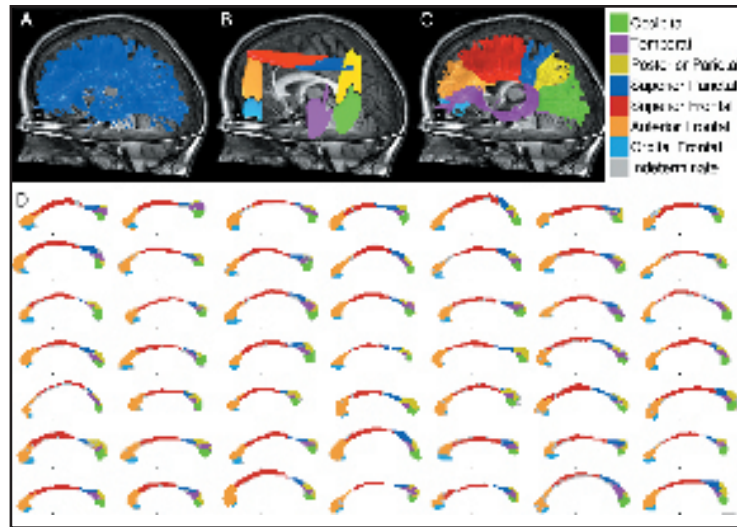
# Temporal Callosal Pathway Diffusivity Predicts Phonological Skills in Children

R.F. DOUGHERTY, M. BEN-SHACHAR, G.K. DEUTSCH, A. HERNANDEZ, G.R. FOX, B.A. WANDELL  
DEPARTMENT OF PSYCHOLOGY

**Background:** The development of skilled reading requires efficient communication between distributed brain regions. Using diffusion tensor imaging (DTI) we assessed the interhemispheric connections in a group of children with a wide range of reading abilities. These children are participating in a longitudinal study of reading and brain development.

**Methods:** Using deterministic fiber tracking methods (STT), we identified a large set of potential fibers crossing through the corpus callosum. For each child, we classified the callosal fibers based on their likely cortical projection zones. This classification then segmented the corpus callosum into several zones, depending on the cortical projection zone of the fibers (see Figure). We measured diffusion properties separately for the each of these segmented regions. We further examined the relationships between diffusion in these regions and neuropsychological measures of reading for each child.

**Results:** A key factor in reading acquisition, phonological awareness, was positively correlated with diffusivity perpendicular to the main axis of the callosal fibers that connect the temporal lobes. Other measures of reading also correlated, but slightly less powerfully. These



*Segmenting the corpus callosum. (A) All pathways in the right and left hemisphere are estimated; only those pathways that pass through the corpus callosum are analyzed. (B) The callosal pathways are segmented based their intersection with one of seven possible planar regions, shown as the colored planes. (C) The segmentation of all the callosal pathways is shown using the same color scheme as the planar segmentation regions. These are occipital (green), posterior parietal (yellow), superior parietal (blue), temporal (purple), superior frontal (red), anterior frontal (orange), orbito-frontal (cyan). (D) The outline of the callosum is color coded by the projection zone of the fibers within each segment. The black point below each corpus callosum indicates the location of the anterior commissure.*

results could be explained by several physiological properties of the fibers in the temporal-callosal fiber tracts. For example, good readers may have fewer but larger axons connecting left and right temporal lobes; or their axon membranes in these regions may be more permeable than the membranes of poor readers.

**Conclusions:** These measurements are consistent with previous work suggesting that good readers have reduced interhemispheric connectivity and are better at processing rapidly changing visual and auditory stimuli, which require larger axons connecting the hemispheres for rapid signal conduction. A modest inability to distinguish the sounds of speech, because of poor signal conduction on pathways such as these, may serve as an impediment to learning the relationship between these sounds and printed text.

## REFERENCES/FUNDING SOURCE

Temporal-callosal pathway diffusivity predicts phonological skills in children. RF Dougherty, M Ben-Shachar, GK Deutsch, A Hernandez, GR Fox, and BA Wandell (2007). *Proceedings of the National Academy of Sciences (US)*, vol. 104, p 8556-8561.  
NIH EY015000 and the Dana Foundation

## Population Receptive Field Estimation in Human Visual Cortex

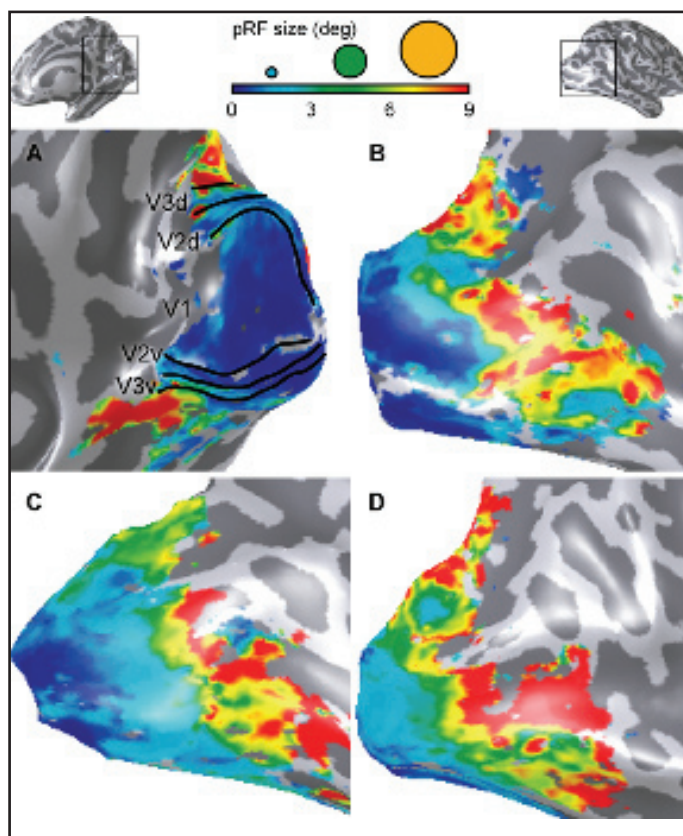
SERGE DUMOULIN AND B.A. WANDELL  
DEPARTMENT OF PSYCHOLOGY

**Background:** Bridging the gap between technologies that measure neural signals at different length scales is an important objective in neuroimaging research. Here, we introduce new experimental and computational methods that quantitatively couple fMRI signals, measured at the millimeter scale, with population receptive field (pRF) properties of visual neurons measured at the micron scale.

**Methods:** The pRF parameters were estimated from the time series data using a linear spatio-temporal model of the fMRI response. An important advantage of the pRF model-based method is that visual field maps can be derived from responses to a wide array of stimuli, including those that are not well-suited to the phase-encoding method. In the model-based analysis developed here, the prediction  $p(t)$  is calculated using a parameterized model of the underlying neuronal population and the stimulus. We estimated the neuronal model by finding the model parameters that best predict the observations. The value of this procedure is that the estimated parameters are connected meaningfully to the neuronal parameters. Various descriptions of the data can be derived from the pRF fit, including traditional eccentricity and polar-angle maps. Importantly, the Gaussian width parameter is a novel estimate that provides information about the population receptive field size.

**Results:** Fitting a symmetric Gaussian pRF model produces both visual field map and pRF size estimates (s.d.). The pRF size estimates from a 14 degree radius field of view are shown for three subjects in Figure 6. There is a significant increase in pRF size as one compares the responses in V1-V3 (s.d. ~ 0.5-2 deg) with those in LO and VO (s.d. 4-8 deg). A statistical parameter map showing the estimated population receptive field size across visual cortex is shown in the Figure. pRF size in V1 is less than 1 deg of visual angle and confined to the contralateral visual field, consistent with expectations from electrophysiology. These are the first quantitative measurements of pRF size in human lateral occipital cortex. We estimate that the pRF size is 7-9 deg and the pRFs cross the vertical midline.

**Discussion:** In the analyses described here we use a single pRF model: an isotropic 2D Gaussian. This model provides a compact description of the pRF using only three parameters. As we collect more data it will become possible to compare more complex pRF models with significant statistical power. For example, the pRF can be modeled as an anisotropic Gaussian to test hypotheses concerning integration biases in the pRF at different locations within the visual field. Furthermore, we note that some investigators include visual field maps and 2D Gaussian pRF models in algorithms for inferring the stimulus from the fMRI response. Preliminary work on this topic has incorporated a constant pRF size (s.d.=0.75deg). Better estimates of the pRF properties from the data should improve algorithms in that field.



pRF size estimates on an inflated cortical surface. The pRF size maps are displayed on the enlarged part of the occipital lobe, as indicated by the black squares in the top two cortical surfaces. The colors indicate the different pRF sizes as shown in the colorbar. The pRF size map for one subject is shown from the medial (A) and lateral view (B). The borders between visual field maps V1-V3 are delineated by the solid lines. Lateral views from two additional subjects are shown in panels (C & D). The pRF sizes are much smaller in the maps near V1 than those on the lateral occipital surface.

### REFERENCES/FUNDING SOURCE

Dumoulin SD and Wandell BA. (2007). Population receptive field estimates in human visual cortex. *Neuroimage* (in press)  
Hillblom Fellowship to Dumoulin and NEI EY 03164 to Wandell

## Individual Differences in Emotional Experience

LAURA L. CARSTENSEN<sup>1</sup>, SASHA GIBBS<sup>1</sup>, GREGORY SAMANEZ LARKIN<sup>1</sup>, MARA MATHER<sup>2</sup>  
DEPARTMENTS OF <sup>1</sup>PSYCHOLOGY, STANFORD UNIVERSITY AND <sup>2</sup>PSYCHOLOGY, UCSC

Recent research has challenged long-held beliefs that emotional experience becomes more negative with age. On the contrary, there is increasing evidence that emotion regulation is well-maintained in the later years, and may even improve. For the past 10 years, we have been conducting a longitudinal study of emotional experience in everyday life. In the present study, we will draw a subset of participants from our longitudinal study to see if we can associate performance on laboratory tasks with emotional experience in daily life.

We aim to obtain a deeper and more comprehensive understanding of age and individual differences in the processes underlying the effective regulation of emotion, including the neural, biological, and cognitive associates of emotion regulation. Although improved emotion regulation is well documented in older adults, little is known about the underlying reasons for this phenomenon. Recent findings from our laboratory suggest that, compared with their younger counterparts, older people disattend to negative stimuli and let go of negative emotions more quickly once they have occurred. Although we have argued that

these shifts are related to changes in motivation, they could alternatively reflect serendipitous consequences of brain aging, with older people coming to rely on automatic processing more than they do on deliberative or analytical processes. By exploring individual differences, we can address the pervasiveness of the observed changes in older people, which will help to resolve the issue of brain aging versus motivation, and will illuminate specific strategies involved in emotion regulation.

We have run twenty nine participants; twelve participants have participated in the fMRI portion of the study. We are halfway through our data collection and are conducting preliminary analyses. In the next three months time we plan to finish our data collection and run nineteen to twenty-three participants in the scanner.

### REFERENCES/FUNDING SOURCE

Carstensen, L.L., Pasupathi, M., Mayr, U. & Nesselroade, J. (2000). Emotional experience in everyday life across the adult life span. *Journal of Personality and Social Psychology*. 79, 644-655. Supported by NIH.

## Differential Effects of Age on Tissue Water-Referenced Proton Metabolites in Basal Ganglia, Pons, and Cerebellum Using an MRS Sequence Optimized for Glutamate Detection

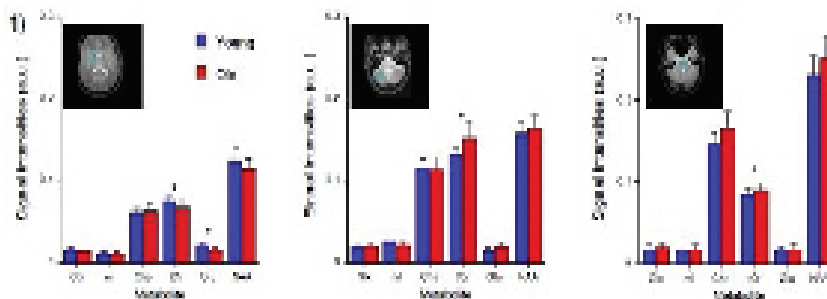
NATALIE M. ZAHR<sup>1</sup>, DIRK MAYER<sup>2</sup>, EDITH V. SULLIVAN<sup>1</sup>, ADOLF PFEFFERBAUM<sup>1,3</sup>  
DEPARTMENTS OF <sup>1</sup>PSYCHIATRY & BEHAVIORAL SCIENCES, <sup>2</sup>RADIOLOGY, AND <sup>3</sup>SRI NEUROSCIENCE PROGRAM

The non-invasive in vivo detection of the neurotransmitter glutamate (Glu) using magnetic resonance spectroscopy (MRS) at a field strength of 3T has been challenging because of spectral overlap with signals from other metabolites and a complicated multiplet structure due to strong J-coupling. Constant Time PRESS (CT-PRESS) was introduced to detect J-coupled resonances with high signal-to-noise ratio by using effective homonuclear coupling. We used CT-PRESS optimized for the detection of Glu in 24 healthy human subjects (12 elderly) and compared the proton metabolite profile of three brain regions commonly affected in normal aging and neuropsychiatric conditions, such as alcohol dependence: the basal ganglia, cerebellum and pons.

MRS was performed on a GE 3T MR scanner. Single voxels were manually positioned in the three brain regions. The acquisition time was ~9min per voxel. An acquisition without water suppression was carried out to measure tissue water content which was used to normalize metabolite signal intensities. The quality of the spectra allowed evaluation of signals from N-acetyl-aspartate (NAA), choline containing compounds (Cho), total creatine (tCr), myo-Inositol (mI), Glu, and Glu+Glutamine (Glx). A 2-group (young vs. elderly), repeated measures analysis of variance revealed two sig-

nificant interactions: group-by-region ( $F(1,2)=3.772$ ,  $P_{GG}=0.0355$ ) and group-by-region-by-metabolite ( $F(1,10)=4.578$ ,  $P_{GG}=0.0025$ ). Irrespective of age, metabolite values were generally higher in the pons and cerebellum than basal ganglia; NAA was highest in the pons, and tCr was highest in the cerebellum. The 3-way interaction indicated a significant influence of age: tCr levels were lower in the basal ganglia ( $P=0.0132$ ) but higher in the cerebellum ( $P=0.005$ ) and pons ( $P=0.05$ ) of

the elderly than the young. Glu was lower in the basal ganglia ( $P=0.0004$ ), while Cho was higher in the pons ( $P=0.0169$ ) of the elderly. Determining the profile of proton metabolite spectral intensities across brain regions in normal aging is a critical first step in establishing changes due to neurological conditions such as alcohol dependence.



Average signal intensity of metabolites in ratios relative to tissue water. \* $P<0.05$ , basal ganglia  $n=22$ , cerebellum  $n=19$ , pons  $n=23$ .

### REFERENCES/FUNDING SOURCE

Differential effects of age on tissue water-referenced proton metabolites in basal ganglia, pons, and cerebellum using an MRS sequence optimized for glutamate detection (Proceedings ISMRM 2007). Supported by NIAAA (AA05965, AA13521, AA12388), NIA (AG 17919).



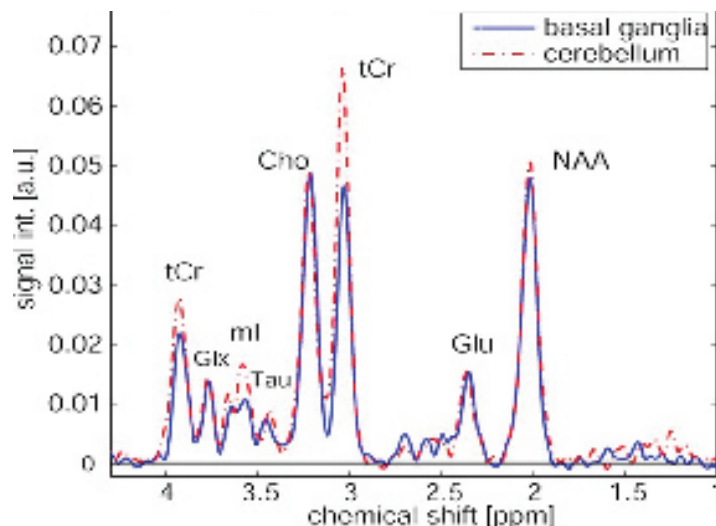
# In Vivo Metabolite Differences Between the Basal Ganglia and Cerebellum of the Rat Brain Detected with Proton MRS at 3T

D. MAYER<sup>1</sup>, N.M. ZAH<sup>2</sup>, E.V. SULLIVAN<sup>2</sup>, A. PFEFFERBAUM<sup>2,3</sup>

DEPARTMENTS OF <sup>1</sup>RADIOLOGY, <sup>2</sup>PSYCHIATRY & BEHAVIORAL SCIENCES, STANFORD UNIVERSITY  
AND <sup>3</sup>NEUROSCIENCE PROGRAM, SRI INTERNATIONAL, MENLO PARK, CA

**Introduction** In vivo magnetic resonance spectroscopy (MRS) permits non-invasive longitudinal tracking of brain chemistry changes that can accompany aging, alcohol dependence, and experimental manipulations modeling such conditions. As 3 T human scanners have become widely available, animal research at the same field strength with the same protocols should facilitate preclinical to clinical translational research. Constant Time PRESS (CT-PRESS) has been introduced as a method to detect coupled resonances with high signal-to-noise ratio by using effective homonuclear decoupling. Here, we tested the feasibility of using CT-PRESS optimized for the detection of glutamate (Glu) in the rat to dissociate the biochemical profile of two brain regions affected by alcohol dependence, the basal ganglia and cerebellum. Our aim was to establish baseline levels of principal metabolites detectable with proton MRS in different brain regions using tissue water as an internal reference.

**Methods and Results** Six healthy male adult Wistar rats were scanned in a clinical GE 3T MR scanner equipped with self-shielded gradients and a custom quadrature birdcage coil. The average echo time (TE) of the CT-PRESS sequence was 139 ms optimized for the detection of Glu. For each rat, spectra were acquired from two voxels: the first contained mostly the cerebellum, the second the striatum. The voxel size was 0.2 ml. The



Representative CT-PRESS spectra from voxels in the basal ganglia (solid blue) and cerebellum (dashed red) of a single rat.

quality of the spectra allowed evaluation of signals from N-acetyl-aspartate (NAA), total creatine (tCr), choline containing compounds (Cho), Glu, Glu+glutamine (Glx), myo-inositol (mI), and taurine. Using the amount of tissue water as an internal reference, both tCr and mI were lower in the basal ganglia than cerebellum.

**Conclusion** This study demonstrates the feasibility of using in vivo CT-PRESS to quantitate differences in metabolite signals between brain regions of the rat. CT-PRESS provides the enhanced signal

separation necessary to reliably measure J-coupled resonances, including Glu and mI, in the rat brain at 3 T. Our findings, which indicate variation of tCr across brain regions, emphasize the benefit to in vivo MRS of incorporating methods to establish baseline metabolite signals relative to water. Such advances should contribute to validating an animal model of chronic alcoholism, a disease which induces glutamatergic neurotransmitter system changes in striatal regions and structural and biochemical changes to cerebellar regions.

## REFERENCES/FUNDING SOURCE

In vivo metabolite differences between the basal ganglia and cerebellum of the rat brain detected with proton MRS at 3T. *Psychiatry Research: Neuroimaging* (2007), doi:10.1016/j.psychres.2006.11.005  
NIH grants AA005965, AA012388, and AA013521

## Neural Correlates of Attentional Control of Conflict Processing: fMRI Evidence from a Stroop Match-to-Sample Task

TILMAN SCHULTE<sup>1</sup>, EVA M. MÜLLER-OEHRING<sup>2</sup>, DIRK MAYER<sup>3</sup>, SHARA VINCO<sup>1</sup>, ADOLF PFEFFERBAUM<sup>1,2</sup> AND EDITH V. SULLIVAN<sup>2</sup>

<sup>1</sup>NEUROSCIENCE PROGRAM, SRI INTERNATIONAL, MENLO PARK, CA AND

DEPARTMENTS OF <sup>2</sup>PSYCHIATRY & BEHAVIORAL SCIENCES AND <sup>3</sup>RADIOLOGY, STANFORD UNIVERSITY

To identify the neural circuits of conflict processing and attentional allocation with fMRI, we devised a Stroop Match-to-Sample task requiring a decision based on a color cue that directed attention to a specific color and primed the color processing of the Stroop stimulus. In addition, conflict processing may be mediated by motor response repetition vs. switching.

Healthy right-handed adult volunteers (7 women, 7 men; mean age = 23.7±2.7 years) underwent fMRI while performing the Stroop Match-to-Sample task. Subjects matched the color of a cue stimulus displayed for 450 ms in the center of the screen to the color of a Stroop target stimulus that appeared for 1100 ms after an interstimulus interval of 300 ms. Subjects pressed a YES-key for cue-target color matches and a NO-key for nonmatches, yielding accuracy and reaction time measures. To mix YES- and NO responses two blocks were presented, one containing incongruent match and non-match trials (incongruent) and the other containing congruent match and nonmatch trials (congruent).

Cued-Stroop processing activated a fronto-temporo-parietal attention network involving left anterior and posterior cingulate

cortices, superior temporal gyrus and right parietal cortex. Despite lack of difference between comparisons in RT, response switching activated a motor network involving the left precentral and postcentral cortices and the cerebellum bilaterally that was not activated in response repetition.

Taken together, these findings show involvement of a fronto-temporo-parietal attention network in cued-Stroop processing, i.e., resolving conflict posed by competing stimulus attributes. These data complement clinical studies that have shown impairment in conflict processing and selective attention in neuropsychiatric conditions that can disrupt this circuitry, including alcoholism. This paradigm provides a novel differentiation of frontal-parietal attention systems and motor systems and lays a foundation for clinical research on identifying sources of disruption of neural systems of attention, conflict processing and motor control.

### REFERENCES/FUNDING SOURCE

This work was supported by NIAAA grants: AA10723, AA05965.

## V1 Projection Zone Signals in Human Macular Degeneration Depend on Task, Not Stimulus

YOICHIRO MASUDA<sup>1,2</sup>, SERGE O. DUMOULIN<sup>1</sup>, SATOSHI NAKADOMARI<sup>2</sup>, BRIAN A. WANDELL<sup>1</sup>

DEPARTMENT OF <sup>1</sup>PSYCHOLOGY, STANFORD UNIVERSITY, STANFORD, CA AND <sup>2</sup>OPHTHALMOLOGY, JIKEI UNIVERSITY, SCHOOL OF MEDICINE, TOKYO, JAPAN

**Introduction.** There is a controversy about the degree to which the adult visual cortex adapts following retinal damage. Some studies identified large-scale reorganization in human macular degeneration (MD) patients whereas others did not (Baker et al., 2005; Sunness et al., 2004). We have examined the signals in human JMD subjects to understand the extent and nature of any reorganization.

**Methods.** We describe functional magnetic resonance imaging (fMRI) experiments in four adult human subjects with juvenile macular degeneration (JMD). We measured the fMRI signals in visual cortex elicited by a variety of stimuli. The subjects either viewed the stimulus passively or performed a task. In addition to the JMD subjects we measured in healthy subjects where we mimicked the viewing conditions of the JMD subjects.

**Results.** In all JMD subjects we observed stimulus-synchronized fMRI signals in the cortical projection zones of their intact retina. In three out of four JMD subjects, we observed additional stimulus-synchronized signals within the cortical projection zone of the lesioned retina (lesion projection zone, LPZ). The stimulus-synchronized signals in the LPZ were observed only when the JMD subjects performed a stimulus-related visual matching task; the LPZ did not respond during passive viewing or unrelated tasks. In healthy control subjects we did not observe any signals in the simulated LPZ using identical stimuli and tasks.

**Discussion.** Our results provide a unifying framework for previously conflicting observations (Sunness et al., 2004; Baker et al., 2005)(Baker et al., 2005, Sunness et al., 2004). We propose that stimulus-synchronized activation in the LPZ is due to cortico-cortical signals elicited by the stimulus-related visual matching task. The cortico-cortical signals are normally balanced by geniculo-cortical signals specifying zero image contrast. In the absence of geniculo-cortical input in the LPZ, we propose that these cortico-cortical signals are the dominant modulator of the neuronal activity. Thus, we propose that the LPZ stimulus-synchronized activations do not necessarily reflect large-scale reorganization but result from disrupting the balance between geniculo-cortical and cortico-cortical projections to the LPZ.

### REFERENCES

Baker CI, Peli E, Knouf N, Kanwisher NG (2005) Reorganization of visual processing in macular degeneration. *J Neurosci* 25:614-618.  
Sunness JS, Liu T, Yantis S (2004) Retinotopic mapping of the visual cortex using functional magnetic resonance imaging in a patient with central scotomas from atrophic macular degeneration. *Ophthalmology* 111:1595-1598

## Loss of Arcuate Fasciculus in a Case of Radiation Necrosis

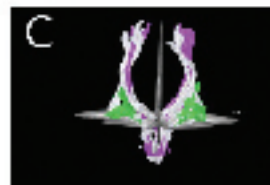
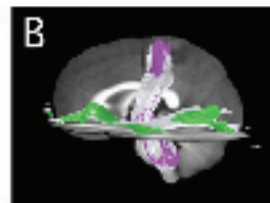
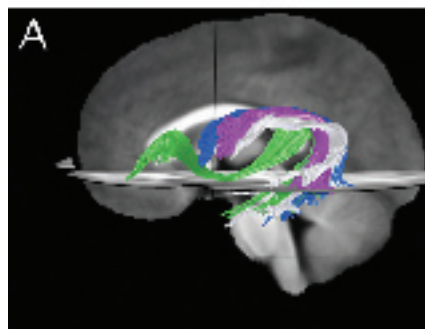
A.M. RAUSCHER<sup>1</sup>, G.K. DEUTSCH<sup>2</sup>, M. BEN-SHACHAR<sup>2</sup>, A. SCHWARTZMAN<sup>3</sup>, B.A. WANDELL<sup>2</sup>, R.F. DOUGHERTY<sup>2</sup>

<sup>1</sup>MEDICAL SCIENTIST TRAINING PROGRAM, <sup>2</sup>PSYCHOLOGY, STANFORD UNIVERSITY, <sup>3</sup>BIostatistics, HARVARD UNIVERSITY, BOSTON, MA

**Background:** Subject S1 was treated with radiation therapy at age 5 for a recurrent malignant tumor in her upper spine and brain. While cured of cancer, S1 developed radiation-induced tissue necrosis, primarily affecting cerebral white matter. She was introduced to us at age 15 because of her profound dyslexia. We assessed cognitive abilities and performed diffusion tensor imaging (DTI) to assess cerebral white matter pathways.

**Methods:** S1's DTI data were transformed to a standard brain coordinate system and compared to a matched control group (N=54) using a one-sample version of the log-normal test for tensor orientation differences (Schwartzman 2006). This test compares the orientation (eigenvectors) of each of S1's tensors to the orientation of the corresponding tensors in the control brains. The resulting statistical map indicates the probability of obtaining tensors with orientations such as those of S1 from the distribution of the control-brain tensors. We controlled the false discovery rate to ensure that no more than 5% of the significant voxels were expected to be false-positives. Fiber tractography was used to interpret the statistical results.

**Results:** Diffuse white matter differences were evident in T1-weighted, T2-weighted, diffusion anisotropy, and mean diffusivity measures in S1 compared to controls. While principal diffusion direction maps appeared consistent with those of controls over most of the brain, there were tensor orientation abnormalities in the fiber tracts



that form the arcuate fasciculus (AF) in both hemispheres. Tractography analysis indicated that substantial portions of the left and right AF were missing in S1. Other major white matter tracts, such as the corticospinal and inferior occipitofrontal pathways, were intact. Functional MRI measurements indicated that S1 is left-hemisphere dominant for language with a normal activation pattern.

**Discussion:** The left AF forms a major set of connections between frontal and temporal/parietal language areas. The right AF connects anatomically homologous regions within the right hemisphere and may mediate visuospatial processing. Despite the left AF abnormality, S1 had preserved oral language with average sentence repetition skills. In addition to profound dyslexia, S1 exhibited impaired auditory and spatial working memory and visuospatial deficits. We attribute the reading and visuospatial deficits to the abnormal left and right AF pathways, respectively. These results are the first to link radiation necrosis with selective damage to a specific fiber tract, and advance our understanding of the functional significance of the arcuate fasciculus.

### REFERENCES/FUNDING SOURCE

Presented at Society for Neuroscience, 2007.

Rauschecker funded by Stanford MSTP Training Program and NIH/NEI EY 15000.

## Regional Cerebral Gray Matter Density Changes Associated with Creativity in Healthy Volunteers

JULIE C. BONNER, TERENCE A. KETTER, PO W. WANG, MARGARITA GARCIA-AMADOR, JOHN O BROOKS III

PSYCHIATRY AND BEHAVIORAL SCIENCES

**Objective:** Few studies have assessed relationships between creativity and neurobiology. We explored relationships between regional cerebral gray matter density and non-eminent creativity as measured by the Baron-Welch Art Scale (BWAS).

**Method:** 25 healthy volunteers (mean age 36.4 years, 60% female), with no history of psychiatric, substance use, or major medical disorders, received 1.5T cerebral Magnetic Resonance Image (MRI) scans and completed the BWAS to assess non-eminent creativity. MRI images were stereotactically normalized and segmented into gray matter using Statistical Parametric Mapping (SPM5). Voxel-based morphometry (VBM) was used to assess relationships ( $p < 0.001$ ) between total BWAS scores and regional cerebral gray matter density.

**Results:** Higher total BWAS scores were associated with increased gray matter density in bilateral precuneus (BA7), right middle temporal gyrus (BA21), right claustrum/insula, and left fusiform gyrus (BA 18). Higher total BWAS scores were associated with decreased gray matter density in right middle frontal gyrus (BA11), left middle frontal gyrus (BA6), left post-central gyrus (BA2), and the right middle posterior

temporal gyrus (BA39). As BWAS inversely correlated with age ( $r = -.27, p < 0.05$ ), age was a covariate in all VBM analyses.

**Conclusion:** Our data suggest that increased paralimbic gray matter density coupled with decreased frontal gray matter density may be related to greater creativity in healthy volunteers. Previous studies have revealed associations between creativity and cerebral metabolism in regions overlapping those found in this structural study, such as precuneus, right frontal, right insula, and posterior temporal gyri. Our findings are also consistent with our observations in patients with bipolar disorder of not only increased creativity, but also structural and metabolic changes the frontal and limbic regions.

### REFERENCES/FUNDING SOURCE

Neural responsiveness to incentives in younger and older adults. Sasha E.B. Bonner, J.C., et al. Regional Cerebral Gray Matter Density Changes Associated with Creativity in Healthy Volunteers. in Society of Biological Psychiatry Annual Scientific Convention and Program. 2007. San Diego, CA. Supported by the National Alliance for Research in Schizophrenia and Depression, and the Stanley Foundation Research Awards Program.



## Associative Retrieval and Mismatch Signals in the CA Fields of Human Hippocampus

CHEN, J, OLSEN, RK, PRESTON, AR, WAGNER, AD, DEPARTMENT OF PSYCHOLOGY AND NEUROSCIENCES PROGRAM

While the role of the hippocampus in declarative memory is well established, the mechanisms subserved by component subfields remain underspecified. Within the hippocampus—which includes dentate gyrus, CA3, CA1, and subiculum—it has been hypothesized that CA3 and CA1 differentially support memory-based associative predictions and the detection of associative prediction error. From this perspective, CA3 is posited to encode conjunctive memories that are subsequently “pattern completed” during associative retrieval, in essence making predictions about the present based on associative knowledge acquired in the past. CA3 is thought to pass these predictions to CA1, which is positioned to compare this output from memory with input from entorhinal cortex that transmits the present state of “sensory reality”. To examine the functional contributions of human CA3 and CA1 to associative retrieval and the detection of associative prediction error, we used highRdecision. On each recall trial, one element of a studied pair

served as the retrieval cue, which was followed by a 7.5-s delay during which the subject attempted to retrieve the associate. Following the delay, a probe was presented—either the correct associate (match) or an incorrect item (mismatch); subjects had 750 ms to respond. Initial fMRI analyses revealed that delay-period activity in bilateral CA3 was greater for successfully vs. unsuccessfully retrieved associations. On successful trials, probe period activity in bilateral CA1 was greater when the probe mismatched vs. matched memory, with this associative mismatch effect being significant when the probe was a house. These results support the hypothesis that CA3 and CA1 differentially subserve pattern completion (associative retrieval) and the detection of associative prediction errors.

### REFERENCES/FUNDING SOURCE

NIMH 1R01MH076932-01A1 and NARSAD.

## Encoding Predictors of Graded Source Recollection: A High-resolution fMRI Study of Conjunctive Encoding in the Medial Temporal Lobe

CRYSTAL L. COOK REECK<sup>1</sup>, ALISON R. PRESTON<sup>3</sup>, GWEN M. LAWSON<sup>1</sup>, & ANTHONY D. WAGNER<sup>1,2</sup> - <sup>1</sup>DEPARTMENT OF PSYCHOLOGY AND <sup>2</sup>NEUROSCIENCES PROGRAM, STANFORD UNIVERSITY AND <sup>3</sup>DEPARTMENT OF PSYCHOLOGY, UNIVERSITY OF TEXAS AT AUSTIN

The medial temporal lobe is critical for declarative memory, including item recognition and source recollection. While prior data have documented that the magnitude of encoding activation in the anterior medial temporal cortex (~perirhinal cortex) varies in a continuous manner that tracks gradations in subsequent item familiarity, it is unclear whether encoding activation in the medial temporal lobe also continuously varies according to gradations in subsequent source recollection. The present high-resolution fMRI study examined the relationship between encoding activation and partial vs. full subsequent source recollection. Participants were scanned while incidentally encoding visually-presented words in one of four imagery orienting conditions: generating an image of an (1) indoor or (2) outdoor scene, or generating the name of a famous (3) male or (4) female person. A post-scan memory test evaluated item and conjunctive (source) memory, using a three-step procedure that assessed item recognition (old/new), task recollection (scene/person), and specific detail recollection (indoor/

outdoor; male/female). Initial fMRI analyses (n=20) revealed that activation in entorhinal and perirhinal cortices showed greater activation for recollection of source information as compared to item recognition (specific recollection and task recollection>item only). In contrast, activation of the CA1 field of the hippocampus demonstrated a continuous encoding effect, tracking the extent of subsequent recollection (specific recollection>task recollection>item only). These results indicate that conjunctive encoding in the hippocampus can vary in a continuous manner, whereas anterior MTL cortical processes contribute to the encoding of source information but do not vary based on the amount of detail subsequently recollected. This distinction suggests that hippocampus and anterior MTL cortex differentially subserve the encoding of information into a conjunctive representation.

### REFERENCES/FUNDING SOURCE

NIMH 1R01MH076932-01A1 and NARSAD

## Modulation of Brain Networks via Real-time fMRI Feedback Training

AXEL LUCCA<sup>1</sup>, JARRED YOUNGER<sup>1</sup>, JANE LAWRENCE<sup>1</sup>, TAKEFUMI UENO<sup>1</sup>, KRISTEN LUTOMSKI<sup>3</sup>, SAXON MACLEOD<sup>3</sup>, FUMIKO HOEFT<sup>1</sup>, GARY GLOVER<sup>2</sup>, RAYMOND GAETA<sup>1</sup>, CHRISTOPHER DECHARMS<sup>3</sup>, SEAN MACKAY<sup>1</sup>, DEPARTMENTS OF <sup>1</sup>ANESTHESIA AND <sup>2</sup>RADIOLOGY

Rumination, or recursive thinking about one's depressive symptoms. Many types of chronic pain may involve the dysregulation of complex networks in the central nervous system. The modulation of these networks may be one therapeutic route for reducing pain. Previously, we have demonstrated that patients can be trained to modulate their brain activity in a way that attenuates their experience of pain. This method involved feeding functional magnetic resonance imaging (fMRI) data back to patients in real-time. While data have shown that this real-time fMRI technique can both modulate brain activity and pain intensity, it is unknown how this training might change pain-related neuronal networks in the brain. In order to determine the impact of real-time fMRI training on pain processing, we employed a Granger Causality Mapping (GCM) algorithm. GCM allows the detection of voxels or regions of brain activity that precede or follow activity in a specific region of in-

terest (ROI). Participants were 10 patients with chronic pain who had demonstrated an ability to modulate activity in the rostral anterior cingulate cortex (rACC). GCM analyses revealed a consistent pattern of activity across participants. At the beginning of the training program, rACC activation was preceded by prefrontal activity. At the end of the training program, however, there was no relationship between prefrontal and rACC activity. Instead, insular activity reliably preceded rACC activity. This change in brain regions showing directed influence over the rACC may reflect a shift from conscious to more automated control over brain modulation.

### REFERENCES/FUNDING SOURCE

This research was supported by the NINDS, NIH P41 RR09784, and the Rosekrans Pain Research Endowment

## Attention-Dependent Modulation of Medial Temporal Lobe Encoding Processes

NICOLE M. DUDUKOVIC, ALISON R. PRESTON, JERMAINE J. ARCHIE & ANTHONY D. WAGNER.  
DEPARTMENT OF PSYCHOLOGY AND NEUROSCIENCES PROGRAM

Goal-directed attention has been shown to modulate activation in lateral cortical regions known to process faces (fusiform cortex) and scenes (parahippocampal cortex), but an open question is whether these effects propagate along the medial temporal lobe (MTL) circuit. The present study investigated how selective attention modulates stimulus-specific encoding processes in MTL cortex and the hippocampus, including how attention impacts MTL responses that predict subsequent memory. High-resolution functional magnetic resonance imaging (fMRI) of the human MTL was conducted on a 3.0 Tesla GE Signa scanner at the Lucas Center while 20 participants attended, ignored, or passively viewed face and scene stimuli. Each trial consisted of four sequentially presented images, two faces and two scenes, and participants were instructed to 1) Remember Faces and Ignore Scenes, 2) Remember Scenes and Ignore Faces, or 3) Passively View both Faces and Scenes (Gazzaley et al., 2005). After a brief delay, either a probe stimulus appeared and participants indicated whether it was in the current memory set (Remember Faces/Remember Scenes conditions), or an arrow appeared and participants indicated the direction it pointed (Pas-

sive View condition). A surprise post-scan recognition memory test revealed that participants were more accurate and had higher confidence in their memory judgments for stimuli that were attended as opposed to those that were ignored or passively viewed. Anatomical and functional region of interest (ROI) analyses differentiated between individual MTL subregions and demonstrated that goal-directed attention modulates encoding activation in perirhinal cortex (for faces) and parahippocampal cortex (for scenes) and that these effects propagate into hippocampal subfields. In addition, attention-dependent subsequent memory effects were observed within MTL subregions, suggesting that attention is critical for the encoding responses that give rise to later memory. We are currently finishing data analysis. Preliminary results were presented at a scientific meeting in October 2006, and we plan to submit the study for publication in a peer-reviewed scientific journal this fall.

REFERENCES/FUNDING SOURCE: National Science Foundation (BCS 0401641), NARSAD.

## Functional Connectivity Reflects Structural Connectivity in a Human Memory Network

MICHAEL D. GREICIUS<sup>1,2</sup>, KAUSTUBH SUPEKAR<sup>3</sup>, VINOD MENON<sup>2,4</sup>, ROBERT F. DOUGHERTY<sup>5</sup>  
DEPARTMENTS OF <sup>1</sup>NEUROLOGY, <sup>2</sup>PSYCHIATRY, <sup>3</sup>BIOMEDICAL INFORMATICS, <sup>4</sup>PROGRAM IN NEUROSCIENCE, AND <sup>5</sup>PSYCHOLOGY

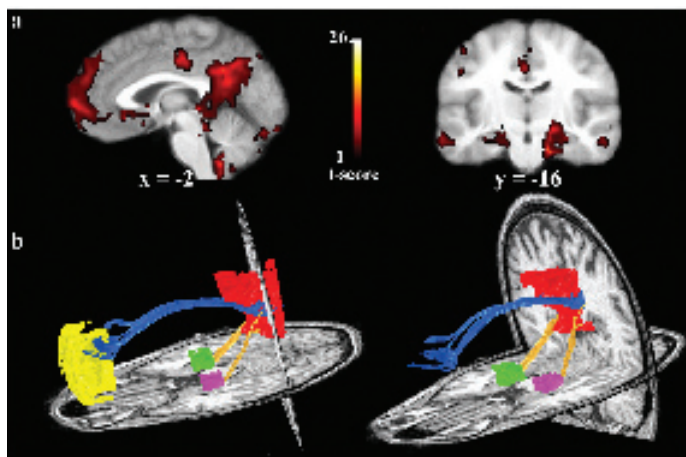


Figure 1: Functional connectivity reflects structural connectivity in the default mode network. (a) Task-free, functional connectivity in the DMN is shown in a group of 6 subjects. The posterior cingulate/retrosplenial cortex (PCC/RSC) and medial prefrontal cortex (MPFC) clusters are best appreciated on the sagittal view. Prominent bilateral medial temporal lobe (MTL) clusters are seen on the coronal image (left side of image corresponds to left side of brain). (b) DTI fiber tractography in a single subject demonstrates the cingulum bundle (blue tracts) connecting the PCC/RSC to the MPFC. The yellow tracts connect the bilateral MTL to the PCC/RSC. Note that generally the tracts from the MPFC enter the more rostral aspect of the PCC/RSC ROI corresponding to the PCC proper, whereas the tracts from MTL enter the more caudal aspect of the PCC/RSC ROI corresponding to the RSC proper.

Tracer studies in non-human primates have revealed connections between the retrosplenial cortex and the medial temporal lobe. Functional connectivity and lesion studies suggest that similar pathways exist in humans. Here we combine diffusion tensor imaging tractography with task-free functional connectivity MRI to identify these pathways in individual subjects. These two modalities were used to investigate connectivity within the default mode network, a set of brain regions—including medial prefrontal cortex, medial temporal lobes, and posterior cingulate/retrosplenial cortex—implicated in episodic memory retrieval. Using seed regions from the functional connectivity maps, the tractography analysis revealed robust structural connections between the medial temporal lobes and the retrosplenial cortex whereas tracts from the medial prefrontal cortex contacted the posterior cingulate cortex (adjacent but rostral to the retrosplenial cortex). There were no tracts connecting the medial prefrontal cortex to the medial temporal lobes suggesting that functional connectivity between these two nodes is mediated by a third region, perhaps the posterior cingulate cortex. The results demonstrate that intrinsic, task-free functional connectivity reflects structural connectivity in a human memory network.

### REFERENCES/FUNDING SOURCE

This work was funded by grants from the Alzheimer's Association (NIRG-04-1060) and the NIH (NS048302; EY015000).

# Fat Suppression for $^1\text{H}$ MRSI at 7T Using Spectrally Selective Adiabatic Inversion Recovery

P. BALCHANDANI<sup>1,2</sup>, D. SPIELMAN<sup>2</sup>, DEPARTMENTS OF <sup>1</sup>ELECTRICAL ENGINEERING, <sup>2</sup>RADIOLOGY

$^1\text{H}$  Magnetic resonance spectroscopic imaging ( $^1\text{H}$  MRSI) is a useful technique for measuring metabolite levels in the brain. Some of the main metabolites of interest are Choline (Cho), Creatine (Cr) and N-Acetyl-Aspartate (NAA).  $^1\text{H}$  MRSI at higher fields, such as 7T, offers the advantages of increased SNR and spectral separation. However, it suffers signal losses from increased  $B_1$  inhomogeneity (40%  $B_1$  variation from center to periphery of head at 7T),  $B_0$  inhomogeneity and chemical shift localization

(CSL) errors. These factors place the added requirements of  $B_1$ -immunity, robustness to  $B_0$  shifts and conservation of metabolite signal on any 7T fat-suppression scheme. One technique available to suppress fat is the use of an inversion pulse before the  $90^\circ$  excitation pulse in a PRESS sequence so that species with short  $T_1$ 's such as fat pass through their null when excitation occurs. Metabolites have longer  $T_1$ 's than fat resulting in a partial loss on the order of 50% of metabolite signal at 7T. However, the increased spectral separation at 7T makes it possible to design a spectrally selective adiabatic inversion pulse that only inverts lipid frequencies, leaving most of the metabolites untouched. Such a pulse was designed and inserted into a standard PRESS sequence.

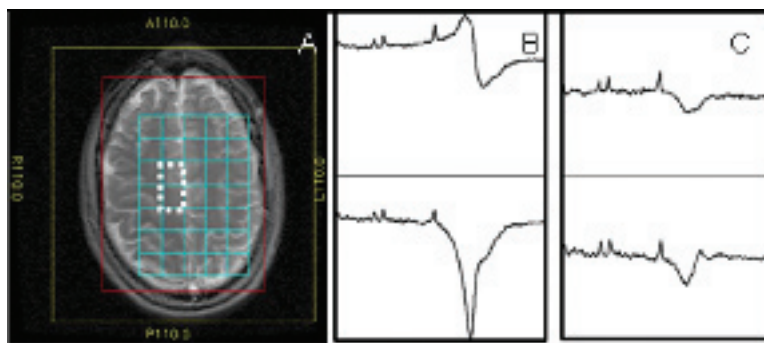


Figure: In vivo data from normal volunteer: (A) FOV, PRESS box, spectral grid location and two central voxels (dotted line), (B) central voxels using standard GE PRESS and (C) central voxels with fat-selective inversion recovery (fat is significantly suppressed while metabolite signal is retained).

In vivo data show that the adiabatic fat-selective inversion pulse successfully suppressed fat while not degrading signal from most of the metabolites of interest in the brain when compared to the standard GE PRESS sequence at 7T. The pulse will eventually be inserted into an interleaved adiabatic SPSP sequence (currently under development) so that, in addition to fat suppression, excitation is adiabatic and immune to CSL errors. This will allow for increased volumetric coverage

without degraded metabolite signal for  $^1\text{H}$  MRSI at 7T. Other options such as adiabatic inversion pulses with asymmetrical profiles or selective adiabatic excitation pulses may also be explored and compared in terms of selectivity, suppression efficiency and Specific Absorption Rate (SAR) levels.

## REFERENCES/FUNDING SOURCE

Fat suppression for  $^1\text{H}$  MRSI at 7T using a spectrally selective adiabatic inversion pulse, Poster at ISMRM-ESMRMB, 2007.

Lucas Foundation & NIH RR09784

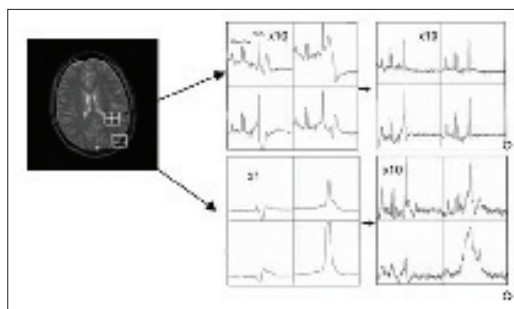
# Robust Water and Lipid Suppression Using Multiple Dualband Frequency Selective RF Pulses for $^1\text{H}$ Spectroscopic Imaging at 3T

<sup>1</sup>MENG GU, <sup>2</sup>DANIEL MARK SPIELMAN, DEPARTMENTS OF <sup>1</sup>ELECTRICAL ENGINEERING AND <sup>2</sup>RADIOLOGY, STANFORD UNIVERSITY

$^1\text{H}$  magnetic resonance spectroscopic imaging has been increasingly used in diagnosis and treatment assessment in recent years. For in-vivo studies, water and lipid signals are large and, if not suppressed, greatly contaminate the desired metabolic information. Water suppression is typically achieved with a series of chemical shift selective (CHESS) pulses and dephasing gradient. Ogg et al, have previously demonstrated that optimizing the flip angles of the CHESS pulse train yields T1- and-B1 insensitive water suppression. Taking advantage of increased chemical shift dispersion at 3T, we extend this approach by using dualband frequency-selective preparatory RF

pulses to suppress both water and lipid resonances. This approach yields robust water and lipid suppression with no loss of metabolic signals.

To rotate water and lipid magnetization at the same time while not disturbing the singlet resonances of, Choline Creatine and NAA, under study, RF pulses with a dual-band rotation profile were designed using the Shinnar-Le Roux algorithm. To count for B1 inhomogeneity and different T1s of water and lipid spins, four such pulses, 10ms apart, with different flip angles were used. The optimized flip angles were found by minimizing the maximum absolute value of residue longitudinal magnetization for 4 representative water and lipid T1s, 1.5s and 170/260/280 ms, at the time of excitation under the condition of 20 percent B1 inhomogeneity. In-vivo brain MRSI data were acquired with standard CHESS water suppression and no lipid suppression and



Caption - The figure shows Spectra from representative regions with CHESS water suppression/no lipid suppression and multi-pulse dualband water/lipid suppression.

compared to data using the proposed multi-pulse dualband method with the following characteristics: TR/TE=2000/144 ms, single slice, 4.5 cc voxels and 6 minute acquisition time.

Attached figure shows spectra from two regions with CHESS water suppression/no lipid suppression and multiple rotation water/lipid suppression obtained from in vivo studies. The two representative regions are chosen such that one is in the subcutaneous fat on the back of the head and the other is within the brain. Excellent water suppression is clearly demonstrated with a flat baseline. The spectra from the voxel

in the subcutaneous fat clearly show that the lipid signal is suppressed with multiple dualband pulses. The measured suppression is on the order of 20. The spectra from voxels within the brain show significantly reduced lipid artifacts and undisturbed metabolite peaks.

We have designed and implemented a robust method to suppress both water and lipids using multiple dualband frequency-selective pulses for  $^1\text{H}$  MRSI imaging at 3T. The effectiveness of the method is demonstrated in-vivo.

## REFERENCES/FUNDING SOURCE

Robust water and lipid suppression using multiple dualband frequency-selective RF pulses for  $^1\text{H}$  spectroscopic imaging at 3T, ISMRM, 2007. Lucas foundation, NIH RR09784, CA098523



# <sup>1</sup>H MRSI at 7T Using an Interleaved Narrow-band PRESS Sequence with Spatial-spectral Adiabatic Refocusing Pulses

P. BALCHANDANI<sup>1,2</sup>, J. PAULY<sup>1</sup>, D. SPIELMAN<sup>2</sup>  
DEPARTMENTS OF <sup>1</sup>ELECTRICAL ENGINEERING, AND <sup>2</sup>RADIOLOGY

<sup>1</sup>H Magnetic resonance spectroscopic imaging (<sup>1</sup>H MRSI) is a useful technique for measuring metabolite levels in the brain. Some of the main metabolites of interest are Choline (Cho), Creatine (Cr) and N-Acetyl-Aspartate (NAA). <sup>1</sup>H MRSI at higher fields, such as 7T, offers the advantages of increased SNR and spectral separation. However, severe  $B_1$  inhomogeneity and chemical shift localization (CSL) errors limit the spatial coverage that can be achieved. Approximately 40%  $B_1$  variation was measured across the adult human head in our 7T GE whole body magnet. Adiabatic spectral-spatial (SPSP) pulses may be used instead of standard sinc 180° pulses to provide some immunity to  $B_1$  variations as well as CSL errors. However, simulations show that adiabatic SPSP pulses hit peak RF amplitude limits (approx 17  $\mu$ T) at a spectral bandwidth of approx 500 Hz, leaving no room to overdrive the pulses. In addition, the increased spectral separation at 7T combined with the limited spectral passband makes the pulses less robust to shifts due to  $B_0$  inhomogeneity. Therefore, we have developed an interleaved narrow-band adiabatic SPSP PRESS sequence that acquires two separate spectral passbands (one for Cho/Cr and a second for NAA) within one TR. Since each pulse now has a narrower bandwidth, greater immunity to  $B_0$  shifts and a higher overdrive factor can be achieved, without an increase in scan time. Each band is acquired using a linear phase SPSP 90° pulse followed by two narrow-band adiabatic SPSP 180° pulses for volume localization. The adiabatic SPSP 180° pulses

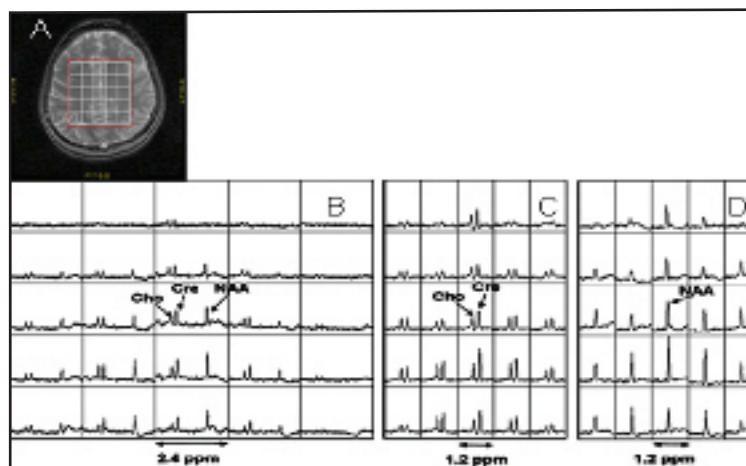


Figure 1: In vivo data from normal volunteer: (A) ROI and PRESS box, (B) spectral grid using standard GE PRESS, (C) spectral grid for Cho & Cr band using adiabatic SPSP 180° pulses, and (D) spectral grid for NAA band using adiabatic SPSP 180° pulses (all spectra are plotted to the same scale).

are adiabatic over a 60% variation in  $B_1$  before hitting peak RF amplitude limits for our 7T magnet. Additionally, there is negligible CSL error since the transmit frequency is centered between Cho and Cr for the first band and on NAA for the second band.

In vivo data show that the interleaved narrow-band adiabatic SPSP sequence provides much better spatial coverage and increased signal even at the isocenter of the coil. In the spectra obtained using the standard PRESS sequence (Figure 1 B), voxels away from the isocenter of the coil have reduced signal overall due to severe  $B_1$

drop off. The interleaved narrow-band sequence provides much more signal in these areas (Figures 1 C & D). The SPSP 90° pulse is still not adiabatic and the  $B_1$  receive profile is unchanged, so some signal loss off isocenter is to be expected. For the standard PRESS sequence (Figure 1 B), voxels in the rightmost region of the PRESS box contain almost no NAA signal due to chemical shift localization error. This is considerably improved in the interleaved narrow-band acquisition (Figures 1 D). In the future, we plan to include a fat selective inversion pulse for fat suppression although some fat suppression is provided by the spectral selectivity of SPSP pulses.

## REFERENCES/FUNDING SOURCE

Interleaved narrow-band adiabatic spatial-spectral pulse sequence for <sup>1</sup>H MRSI at 7T. Presented at ISMRM-ESMRMB, 2007.  
Lucas Foundation & NIH RR09784.

Fast  $^1\text{H}$  Missing-Pulse SSFP Chemical Shift Imaging of the Human Brain at 7 Tesla

D. MAYER AND D.M. SPIELMAN - DEPARTMENT OF RADIOLOGY, STANFORD UNIVERSITY

**Introduction:** Recently, steady state free precession (SSFP) chemical shift imaging techniques have been introduced which are particularly attractive because of their short measurement time ( $T_{\text{acq}}$ ) and high sensitivity ( $\text{SNR}/\sqrt{T_{\text{acq}}}$ ). The main disadvantages of SSFP-based methods are that the effects of both  $T_1$  and  $T_2$  on the signal intensities complicate quantitation and the spectral resolution is limited due to the short TRs. Whereas the former is an

inherent problem, the latter is less problematic at high field strengths such as 7 T due to the increased dispersion of the chemical shift. Spectroscopic missing pulse SSFP (spMP-SSFP) has the advantage that the full echo can be acquired. This allows data to be analyzed in magnitude mode without spectral line broadening. Therefore, the aim of this work was to implement spMP-SSFP with a spectral-spatial radiofrequency pulse (RF) for both slice selection and combined water and lipid suppression at 7 T.

**Method:** For phantom experiments,  $32 \times 32$  phase encoding steps in  $k_x$  and  $k_y$  (FOV = 24 cm) were carried out corresponding to a nominal resolution of  $0.3 \text{ cm}^3$ . For the in vivo experiment, the matrix size was  $16 \times 16$  ( $1.1 \text{ cm}^3$ ). The flip angle was  $45^\circ$ .

With a pulse interval  $\tau = 61 \text{ ms}$ , TR was  $3\tau = 183 \text{ ms}$ . The acquisition time per TR was 102 ms (spectral width = 10 kHz). With 2 averages for the phantom and 8 averages for the in vivo experiment to increase the SNR, the total measurement time was 6:26 min including 64 cycles without acquisition to establish a steady state. **Results:** The pulse sequence was tested on a spherical phantom containing a solution of various brain metabolites. Although the acquisition time corresponds to a nominal spectral resolution of only 10 Hz, the signals from creatine (Cr) and choline containing compounds (Cho) were

completely separated even in magnitude mode, owing to the increased frequency dispersion at 7 T and the symmetric acquisition of the echo in spMP-SSFP. N-acetyl-aspartate (NAA), *myo*-inositol (mI) and glutamate (Glu) could also be detected. Due to the severe  $B_1$  inhomogeneity of the RF coil used, the signal intensity varied considerably over the phantom. The figure shows a magnitude spectrum from a voxel from the center

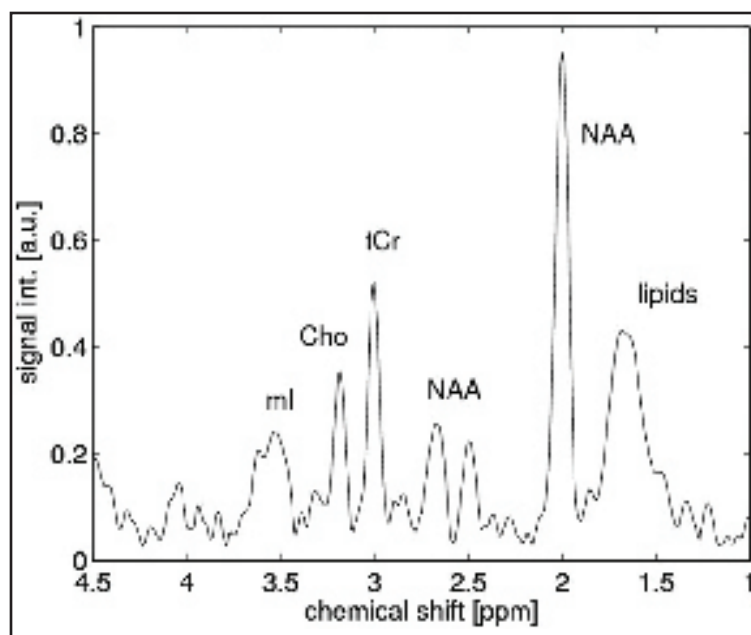
of the brain (just superior to the ventricles) of a healthy volunteer. Similar to the phantom results, the signals from total Cr and Cho are well separated. Although the depicted voxel was near the center of the brain, artifact signal from subcutaneous lipids in the scalp were detected because of incomplete suppression and Gibbs-ringing. Nevertheless, the NAA singlet at 2 ppm was not affected.

**Conclusion:** The presented data demonstrate the advantages and current challenges of spMP-SSFP at 7 T. The higher field strength provides better signal separation and higher SNR relative to low- and midfield systems. Even when using a

relatively small flip angle ( $45^\circ$ ) with the currently available RF coil,  $B_1$  inhomogeneity has a substantial impact on data quality. Better coil designs and parallel RF transmission techniques should help to reduce the artifacts caused by  $B_1$  inhomogeneity. When signal averaging is necessary to increase the SNR, a 3D variant of the technique can be used alternatively without time penalty.

## REFERENCES/FUNDING SOURCE

NIH grants RR09784, AA12388, and AA13521.



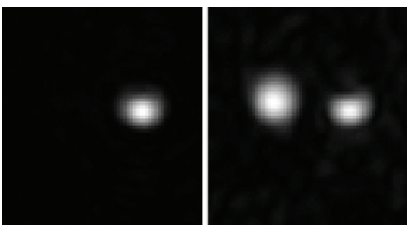
Caption – Magnitude spectrum from a voxel from the center of the brain of a healthy volunteer.

## Fast Spectroscopic Imaging Using Spiral Trajectories in the Context of Hyperpolarized $^{13}\text{C}$

YS LEVIN<sup>1</sup>, D MAYER<sup>1</sup>, A LIN<sup>2</sup>, P BHATTACHARYA<sup>2</sup>, KHARRIS<sup>2</sup>, K CHEKMENEV<sup>2</sup>, WH PERMAN<sup>3</sup>, BD ROSS<sup>2</sup>, DM SPIELMAN<sup>1</sup>  
<sup>1</sup>STANFORD UNIVERSITY DEPARTMENT OF RADIOLOGY AND <sup>2</sup>HUNTINGTON MEDICAL RESEARCH INSTITUTES <sup>3</sup>SAINT LOUIS UNIVERSITY

The introduction of techniques to hyperpolarize  $^{13}\text{C}$  allow for imaging of metabolic processes in real-time. Fast imaging is necessary because hyperpolarized signal decays with T1, and because some physiologic processes exhibit motion or other significant temporal variation. The purpose of this work is to demonstrate the feasibility of rapid imaging and spectroscopic imaging in the context of hyperpolarized  $^{13}\text{C}$  using spiral k-space trajectories and an agent hyperpolarized using the PASADENA technique.

**Methods:** To demonstrate the feasibility of fast imaging in the context of hyperpolarized  $^{13}\text{C}$ , a syringe (diameter  $\sim 1.5$  cm) was filled with 3.5 mL of 5 mM  $^{13}\text{C}_1$  hydroxyethyl propionate (HEP) hyperpolarized to  $>25\%$  polarization, and placed at the isocenter of a 1.5 T Magnetic Resonance scanner. Following a small-tip excitation, a single-interleaf spiral k-space trajectory was used to image a single slice (FOV = 8 cm, resolution = 0.5 cm X 0.5 cm in-plane, 1 cm slice thickness). Using this method, 32 images were acquired after the small-tip excitation. Each of the images was acquired in 11.5 ms, and there was a 3 ms delay between images. The small-tip excitation and data acquisition procedure was repeated for a total of 24 excitations, spaced 5s from each other, in order to measure T2\* decay and T1 with one polarization. Thus, 768 images were acquired in two minutes.



[a] HEP spectroscopic image. [b] Acetate spectroscopic image with HEP contamination (right).

A second experiment was performed to demonstrate rapid chemical shift imaging (CSI). A spherical phantom containing 4 M  $^{13}\text{C}_1$  acetate was placed adjacent to the syringe. An 8-interleaf spiral CSI experiment was used, and each interleaf was acquired after a single small-tip excitation (spectral width (SW) = 205 Hz, spectral resolution = 6.4 Hz). Each of the remaining interleaves was acquired in a similar manner, with small-tip excitations performed at 2-second intervals. A 2-second

delay between excitations is not ideal for imaging the hyperpolarized HEP, because there is some T1 decay during this interval. However, a delay was necessary in order to allow for recovery of the acetate, which was not hyperpolarized.

**Results:** The rapid imaging resulted in T1 and T2\* estimates of 47.9 s and 11 ms, respectively, for the HEP compound. In the CSI experiment, there was spectral overlap between the acetate phantom, which exhibited a long T2\* and narrow linewidth, and HEP, whose short T2\* resulted in a very broad line. The figure depicts spectroscopic images, with [a] showing the HEP phantom and [b] showing the acetate phantom along with HEP contamination. Future work focus on spectral separation of multiple hyperpolarized compounds, and novel reconstruction techniques.

**REFERENCES/FUNDING SOURCE**  
 ARCS Foundation, NIH RR09784.

## Image Based Ghost Correction for Oblique Imaging

A. NORDELL<sup>1,2</sup>, R. BAMMER<sup>1</sup>, AND S. SKARE<sup>1</sup>

<sup>1</sup>DEPARTMENT OF RADIOLOGY, RICHARD M. LUCAS IMAGING CENTER, STANFORD, PALO ALTO, CA AND

<sup>2</sup>DEPARTMENT OF CLINICAL NEURO SCIENCE, KAROLINSKA INSTITUTE, STOCKHOLM, SWEDEN

Nyquist or FOV/2-ghosting is a common artefact in echo planar imaging (EPI). The sources that lead to ghosting are manifold, but are primarily caused by gradient hardware time delays. Since even and odd echoes in the EPI readout are acquired under positive and negative gradient waveforms, the delays create misalignments between odd and even echoes along the readout direction  $\Delta k_{RO}$ . If the readout gradient is a combination of physical gradients e.g. as in an oblique imaging plane, and the gradient delays differ between the physical axes, the echo will also be shifted in the phase encoding direction,  $\Delta k_{PE}$ . This doesn't only shift the data, but also introduces some degree of under sampling in k-space. It has previously been shown that the  $\Delta k_{PE}$ -shift can be resolved using parallel imaging or gradient compensation blips. In this work, we have extended our previous image entropy based method, to also estimate this  $\Delta k_{PE}$ -shift. This method is independent of any reference scan and does not require any pulse sequence changes. We have compared conventional ghost correction in the  $k_{RO}$ -direction with  $k_{RO} + k_{PE}$ -correction. We also investigated the upper limit of the  $\Delta k_{PE}$ -shift that can be corrected for.

In order to test this method the scan plane was rotated around the z-axis and k-space was acquired at different angles between 0 and 180°. Simulations showed that it is possible to resolve a  $\Delta k_{PE}$ -shift of up to  $\pm 0.075$  voxels. Beyond this limit, k-space becomes too under-sampled. However, in our acquired phantom data, the maximum  $\Delta k_{PE}$ -shift was approx.  $\pm 0.045$  voxels, which is under the critical value found in the simulation.

We have shown that it is possible to perform an image

based ghost correction in two directions. This work applies to oblique image plane orientations in EPI scans and is by far superior to corrections applied in the readout direction only.

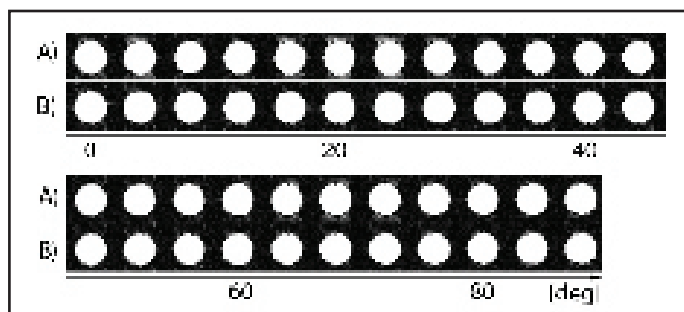


Figure shows the same dataset as fig. 3 (every 2nd image from 0-90 deg.). The x-axis is the rotational angle from 0 to 90 around the z-axis. Row A) show images corrected in the  $k_{RO}$ -direction, B) show images corrected in both  $k_{RO}$  and  $k_{PE}$ . The large differences in residual ghost originate from anisotropic gradients (i.e. in this case different time delays on the physical x- and y-axis).

**REFERENCES/FUNDING SOURCE**

Presented at ISMRM, 2007.

Karolinska University Hospital, Stockholm, Sweden  
 Stiftelsen Frimurare, Stockholm, Sweden.



## Evaluation of Chronic Cryoablated Prostate Lesions by Diffusion-weighted MRI

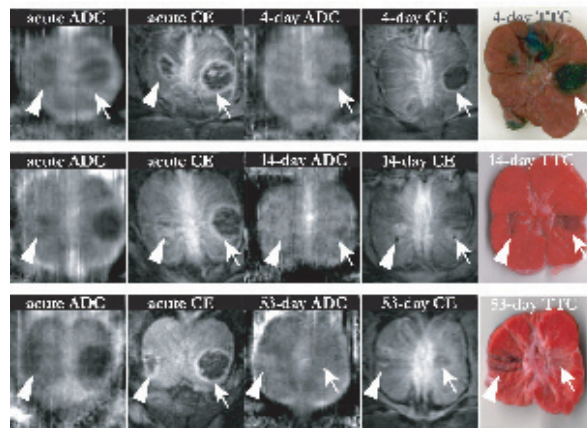
JING CHEN<sup>1,2</sup>, DONNA BOULEY<sup>3</sup>, BRUCE DANIEL<sup>2</sup>, MAURICE VAN DEN BOSCH<sup>2</sup>, KIM BUTTS PAULY<sup>2</sup>

DEPARTMENTS OF <sup>1</sup>ELECTRICAL ENGINEERING, <sup>2</sup>RADIOLOGY, AND <sup>3</sup>COMPARATIVE MEDICINE, STANFORD UNIVERSITY

Cryosurgery has been shown to be a promising treatment method for prostate cancer. Our group has demonstrated that diffusion-weighted MRI (DWI) provided delineation of the acute cryo lesion. In this work, we further investigate the use of DWI to evaluate chronic prostate lesion after cryoablation and compare the result to contrast enhanced MRI and histology.

All animal experiments were approved by the Administrative Panel on Laboratory Animal Care. MR-guided cryoablation was performed on 3 dogs to create two distinct cryo lesions in each dog. The lesion in the right lobe of the gland was frozen slowly to  $-10^{\circ}\text{C}$  once ("soft freeze"), while the lesion in the left lobe was rapidly frozen to lower than  $-40^{\circ}\text{C}$  ("hard freeze"). After the procedure, the dogs survived for 4 days (dog #1), 14 days (dog #2) and 53 days (dog #3), respectively.

All acute lesions presented on the apparent diffusion coefficient (ADC) trace map as low ADC value. The follow-up images were more complicated with the general trend of low initial ADC values increasing over time. More specifically, the "soft freeze" lesion of dog #1 (4 days post-treatment) was still visible as low ADC value (arrow), while



ADC trace map, T1-weighted contrast-enhanced images, and TTC staining result from all 3 canine prostates at different time post treatment. Each row of images is from one particular dog. At different recovery stage, the ADC value increased from lower than normal tissue to higher than normal tissue.

appeared smaller than the acute lesion acquired right after the treatment. Histological results revealed a large central area of hemorrhage surrounded by a narrow rim of regeneration. For dog #2 scanned 14 days after the cryoablation, the ADC value was slightly lower than normal untreated prostate tissue. Histology showed that this lesion had a central region of fibrosis and few glands surrounded by a large area of regeneration. For dog #3 53 days post treatment, the ADC was elevated (arrowhead), with histology revealing fibrosis and regeneration of glands.

In summary, at different recovery and regeneration stage, the lesion appeared differently on the ADC trace map from low ADC in the acute lesion, to high ADC in the regenerated gland. Our future work includes improving the

LSDI sequence for higher image resolution and better signal noise ratio, and registering MR image to histologic result for further investigation.

### REFERENCES/FUNDING SOURCE

ISMRM abstract, 2007

NIH P41 RR009784, NIH R01 CA092061, Lucas Foundation.

## Monitoring Prostate Thermal Therapy with Diffusion-weighted MRI

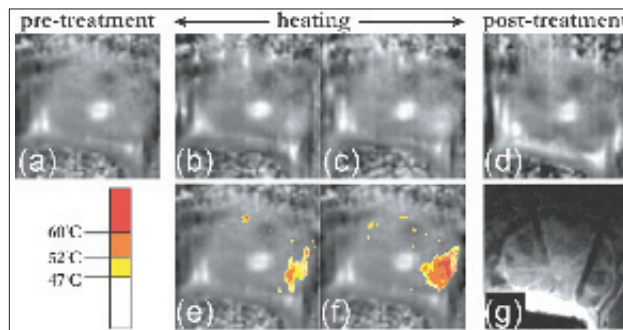
JING CHEN<sup>1,2</sup>, CHRIS DIEDERICH<sup>3</sup>, BRUCE DANIEL<sup>2</sup>, MAURICE VAN DEN BOSCH<sup>2</sup>, GRAHAM SOMMER<sup>2</sup>, KIM BUTTS PAULY<sup>2</sup> -

DEPARTMENTS OF <sup>1</sup>ELECTRICAL ENGINEERING, <sup>2</sup>RADIOLOGY, STANFORD UNIVERSITY, AND

<sup>3</sup>DEPARTMENT OF RADIATION ONCOLOGY, UCSF, SAN FRANCISCO, CA

A significant advantage of MR guidance for minimally invasive therapy is the ability to monitor the heat deposition and tissue viability in vivo. It has been shown that diffusion weighted MR imaging (DWI) provides a depiction of the thermal lesion in the prostate after thermal therapies. DWI is also well known to be temperature dependent. The purpose of this work was to investigate the use of DWI for monitoring the evolution of the acute thermal lesion and to describe the implications for MR thermometry based on diffusion.

All animal experiments were approved by the Administrative Panel on Laboratory Animal Care. The heating was applied for ~16 min using an interstitial high intensity ultrasound applicator in a canine prostate, with the amplifier power ranging from 5 W to 14 W. DWI was performed throughout the whole procedure with a temporal resolution of 30 sec under free breathing, and good correspondence between increased apparent diffusion coefficient (ADC) value and power application was obtained. As shown in Fig a-c, the heated region appeared as elevated ADC value on the ADC trace map. Assuming  $1^{\circ}\text{C}$  temperature change



ADC trace map acquired before heating (a), at the beginning (b) and at the end of the heating (c), and at the end of the whole procedure (d). (e) and (f) are the color coded temperature maps calculated from (b) and (c). There is a clear correspondence between the heated region and the thermal lesion showed on the post-treatment ADC map (d) and the contrast enhanced T1-weighted image (g).

caused a 2.4% change in ADC, the temperature map was calculated and superimposed onto the ADC map (Fig e, f). After the whole prostate returned to body temperature, similar lesions presented on both the ADC trace map and contrast enhanced image (Fig d, g).

However, since the temperature-based ADC increase and the ADC change from tissue damage are competing effects, the calculated ADC-based temperature should be carefully interpreted. These temperature calculations may be accurate at low temperatures. However, the competing effects described here for the core of

the thermal lesion mean that ADC-based temperature does not follow a simple linear relationship. Our future work includes correlating the DWI thermometry to proton resonance frequency method and further investigation of the use of the mixed information in treatment planning.

### REFERENCES/FUNDING SOURCE

ISMRM abstract, 2007

NIH R01 CA077677, R01 CA111981, P41 RR009784, Lucas Foundation.

## PRF Shift Thermometry Using Multiple-acquisition Phase-cycled Balanced SSFP

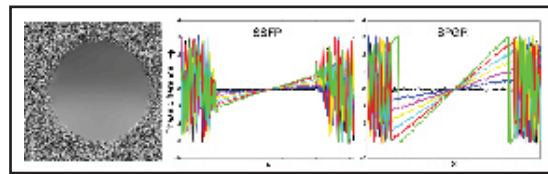
VIOLA RIEKE, BRIAN HARGREAVES, KIM BUTTS PAULY  
DEPARTMENT OF RADIOLOGY

SSFP sequences consist of RF excitation pulses with flip angle  $\alpha$  and phase angle  $\rho$  and have a characteristic magnitude and phase profile. The phase profile is nonlinear with temperature such that SSFP cannot easily be used for temperature imaging with proton resonance frequency (PRF) shift method. Changing the RF and acquisition phase by  $\Delta\rho$  shifts the profiles.

Adding multiple phase-cycled SSFP acquisitions in quadrature gives a relatively flat magnitude profile and, more importantly for PRF thermal mapping, leads to a fairly linear phase profile. If frequency shift maps linearly to a measurable phase shift in the combined image, it can be used for temperature estimation with the PRF shift.

Computer simulations were performed to study the phase behavior (linearity and slope) for different imaging parameters ( $T_1$ ,  $T_2$ , TR, flip) and number of phase cycles ( $n=2-4$ ). MR temperature maps of an agar phantom were acquired at 1.5T with the proposed balanced SSFP sequence and compared to SPGR. A temperature change was simulated by creating a linear field change with the gradient shim in x-direction.

Results of the simulations showed that averaging images acquired at different phase angles gives a linear relation between phase and frequency. The linearity is dependent on the tissue and imaging parameters and number of averages. In general, the amount of ripple in both magnitude and phase decreases significantly as the flip angle increases or as



Phase difference image (left) from a three cycle combination showing the linear phase change in x-direction created by the gradient shim and profiles through the phantom.

the  $T_2/T_1$  ratio decreases [1]. Depending on the tissue parameters more than three averages might be necessary, but in some cases as little as two averages could be sufficient.

The MR imaging results are shown in Fig 1. The results show that the phase profile is linear enough to accurately measure the frequency change introduced by the

gradient shim. Comparing the results to the SPGR acquisition shows that  $\Delta\phi(\Delta T)$  is exactly three times larger in the SPGR images, as expected due to the three times longer TE compared to the SSFP acquisition, but the phase measurement is more noisy. Indeed, the temperature uncertainty  $\sigma T$  in both methods was very similar;  $1.1^\circ\text{C}$  in SSFP and  $1.0^\circ\text{C}$  in SPGR.

The results of simulations and phantom measurements have shown that combining the signals of multiple-acquisition phase-sensitive SSFP acquisitions results in a linear phase profile with frequency and can be used to measure temperature with the PRF shift method. Further studies are needed to evaluate if and in which tissues and applications the proposed method is better suited to monitor temperature than an SPGR sequence.

### REFERENCES/FUNDING SOURCE

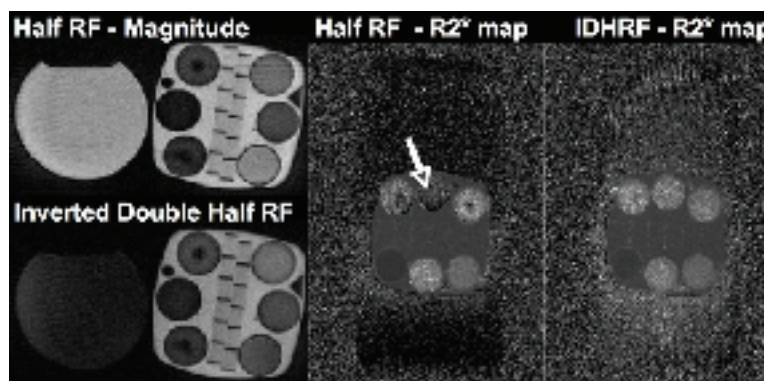
Proceedings of the 15<sup>th</sup> ISMRM, 2007.

NIH RO1 CA 111891, NIH P41 RR009784, NIH RO1 CA077677.

## Inverted Double Half RF for Ultrashort T2 Imaging

SONAL JOSAN<sup>1,2</sup>, JOHN PAULY<sup>2</sup>, KIM BUTTS PAULY<sup>1</sup>, BRUCE DANIEL<sup>1</sup>  
DEPARTMENTS OF <sup>1</sup>RADIOLOGY, AND <sup>2</sup>ELECTRICAL ENGINEERING

Image-guided cryoablation is a promising minimally invasive therapy for prostate cancer. MRI provides the promise of temperature mapping throughout the frozen area to better guide the procedure than the placement of discrete thermocouples. Previous studies have shown the tissue transverse relaxation rate  $R_2^*$  ( $1/T_2$ ) to be relatively linear over the temperature range of interest. In order to quantitate  $R_2^*$  in frozen tissue, half pulses are used to obtain ultrashort echo times (UTE). Their slice profile is sensitive to eddy currents that make it difficult to quantitate  $R_2^*$ . Also, the signal in UTE images is often dominated by long  $T_2$  components, which need to be suppressed to enhance the contrast of the short  $T_2$  species. The purpose of this work is to develop an RF pulse that does slice selective long  $T_2$  suppression while exciting short  $T_2$ , thus making short  $T_2$  imaging and quantitation less sensitive to eddy currents.



Magnitude and  $R_2^*$  images with the half pulse and the inverted double half pulse. The inverted double half pulse suppresses long  $T_2$  signal, and improves  $R_2^*$  measurements.

Experiments were performed on a 0.5T GE Signa SP interventional MR scanner. A phantom containing several short and long  $T_2$  values (0.5-60ms) was imaged with both the half pulse and the inverted double half pulse ( $TE=100\mu\text{s}$ ). The inverted double half pulse suppresses the long  $T_2$ , which improves contrast for the shortest  $T_2$  (Figure).

$R_2^*$  maps were also measured for the short  $T_2$  phantom, with a long  $T_2$  phantom placed next to it in the slice di-

rection. The half pulse  $R_2^*$  image has significant out of slice signal due to eddy current distortions, which corrupts the  $R_2^*$  measurements. The out of slice signal is greatly reduced in the case of the inverted double half RF pulse giving cleaner  $R_2^*$  measurements.

### REFERENCES/FUNDING SOURCE

Inverted Double Half RF for Long  $T_2$  Suppression in Ultrashort  $T_2$  Imaging, ISMRM, 2007. NIH P41 RR09784, NIH RO1 CA092961.

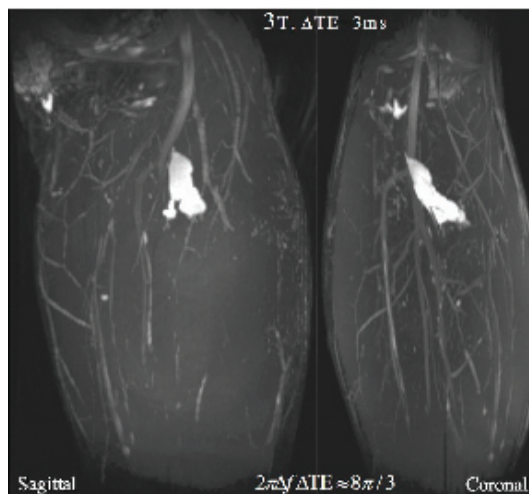


## Multi-Resolution Non-Iterative Field Map Estimation for Water and Fat Separation

W. Lu<sup>1</sup>, G.E. Gold<sup>2</sup>, H. Yu<sup>3</sup>, B.A. HARGREAVES<sup>2</sup>, DEPARTMENTS OF <sup>1</sup>ELECTRICAL ENGINEERING, <sup>2</sup>RADIOLOGY, AND <sup>3</sup>GE RESEARCH

Water and fat separation methods based on chemical-shift induced phase and fast multi-echo sequences are of great clinical interest. Multi-echo sequences, which are less sensitive to subject motion, enable highly SNR efficient water/fat separation. However, increased echo-spacing in multi-echo sequences imposes great challenges on existing Dixon methods, which works less robustly when echo-spacing is long. Hence the application of existing methods is limited with multi-echo sequences: short echo-spacing dictates large readout bandwidth and/or low spatial resolution, hence degraded image quality. In this work we propose a non-iterative field map estimation method that works robustly with multi-echo sequences.

The proposed method consists of two modules. Module I multiple local minima searches limits the search of the field map values within one period. Multiple local minima within a single period are located by applying multiple golden section searches. Upon completion of Module I, each pixel has several possible field map values, of which only one is selected by Module II field map smoothing. Specifically, Module II first identifies a reliable starting pixel of which the field map value is numerically close to the global median of all field map estimates and the spatial location is close to the centroid of



Sagittal and coronal MIP images of a lower-leg study at 3T with long echo-spacing 3ms. Excellent water and fat separation enables depiction of artillery structure (bright residue is a cyst).

the foreground mask. Subsequently the field map is progressively grown such that no abrupt change between neighboring field map values is allowed.

To improve computational efficiency and estimation robustness, the non-iterative method is only applied at the coarsest level of a multi-resolution pyramidal structure, in which each pixel at a coarse level corresponds to a group of 4 pixels at next finer level. Hence a coarse resolution field map is magnified by a factor of 2 as an initial field map for the next finer resolution. Initial field map values are evaluated based on the estimation error. Large error indicates the initial estimate from the coarser level is inaccurate and need to be refined based on its neighboring field map values. This coarse-to-fine field map propagation significantly reduces computational cost and corrects erroneous field map estimates obtained from

the non-iterative method.

The proposed method has successfully separated water and fat for various anatomical regions acquired with multi-echo sequences at both 1.5T and 3T. Fig.1 shows sagittal and coronal maximum-intensity

### REFERENCES/FUNDING SOURCE

American Medical Association  
NIH EB002524 and RR009784.

## Incorporating a Vascular Term into a Reference Region Model for Analysis of DCE-MRI Data

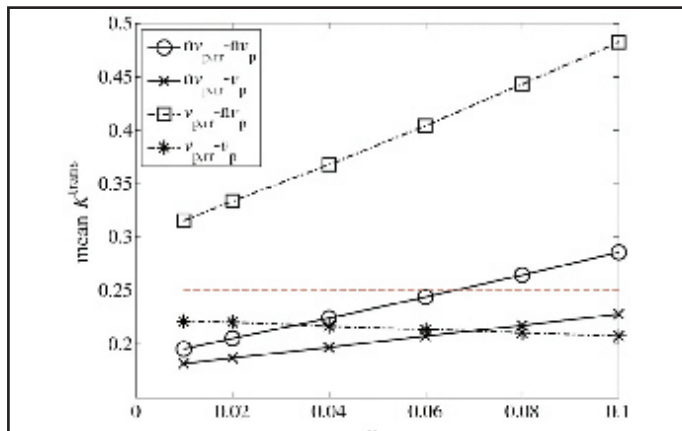
ANTHONY Z. FARANESH<sup>1</sup> AND THOMAS E. YANKEELOV<sup>2</sup>, <sup>1</sup>STANFORD RADIOLOGY, <sup>2</sup>RADIOLOGY AND RADIOLOGICAL SCIENCES, VANDERBILT UNIVERSITY

Dynamic contrast-enhanced MRI can be used to characterize tumor physiology by tracking the movement of contrast throughout tissue. Models have been developed that allow for data analysis without having to characterize the plasma time course. These "reference region" methods do not yet account for the plasma volume contribution, though several investigators have pointed out its significance in tumor studies. In this work we explicitly incorporate a vascular term into the model and analyze its effect on the extracted pharmacokinetic parameters.

Simulations were run to calculate the transfer constant K<sub>trans</sub> using a reference region model to examine the effects of the plasma volume fraction (vp). If vp was excluded from both regions (nvp,rr-nvp), K<sub>trans</sub> was underestimated then overestimated. If vp was excluded from the reference region and included in the tissue of interest (nvp,rr-vp), K<sub>trans</sub> increased with vp, but was underestimated. If vp was included in the reference region and excluded from the tissue of interest (vp,rr-nvp), K<sub>trans</sub> was overestimated by an amount that increased linearly with vp. If vp was included in both regions (vp,rr-vp), K<sub>trans</sub> was slightly underestimated.

The importance of the plasma term in calculating K<sub>trans</sub> and v<sub>e</sub> from the reference region model were analyzed. If the vp term was included in both regions, this resulted in an error of 10-15%. If the vp is not known in the reference region, then it should also be excluded from the tissue of interest calculations. The largest errors re-

sulted if vp was included in the reference region and excluded from the tissue of interest. Planned studies will apply these methods in vivo to directly compare a reference region model incorporating the vascular term to that of a standard arterial input function analysis.



Mean K<sub>trans</sub> vs. vp. True value of K<sub>trans</sub> (0.25) is shown by the red dashed line.

### REFERENCES/FUNDING SOURCE

NIH T32 CA09695



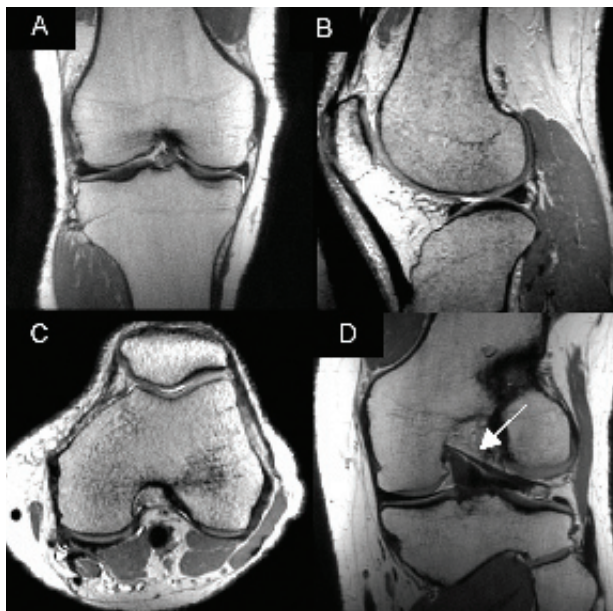
## Isotropic MRI of the Knee at 1.5T with 3D-FSE-XETA (Extended Echo Train Acquisition)

GARRY GOLD, REED BUSSE, KATHRYN STEVENS, ERIC HAN, ANJA BRAU, PHILIP BEATTY,  
CHRISTINA CHEN, SANJAY JOSHI, SHAORONG CHANG, CHRISTOPHER BEAULIEU  
DEPARTMENT OF RADIOLOGY

**Introduction:** MRI with two-dimensional fast spin-echo (2D-FSE) requires multiple acquisition planes because of slice gaps and partial-volume artifacts. Volumetric acquisitions [1] with isotropic resolution overcome these limitations, allowing reformations in arbitrary planes. We developed a 3D isotropic fast spin-echo acquisition using an eXtended Echo Train Acquisition (3D-FSE-XETA) and compared it with conventional 2D-FSE in the knee at 1.5T.

**Methods:** Ten knees of healthy volunteers were imaged in the coronal plane using a GE Signa 1.5T MRI scanner (GE Healthcare, Milwaukee, WI) and an 8-channel knee coil. 3D-FSE-XETA used variable flip angle refocusing to constrain T2-decay over a long echo train [2]. Partial Fourier and auto-calibrated parallel imaging [3] reduced echo train length by 3.4x (78 echoes encode 256 lines). With 1D acceleration, 184 coronal 0.7 mm sections were acquired in 8:40. Two-dimensional parallel imaging acceleration was then used to reduce scan time to 5:07 (104 TRs encode 184 slices). Image reconstruction took 90 seconds for 2D acceleration. Coronal 2D-FSE images were acquired with 2 mm slices and a 0.5 mm gap, 3 acquisitions, echo train length 8, and a scan time of 5:27.

All scans had the following parameters: TR/TE 3000/35ms, 256x256 matrix, 17 cm field-of-view, and bandwidth  $\pm 31$  kHz. 2D-FSE was acquired in the axial plane for comparison with reformats of the 3D data, and both 2D-FSE and 3D-FSE-XETA were acquired with and without fat suppression. For each method, the signal-to-noise ratio (SNR) was measured in cartilage, muscle, and joint fluid. A paired t-test



3D-FSE-XETA images of a healthy volunteer showing a coronal source image, sagittal and axial reformats, and an oblique reformat demonstrating the Ligament of Wrisberg.

was used to compare SNR.

**Results:** Cartilage SNR (Figure 1) was significantly higher using 3D-FSE-XETA with one-dimensional acceleration ( $52 \pm 9$ ) than the 2D-FSE ( $30 \pm 10$ ;  $p < .01$ ). Muscle SNR ( $44 \pm 10$ ) with 3D-FSE-XETA with one-dimensional acceleration was also significantly higher than 2D-FSE ( $22 \pm 3$ ;  $p < .01$ ). Fluid SNR was also higher using 3D-FSE-XETA ( $118 \pm 10$ ) with one-dimensional acceleration than 2D-FSE ( $78 \pm 18$ ;  $p < .01$ ).

Cartilage, muscle, and fluid SNR using 3D-FSE-XETA with two-dimensional acceleration was not statistically different than 2D-FSE ( $p > .07$ ). 3D-FSE-XETA allowed reformation of the images in arbitrary planes (Figure 2). The axial reformations of the 3D-FSE-XETA images were similar to the directly acquired 2D-FSE data, except the 3D-FSE-XETA had much thinner slices. Fat suppression was uniform

on all sequences, and no significant blurring was seen on the 3D-FSE-XETA images.

**Discussion:** Isotropic data from 3D-FSE-XETA allows for reformations in arbitrary planes, making multiple 2D acquisitions unnecessary. Slice thickness is up to 7 times less than 2D-FSE, decreasing partial-volume artifacts. 3D-FSE-XETA is promising high-resolution MR imaging technique which may improve depiction of complex knee anatomy.

## REFERENCES/FUNDING SOURCE

Gold, et al. *Am J Roentgen*, In Press 2007.  
NIH EB 002524, NIH EB005790, GE Healthcare

## In Vivo T2, T1r, and Sodium Imaging of Articular Cartilage at 3.0T: Initial Experience

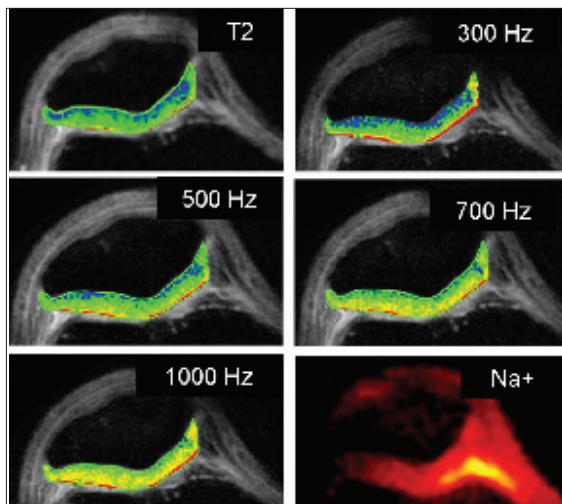
GARRY GOLD<sup>1</sup>, NEAL BANGERTE<sup>1</sup>, ERNESTO SAROSWIECKI<sup>1</sup>, ERIC HAN<sup>2</sup>, PAUL GURNEY<sup>2</sup>, GRAHAM WRIGHT<sup>2</sup>, BRIAN HARGREAVES<sup>1</sup>DEPARTMENTS OF <sup>1</sup>RADIOLOGY AND <sup>2</sup>ELECTRICAL ENGINEERING

Detection of matrix changes of articular cartilage in early osteoarthritis is important for drug discovery. We studied the feasibility of comparing T2, T1r, and sodium imaging in healthy volunteers and one subject with knee pain at 3.0T. T2 mapping was done with a T2-prepared spiral method. T1r imaging was performed using a continuous spin-lock pulse at several locking frequencies. Sodium imaging was done with a custom surface coil and a short echo-time 3D cones trajectory. Our results indicate it is feasible to compare these methods in vivo at 3.0T for early cartilage matrix changes. Introduction: Early detection of proteoglycan depletion in cartilage is important in development of treatments for osteoarthritis. T1r imaging, or relaxation

of spins under the influence of a radio-frequency field, has been shown to be sensitive to changes in the cartilage matrix [1-2]. T2 mapping is thought to reflect changes in the collagen matrix of cartilage [3]. Sodium imaging has also been used to measure proteoglycan content in cartilage [4-5]. We studied the feasibility of using these techniques in vivo at 3.0T.

Methods: Four volunteers (ages 34-43) were imaged in the axial plane at 3.0T on a GE Signa MRI (GE Healthcare, Milwaukee, WI) using 3-inch coil. One volunteer had a history of anterior knee pain. Measurements of T1r were made with a continuous RF spin locking pulse at the same anatomic locations with spin lock frequencies of 300, 500, 700 and 1000 Hz. The maximum spin-lock frequency in the continuous RF sequence was limited by RF power deposition limits. T2 relaxation time at the same location was measured using a T2-prepared spiral sequence. The T1r and CPMG T2 sequences had identical imaging parameters: TR of 2000 ms, 14 spiral arms, 4096 points, and bandwidth +125 kHz. In-plane resolution was 0.7 mm with a 16 cm FOV, 4 mm slice thickness. A single slice through the patella cartilage was acquired in 5 minutes with two signal averages. The T1r sequences acquired 4 spin lock times (TSL) of 3, 15, 35, and 80 ms. The CPMG T2 sequence acquired 6 echoes at approximately 6, 17, 28, 49, 71 and 92 ms.

Sodium imaging was performed with a custom 3-inch surfaces



*This image demonstrates in vivo results with T2, T1rho at different spin lock frequencies, and sodium imaging in the same volunteer.*

coil and a short echo time “cones” trajectory [6-7]. Sodium acquisitions were obtained at a voxel size of 1.25x1.25x4 mm. Parameters for the scan were: TR/TE = 50/0.6 ms, FOV = 16x16x12.8cm, matrix = 128x128x32, readout time = 8 ms, alpha = 70 deg, and 16 averages for a total scan time of 17 min 8 s.

T1p and T2 relaxation times for each subject were measured in 10 cartilage locations on the medial and lateral patella facets. Sodium SNR was also measured in 10 locations on the medial and lateral facets, and in an area of increased relaxation times in the subject with knee pain. Relaxation measurements and maps were created using Osirix software [8].

Results: Across the range of spin lock frequencies, T1r values significantly increased with spin lock frequency (Figure 1). Measured T1r relaxation times significantly increased from 300 Hz to 500 Hz ( $p < .01$ ), from 500 Hz to 700 Hz ( $p < .01$ ), and from 700 Hz to 1000 Hz ( $p < .01$ ). This is also seen on the color maps of relaxation times in healthy volunteers (Figure 1). An area of probable cartilage damage near the apex of the patella was identified by increased T2 relaxation times and elevated T1r values in the subject with knee pain (Figure 2). Sodium images from this region showed significantly lower SNR ( $12.3 \pm 0.7$  vs.  $10.3 \pm 0.5$ ;  $p < .05$ ) compared with the lateral facet in that subject which had similar relaxation times and sodium values to the healthy volunteers.

Conclusion: This study demonstrates that comparison of T1r imaging, T2 mapping, and sodium imaging is feasible in vivo on a clinical 3.0T scanner. The optimum spin lock frequency may be higher than achievable with RF power deposition limits at 3.0T. The sodium imaging results were uniform in all healthy subjects, and showed decreased signal in the area of increased T2 and T1r relaxation times. Further studies with these methods in subjects prior to total knee replacement will enable the comparison of cartilage histology with imaging results.

## REFERENCES/FUNDING SOURCE

NIH EB 002524, NIH EB 005790, GlaxoSmithKline Inc.

# Chemical Shift Correction in Bipolar Multi-Echo Sequences for Water and Fat Separation

W. LU<sup>1</sup>, S.B. REEDER<sup>2</sup>, B. DANIEL<sup>2</sup>, B.A. HARGREAVES<sup>2</sup>, DEPARTMENTS OF <sup>1</sup>ELECTRICAL ENGINEERING AND <sup>2</sup>RADIOLOGY

The main disadvantage of water and fat separation methods based on chemical-shift induced phase, such as multi-point Dixon methods, is long scan time and suboptimal SNR efficiency. To improve imaging efficiency and reduce motion induced artifacts, multi-echo sequences have been developed to acquire images at different echo times in a single repetition interval (TR). In this case the echo-spacing depends on spatial resolution and readout bandwidth; hence the echo-spacing can be long even at a medium bandwidth, which leads to less robust field map estimation. Both improved imaging efficiency and more robust field map estimation can be achieved by acquiring data using a “bipolar multi-echo” sequence (Fig. 1).

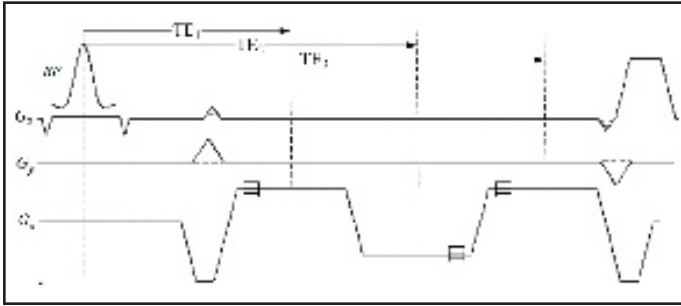


Fig. 1. Diagram of a bipolar multi-echo sequence. The time instances when  $s_n(k_x, k_y)$  ( $n=1, 2, 3$ ) are sampled are marked with symbols.

After time reversal of the second echo, the alternating readout polarity results in misalignment between even and odd echoes due to gradient delays and eddy currents that need to be corrected for. More importantly, the chemical-shift induced misregistration between water and fat exists in opposite readout directions between even and odd echoes. In this work we demonstrate a method that effectively eliminates such chemical-shift induced artifacts in separated water/fat images.

The proposed method consists of two steps:

1) *Field map estimation using low-resolution image data:* This step exploits the fact that field maps are smoothly varying and the fat signal shift can be neglected at low resolution. We obtain low-resolution images by low-pass filtering the k-space data along the readout direction. Subsequently from the low-resolution image data a field map is estimated.

2) *Water and fat separation using field map corrected k-space data:* After demodulating the field map, the field map corrected image data is transformed back to k-space. The water and fat separation in k-space is done by solving the least-squares solutions of  $s_w$  and  $s_f$ . The k-space water-fat separation eliminates the phase factor due to the chemical shift  $\Delta f_{cs}$ , which is the source of the chemical-shift induced artifacts. The separated water and fat images are the Fourier transforms of  $s_w$  and  $s_f$  respectively.

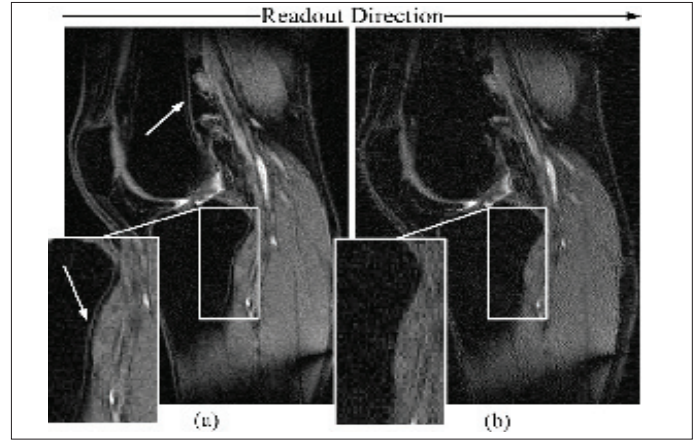


Fig. 2. Chemical-shift induced artifacts are identified with boxes in the water image (a) obtained using an existing separation method. (b) shows the water image obtained using the proposed method, which eliminates the artifacts.

Bipolar multi-echo sequences offer many advantages such as high SNR efficiency, reduced echo-spacing compared to multi-echo sequences, and reduced motion induced artifacts. We proposed a method that resolves the associated opposite fat/water signal shifts in even and odd echoes by using a robust field map estimation followed by a least-squares water and fat separation in k-space. In short, the proposed method enables bipolar multi-echo sequences to achieve fast and efficient scanning with robust water and fat separation.

REFERENCE/FUNDING SOURCE  
NIH EB002524 and RR009784.



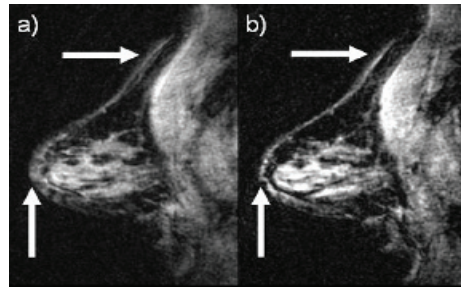
## Linear Off-resonance Correction for Partial-k-space 3D Spiral Imaging

KRISTIN L GRANLUND<sup>1,2</sup> AND BRIAN A HARGREAVES<sup>2</sup> - <sup>1</sup>RADIOLOGY, <sup>2</sup>ELECTRICAL ENGINEERING

3D stack-of-spiral scans of large or multiple volumes can benefit significantly from slice-by-slice off-resonance correction when the field inhomogeneity varies enough that linear shimming is insufficient. When higher temporal resolution or shorter scan times are desired, partial k-space acquisition can be used in the phase-encoding (z) direction followed by a homodyne reconstruction. Linear off-resonance correction must be applied in kx-ky-z space and homodyne is typically applied in x-y-kz space; this approach integrates the two algorithms.

Linear off-resonance correction and partial k-space reconstruction are not separable, but they can be combined by performing the steps in the appropriate order. Because in-plane linear off-resonance correction can be performed on each slice individually with only minor extra computation, we can also correct for an arbitrary (i.e., not necessarily linear) variation in z. This work presents a modified homodyne algorithm with in-plane linear off-resonance correction for partial 3D spiral data sets.

Field maps are created for each slice using the phase difference between the two images collected with the fat and water signals in phase.



Phantom image reconstructions using a) full k-space and uncorrected data b) 5/8 k-space and corrected data. The images demonstrate that the field map correction produces sharper edges, while the observed SNR does not differ significantly between the images.

The field variations are approximated with constant and linear terms. The modified homodyne algorithm begins with an IFFTz performed on both the symmetric k-space data and the weighted partial k-space data. The k-space trajectory is modified according to the field map estimation to compensate for linear variation, and then used to grid both the symmetric and weighted data before each is Fourier transformed in kx/ky. Finally, the weighted partial k-space data is demodulated by the phase of the symmetric reference, and the real part taken as in standard homodyne reconstruction.

We have demonstrated a simple procedure to combine linear off-resonance correction with homodyne reconstruction for partial k-space 3D spiral data acquisitions. This algorithm should prove to be very useful in studies where the field inhomogeneity is considerable across the imaging volume and linear shimming is unlikely to sufficiently correct the local variations in z.

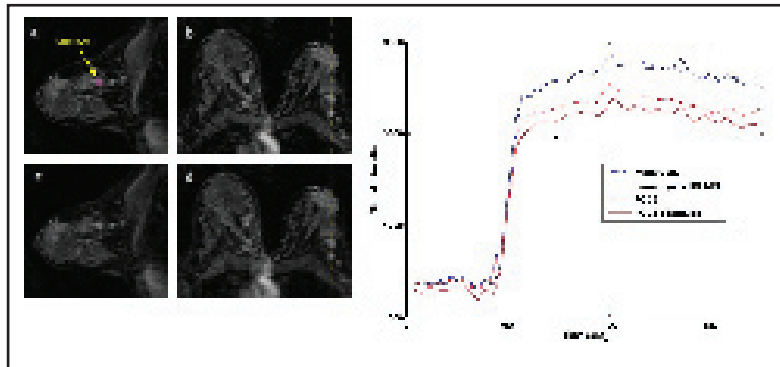
FUNDING SOURCE: NIH Grant RR009784, Richard M. Lucas Foundation

## Accelerated Bilateral DCE 3D Spiral Breast Imaging Using TSENSE and Partial Fourier Methods

<sup>1,2</sup>MISUNG HAN, <sup>1</sup>BRUCE L. DANIEL, <sup>1</sup>BRIAN A. HARGREAVES, DEPARTMENTS OF <sup>1</sup>RADIOLOGY, AND <sup>2</sup>ELECTRICAL ENGINEERING

Dynamic contrast breast MRI requires both high temporal and spatial resolution. To increase temporal resolution in bilateral breast imaging which needs to cover two breast volumes, we combine rapid 3D spiral imaging and temporal sensitivity-encoding (TSENSE) acceleration. TSENSE allows for estimation of sensitivity maps from acquired data.

By using a GE 1.5 T Excite scanner and an 8 channel "VIBRANT" phased-array breast coil, we have scanned 60 patients with the injection of Gd-DTPA during a scanning. To excite both breasts, a dual-band spectral-spatial pulse [3] was used, providing robust fat suppression and phase modulation [4]. For the readout, 3D spiral imaging was used with the TSENSE acceleration in the slab direction. With an acceleration factor of 2, phase-encode planes were acquired in a time-interleaved manner, alternating between even and odd planes. For the reconstruction, spiral gridding and off-resonance correction, followed by sensitivity encoding (SENSE), were applied in the right-left direction. Sensitivity maps were estimated by averaging several temporal frames. To reduce any error on sensitivity maps by rapid signal enhancement, sensitivity maps to reconstruct pre-contrast frames were estimated using data from pre-



(a-b) One sagittal and axial slice reconstructed from homodyne + TSENSE and (c-d) POCS + TSENSE. (e) Signal enhancement curves of tumor measured in a ROI located in (a) with TSENSE and without TSENSE.

contrast frames, and sensitivity maps for post-contrast frames were estimated using data from late post-contrast frames.

The images show two unfolded sagittal slices which are FOV/2 apart, and an axial reformat from the TSENSE reconstruction and the signal enhancement curves measured in a ROI in a tumor from the original and accelerated images. The improvement in temporal resolution with TSENSE over non-accelerated reconstruction is reflected by the steeper initial slope on the enhancement curve.

By combining TSENSE with 3D spiral imaging, temporal resolution of 10 s and spatial resolution of 1.1 x 1.1 x 3 mm<sup>3</sup> can be achieved in bilateral breast imaging. Currently, we are comparing the diagnostic accuracy of TSENSE DCE data with non-accelerated DCE data. In the future, we will investigate higher acceleration factors.

REFERENCES/FUNDING: This work was supported by NIH 2P41RR009784-11 and NIH 5R01CA066785-08

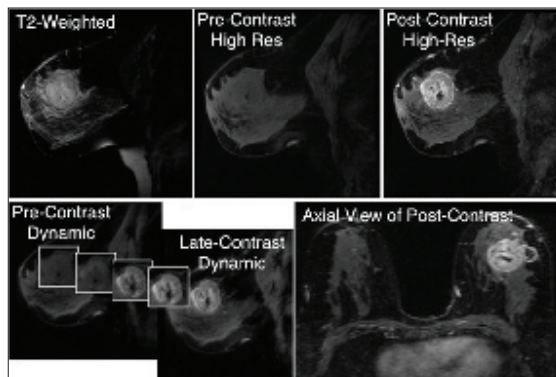
M. Han, B. L. Daniel, B. A. Hargreaves, Accelerated Bilateral DCE 3D Spiral Breast Imaging using TSENSE and Partial Fourier Methods. . 15th ISMRM Meeting 2007, P.3359.

## Clinical Bilateral Breast MRI at Stanford

BRIAN A. HARGREAVES<sup>1</sup>, MISUNG HAN<sup>1</sup>, MARCUS T. ALLEY<sup>1</sup>, PHILIP J. BEATTY<sup>2</sup>, ANJA S. BRAU<sup>2</sup>, BRUCE L. DANIEL<sup>1</sup>  
<sup>1</sup>RADIOLOGY AND <sup>2</sup>GENERAL ELECTRIC HEALTHCARE

Breast cancer is the second leading cause of mortality in women. The American Cancer Society now recommends MR mammography for women who are at 25% or greater risk of breast cancer. Bilateral breast MRI is favored as it allows direct comparison between breasts, because cancer in one breast significantly increases risk of a contralateral cancer, and because it reduces by two the number of MRI exams each woman must undergo. Over 5000 high-quality unilateral dynamic contrast-enhanced breast MRI exams have been performed at Stanford over the last decade. The goal of this work was to implement a fully-bilateral MRI protocol, without sacrificing the high image quality or increasing scan times.

The breast MRI protocol begins with 5-minute axial T1-weighted spin echo images that can be used as a scout scan. T2-weighted fat-suppressed fast spin-echo scans are interleaved, covering both breasts in 7 minutes. A dynamic bilateral 3D spiral time series is used to resolve temporal dynamics of contrast uptake following injection. This is combined with high-resolution 3D T1-weighted scans pre- and post-contrast, and a 2nd series of dynamic spiral images during



Sample images showing a large tumor. Top: T2 and high-resolution pre- and post-contrast images show tumor structure. Bottom: Dynamic enhancement series shows the spatio-temporal uptake pattern, while an axial post-contrast view shows full bilateral coverage.

contrast washout, to show spatial and temporal contrast uptake features in lesions and help assess malignancy. The dynamic spiral images use a combination of advanced excitation pulses and temporal sensitivity encoding to image a full 3D volume over both breasts every 10 seconds. High-resolution images allow sub-millimeter resolution over the same volume in 6 minutes, using auto-calibrating reconstruction for Cartesian imaging (ARC).

Over two months, approximately 118 patients have been scanned at the hospital using this protocol, without loss of image quality. We expect this number to rise to approximately 25 patients per week, and later increase with the opening of

Stanford's new outpatient facilities. We will continue to work to further improve image quality, and both spatial and temporal resolution of the dynamic scanning, as well as implementing a similar protocol at 3T.

## REFERENCES/FUNDING SOURCE

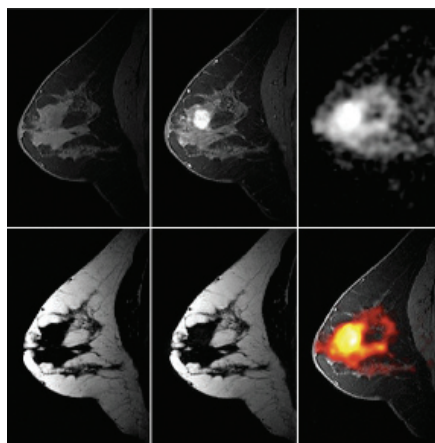
This work was supported by the NIH, GE medical systems and the Richard M. Lucas Foundation.

## Sodium and Proton Breast MRI

BRIAN A. HARGREAVES<sup>1</sup>, NEAL K. BANGERTER<sup>2</sup>, ERNESTO STAROSWIECKI<sup>2</sup>, BRUCE L. DANIEL<sup>1</sup>  
<sup>1</sup>DEPARTMENT OF RADIOLOGY, STANFORD UNIVERSITY, <sup>2</sup>GE HEALTHCARE

Dynamic contrast enhanced (DCE) proton MRI is the current standard MR method for detection and characterization of breast tumors, providing information about tumor vasculature and excellent delineation of tumor. Sodium MRI has recently been suggested as a novel and potentially very useful component in improving the specificity and sensitivity of breast MRI. Sodium MRI detects tumors through pathophysiologic mechanisms complementary to proton MRI techniques, resulting in signal increases of up to 400% in tumors compared with normal tissue.

Sodium MRI has historically been difficult due to low concentration and lower polarization of sodium. However, though a combination of efficient pulse sequences, high field strength (3.0T) and sensitive receive coils, we are able to achieve 2x2x4 mm resolution over the breast in reasonable scan times (15-20 minutes). We have compared sodium imaging to standard DCE breast imaging in 4 patients using a dual-tuned (water and sodium) coil. The total protocol takes



Example images in a patient with a breast tumor. Left: pre-contrast water (top) and fat (bottom) images. Center: post-contrast water (top) showing tumor enhancement and fat (bottom). Right: Sodium image (top) and overlaid sodium/post-contrast water image (bottom) show high correlation between elevated sodium and increased enhancement.

approximately 60 minutes, and includes sodium imaging combined with T1-weighted, T2-weighted and DCE proton imaging. Example images in a patient with breast cancer are shown below. The tumor, clearly shown in contrast enhanced images, shows significantly increased sodium signal. More interestingly, the sodium levels are elevated outside the enhancing portion of the tumor, suggesting a potentially complementary marker of tissue abnormality.

We are currently developing a protocol to quantify sodium levels on a voxel-by-voxel basis. We will then study sodium levels in patients known to have breast cancer, to determine the feasibility of sodium MRI for improved detection and classification of breast cancer, as well as prediction of response to different therapies.

## REFERENCES/FUNDING SOURCE

This work was supported by the NIH, California Breast Cancer Research Program, GE medical systems and the Richard M. Lucas Foundation

## BOLD Contrast in the Breast at 3T with Heart Saturation

REBECCA RAKOW-PENNER, LAURA PISANI, BRUCE DANIEL, GARY GLOVER, DEPARTMENT OF RADIOLOGY

The beating heart is a source of significant noise in breast MRI imaging. By diminishing the noise from this source, image quality improves for both BOLD contrast images as well as standard contrast-enhanced images. We developed a breast heart saturation sequence applied to BOLD imaging, and in the near future plan to apply the saturation pulse to a standard breast MRI protocol. We are particularly interested in exploring BOLD contrast in the breast because it may help improve the specificity of MRI in detecting breast cancer.

We are developing the technique on healthy volunteers. Results at 1.5T proved promising and in hope of increased BOLD signal, we conducted the study at 3T. The protocol was similar as at 1.5T, with a few slight changes (3T-- GE Healthcare, Waukesha, WI, 7 channel breast coil -- MRI Devices, Waukesha, WI, TE = 30 ms, TR = 1.2 s, Flip

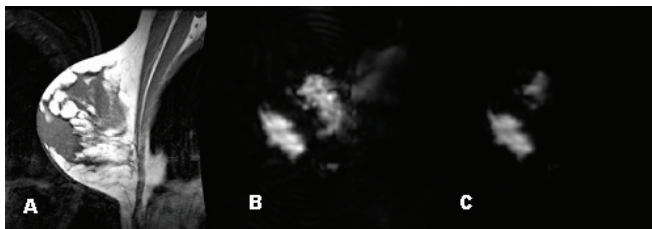


Figure. (A) Anatomical image at 3T. (B) Raw BOLD contrast image at 3T without heart saturation (C) with heart saturation

Angle = 60, Bandwidth = 125 kHz, matrix size = 80 x 80, FOV = 20, Slice Thickness/Spacing = 5 mm/ 5 mm, 1 interleave, 12 slices, 600 time frames/slice). The stimulus consisted of block breathing of pure oxygen over 12 minutes with the following pattern: 1 minute room air, 3 minutes pure oxygen, 3 minutes room air, 3 minutes pure oxygen, 2 minutes pure air.

The experiment was conducted on one healthy volunteer at 3T. Heart saturation played a significant role in decreasing insignificant signal. Future studies include testing this protocol on 4 more healthy volunteers at 3T and then begin testing the protocol on cancer patients.

### REFERENCES/FUNDING SOURCE

DOD pre-doctoral breast cancer fellowship, P41-09784

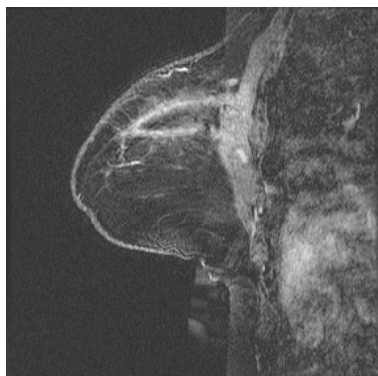
## Characteristic Breast MRI Findings After Accelerated Partial Breast Irradiation.

KRISTINA L. JONG<sup>1</sup>, KATHLEEN C. HORST<sup>2</sup>, DEBRA M. IKEDA<sup>1</sup>, MAURICE VAN DEN BOSCH<sup>1</sup>, SUNITA PAL<sup>1</sup>, ROBERT HERFKENS<sup>1</sup>, BRUCE L. DANIEL<sup>1</sup>, FREDERICK M. DIRBAS<sup>3</sup>, DEPARTMENTS OF <sup>1</sup>DIAGNOSTIC RADIOLOGY, <sup>2</sup>RADIATION ONCOLOGY, AND <sup>3</sup>SURGERY

**Background:** Accelerated partial breast irradiation (APBI) is an emerging treatment option for selected women with limited early stage breast cancer after breast conserving surgery (BCS). APBI using Intra-Operative Radiotherapy (IORT) or Three-Dimensional Conformal External Beam Radiation (3D-CRT) limits the radiation field to the breast cancer tumor bed. In contrast to whole breast irradiation (WBI) which takes 6 to 7 weeks, IORT or 3D-CRT occurs over a short period of time (15 intra-operative minutes or 5 days, respectively), potentially offering increased use of BCS and reduced treatment-related morbidity. APBI leaves untreated breast tissue outside the irradiated field. The high sensitivity of MRI for cancer could be harnessed to detect early in breast tumor recurrence (IBTR) or new primary carcinoma in the non-irradiated tissue. It is important, therefore, to characterize the typical appearance of the breast on MRI after APBI.

**Purpose:** To characterize and describe typical or unique breast MRI appearances after APBI (IORT or 3D-CRT).

**Methods:** We reviewed records of 9 patients with Stage 0 or 1 breast cancer enrolled on an IRB-approved protocol evaluating lumpectomy or re-excision lumpectomy and APBI who also underwent pre- and post-APBI MRIs. APBI was performed with 17 Gy IORT using a 200 kV intra-operative orthovoltage unit (IORT, 5/9 patients, 55%) or post-operative external-beam irradiation delivering 385 cGy twice daily for 5 days (3D-CRT, 4/9 patients, 44%) delivered to the tumor bed and margin. MRIs and post-biopsy/APBI mammograms were reviewed by two MQSA-certified radiologists experienced in breast MRI who



Sagittal post-contrast 3DSSMT after 3D-CRT showing a cylindrical fluid-containing post-surgical cavity extending to the chest wall with susceptibility artifact in the surgical tract.

evaluated skin thickening, breast edema, post-surgical changes, pectoralis muscle enhancement and susceptibility artifacts (MRI only).

**Results:** Between 1/14/04 and 8/22/06, 9 women qualified for the study, and had MRIs 3-100 days (mean, 39 days) before APBI and 168-483 days (mean, 271 days) after APBI. Post-APBI MRIs showed striking, characteristic parenchymal changes which extended from the skin to the chest wall in every case. The post-surgical changes ranged from cylindrical distortion or cavity, sometimes containing fluid, to a thin linear scar. There was relative absence of generalized skin thickening often seen after whole breast irradiation. In addition, 77% (7/9 patients) had susceptibility artifacts in either the tumor bed or surgical tract without metallic artifacts on the mammograms (4 IORT, 3 3D-CRT), 56% (5/9 patients, 3 IORT and 2 3D-CRT) had focal skin thickening, and 44% (4/9 patients, 2 IORT and 2 3D-CRT) had focal pectoralis muscle enhancement.

**Conclusion:** MRI after IORT or 3D-CRT results in characteristic post-treatment changes which extend from the skin to the chest wall. Radiologists should be aware of this novel treatment approach and recognize the characteristic MRI appearance of the APBI field in order to accurately detect treatment field recurrences, as well as the development of new primary carcinoma elsewhere in the breast.

### REFERENCES/FUNDING SOURCE

The Stanford APBI trial is funded in part the Vadasz Family Foundation, the Northern California Chinese Unit of the American Cancer Society, as well as the Chung-Sie Hsiao Fund

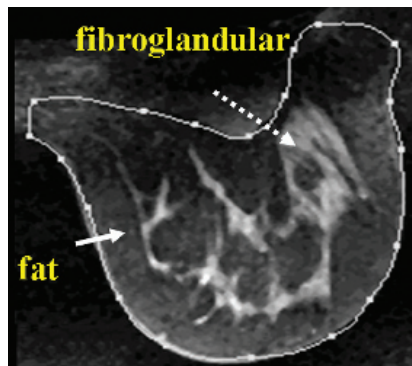


## MRI of the Breast: Quantification of Breast Density and Background Enhancement in Healthy Volunteers

AVA KWONG<sup>1</sup>, CATHERINE KLIFA<sup>2</sup>, GLADYS LO<sup>5</sup>, MAURICE A.A.J. VAN DEN BOSCH<sup>3</sup>, BRUCE L. DANIEL<sup>3</sup>, NOLA HYLTON<sup>2</sup>, DEBRA M. IKEDA<sup>3</sup> DEPARTMENTS OF <sup>1</sup> SURGERY, <sup>2</sup> UCSF RADIOLOGY, <sup>3</sup> STANFORD UNIVERSITY RADIOLOGY, AND <sup>5</sup> RADIOLOGY, HONG KONG SANATORIUM AND HOSPITAL

Quantification of breast density is important for two reasons. First, it is used to indicate the relative sensitivity of the mammographic examination for detection of breast cancer, which is lower in patients with dense breasts. Second, there is an association between increased mammographic breast density and increased breast cancer risk. MRI is increasingly used for imaging and staging of breast cancer patients. There is limited knowledge on the relationship of quantification of mammographic density and MRI breast density and its relationship with background enhancement.

We compare the quantitative assessment of mammographic breast density and correlate it with quantitative assessment of MRI breast density. In addition, a semi-automated method was developed for assessment of breast density. The amount of background enhancement on breast MRI and its relationship to breast density is assessed.



*Example of breast density scoring: density scored on mammography as 25-50% (scattered fibroglandular), MRI density 3D 25-50% scattered fibroglandular and MRI density after 3D segmentation: volume of fibroglandular tissue / volume whole breast = 0.18 (<25% fatty).*

37 Mammography films and Breast MRI scans of 36 healthy female volunteers were scored for both mammographic and MRI breast density using both subjective quantitative method and semi-automated method. The MRI background enhancement was also scored and correlated with breast density.

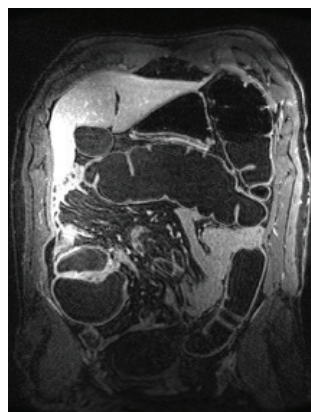
Mammographic BI-RADS breast density score, a 2-D scoring method tends to over-estimate the amount of fibroglandular tissue compared to whole breast volume -3D score using MRI assessment. Based on our study results we hypothesized that 3D MRI density quantification is a more reliable method for breast density assessment. To allow reproducible 3D MRI breast density measurements we developed a semi-automatic quantification method. Our study also shows that there was no relation between breast density and amount of background enhancement in healthy volunteers.

REFERENCES/FUNDING SOURCE  
ISMRM, 2007.

## MR Colonography at 3T using 1D- and 2D- Accelerated Autocalibrated Parallel Imaging

LEWIS K SHIN<sup>1</sup>, BRIAN HARGREAVES<sup>1</sup>, CHRISTOPHER BEAULIEU<sup>1</sup>, ROBERT HERFKENS<sup>1</sup>, SUBHAS BANERJEE<sup>2</sup>, ANJA C BRAU<sup>3</sup>, THEODORE STEGER<sup>4</sup>, PHILIP J. BEATTY<sup>3</sup>, AND R. BROOKE JEFFREY<sup>1</sup>, DEPARTMENTS OF <sup>1</sup> RADIOLOGY, AND <sup>2</sup> GASTROENTEROLOGY, STANFORD UNIVERSITY, <sup>3</sup> GLOBAL APPLIED SCIENCE LAB, GE HEALTHCARE, MENLO PARK, CA, <sup>4</sup> GE HEALTHCARE, WAUKESHA, WI

Magnetic Resonance Colonography (MRC) in recent years is gaining favor as a viable alternative to traditional CT colonography. Proponents of MRC favor the lack of ionizing radiation along with the excellent safety profile of MR intravenous contrast, which can further characterize colonic lesions. The challenge of MRC is to acquire high-resolution volumetric images spanning the full extent of the colon within a reasonable breathhold time. The purpose of this study was to investigate the feasibility of performing MRC at 3T using 1D- and 2D-accelerated autocalibrated parallel imaging. We hypothesized that parallel imaging acceleration could permit increased spatial resolution and anatomic coverage, while SNR losses from parallel imaging would be partially offset by the additional SNR available at 3T. Seven MRC patients were recruited from a high-risk screening population for optical colonoscopy (OC) who had prior polyps or a family history of colon carcinoma. 1D- and/or 2D-accelerated 3D T1-weighted fat-suppressed spoiled gradient echo data was acquired in the oblique coronal plane before and after intravenous contrast administration. For 1D-acceleration scans, data acquisition was accelerated by 1.9x in the phase-encode direction for a 44-s breath-hold. For 2D-acceleration scans, data acquisition was accelerated in both the phase- and depth-encode directions for a net acceleration of 3x and a 31-s breath-hold. All parallel imaging reconstruction was performed on-



*2D-accelerated postcontrast, dark-lumen 3D T1-weighted MRC examination demonstrating excellent image quality and reduced blurring.*

line using an autocalibrated parallel imaging technique called ARC (Autocalibrating Reconstruction for Cartesian sampling). Typical imaging parameters for the T1-weighted gradient echo scans covered a 42x34x18cm volume with acquired voxel size of 1.3 x 0.8 x 1.9 mm<sup>3</sup>.

Initial experience with 2D-accelerated MRC images suggests that image quality is superior to 1D-accelerated images, likely due to shorter scan times with reduced artifacts from peristalsis and/or less motion artifacts due to improved breathhold compliance with no appreciable degradation of image quality or SNR. Initial experience with 2D ARC is very promising as it may allow clinically feasible breathhold times for reduced motion artifact without sacrificing spatial resolution or anatomic coverage. Nine adenomatous diminutive polyps (<6mm) were found at OC with only the largest polyp (5mm) identified prospectively with MRC. As preliminary results are promising, ARC and 3T MRC may become a viable alternative to virtual CT colonography and optical colonoscopy for screening.

Larger studies and further research including fecal tagging and minimal cathartic preparations to improve patient compliance are necessary.

REFERENCES/FUNDING SOURCE  
CA09695 - T32 Advanced Techniques for Cancer Imaging  
CA72023 - Three Dimensional CT Colonography

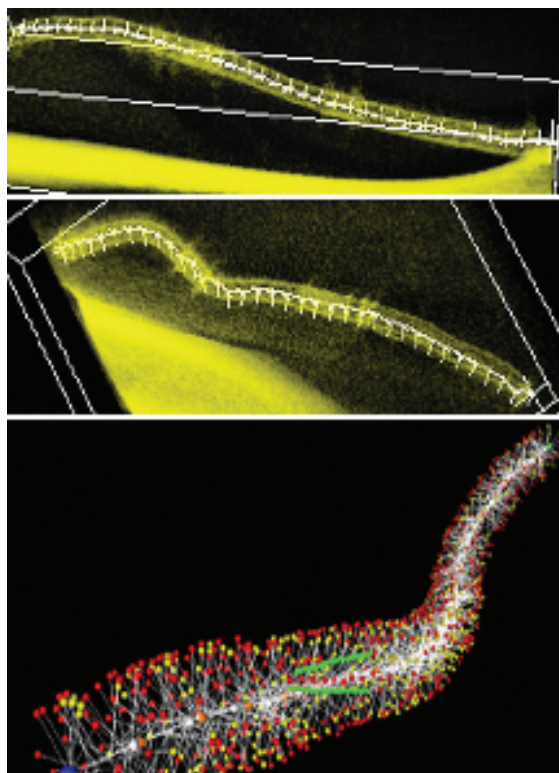
## Angular distribution of Bremsstrahlung X-rays

ARUNDHUTI GANGULY AND NORBERT PELC, DEPARTMENT OF RADIOLOGY

We have analyzed the angular dependence of Bremsstrahlung x-rays resulting from high energy electrons hitting a tungsten(W) target. This is important in optimizing x-ray tube design for increased x-ray flux. Novel imaging technologies using carbon nanotubes or scanning electron beams are being reported<sup>1, 2</sup>. While these have advantages, they are photon starved and could benefit from such strategies.

The angular distribution of x-rays resulting from single interaction of a high energy electron with a single-atom target is a function of the incident-electron energy, direction and target material<sup>3, 4</sup>. We performed Monte Carlo(MC) simulations for studying how this angular distribution is affected by multiple interactions of the electrons and photons in thick targets. The theoretical distribution for single-atom interaction was verified using a 4nm tungsten sphere. For the thick target, the electron gun was positioned at various angles (20°, 40°, 80°, and 90° measured from the surface) to a 4mm thick target.

For single interactions, the theoretical peak for 120keV electrons occurs at 28° and is 8.2 times higher than the minimum value. Corresponding values from MC simulations were 7° and 9.8, respectively. These discrepancies arise from the low energy interpolation of physical processes in the MC tool which are typically optimized for high energy physics. For the solid target, the



Angular distribution of reflected x-rays from a 4mm thick tungsten(W) target for different angles of incidence  $\theta$

output is highest at 180° to the electron beam which is incident at 90° to the target, with the peak location remaining unchanged with angulations. The angular distribution is dominated by target x-ray attenuation. However as the incidence angle decreases, there is an increased asymmetry in the reflected x-ray spectrum. The maximum difference between the reflected photons in the two quadrants is 8.8% for electrons incident at 20°.

Future work will involve evaluation of the contributions of the individual processes undergone by the electrons and photons to the overall angular distribution.

### REFERENCES/FUNDING SOURCE

1. J. Zhang; G. Yang; Y. Lee; S. Chang; J. P. Lu; O. Zhou "Evaluation of frequency multiplexing radiography based on multi-pixel x-ray technology", Proc of SPIE May 2007, 6510(1) 65103Q.
2. Solomon, E. G., Wilfley, B. P., Van Lysel, M. S., Joseph, A. W., Heanue, J. A., "Scanning-beam digital x-ray (SBDX) system for cardiac angiography", Proc SPIE Med Img, May 1999, 3659 246-257.
3. Tseng, H. K., Pratt, R. H., "Exact Screened Calculations of Atomic-Field Bremsstrahlung", Phys Rev A Jan 1971, 3(1) 100-115.
4. Kissel, L., Quarles, C. A. "Shape function for atomic field bremsstrahlung from electrons of kinetic energy 1-500 keV on selected neutral atoms  $1 \leq Z \leq 92$ ", Atomic Data and Nuclear Data Tables, May 1983 2.3(3) 381-460. GE HealthCare, NIH EB006837, Lucas Foundation.

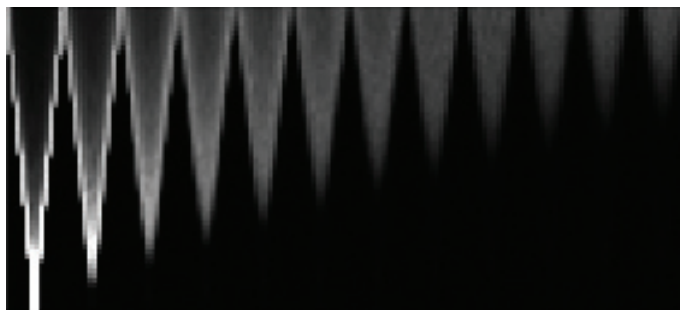
## Effect of the Frequency Content and Spatial Location of Raw Data Errors on CT Images

ADAM WANG<sup>1,2</sup>, YAO XIE<sup>1,2</sup>, NORBERT PELC<sup>1,2,3</sup>

DEPARTMENTS OF <sup>1</sup>ELECTRICAL ENGINEERING, <sup>2</sup>RADIOLOGY, <sup>3</sup>BIOENGINEERING

As CT scanners continue to collect more data per scan, transmitting raw data across the slip ring and storing raw data can be very challenging. While lossy compression can offer a significant reduction in dataset size, it introduces errors to the measurements. Thus, it is important to characterize how these errors present themselves in the final reconstructed image. Since these compression errors can be considered as a source of noise, our results are relevant to other sources of noise, such as electronic noise.

In our work, quantization combined with companders serves as an elementary form of compression to illustrate various effects. We examined the effect of noise of different frequencies in the view (time) direction as well as at different locations in the detector arc. Our research showed that only low temporal frequency errors in the center detectors can contribute to errors in the center of the reconstructed field-of-view (FOV). On the other hand, high temporal frequency errors only contribute to errors in the periphery of the reconstructed FOV. The image errors can also be object-dependent since they depend on the



Each frequency subband (increasing from left to right) is subdivided into detector subbands. The intensity of each pixel represents the standard deviation of the image error (HU) of a thin ring of a particular radius (increasing from bottom to top), contributed from a particular frequency and detector subband.

transmitted intensity.

Whether image errors arise from compression or electronic noise, their relative sensitivity to different frequencies and detectors is an important consideration for applications such as cardiac CT, where the center of the FOV may be considered the most critical region. Therefore, when limiting data rate is essential, detectors could be allocated different bit-rates for compression based on the frequency content of their errors and their spatial location.

### REFERENCES/FUNDING SOURCE

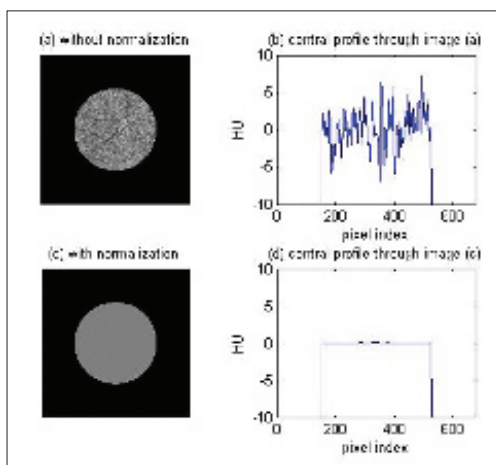
A. S. Wang, Y. Xie, and N. J. Pelc, "Effect of the Frequency Content and Spatial Location of Raw Data Errors on CT Images," submitted to SPIE Medical Imaging 2008: Physics of Medical Imaging. Funded by GE Healthcare, NIH Grant EB006837, and The Lucas Foundation.

## Raw Data Normalization in Inverse Geometry CT System

JONGDUK BAEK<sup>1,2</sup>, NORBERT J. PELC<sup>1</sup>

DEPARTMENTS OF <sup>2</sup>ELECTRICAL ENGINEERING AND <sup>1</sup>RADIOLOGY

An inverse-geometry volumetric CT (IGCT) system uses a large source array opposite a smaller detector array. Because the source and detector have same extent in the axial direction, the IGCT system provides sufficient sampling, and therefore it can prevent cone beam artifacts. In the IGCT system, each X-ray source illuminates a small portion of FOV. During raw data acquisition, any x-ray source intensity variations can cause artifacts, and must be corrected, a process generally called "normalization". Conventional CT scanners use "reference channel" to correct source fluctuations. Because each source of the IGCT system illuminates a portion of the FOV, it is difficult to illuminate the reference channel. Projection data from each source can be mapped into 2D Radon space, and there is an overlap region between sources in 2D Radon space. As a result, substantially same projection data can be generated from different sources at different gantry positions. In the IGCT system, at least one source can illuminate the reference channel, and therefore its data can be easily normalized.



(a) Reconstructed image without intensity normalization (b) central profile through image (a) (c) Reconstructed image with intensity normalization (d) central profile through image (c)

This normalized projection data can be used to normalize the raw data of another source with which it shares an overlap region. By performing this normalization process sequentially, we can do intensity normalization for all sources. To evaluate the normalization algorithm, we generated projection data for a centered cylinder water phantom. We used 200 views in step-and-shoot mode over 360 degrees. During data acquisition, we intentionally introduced 10% source output fluctuations. Grid driven interpolation was used to resample the IGCT data into fan beam data. The resampled fan beam data were filtered and backprojected. The reconstructed image shows the image artifacts that result from uncorrected fluctuations, seen more clearly in the central profile. After applying the proposed normalization algorithm, image artifacts are removed.

### REFERENCES/FUNDING SOURCE

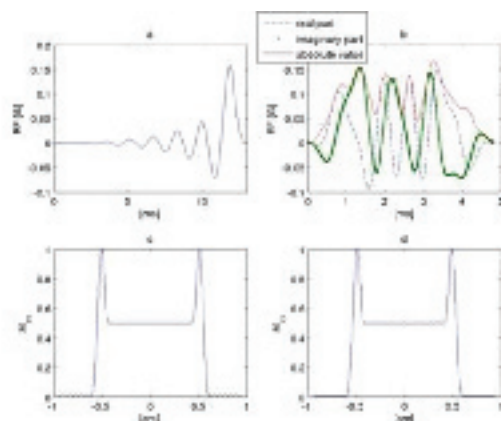
GE Health care, Lucas Foundation. NIH grant EB006837



## RF Pulse Design for High-Resolution Imaging with FLASE

J. K. BARRAL, M. LUSTIG, N. STIKOV, AND D. G. NISHIMURA, DEPARTMENT OF ELECTRICAL ENGINEERING

**Introduction:** The Fast Large Angle Spin Echo (FLASE) sequence has been used with a surface transmit coil to provide high-resolution imaging of the skin. On most clinical scanners however, it is preferable to use the body coil for transmit. The main challenge then is to adapt the large-angle pulse to bear with peak B1 limitations, while keeping the pulse duration short. In this work, we show that using a non-linear-phase pulse instead of a minimum-phase pulse allows a reduction in pulse length by a factor of 3, minimizing through-slice chemical shift artifacts, while preserving the spatial selectivity. **Methods:** The balanced-FLASE pulse sequence features a large flip-angle excitation pulse refocused by a non-selective 180° phase-cycled pulse. Thus, the challenge is to excite a well-defined slice profile. A high bandwidth is desirable to keep the unavoidable overshoot of the magnetization profile on the slice boundaries within a couple of slice encodes. The encoding along the slice direction makes the phase dispersion of non-linear pulses and its induced signal loss negligible. A Shinnar-Le Roux (SLR) minimum-phase RF pulse has the shortest isodelay, which makes it the ideal choice for short-T2 imaging. However, when using the body coil



Top: 12.8 ms minimum phase SLR (a) vs. 4.8 ms non-linear-phase (c). Bottom: 1.08 cm excited profiles. TBW=16, 150° flip angle for both.

for transmit, peak B1 limitations make it undesirably long (Fig. 1a, 150° flip angle). We designed a minimum-peak non-linear-phase pulse by inverting pass-band roots of the minimum-phase SLR pulse. **Results and Discussion:** A 4.8 ms pulse is achieved with 17  $\mu$ T maximum B1 (Fig. 1b). It presents a profile very similar to the original one (Fig. 1c and 1d). Chemical shift in the slab-select direction leads to fat displacement of 6 slices (out of 32) with the minimum phase pulse (1.25 kHz bandwidth) and only 2 with the non-linear-phase pulse (3.33 kHz bandwidth). We checked this reduction of fat contamination in-vivo. It will be even more pronounced with higher field systems.

Specific absorption rate (SAR) increases from 0.35 to 0.89 W/kg, but is still well below the limit of 4 W/kg for any 15 minute-period. **Conclusion:** We have shown that a non-linear-phase design enables shorter pulses for use in 3D FLASE sequence, without incurring an SNR penalty, and greatly reducing through-slice chemical shift artifacts. FLASE is thus a promising sequence for clinical high-resolution imaging.

### REFERENCES/FUNDING SOURCE

This work was supported by NIH grant 1R01 HL075803.

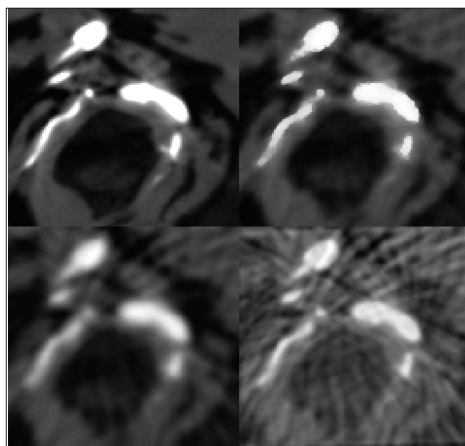
## Piece-wise Smooth Level Set Method Reconstruction for Sparse Angularly Sampled Data

SUNGWON YOON<sup>1,2</sup> AND REBECCA FAHRIG<sup>2</sup>, DEPARTMENTS OF <sup>1</sup>RADIOLOGY AND <sup>2</sup>ELECTRICAL ENGINEERING

We are interested in reconstructions where the number of projection images is limited by a small temporal window at acquisition to facilitate faster acquisition or deliver lower dose to the patients. Reconstructions for cardiac data and sparsely sampled angiography are examples of such case. Regularized iterative reconstructions with underlying data priors as regularizations are common.

We propose a reconstruction technique for sparse angularly sampled projections using the level set method. By assuming piece-wise smooth functions within each region determined by the level set curve, the underlying data can be modeled as consisting of a finite number of distinct regions, each region consisting of materials with similar attenuation coefficients. Piece-wise smooth assumption is a relaxation of the stronger prior of piece-wise constancy we investigated in 2006. We incorporate this prior information into the iterative reconstruction technique by simultaneously estimating the piece-wise smooth functions within each region and updating the level set curve that determine the regions at each iteration.

In this work, we applied the proposed tech-



Original data and three different reconstruction results for comparison. Top left: Original image from an actual CT data. Top right: Piece-wise smooth level set method reconstruction. Bottom left: Preconditioned conjugate gradient reconstruction applied globally with non-negativity and smoothness constraint. Bottom right: Filtered back-projection reconstruction.

nique using one level set curve with different smoothness and value range assumptions for each region. Underlying functions were estimated using a preconditioned conjugate gradient (PCG) method with non-negativity constraint. The level set curve was updated after each underlying function estimation. For comparison, we show reconstruction results using 20 noise projections using the proposed method, global PCG method, and the filtered back-projection (FBP) method. MSE for the global PCG method is 21.13% of that for the FBP method, and the MSE for the the proposed method is 7.66% of that for the FBP method.

We are investigating the convergence characteristics of the algorithm and plan to extend the algorithm to 3D data. We are also investigating other applications where only sparsely sampled projection images are available.

### REFERENCES/FUNDING SOURCE

This work is supported by the Whitaker Foundation, the Baxter Foundation, and the Lucas Foundation.

## Accurate Reconstruction in PR-MRI despite Truncated Data

J. K. BARRAL<sup>1</sup>, H. H. WU<sup>1</sup>, G. E. GOLD<sup>2</sup>, N. J. PELC<sup>2</sup>, J. M. PAULY<sup>1</sup>, AND D. G. NISHIMURA<sup>1</sup>

DEPARTMENTS OF <sup>1</sup>ELECTRICAL ENGINEERING AND <sup>2</sup>RADIOLOGY

**Introduction:** In computed tomography (CT), artifacts due to truncated projections are a major concern. The same truncation problem arises in 2D Projection Reconstruction Magnetic Resonance Imaging (PR-MRI), whenever the object is elongated in one direction and not fully encompassed in the FOV (coronal or sagittal plane). In this work we introduce the Derivative Back Projection-Finite Hilbert Inverse (DBP-FHI) algorithm, recently presented in CT, to accurately reconstruct from truncated MRI data, and we compare it to the conventional Filtered Back-Projection (FBP) algorithm.

**Methods:** The 1D radial inverse Fourier transform of PR-MRI k-space data gives projection data (sinogram) analogous to a CT parallel-beam geometry acquisition. The FOV is determined by the sampling rate and bandwidth of the antialiasing filter. When images from truncated projection data are reconstructed by FBP, the rho filtering operation spreads out the inconsistency of the projection data over the entire FOV, resulting in image shading. A way to avoid the rho filter  $|\rho|$  is to replace it by  $-i \cdot \text{sign}(\rho) \cdot (i \rho)$ . In Fourier space,  $(i \rho)$  corresponds to a derivative and  $\text{sign}(\rho)$  to an inverse Hilbert transform - hence the two steps of the DBP-FHI algorithm. The derivative is a local operation that does not spread the error as the rho filter does.

The 1D inverse Hilbert transform can not be performed directly, since

we only know the Hilbert image after derivative back projection (DBP) on finite segments (delimited by the FOV). However, if the object has a limited extent within this segment, a Finite Hilbert Inverse (FHI) can be used. Therefore, the DBP-FHI algorithm holds only for oblong objects where one direction is free from truncations. The direction in which the 1D FHI is performed is determined by the boundaries of the backprojection.

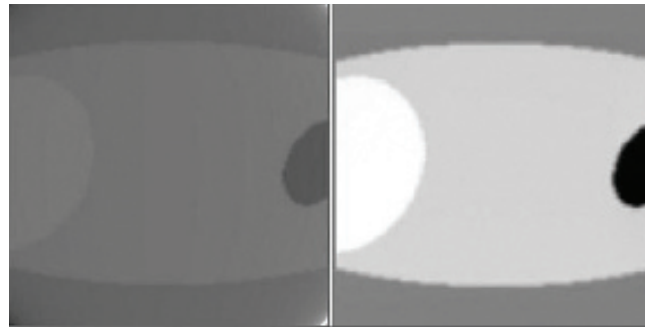
**Results:** We compared our DBP-FHI results to FBP. Simulations were performed using a "Popeye" phantom. DBP-FHI (Fig. 1, right) provides significant improvement over FBP (Fig. 1, left). All the shading artifacts disappear, and no new artifacts are introduced.

**Conclusion:** The Derivative Back Projection-Finite Hilbert Inverse algorithm gives an accurate

reconstruction for Projection Reconstruction truncated data within a region of interest, provided that a given orientation is free from truncation. DBP-FHI reconstruction could be particularly useful in ultra-short TE (UTE) imaging - which uses PR to acquire data right after excitation - where it would allow smaller FOVs and shorter scan times

### REFERENCES/FUNDING SOURCE

Proceedings of the ISMRM, 15th annual meeting, 2007.  
This work was supported by NIH grant 1R01 HL075803.



FBP (left) and DBP-FHI (right) reconstruction of the "Popeye" phantom. Since FBP needs to redistribute data from an inconsistent sinogram, it overestimates the object, especially at the edges, hence the shading artifacts seen on the left image, and the disrupted contrast. DBP-FHI (right) provides an accurate reconstruction within an ROI.

## A Fast 3D Reconstruction Algorithm for Inverse-Geometry CT Based on an Exact PET Rebinning Algorithm

SAMUEL R. MAZIN<sup>1,2</sup> AND NORBERT J. PELC<sup>1,2,3</sup>, DEPARTMENTS OF <sup>1</sup>RADIOLOGY, <sup>2</sup>ELECTRICAL ENGINEERING AND <sup>3</sup>BIOENGINEERING

Inverse-geometry CT (IGCT) employs a large area x-ray source array opposite a small area detector array. The system is expected to provide sub-second volumetric imaging with isotropic resolution and no cone-beam effects. Due to the large amount of data, it is desirable to have an exact 3D reconstruction algorithm that is fast. Currently known IGCT algorithms are either slow, due to 3D backprojection, and/or require a reprojection step, or are inexact. Defrise et. al developed an exact Fourier rebinning algorithm (FORE-J) for 3D PET. This algorithm first rebins the 3D PET data into in-plane sinograms and then reconstructs the series of axial slices using any 2D method. FORE-J is fast, exact, and efficiently uses all of the acquired PET data. We have adapted this algorithm to the IGCT geometry, requiring a few modifications. The main difference in the modified algorithm is in the estima-



(a) Fourier rebinning without the correction term. Loss of contrast in the center is a cone-beam artifact. (b) Cone-beam artifacts are gone in the FORE-J reconstruction.

tion of the second-derivative in  $z$  of the projection data. The original FORE-J algorithm used adjacent PET detector ring data. The modified approach uses a single source-row and adjacent detector-rows due to the sparser  $z$ -sampling of the source array in IGCT. Experiments were performed using a numerical "Defrise" phantom consisting of high-intensity discs spaced in  $z$  to assess the accuracy of the modified

algorithm as well as highlight any cone-beam effects. A noise simulation was performed to analyze the noise properties of FORE-J and the modified algorithm. The modified algorithm proved to be very fast and slightly more accurate than the original algorithm with a very small noise penalty in the central axial slices.

### REFERENCES/FUNDING SOURCE

GE Healthcare and The Lucas Foundation.

## Lossy Raw Data Compression in Computed Tomography with Noise Shaping to Control Image Effects

YAO C. XIE<sup>1,2</sup>, ADAM S. WANG<sup>1,2</sup>, NORBERT J. PELC<sup>1,2,3</sup> DEPARTMENTS OF <sup>1</sup>ELECTRICAL ENGINEERING, <sup>2</sup>RADIOLOGY, AND <sup>3</sup>BIOENGINEERING

The data rate requirements for raw data transmission through the slip ring of a CT scanner can be quite challenging, especially as the scanning speed and number of detector channels increase. Compression can be used to reduce the size of the data rate array, and therefore the data rate requirements. Compression can also be applied to raw data storage and transmission through the computation system. Currently, raw data are stored only for a short period. Compression may encourage longer-term storage of raw data, increasing the flexibility for retrospective reconstructions.

While lossy compression can offer a significant reduction in data set size, it introduces errors to the measurements. The design and evaluation of compression methods need to take into account the nature of the sinogram and how errors in the sinogram contribute to noise in the reconstructed image. Further, it is possible to control the relative distribution of errors in the reconstructed image. This may be important to ensure higher image quality in some region of

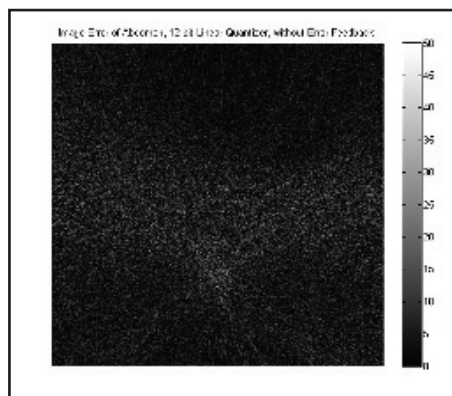


Figure above: Image error of abdomen, 12-bit linear quantizer, without error feedback.

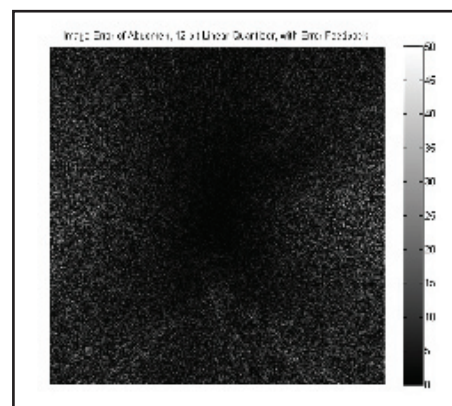


Figure above: Image error of abdomen, 12-bit linear quantizer, with error feedback.

the image (e.g., the center of the field of view). We found that low frequency errors in the angular direction of the rays dominate the errors in the central ROI, whereas the high frequency error contributes more to the peripheral region of the image.

In this paper, we present two noise shaping methods for fixed rate lossy compression of CT raw data that achieve a lower error level in the center region of the reconstructed image: error feedback filters and sub-band coding with bit allocation. Our preliminary numerical examples show the effectiveness of both methods.

### REFERENCES/FUNDING SOURCE

A. S. Wang, Y. C. Xie, and N. J. Pelc, "Lossy Raw Data Compression in Computed Tomography with Noise Shaping to Control Image Effects," submitted to SPIE Medical Imaging, 2007.  
NIH grant EB006837.

## Cardiac C-arm CT: Evaluating the Accuracy of Motion Correction for C-arm CT Using Ultrasound Imaging

ERIN GIRARD-HUGHES, MARCUS PRÜMMER, LARS WIGSTROM  
REBECCA FAHRIG, DEPARTMENT OF RADIOLOGY

The research and technology development on the C-arm CT system by the Fahrig group will allow the acquisition, reconstruction, display and interaction with 3D CT volumes during a procedure in the interventional cardiology suite, where C-arm mounted x-ray fluoroscopy is already typically installed and used. This is in contrast to the current standard of obtaining 3D cardiac images of a patient only before an interventional procedure or relying solely on 2D fluoroscopic images for guidance during a procedure.

Initial work on ECG-gated cardiac imaging and image processing techniques to reduce image noise and image artifact has resulted in in vivo cardiac C-arm CT images that are comparable to clinical CT. One method being developed by our lab uses retrospective motion correction to improve the temporal resolution of reconstructed images.

The 4D deformation of the heart over a cardiac cycle is computed and then the desired cardiac phase is reconstructed again considering the prior-motion knowledge. A method has been developed to determine the limitations and accuracy of the temporal and spatial resolution of this approach. Using a phantom model and in vivo cardiac data from pigs, we can evaluate the accuracy of the estimated 4D motion field compared to the observed motion, as determined by M-mode echocardiography. This evaluation method works by aligning markers within the ultrasound and CT images to determine the corresponding M-mode line within the CT-data set. By projecting the estimated 3D motion vector from the CT data set onto the M-mode line, the mean and standard deviation between the ultrasound measured and C-arm CT-estimated motion can be calculated.



## In Vivo Imaging of SFA Stents

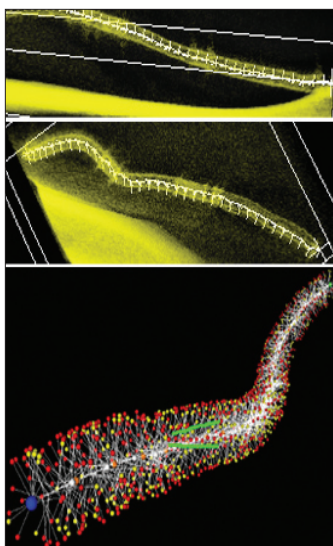
ARUNDHUTI GANGULY<sup>1</sup>, BENJAMIN KECK<sup>1</sup>, AND REBECCA FAHRIG<sup>1</sup>

<sup>1</sup>DEPARTMENT OF RADIOLOGY, STANFORD UNIVERSITY AND <sup>2</sup>FRIEDRICH-ALEXANDER UNIVERSITY, ERLANGEN-NUREMBERG

We are using high-resolution 3D-imaging to evaluate the deforming forces on superficial femoral artery (SFA) stents placed in patients. The SFA is susceptible to the development of atherosclerotic lesions that are typically treated with percutaneous transluminal angioplasty and stent deployment. However, it has been found that these stents have a rate of fracture as high as 35%<sup>1</sup>. Stent fracture is usually accompanied by restenosis and stent reocclusion<sup>2</sup>. The exact cause for the fracture is unknown and is hypothesized to be resulting from the deforming forces due to hip and knee flexion.

A high-resolution (250 $\mu$ m) C-arm CT imaging system (Axiom Artis dTA, Siemens Medical Solutions, Forchheim, Germany) was optimized for imaging SFA stents in patients. The subjects were placed on the imaging table which had a specially constructed extension. Imaging was performed with the leg placed in the straight and bent positions. Projection images obtained during 20s scans with  $\sim 200^\circ$  of rotation of the C-arm were back-projected to obtain 3D volumes.

Using a semi-automatic software written in-house, the centerline for each reconstructed stent was found and ellipses were fitted to slices normal to the centerline. Image quality was adequate for calculations in 11/13 patients. Bending the leg was found to shorten



*Calculated centerline in reconstructed SFA stents in patient with the leg straight (top) bent (middle) and after registration and overlay of node graphs generated from the data (bottom). Reference points are in red and registered ones in yellow.*

the stents in 10/13 cases with the maximum change being 9% (12mm in a 133mm stent). It remained unchanged in one case ( $\leq 1$ mm measurement error). The eccentricity of the ellipses showed a maximum change of 36% in a case where the stent extended behind the knee.

For calculating the equivalent stress, strain and torsion forces on the stents, we have developed a registration method by using nodes on the stents in the straight and bent positions. This algorithm has been trained on phantom data where the exact loading was known. It is currently being applied to the in vivo studies.

### REFERENCES/FUNDING SOURCE

1. Scheinert D, Scheinert S, Sax J, Piorowski C, Braunlich S, Ulrich M, Biamino G, Schmidt A. Prevalence and Clinical Impact of Stent Fractures After Femoropopliteal Stenting. *Journal of the American College of Cardiology*. 45 (2): 312-315. 2005.
  2. Allie DE, Hebert CJ, Walker CM. Nitinol Stent Fractures in the SFA. *Endovascular Today*. 2004:22-34.
- The sponsors of the RESISTent program: Abbott, Angiomed, Boston Scientific, Cordis, Medtronic, and W. L. Gore, NIH/NIBIB grant R01 EB003524, Siemens Medical Systems, The Lucas Foundation.

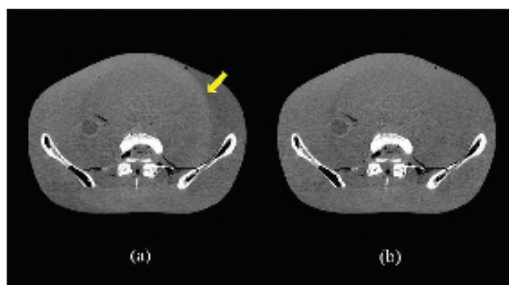
## Reduction of Lag in Flat Panel Digital X-Ray Detectors

JARED STARMAN<sup>1,2</sup>, STEVE BANDY<sup>3</sup>, GARY VIRSHUP<sup>3</sup>, CARLO TOGNINA<sup>3</sup>, REBECCA FAHRIG<sup>2</sup>

<sup>1</sup>DEPARTMENTS OF ELECTRICAL ENGINEERING, <sup>2</sup>RADIOLOGY, AND <sup>3</sup>VARIAN MEDICAL SYSTEMS

Image lag is defined as signal present in frames following the frame in which it was generated. Thus a given frame from the x-ray detector is actually the summation of the current frame, plus a complicated, weighted sum of previous frames of the detector that is spatially varying over the detector and object dependent. In projections, image lag causes temporal blurring and can actually increase SNR, but at the cost of decreasing temporal resolution. In CT reconstructions, image lag can lead to a range of image artifacts, such as streaking, azimuthal blurring, and/or shading artifacts. Specifically for a pelvic phantom scan, image lag can lead to shading artifacts of up to 30HU.

The main contributor to image lag in a-Si digital flat panel x-ray detectors is believed to be charge trapping in the a-Si layer. Other effects that may or may not contribute are afterglow in the scintillator and incomplete readout of the amplifiers. For the charge trapping phenomenon, charge enters defect states inside the 'forbidden' band gap in the a-Si during the irradiation frame, and is slowly released by thermal processes over subsequent frames. The rates of charge uptake and



*(a) Shows a reconstructed slice from a pelvic phantom. The yellow arrow highlights the edge of the shading artifact which has an intensity difference of 30HU. (b) Shows a reconstruction from the same dataset that has been corrected for lag using our software model. The artifact is reduced to around 1HU.*

release can differ, which make the process a non-linear system.

A simple software model has been developed to monitor and correct for charge trapping in the a-Si. Even though the defect states that cause charge trapping exist at a continuous spectrum of energies, the states are discretized into three or four energy bins. Then, each energy bin is modeled as a branch of an RC circuit. To approximate the non-linearity of the system, the R and C parameters are allowed to change as a function of whether the model determines charge is being released or captured by the system.

Current and future work involves using a hardware approach to reduce image lag.

In between frames each photodiode in the a-Si can be forward biased, which in turn will saturate the defect states with charge. Thus, little or no signal charge will enter the defect states. Initial results are promising, but effects on panel DQE still need to be further investigated.

### REFERENCES/FUNDING SOURCE

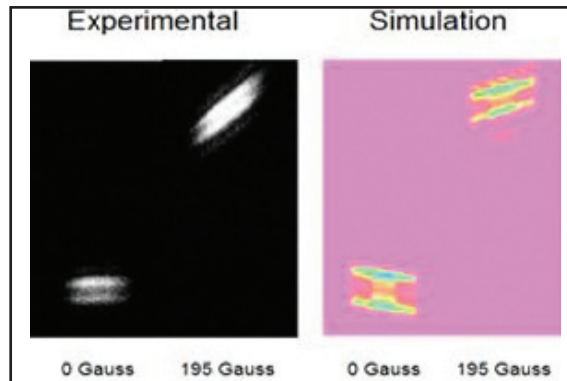
- Varian Medical Systems, Stanford/NIH. Biotechnology Training Grant.

## Development of an MR Compatible Rotating Anode X-Ray Tube

PRASHEEL LILLANEY<sup>1,3</sup>, JOHN BRACKEN<sup>2</sup>, JOHN ROWLANDS<sup>2</sup>, REBECCA FAHRIG<sup>1</sup>

<sup>1</sup>DEPARTMENT OF RADIOLOGY, STANFORD UNIVERSITY, <sup>2</sup>DEPARTMENT OF MEDICAL PHYSICS, UNIVERSITY OF TORONTO AND SUNNYBROOK HEALTH SCIENCES CENTER, AND <sup>3</sup>DEPARTMENT OF BIOENGINEERING, STANFORD UNIVERSITY

Our previous work in hybrid X-ray/MR technology focused on integration of a digital flat panel x-ray system into the bore of an open, 0.5T GE Signa SP interventional magnet. Currently, there are only 13 such MR systems in the world, and we are therefore investigating the close integration of the same digital x-ray detector system with a closed-bore 1.5T magnet. In order to achieve a truly hybrid, high quality X-ray/MR system one must have a rotating anode x-ray source as close as possible to the bore of the high-field MR magnet. This placement allows switching between modalities with a minimum of disturbance to critically placed catheters and other devices. Such a highly integrated system could lead to a reduction in total time, risk and dose of procedures, could lead to an increase in procedure accuracy, and perhaps most significantly, in the development of new, unanticipated minimally invasive procedures. Full integration between a closed bore MR system and an x-ray fluoroscopy system presents two main challenges that must be addressed: x-ray tube motor operation and efficiency in an external field, and focal spot deflection. With regards to the first challenge our results have shown that an AC induction motor operating in external fields will experience a drop off in efficiency. Specifically, fields on the order of 0.1 T perpendicular to the rotor decrease the rotation speed from 3600



*Preliminary results comparing experimental and simulated focal spot deflection for the non-magnetic x-ray tube when placed in an external field of 195 Gauss perpendicular to the anode-cathode axis (BR direction). Both the experimental and finite element simulation indicate a deflection of approximately 5 mm in the focal spot.*

RPM to below 2000 RPM. We are currently analyzing an alternate brushless DC motor design that would exploit the presence of the external MR fringe field and our initial finite element results indicate that the necessary amount of torque is produced. With regards to the second challenge, focal spot deflection, our results show that an external field of 195 Gauss perpendicular to the anode-cathode axis (BR direction) produces a focal spot deflection of 5 mm (see figure). For the fields at which we want to operate the x-ray tube (up to approximately 0.1T along BR) this magnitude of deflection would be unacceptable, and a correction technique is necessary. We propose a design that

includes active deflection coils which serve to counteract the presence of the external field and reduce the focal spot deflection to less than 1 mm in our simulations. Our experimentally verified finite element model of the x-ray tube electron optics (see figure) will be used to optimize the deflection coil design and placement within the x-ray tube.

### REFERENCES/FUNDING SOURCE

Stanford School of Medicine Bio-X Fellowship, the Lucas Foundation

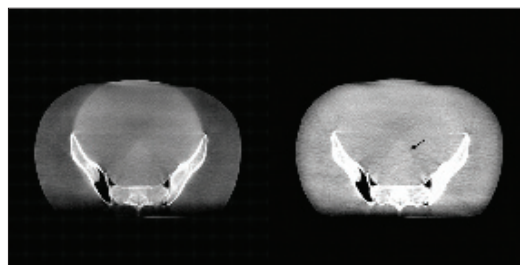
## Improved Scatter Correction for X-ray Conebeam CT Using Primary Modulation

LEI ZHU<sup>2</sup>, JOSH STAR-LACK<sup>4</sup>, N. ROBERT BENNETT<sup>2</sup>, TIANFANG LI<sup>3</sup>, LEI XING<sup>2</sup>, AND REBECCA FAHRIG<sup>2</sup>

DEPARTMENTS OF <sup>1</sup>ELECTRICAL ENGINEERING, <sup>2</sup>RADIOLOGY, <sup>3</sup>RADIATION ONCOLOGY, STANFORD UNIVERSITY, AND

<sup>4</sup>VARIAN MEDICAL SYSTEMS, PALO ALTO, CA

Recently, we proposed a scatter correction method for x-ray imaging using primary modulation. A primary modulator with spatially variant attenuating materials is inserted between the x-ray source and the object to make the scatter and part of the primary distributions strongly separate in the Fourier domain. Linear filtering and demodulation techniques suffice to extract and correct the scatter for this modified system. The method has been verified by computer simulations and preliminary experimental results on a simple object. In this work, we improve performance by using a new primary modulator with a higher modulation frequency and by refining the algorithm. The improved method is evaluated experimentally using a pelvis phantom. The imaging parameters are chosen to match the Varian Acuity CT simulator, where scatter correction has been shown to be challenging due to complicated artifact patterns. The results using our approach are compared with those without scatter correction, and with scatter inherently



*Reconstructions of the pelvis phantom. Left: without scatter correction; right: scatter corrected using the primary modulation method. Using the proposed method, the shading artifacts are removed and the low-contrast objects are more visible.*

suppressed using a slot-scan geometry. The comparison shows that the primary modulation method greatly reduces the scatter artifacts and improves image contrast, and the CT HU accuracy is better than that obtained using a slot-scan geometry.

### REFERENCES/FUNDING SOURCE

1. Lei Zhu, Josh StarLack, N. Robert Bennett, Tianfang Li, Lei Xing, and Rebecca Fahrigh Improved scatter correction for x-ray conebeam CT using primary modulation, Proceedings of

the SPIE, Volume 6510, pp. 65101U, 2007.

2. Lei Zhu, N. Robert Bennett, and Rebecca Fahrigh, Scatter correction method for X-ray CT using primary modulation: theory and preliminary results, *IEEE Trans. on Med. Imaging*, Vol. 25, No. 12, pp. 1573-1587, December 2006.

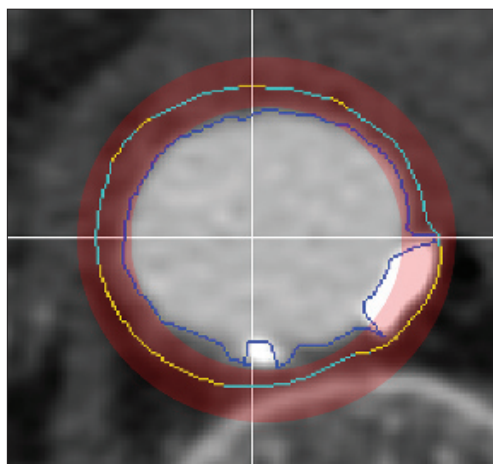
The authors would like to acknowledge Varian Medical Systems for hardware support. This project is supported by NIH R01 EB003524 and the Lucas Foundation.

## Identification of Aortic Arterial Wall as a Prerequisite for Quantification of Atherosclerotic Burden using CT Angiography

BHARGAV RAMAN, RAGHAV RAMAN, SANDY NAPEL, GEOFFREY RUBIN  
DEPARTMENT OF RADIOLOGY

**Purpose:** Research into the quantification of the atherosclerosis usually focuses the coronary arteries, as it is the proximal cause of heart disease. Initial effects of this disease result in the deposition of “plaques,” which can reduce or interrupt blood flow to distal tissue, which, in turn, causes loss of function of the affected tissue. While atherosclerosis can also contribute to disease in the other arteries, it stays largely asymptomatic until after serious degeneration has occurred, such as an aneurysm or dissection developing over many years. We intend to quantify the atherosclerotic burden in the extra-coronary arteries, specifically in arteries most prone to vascular disease, starting with the aorta. Further, we intend to characterize atherosclerotic plaque by measuring soft (thought to be unstable) and well as calcified (thought to be stable) plaque.

**Materials and Methods:** Our algorithm first uses established methods to determine the inner (luminal) wall of the contrast-enhanced artery, thereby defining the border between the lumen and the soft and calcified plaque. The outer wall of the aorta is sometimes well



*A cross-section through the aorta: Dark Blue: Inner wall excluding calcifications encloses flow channel containing iodine-enhanced blood (bright); Red: Search Area; Yellow: Well defined outer wall segments used as anchors; Light Blue+Yellow: Final calculated outer wall*

defined when there is a thick enough layer of adjacent low density fat or high density bone. However, in many places along the length of the aorta, its outer wall may be indistinct or almost invisible. Using the well-defined segments of the outer wall, a donut-shaped search area is defined. A shortest path algorithm is then used to find the outer wall, including its indistinct segments. The well defined segments are used as anchors to guide the algorithm. The calculated path minimizes path length and tortuosity and tries to follow the indistinct layer of fat while avoiding “cutting across” high density structures and is biased to follow well-defined segments.

**Future Work:** Once methods for identifying the aortic wall are validated, its thickness, irregularity and composition can be characterized. We plan parameter optimization trials followed by validation of the algorithm including comparison to manually created aortic phantoms.

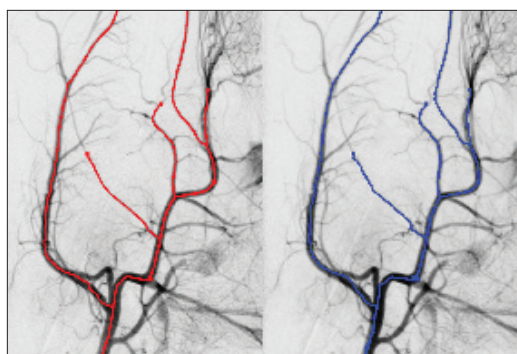
## Localizing a Guidewire in Three Dimensions During Endovascular Interventions Using Single-view Fluoroscopy and a Stereo Roadmap: Method and Feasibility Study.

GENNADIY CHUYESHOV<sup>1</sup>, MARKUS KUKUK<sup>2,3</sup>, SANDY NAPEL<sup>3</sup>

<sup>1</sup>INSTITUTE FOR COMPUTATIONAL AND MATHEMATICAL ENGINEERING, <sup>2</sup>SIEMENS MEDICAL SOLUTIONS, AND <sup>3</sup>RADIOLOGY, STANFORD UNIVERSITY

**Purpose:** To localize an instrument being guided using monoscopic fluoroscopy in 3D so that it can be properly displayed in the context of a stereo roadmap or a 3D reconstruction of the vasculature.

**Method and Materials:** We first acquire stereo pairs of blood vessel roadmaps using offset frames from a rotational run during a contrast injection. We then fluoroscopically image the introduction of the guidewire from an appropriate angle, and overlay the resulting sequence on the roadmap acquired at the same angle. For each short horizontal line crossing the guidewire in the fluoro image, a profile through the corresponding roadmap is weighted, shifted and subtracted from a corresponding weighted profile in the 2nd roadmap image of the stereo pair, and we plot the corresponding point of the guidewire in it at the shift that minimizes the difference. To test this concept, we skeletonized a stereo pair of porcine vascular images, thereby simulating 6 central paths through the major vessels, and used the paths on one as simulated guidewires. We used these paths and their corresponding roadmap image to estimate the path locations in the 2nd roadmap image using the described method. We compared these estimates to the skeletonized 2nd



*Stereo pair of roadmap images. Left: several skeletonized vessels (red) used as simulated guidewires (in red) overlaid on roadmap. (Right) Estimated path locations (blue) in the 2nd roadmap image.*

roadmap image by computing the fraction of overlapping points.

**Results:** The fraction of overlapping points for the 6 paths were 86/98 (88%), 88/90 (98%), 83/197 (93%), 58/65 (89%), 149/152 (98%) and 54/61 (88%), respectively. Estimated paths were relatively smooth, and non-overlapping points were randomly distributed and within a few pixels of their correct locations.

**Conclusion:** It is feasible to find the location of a guidewire in the 2nd image of a stereo roadmap, given its location in the first. Crossing and nearly crossing vessels may create local errors, but these may be detected as discontinuities and corrected by choosing a

local minimum in the shifted profile subtraction, or by interpolation. With projections determined from two views, visualization of the guidewire in stereo, or within a 3D reconstructed volume, becomes possible.

### REFERENCES/FUNDING SOURCE

Presented at RSNA, 2007.

Supported by Siemens Medical Solutions.

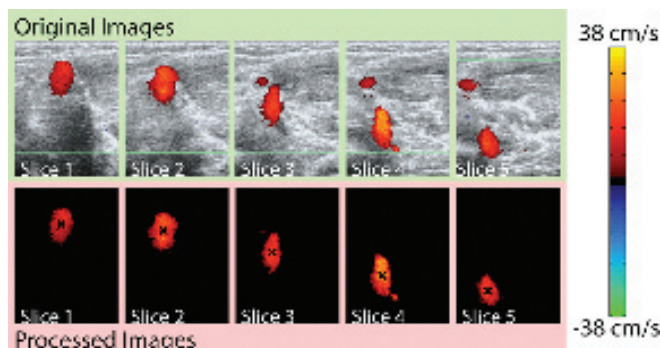


## Automated Detection of Peak Blood Velocity Using a Novel Transducer Array and Intelligent Software

J. FARUQUE<sup>2</sup>, O. ORALKAN<sup>2</sup>, B. JEFFREY<sup>1</sup>, B. T. KHURI-YAKUB<sup>2</sup>, S. NAPEL<sup>1</sup>

DEPARTMENTS OF <sup>1</sup>RADIOLOGY AND <sup>2</sup>ELECTRICAL ENGINEERING

**Purpose:** High peak blood velocity correlates with stenosis, but determination using ultrasound is subject to intra- and inter-operator variability. We seek an operator-independent method, and propose using a stack of parallel cross-sectional color Doppler images produced by a capacitive micromachined ultrasonic transducer (cMUT) array. **Methods and Materials:** Currently, we simulate the output of the cMUT (under development) by acquiring movie sequences of 5 parallel cross-sectional color Doppler images through the brachial artery, using a SiemensAntares ultrasound machine with a VFX9-4 transducer. Using the maximum flow image from each of the 5 movie sequences, we automatically segment the vessel and determine peak velocity in each sequence. We then correct for Doppler angle using the vessel trajectory computed from the segmented cross-sections. We also determine the Doppler angle and peak blood velocity conventionally using longitudinally-acquired images and pulsed Doppler. **Results:** In a preliminary experiment, the Doppler angles in 2 subjects



Color ultrasound images of 5 cross sectional positions in the brachial artery: (top) original images from ultrasound system. (bottom) segmented vessel images. The “x” in each image marks the center of mass of the vessel. For this subject, the Doppler-corrected peak velocity calculated by the proposed method and conventional pulsed Doppler was 71.1 and 65 cm/s, respectively.

determined by our method and conventional pulsed Doppler were 69.9° and 73°, and 62.3° and 73°, respectively. The peak blood velocities in the 2 subjects determined by our method and by pulsed Doppler were 46.2 and 55 cm/s, and 71.1 and 65 cm/s, respectively. **Conclusions:** Our preliminary data show that determination of PBV from parallel cross-sectional images is feasible. Future work includes developing the cMUT array and further testing on subjects and phantoms using our current method. After development of the cMUT array, we will validate our method with a study on patients and healthy volunteers using the new transducer and software. If

successful, this method could reduce operator dependence and make accurate and reproducible determinations of peak blood velocity more widely available, possibly as part of a routine medical checkup.

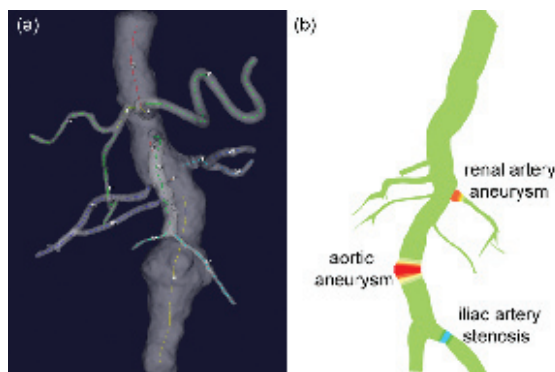
### REFERENCES/FUNDING SOURCE

Bio-X Interdisciplinary Initiatives Program. Grant awarded October, 2006.

## Flattening the Abdominal Aortic Tree for Effective Visualization

JOONG HO WON<sup>1</sup>, GEOFFREY D. RUBIN<sup>2</sup> AND SANDY NAPEL<sup>2</sup>, DEPARTMENTS OF <sup>1</sup>ELECTRICAL ENGINEERING AND <sup>2</sup>RADIOLOGY

**Purpose:** To develop an algorithm that displays CT Angiography (CTA) or MRA images of the abdominal aortic vascular tree with accompanying quantitative assessments in a single image without the appearance of intersections between branches. **Materials and Methods:** We build a tree data structure of the abdominal aortic tree from a collection of 3D centerlines. The first phase of untangling applies a projection mapping as used in stretched Curved Planar Reformatting (CPR) to each node of the tree data structure, and produces a 2D topology-geometry model. The second phase abstracts the projected centerline using a convex primitive called the vessel hull. We then place these primitives in user-specified priority order, using a radial sweep line algorithm to find an available display region for placement, and then determine an optimal placement that minimizes the distortion of the original geometry within the region. The resulting placement is improved by selecting the most distorted primitive and its neighbors and redrawing them in a randomized order. Finally the untangled centerlines are color-coded and modulated by the diameter of the corresponding vessel segments. We evaluated the method using 10 CTA datasets, and for each began with an anterior-posterior projection so as



Example case showing visualization of the abdominal aortic tree. (a) Anterior-posterior surface display and original centerlines, showing intersections and overlap amongst vessel branches. (b) untangled visualization, with intersections removed, showing automatically determined and color-coded relative diameters.

to introduce severe crossings in the renal artery region. Our metrics for distortion between the input orthographic projection of the centerlines and the output centerlines considered scaling, changes to branch angles, and nonlinear bending. **Results:** Processing all datasets resulted in a clear visualization with all false intersections removed, scale distortion close to the ideal value of 1.0 (min=0.76, max=1.05), and branch angle distortion less than 38°. Bending energy was below 2.5 for 8 cases. The other 2 cases showed aggressive stretching, which occurred during the first phase of untangling, of what were originally tortuous vessels. **Conclusion:** Our proposed algorithm eliminates misleading vessel crossings

from conventional projections, and in most cases conserves overall shape, and can convey clinical findings from cross-sectional angiographic examinations in a single 2D image. Our distortion metrics can signal extreme behavior of the algorithm, which may possibly be used to iteratively improve visualization when it occurs.

### REFERENCES/FUNDING SOURCE

Presented at Engineering in Medicine and Biology Society (EMBS), 2006 and 28th Annual International Conference of the IEEE, 2006.  
NIH/NHLBI 1R01HL67194

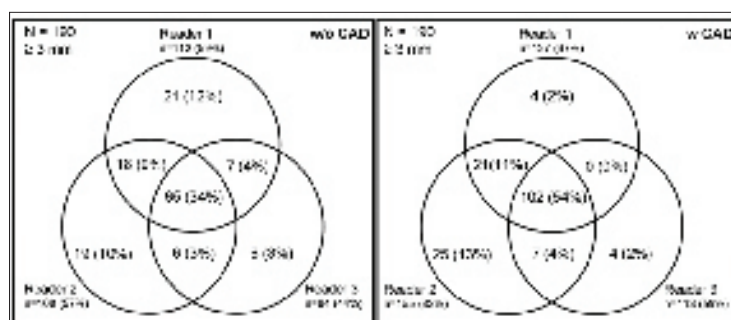
# Potential Equalization of Radiologists' Diagnostic Performance with the Use of Computer Aided Detection (CAD) as a Second Reader in Lung Nodule Detection on Chest CT

JUSTUS E. ROOS, DAVID A. OLSEN, DAVID S. PAIK, SANDY NAPEL, EMILY G. LIU, AND GEOFFREY D. RUBIN  
DEPARTMENT OF RADIOLOGY

**Purpose:** To assess the potential impact of CAD acting as an equalizer on the diagnostic performance of radiologists in detecting lung nodules on chest CT scans.

**Materials and Methods:** Our developmental CAD algorithm was applied to 20 chest MDCT scans with 115 non-calcified  $\geq 4$  mm nodules, where the reference standard was established by two experienced thoracic radiologists in consensus who performed free search and blindly evaluated all reader and CAD detections. Three readers R1/R2/R3 (9, 14, and 24 years of experience reading chest CT) independently analyzed the CT scans on a dedicated 2D+3D lung nodule evaluation platform. They performed a free search for lung nodules followed by an interpretation of CAD detections and assigned a confidence score (0-5) to each detection. Venn diagrams, pair wise comparison of detected nodules among the readers, and Kappa statistics were used to quantify the inter-reader agreement after free search and CAD evaluation.

**Results:** Sensitivity for free search was for R1/2/3 72%/67%/63% at a false positive (FP) rate of 0.5 and increased with CAD to 75%/80%/72% at the same FP rate/patient. During free search, only



*Venn diagrams demonstrate the inter-reader variability and the potential of CAD to equalize the performance among reader in the detection of pulmonary nodules. These diagrams show that all readers made unique detections and that after free search (w/o CAD) only 34% of nodules were detected by all three readers. Adding CAD (w CAD) the agreement among the readers improves and the central intersection increases to 54% of detected nodules with decrease of unique detections by the readers.*

52% (60/115) nodules were identified by all three readers and 18% (20/115) by any reader pair. 16% (19/115) nodules were detected only by one but not the other readers. Following CAD review, 70% (80/115) nodules were identified by all 3 readers, 11% (11/115) nodules by any reader pair and 13% (14/115) by one single reader, respectively. CAD equalized differences in free search detection of reader pairs as follows: R1-R2 by 62% (16/26), R1-R3 48% (12/25) and R2-R3 52% (16/31) Kappa values for reader pairs were 0.45 (R1-R2), 0.51 (R1-R3), 0.40 (R2-R3) after free search and increased with CAD to 0.61, 0.64 and 0.41, respectively.

**Conclusion:** Besides increasing the sensitivity for lung nodule detection, CAD plays a significant role in equalizing the inter-reader differences in diagnostic performance even amongst experienced radiologists.

## REFERENCES/FUNDING SOURCE

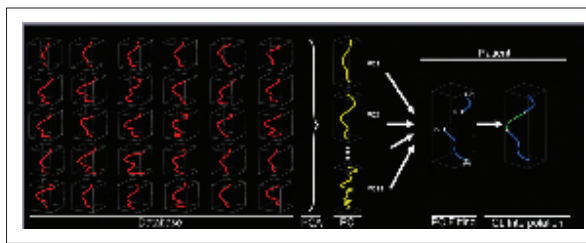
Lung CAD: When is it Enough and When is it Too Much? 9th Annual MDCT Course, 2007.  
NIH/NCI R01 CA109089.

## Automated Centerline Extraction of Femoro-Popliteal Artery (FPA) Occlusions in Lower Extremity CT Angiography (CTA)

JUSTUS E. ROOS, DOMINIK FLEISCHMANN, TEJAS RAKSHE, MATUS STRAKA, MARC SOFILOS, DAVID TRAN, JARRETT ROSENBERG, AND SANDY NAPEL DEPARTMENT OF RADIOLOGY

**Purpose:** To assess the accuracy of a novel knowledge-based algorithm for automatically extracting the centerlines of occluded femoropopliteal arteries (FPA) in lower extremity CT angiograms, in comparison to manual vessel tracking in patients with peripheral arterial occlusive disease (PAOD).

**Material and Methods:** 47 FPA occlusions (mean length 101mm, range (16-398mm)) were retrospectively identified in 30 patients with PAOD (14m/16f; mean age 72y, range 30-89y) and categorized into 4 length groups: <50mm (n=17); 50-100mm (n=13); 100-200mm (n=11) and >200 mm (n=6). The patent FPA portions were identified using a standard density/gradient-based vessel-tracking algorithm. Centerlines of occluded segments were manually determined two times by each of four experts, with the mean of all 8 readings serving as the standard of reference. Each occlusion was also interpolated using a knowledge-based algorithm, which uses shape information extracted from a separate database of 30 non-diseased FPAs using principal component analysis. Accuracy of the interpolated centerlines was quantified by point-wise calculation of the maximum distance between the standard of reference and the automated centerline. A reference range of error was defined as a 3mm radius from the mean



*The figure illustrates the principle of using vascular shapes from CT angiographies of normal individuals (database) to predict the vascular course of an occluded segment (green line) of the patients' femoro-popliteal artery (blue line). Principal component analysis (PCA, a particular statistical analysis) is performed on the vascular shape database to compute principal components (PC) which represent sets of standardized vascular shapes (yellow line). Any femoro-popliteal artery can be considered to be a combination of these PCs where each PC captures some degree of shape variation. The knowledge of these PCs allows then to interpolate the missing (=occluded) arterial segment in a patient.*

of the expert centerlines

**Results:** The mean of maximum error (in mm) for occlusion lengths of <50mm, 50-100mm, 100-200mm, and >200mm was 3.8, 5.9, 10.0, and 12.0, respectively, for readers and 3.9, 6.9, 12.6, and 22.2, respectively for the algorithm. The maximum errors of the algorithm were completely contained within 3mm of the mean of the readers in 25 of 47 cases; in the other 22 cases, the algorithm derived centerline extended beyond 3mm for 3% to 12% of the total occlusion length (mean 8.3%, sd 2.6%).

**Conclusion:** Centerlines of occluded femoropopliteal arteries can be extracted using a knowledge-based algorithm that uses shape information from a database.

The accuracy of the algorithm is within

the variability of experts up to an occlusion length of around 75mm.

### REFERENCES/FUNDING SOURCE

Knowledge-based Algorithm for Automated Centerline Interpolation through Femoro-Popliteal Artery (FPA) Occlusions in Peripheral CTA. 29th Annual Course of the SCBT/-MR, 2006. NIH/NHLBI RO1 HL67194; Justus Roos was supported by the Swiss National Science Foundation, PBBEB 106796.



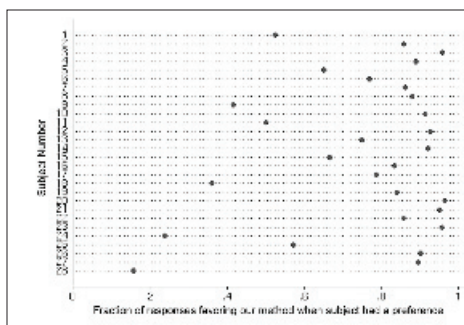
## Co-Visualization of Stereoscopic and Monoscopic Images for Instrument Navigation in the Interventional Room

MARKUS KUKUK<sup>1,2</sup>, JARRETT ROSENBERG<sup>2</sup>, SANDY NAPEL<sup>2</sup>

<sup>1</sup>SIEMENS MEDICAL SOLUTIONS <sup>2</sup>DEPARTMENT OF RADIOLOGY, STANFORD UNIVERSITY

**Purpose:** Procedures requiring endovascular instrument navigation do not yet benefit from stereo visualization, made possible by rotational acquisitions or C-arm CT imaging. The live instrument is imaged using monoscopic fluoroscopy and the conventional method of combining the stereoscopic vessel image with the monoscopic instrument image often places the vessel segment containing the instrument's tip at the wrong depth, creating depth confusion. We present a method that overcomes this problem by tracking the instrument's tip and adjusting the stereo disparity of the vascular images such that the portion of the vessel containing the tip always appears at the same depth as the instrument's tip. We conducted a pilot study to evaluate subjects' preference for either method.

**Materials and Methods:** We randomly presented 28 subjects (radiologists, 3D technologists, others) with 30 pairs of stereo images (anaglyph technique), representing the two methods side-by-side, with the simulated instrument in different vessel segments. Subjects responded to the question, "In which image is the tip of the instrument better depicted as being inside the vessel?" on a 7-point scale, where 0 indicated



A graph showing each subject's tendency to pick our method, when she/he expressed a preference. For example, subject #27 chose our method about 90% of the time when she/he had a preference.

no preference. We correlated subjects' responses with the degree of depth adjustment made in our method, image contrast, and other factors.

**Results:** Subjects had a preference only 56% of the time at depth adjustments <4 units, but 80% of the time at greater depths ( $p < .001$ ). When they had a preference, they chose our method 75% of the time (95% CI: 72-79%). Subject consistency varied: 19 of 28 chose our method from 75-96% of the time, 6 chose it from 42-67% of the time, and 3 chose it from 16-36% of the time.

**Conclusion:** As expected, at small depth adjustments subjects did not prefer one method over the other. For larger differences in depth

between the instrument's tip and the containing vessel, subjects typically had a preference and chose our method 75% of the time. We conclude that adjusting the depth of the vessel tree to the depth of the instrument is a promising technique for avoiding the limitations of the conventional method.

### REFERENCES/FUNDING SOURCE

RSNA, 2007. Supported by Siemens Medical Solutions.

## A Pilot Study Evaluating the Efficiency Of "Patch View": A New Paradigm for Reviewing the Output of a Computer-Aided Polyp Detection Method

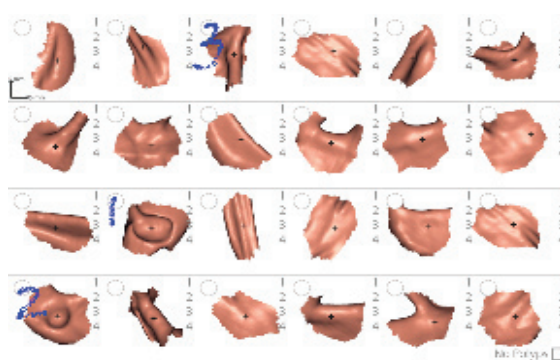
PADMAVATHI SUNDARAM, RONG SHI, CHRISTOPHER BEAULIEU, SANDY NAPEL

DEPARTMENT OF RADIOLOGY

**Purpose:** Computer-aided detection (CAD) methods present radiologists with a sorted list of voxels that are likely to contain a polyp. Since CAD methods are imperfect, true positive (TP) detections are not always found at the top of the sorted CAD output, increasing the radiologist's time to the first TP. In order to address this, we developed and evaluated a new paradigm for reviewing CAD output.

**Materials and Methods:** We ran our CAD method (the Smoothed Shape Operator (SSO)) on 32 supine CT colonography (CTC) cases containing a total of 32 polyps larger than 6 mm. For each case, the output of SSO was a sorted list of 24 surface patches that we arranged in a 4 X 6 grid and presented in print form to four blinded radiologists who scanned the "Patch View" and indicated the top three CAD hits that demanded further investigation. Optical colonoscopy (OC) records verified by an experienced radiologist were considered to be truth.

**Results:** For polyps larger than 6 mm, 77.7%, 83.3%, 66.6% and 55.5% respectively of the top three selections of the readers contained a TP. On average, 70.8% of the top three selections of the readers con-



Sample "PatchView" page used in this study, presented to the radiologist who indicated the top three patches of interest as shown.

tained a TP. The simultaneous availability of all the top 24 CAD outputs enabled the readers to get to the first TP with 1.2, 1.6, 1.6 and 1.4 FP selections respectively. On average, readers reached the first TP with 1.4 FP selections. In comparison, sequential review of CAD output resulted in the reader reaching the first TP with 4.9 FP hits. The average study time was 32 minutes.

**Conclusion:** Preliminary results suggest that this review method may be more efficient than sequential browsing of a sorted list of CAD hits, thereby reducing the radiologist's time to the first

TP by enabling quick rejection of obvious FP CAD outputs. As CTC becomes widely used, efficient incorporation of CAD results into the reading will become important in improving sensitivity and inter-observer variability in this low prevalence setting.

### REFERENCES/FUNDING SOURCE

NIH Roadmap for Medical Research Grant U54 GM 072970, NIH/NCI R01 CA 72023.

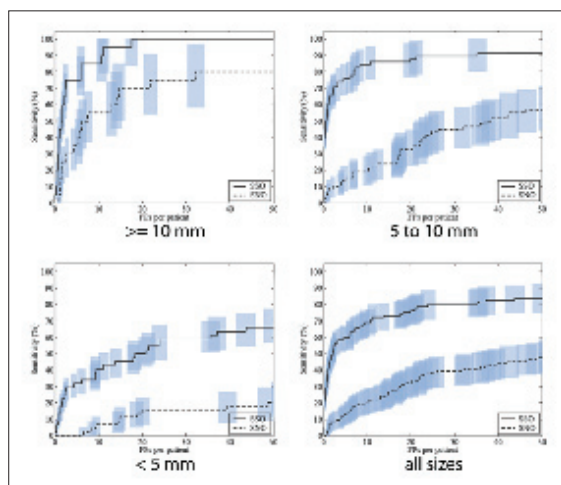
## Colon Polyp Detection Using Smoothed Shape Operators: Preliminary Results

PADMAVATHI SUNDARAM<sup>1</sup>, AFRA ZOMORODIAN<sup>2</sup>, CHRISTOPHER BEAULIEU<sup>1</sup>, SANDY NAPEL<sup>1</sup>

DEPARTMENTS OF <sup>1</sup>RADIOLOGY AND <sup>2</sup>COMPUTER SCIENCE

**Purpose:** Computer-aided detection (CAD) algorithms identify locations in Computed Tomographic (CT) images of the colon that are most likely to contain polyps. While curvature has been used to detect polyps, the estimates are typically noisy. We present the Smoothed Shape Operators method (SSO), which overcomes these issues by using a geometry processing approach to select polyp candidates.

**Materials and Methods:** Starting with a mesh representation of the colon surface, we calculated shape operators (SO) - at each vertex, a  $2 \times 2$  symmetric matrix, whose eigenvalues and eigenvectors are the principal curvatures ( $k_1$ ,  $k_2$ ,  $|k_1| \geq |k_2|$ ), and principal curvature directions respectively. We iteratively smoothed the SOs using a mesh edge length-based Gaussian weighting. We computed principal curvatures from the smoothed SOs and clustered the peak vertices ( $k_1$ ,  $k_2 < 0$ ) on the mesh. The score assigned to each cluster was the product of the maximum  $k_2$  and the integral of Gaussian curvature ( $k_1 * k_2$ ), both computed over the cluster vertices. The output was a list of candidate patches sorted according to this score. For evaluation, we compiled a database of 35 CTC exams containing



ROC curves comparing performance of SSO method (solid line) to SNO method (dashed line). Transparent rectangles at each point on the curve depict 95% confidence intervals for sensitivity and FP rate.

122 lesions: 44 ( $< 5$  mm), 58 ([5,10 mm) and 20 ( $\geq 10$  mm). An optical colonoscopy-based gold standard was used for evaluation. Comparison to an existing algorithm (Surface Normal Overlap (SNO)) was also performed.

**Results:** Our evaluation yielded the following results: (polyp diameter range; sensitivity; false positives/case): ( $\geq 10$  mm; 100%; 17.5), (5 to 10 mm; 89.66%, 21.23), ( $< 5$  mm; 59.09%; 23.89) and (overall; 80.33%; 23.89). At the same FP rates, the evaluation of the SNO method yielded (polyp diameter range; sensitivity): ( $\geq 10$  mm, 75%), (5 to 10 mm, 43.1%), ( $< 5$  mm, 15.91%) and (overall, 38.52%).

**Conclusion:** Preliminary results indicate that our method could act as a reliable first reader ( $\geq 10$  mm polyps) or second reader of CTC cases (5 to 10 mm polyps). This could help improve diagnostic confidence and evolve CTC

into an accepted procedure in the clinical setting.

### REFERENCES/FUNDING SOURCE

NIH Roadmap for Medical Research Grant U54 GM072970, NIH/NCI R01 CA72023.

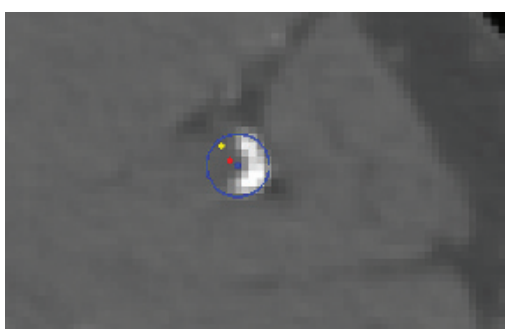
## Improved Vascular Centerline Restoration Through Occlusions Using Automated Detection of Calcified Plaque and Principal Component Analysis (PCA) in Lower Extremity CT Angiography (CTA).

TEJAS RAKSHE<sup>2</sup>, DOMINIK FLEISCHMANN<sup>1</sup>, JARRETT ROSENBERG<sup>1</sup>, JUSTUS ROOS<sup>1</sup>, MATUS STRAKA<sup>1</sup>, SANDY NAPEL<sup>1</sup>

DEPARTMENTS OF <sup>1</sup>RADIOLOGY AND <sup>2</sup>ELECTRICAL ENGINEERING

**Purpose:** To compute accurate estimates of centerlines in occluded parts of femoropopliteal arteries (FPAs), that can be used to create visualizations such as curved planar reformations, by detecting calcified plaque to refine the results of a knowledge-based algorithm.

**Method and Materials:** We built a database of FPA centerlines from lower extremity CTAs of 60 patients (30 with peripheral arterial occlusive disease and 30 without). Normal artery centerlines were tracked by a semi-automated method and diseased ones were tracked twice each by 4 expert readers and the mean was used as a reference standard. For each test case, the remaining set of centerlines from the same side was used as a database. A previously described PCA-based method was used to obtain an initial estimate of centerline in the occlusion. A score was assigned to each voxel in the vicinity of the estimate based on its density, its location and the shape of the cluster of similar intensity voxels around it. A region-growing algorithm segmented calcified plaque on a CT slice starting from each voxel with a high score on that slice. A circle was fitted to the convex boundary of the segmentation. The centers of all the circles were used for applying piecewise linear correction to the initial estimate to



The figure shows how calcification may help improve centerline estimation. The yellow dot is the PCA based centerline estimation and the red dot is the expert opinion. The center of the circle (in blue) fitted to the calcification provides a more accurate estimate.

get a final centerline. Point-wise maximum distance (MD) from the reference standard was used as the error metric. The method was tested on 8 patients with 10 FPA occlusions (5 left, 5 right). The occlusion lengths (OLs) ranged from 94mm to 397mm with mean 201mm.

**Results:** The MD for initial estimate ranged from 1.8mm to 6.1mm with mean 3.2mm. The MD for the estimate incorporating the calcifications ranged from 0.8mm to 4.3mm with mean 2.1mm. There was 38% reduction in MD error over the method using only the database. The estimate stays within the vessel radius for OLs up to 200mm.

**Conclusion:** The algorithm uses a database as well as image space CTA data to reconstruct centerlines with acceptable accuracy up to 200mm OL. It offers significant improvement over the PCA algorithm using only the database.

### REFERENCES/FUNDING SOURCE

Towards Cardiac C-Arm Computed Tomography, Lauritsch, G.; Boese, J.; NIH/NHLBI R01 HL67194; Swiss National Science Foundation, PBBEB 106796.

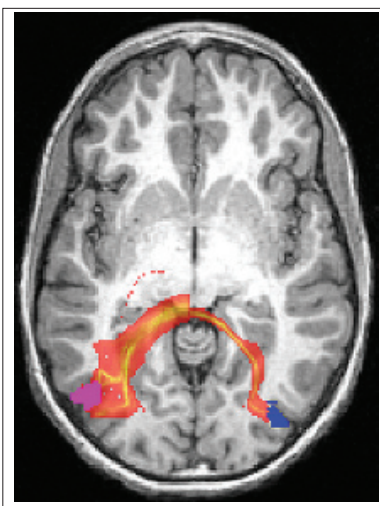
## Identifying the Most Likely White Matter Pathways Between Two Brain Regions

A.J. SHERBONDY<sup>1</sup>, R.F. DOUGHERTY<sup>2</sup>, M. BEN-SHACHAR<sup>2</sup>, S.H. CHEUNG<sup>2</sup>, S. NAPEL<sup>3</sup>, B.A. WANDELL<sup>2</sup>

<sup>1</sup>ELECTRICAL ENGINEERING, <sup>2</sup>PSYCHOLOGY, <sup>3</sup>RADIOLOGY

**Purpose:** Magnetic resonance diffusion weighted imaging coupled with fiber tractography (DFT) is the only non-invasive method for determining white matter pathways in the living human brain. While DFT is often used to discover new pathways, we propose a method that determines the most likely pathways connecting two regions of the brain that we are confident are connected and compare our results to current tractography algorithms.

**Materials and Methods:** Our probabilistic DFT algorithm (ConTrack) consists of three parts: a scoring algorithm to measure the likelihood of a pathway, a sampler to generate a large set of potential pathways, and an inferential step to identify the most likely pathways connecting two regions. We focus on two well-known white matter anatomies, (1) the connections between the corpus callosum (CC) and the middle temporal area (MT) and (2) the course of the optic radiations (OR). For both (1) and (2) we compare results of ConTrack to two of the most popular existing tractography techniques, streamlines tracing technique (STT) and the ProbTrack software package from Oxford University. In (1), we examine the locations of resulting pathways; based on prior anatomical knowledge, we assume these recovered pathways will have a region of significant overlap on



*ConTrack results connecting the left (magenta) and right (blue) MT to the CC. Resulting pathways are presented as projections of the 3D density of maps of the pathways onto an axial slice of a T1-weighted scan. Note that the other two algorithms used, STT and ProbTrack, were unable to find any pathways that were suggestive of connections between the three regions.*

their projection into the CC. In (2), we compare our estimates of likely OR pathways to those reported in the dissection and surgical literature.

**Results:** For experiment (1) ConTrack produces pathways for all subjects connecting the left and right MT to the CC with overlap at the CC (Figure 1). Both STT and ProbTrack are unable to produce pathways that connect these regions and therefore produce zero overlap for all four subjects. For experiment (2), ConTrack reproduces the OR pathways with position measurements along the pathway in agreement with the existing literature. STT and ProbTrack pathway position measurements do not agree with the same population measurements and seem to underestimate or ignore Meyer's loop.

**Conclusions:** ConTrack estimates known pathways at positions that are consistent with previous anatomical knowledge. These pathways are either invisible (MT to CC) or underestimated (OR) by two popular existing tractography algorithms.

REFERENCES/FUNDING SOURCE  
NIH Roadmap GM072970

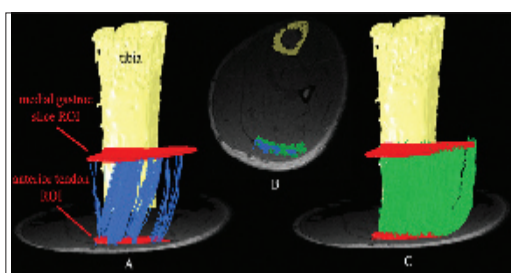
## Measuring Human Gastrocnemius Pennation Angle Utilizing Most Likely Pathway Distributions in Diffusion Tensor Imaging.

ANTHONY SHERBONDY<sup>1</sup>, SILVIA BLEMKER<sup>2</sup>, EDITH ARNOLD<sup>3</sup>, SANDY NAPEL<sup>4</sup>, SCOTT DELP<sup>3</sup>, AND GARRY GOLD<sup>4</sup>

DEPARTMENTS OF <sup>1</sup>ELECTRICAL ENGINEERING, <sup>3</sup>MECHANICAL ENGINEERING, AND <sup>4</sup>RADIOLOGY, AND <sup>2</sup>MECHANICAL ENGINEERING, UNIVERSITY OF VIRGINIA,

**Purpose:** To develop a new diffusion tensor imaging with fiber tractography (DTI-FT) algorithm, named MetroTrac, and to use it to create a distribution of most likely connections between two regions of interest (ROIs), thereby improving the estimation of muscle fascicle arrangements in vivo.

**Materials and Methods:** Recently, a previously available DTI-FT algorithm, called the Streamline Tracking Technique (STT), demonstrated in vivo characterization of three-dimensional arrangements in mouse skeletal muscle and in humans. Researchers have even verified fascicle arrangements estimated by these DTI-FT methods with direct anatomical inspection within Sprague-Dawley rats. However, the tractography literature is filled with examples of fibrous structures imaged with DTI that are invisible to the STT algorithm. We have previously implemented a probabilistic tractography algorithm that is designed to search a much broader space of possible pathways connecting volumetric regions and return the highest scoring subset of these pathways according to a principled scoring function. We compared average fascicle pennation angle of resulting pathways connecting the anterior tendon to a medial cross section of the gastrocnemius, defined before the start of the posterior tendon.



*Fascicle estimation within one subject between a section of the anterior tendon and a transverse slice through the belly of the medial head of the gastrocnemius muscle. (A,C) The curves show the fascicle estimates from the STT (blue) and MetroTrac (green) algorithms. (B) This transverse image shows the intersection of the STT estimates near the tendon ROI as blue dots and the MetroTrac estimates as green dots with area approximately 4 mm per dot.*

**Results:** We measured the mean±s.d. of the pennation angle between a 20 mm fascicle portion and a plane approximation to the tendon segment (Figure) in all three subjects to be 16±5°, 28±15°, 19±11° for STT and 19±8°, 25±8°, 18±9° for MetroTrac. In addition to these measurements demonstrating algorithmic agreement, they are also consistent with ultrasound and cadaveric measurements in the literature.

**Conclusions:** We have shown that our new algorithm estimates the pennation angle within a distal section of the medial head of the human gastrocnemius muscle in agreement on average with the previously used DTI-FT algorithm. However, we also demonstrate our new algorithm's ability to estimate fascicle arrangements within regions of the muscle that

are not represented by the previous DTI-FT algorithm's results. Thus, our method is able to guarantee estimates from any position along the tendon to any other ROI and thus make estimates that are not possible using the previous methods.

REFERENCES/FUNDING SOURCE  
NIH Roadmap GM072970, NIH R01-EB002524 and NIH R01-EB005790.



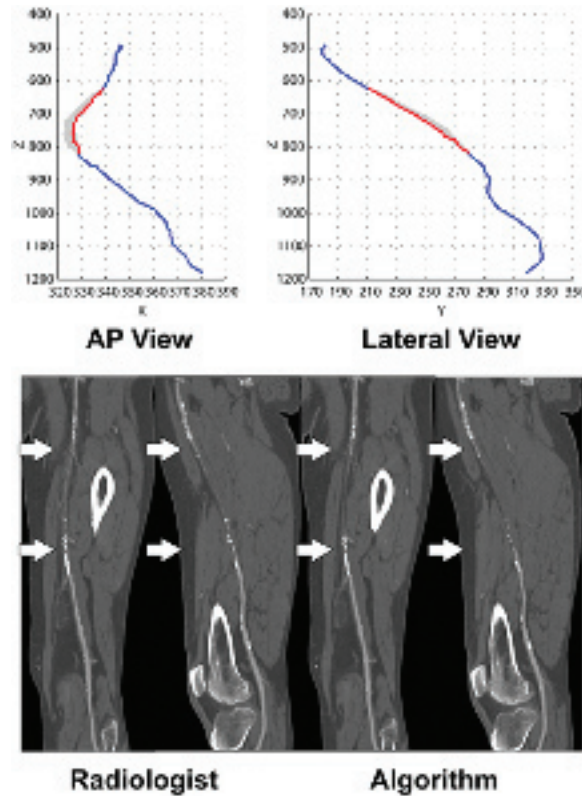
## Femoropopliteal Artery Centerline Interpolation Using Contralateral Shape

DAVID N. TRAN, DOMINIK FLEISCHMANN, TEJAS RAKSHE, JUSTUS E. ROOS, JARRETT ROSENBERG, MATUS STRAKA, AND SANDY NAPEL

DEPARTMENT OF RADIOLOGY

**Purpose:** Curved Planar Reformation (CPR) allows comprehensive visualization of arterial flow channels, but existing semi-automated centerline-extraction algorithms for CPR generation fail in severely diseased and occluded arteries. We explored whether contralateral shape information could be used to reconstruct centerlines through femoropopliteal occlusions.

**Materials and Methods:** We obtained CT Angiography datasets of 29 subjects (17m/13f, 19-86yo) without peripheral arterial occlusive disease and 5 consecutive subjects (1m/4f, 54-85yo) with unilateral femoropopliteal arterial occlusions. A gradient-based method was used to extract the femoropopliteal centerlines in non-diseased segments. Centerlines of the 5 occluded segments were manually determined by 4 experts, two times each. We compared contralateral intrasubject and ipsilateral intersubject femoropopliteal shape variability in the non-diseased subjects, and recorded the mean Euclidean Distance (ED) between the registered curves. Next, we interpolated missing centerlines in 2475 simulated occlusions of various occlusion lengths in non-diseased subjects. We used several curve registration methods to align the non-occluded segments, matched the endpoints of the occluded segments to the corresponding patent



The AP and Lateral views (top) show the patent (blue), interpolated (red), and the 2 standard deviation from the mean of the expert segments (gray bands). The AP and lateral views of expert-drawn CPRs and the AP and lateral views of algorithm-drawn CPRs are shown at the bottom from Left to Right, respectively. The white arrows mark the start and end of the occlusions.

endpoints, and recorded maximum EDs. In the 5 subjects with real femoropopliteal occlusions, we measured the maximum ED and the percentage of the interpolation that remained within a typical 3mm radius vessel.

**Results:** In the non-diseased subjects, we found that the mean  $\pm$  s.d. (mm) of the shape discrepancies were significantly ( $p < 0.001$ ) smaller ( $4.81 \pm 2.38$ ) for the group of intrasubject contralateral centerlines than intersubject ipsilateral centerlines ( $8.89 \pm 2.14$ ). In simulations using non-diseased subjects, our method produced centerlines that stayed within 3mm of a semi-automatically tracked centerline in occlusions up to 100 mm in length. In the actual clinical cases, we found the following [occlusion length (mm): error (mm)]: 16.5: 0.775, 42.0: 1.54, 79.9: 1.82, 145: 3.23, and 292: 6.13.

**Conclusions:** The symmetry in femoropopliteal arteries is conserved across a patient population and, thus the use of contralateral shape information, when available, is a promising method for the interpolation of centerlines through arterial occlusions.

## REFERENCES/FUNDING SOURCE

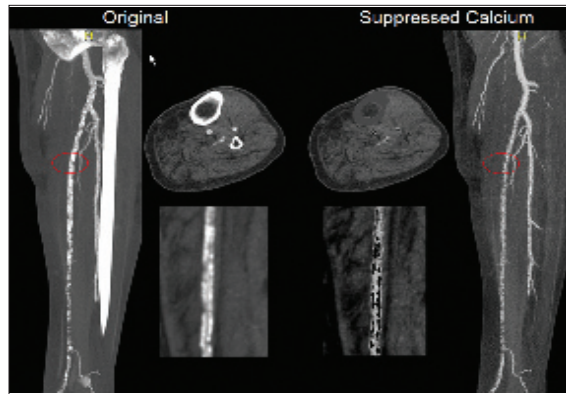
NIH/NHLBI 1R01 HL67194; American Heart Association Western States Affiliate; Stanford University Medical Research Scholars Program; Swiss National Science Foundation.

## Improving Bone And Calcified Plaque Identification and Removal Using Dual-Energy CT In Peripheral CT Angiography

DAVID N. TRAN, JUSTUS E. ROOS, MATUS STRAKA, DOMINIQUE SANDNER, HEDI RAZAVI, MINDY CHANG,  
NORBERT PELC, SANDY NAPEL, DOMINIK FLEISCHMANN, DEPARTMENT OF RADIOLOGY

**Purpose:** Bones and calcified plaque obscure flow channels and complicate interpretation of CT Angiography (CTA) images, requiring intensive postprocessing. We investigated the utility of Dual-Energy CT (DECT) for suppressing bones and calcified plaque in peripheral CTA.

**Methods and Materials:** We used basis material decomposition to compute the fraction of water (Fw), contrast medium (Fcm), and calcium hydroxyapatite (Fca) in each voxel. 1) Samples of contrast medium (CM) (0.1, 0.5, 1, 2mg/ml) and calcium hydroxyapatite (CA) (0, 50, 100, 200mg/ml) were scanned at 140 and 80kVp. We counted correctly identified CM ( $F_{cm} > F_{ca}$ ) and CA voxels ( $F_{ca} = 0$  for 0.0g/ml sample and  $F_{ca} > F_{cm}$  for others) in CM and CA samples, respectively. 2) Single-energy CT (SECT) and DECT runoffs were acquired with a dual-source CT scanner (140 and 80kVp). In 140kVp SECT, we counted correctly identified CM ( $600 \leq CM < 400HU$ ) and bone ( $> 600HU$ ) voxels using semiautomated segmentation as a reference. Similarly in DECT, we counted correctly identified CM ( $F_{cm} > F_{ca}$ ) and bone voxels ( $F_{ca} > F_{cm}$ ). 3) Two pressure-fixed cadaveric femoropopliteal arteries were filled with CM (2.67mg/ml), submerged in 20L of water, and scanned at 140 and 80kVp. New images were constructed by subtracting the computed Fca from each voxel and compared to 47 $\mu$ m



DECT can be used to suppress calcium (right) from the original CT image (left).

resolution microCT images.

**Results:** 1) Attenuation differences ( $\Delta HU$ ) between 140 and 80kVp of CM ( $\Delta HU$ : 11.3, 47.4, 122, 211) were greater than CA ( $\Delta HU$ : 4.03, 24.5, 61, 140). DECT identified 74.5, 96.9, 100, and 100% of CM voxels, and 77.0, 96.9, 96.9, and 100% of CA voxels, in the 4 CM and 4 CA samples, respectively. 2) In the run-offs, DECT identified more CM and bone voxels (85.8 and 82.3%, respectively) than SECT (59.3 and 22.17%, respectively). 3) The cadaver DECT images showed dramatic removal of calcified plaque with little change elsewhere, using microCT images as a reference.

**Conclusion:** DECT improves bone and calcified plaque identification and suppression compared to SECT. The improvement is substantial when concentrations of CM and CA are high, but noise may impact accuracy at lower concentrations. Incorporation of new information from DECT into novel algorithms may improve CTA utilization in patients with peripheral occlusive disease.

### REFERENCES/FUNDING SOURCE

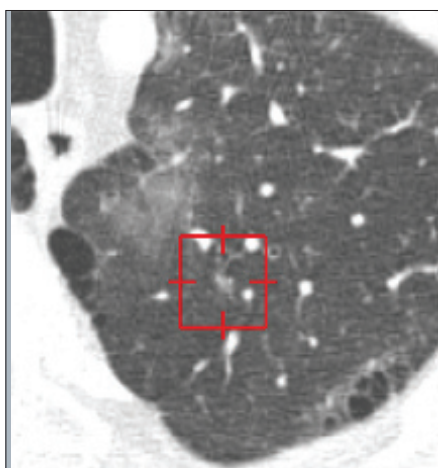
Presented at SCBT/MR 30th Annual Meeting, 2007.  
Supported by American Medical Association Seed Grant and Stanford University Medical Research Scholars Program.

## Characteristics of True Positive (TP) Lung Nodules Detected by Computer-aided Detection (CAD) but Subsequently Rejected by Radiologists on Chest MDCT Scans

C. A. YI, D. A. OLSEN, J. E. ROOS, D. S. PAIK, S. NAPEL, G. D. RUBIN  
DEPARTMENT OF RADIOLOGY

**Purpose:** To understand the reasons why true positive (TP) nodule candidates by computer-aided detection (CAD) are rejected by radiologists, so that we may ultimately improve radiologist's performance using CAD.

**Materials and Methods:** Twenty adult outpatients were examined with chest MDCT (1.25-mm section thickness and 0.6-mm interval) for pulmonary nodules. Three radiologists independently performed a free search of the scans. Subsequently, CAD detections were presented to the radiologists as a list of candidates ordered by CAD score. When a CAD-detected nodule had been identified during free search, the detection was excluded from that radiologist's list. Radiologists assigned confidence levels of 0-5 to each detection. We considered confidence levels of 0-2 and 3-5 as "rejected" and "accepted" lesions, respectively. The reference standard was established by two additional thoracic radiologists in consensus who performed free search and blindly evaluated all reader and CAD detections. All noncalcified pulmonary nodules  $\geq 3$ -mm in diameter in the reference standard were evaluated for size, location, relationship to bronchovascular bundle, contour, margin, and solid vs. non-solid. The



*Axial thin section CT image of the thorax (1-mm section thickness) shows a 4-mm sized nodule (center of the square) in left upper lobe. This nodule is a partly solid lesion with some portion of ground glass attenuation and consolidation internally and an ill-defined margin. This nodule was not detected on free search by any of the three readers. On subsequent presentation as nodule candidate by CAD, one reader accepted this lesion as a nodule with confidence score 3; possibly a nodule, but two readers rejected this lesion as not a nodule with confidence score 0.*

characteristics of rejected nodules were compared to those of accepted nodules using Mann-Whitney test and Fisher's exact test.

**Results:** Of 190  $\geq 3$ -mm noncalcified nodules in the reference standard, 119 were missed by at least one radiologist on free search. 81 of these 119 were detected by CAD. Following radiologist review of CAD detections, 39/81 were accepted by all three radiologists, but 42/81 were rejected by at least one radiologist. When compared with the accepted nodules, the rejected nodules were significantly smaller ( $4.9 \pm 1.8$  vs.  $3.8 \pm 0.8$  mm;  $p < 0.01$ ), had ill-defined margins (0/39 vs. 11/42;  $p < 0.01$ ), and were non-solid (0/39 vs. 8/42;  $p < 0.01$ ).

**Conclusion:** Pulmonary nodules that are detected by CAD, but subsequently rejected by radiologists, are significantly smaller, more likely to have ill-defined margins, and non-solid. The assessment of characteristics of true positive nodules that are detected by CAD, but subsequently rejected by radiologists may be useful for improving CAD efficacies and maximizing the benefit of CAD.

### REFERENCES/FUNDING SOURCE

To be presented at RSNA, 2007.  
Funded by NIH/NCI R01 CA109089.

## Lung Nodule CAD to Detect Lung Tumors in Mice

S. BUDHIRAJA<sup>1,2</sup>, H. JILL LIN<sup>2</sup>, PHUOC T. TRAN<sup>3</sup>, P.K. BENDAPUDI<sup>3</sup>, D. FELSHER<sup>3</sup>, D.S. PAIK<sup>2</sup>  
DEPARTMENTS OF <sup>1</sup>COMPUTER SCIENCE, <sup>2</sup>RADIOLOGY AND <sup>3</sup>MEDICINE

Although previously published SNO CAD algorithm has been used on humans to detect lung nodules for different cancer types, it has not been applied to molecular imaging. The purpose of our study was to apply and evaluate the existing SNO CAD algorithm to detect and localize lung tumors in micro CT studies of transgenic mice. Ultimately, we aim to improve small animal imaging studies by applying automated and quantitative image analysis. SNO CAD uses the local density of normals projected inward from the surface of a structure to obtain a set of candidate locations most likely to be tumors. It is thus able to locate the approximate centers of these structures. We took the top 94 likely tumor locations as detected by SNO CAD. These were correctly labeled as being actual tumors or false positives by comparing them with the reference standard of tumor locations within the dataset. A total of 40 tumors were present in eleven different mice. CT images were

automatically calibrated to obtain the correct air and lung intensities. The lung regions were automatically segmented before SNO CAD was applied to detect tumors. The algorithm was able to achieve a sensitivity of 71.05% at a rate of 11.63 false positives per mice, and a sensitivity of 86.84 at a rate of 15.81 false positives per mice. Most of the tumors are very small being less than 3 mm in size. These findings imply that SNO CAD can run effectively on mice data and can be used to detect lung tumors which can be further used for automated quantification such as volumetric measurement.

### REFERENCES/FUNDING SOURCE

NIH grant P50 CA114747



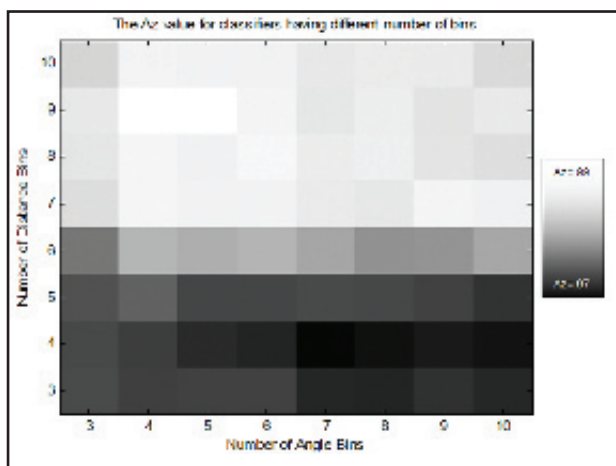
## Robustness of the GSAP (Geometric Shape Analysis without Parameters) FP Reduction Filter for Lung Nodule CAD in Chest CT

ARPIT AGGARWAL, DAVID A OLSEN, JUSTUS E ROOS, GEOFFREY D RUBIN, SANDY NAPEL, DAVID S PAIK  
DEPARTMENT OF RADIOLOGY

**Purpose:** To test the robustness of the GSAP algorithm for FP reduction in lung nodule CAD, we measured its response to (1) different primary CAD methods as input, (2) CAD candidate centeredness, (3) lung segmentation, (4) different machine classifiers and (5) histogram binning.

**Methods and Materials:** The GSAP filter was evaluated on 2 different initial detector CAD algorithms, SNO (Surface Normal Overlap) and CP (Clustering Process). GSAP was also tested using different machine classifiers like LR (Logistic Regression) and SVM (Support Vector Machines). 2D shape signature histogram bins were varied from 3 to 10 and the ROC on the SNO output was calculated for all 64 combinations. To measure the susceptibility of GSAP's features to the centeredness of initial CAD locations, the detections were jittered by varying percentages in random directions. Finally GSAP was tested on segmented and non-segmented lung CT data. For these evaluations, 20 chest CT scans were performed and there were a total of 290 non-calcified nodules (187 nodules  $\geq 3$  mm). 20-fold cross-validation was used to assess GSAP on all 290 nodules.

**Results:** GSAP filter improved SNO performance from 33.5% sensitivity at 10 FPP (FPs per Patient) to 76.8% at 10 FPP. Also CP's



Area under the ROC curve for 20 fold cross validation plotted against the number of bins (lighter intensity cells represents higher Az value). The range of Az values remains very high between 0.97 and 0.99 for all different input parameter combinations.

increased from 43.8% sensitivity to 71.9% at 10 FPP. GSAP with LR achieved a sensitivity of 77.3% at 50 FPP. When SVM was used, a sensitivity of 82.2% was achieved at 50 FPP. ROC Az varied between .970 to .985 as the 2D shape signature histogram bins were varied amongst 64 combinations. In the jitter experiments, the Az values for the ROCs were 0.97 (25% jitter), 0.97 (50% jitter) and 0.96 (75% jitter). GSAP sensitivity was 75.7% at FPP of 10 with SNO on un-segmented lung CT data and 76.8% at 10 FPP on segmented data.

**Conclusion:** GSAP was demonstrated to be extremely robust to various inputs (primary CAD, jitter, lung segmentation) and changes in its own constituents (classifiers, bins). GSAP's

shape signatures are very intrinsic to the specific shapes being analyzed which contributes to its remarkable utility as a FP reduction filter. The GSAP method of FP reduction for CAD has been shown to be very robust to a variety of conditions.

**REFERENCES/FUNDING SOURCE**  
NIH grant R01 CA109089.

## A Novel Statistical Methodology for the Evaluation of Image Segmentation

JIANTAO PU, GEOFFREY D RUBIN AND DAVID S PAIK  
DEPARTMENT OF RADIOLOGY

**Purpose:** Numerous methods exist for evaluating segmentation results but it is still very hard to describe the performance fully in an intuitive and consistent way, which has prevented universal adoption of a single evaluation methodology. Our goal is to provide an intuitive but statistically sophisticated approach to evaluate segmentation performance.

**Methods and Materials:** Any segmentation results possibly including the reference standard can be represented in the form of 2D or 3D shapes or boundaries. To evaluate the fitting between different shapes or boundaries, our proposed method uses the statistical distribution of a novel non-Euclidean shape distance function that distinguishes undersegmentation from oversegmentation. The second-order moment statistic is non-negative, symmetric and satisfies the identity of indiscernible.

**Results:** The histogram generated by the proposed method allows for detailed examination of the segmentation performance, including the proportion and magnitude of under- and over-segmentation errors reminiscent of ROC curves. Unlike the Hausdorff distance metric, our

method satisfies the symmetry property and is not completely reliant on a single (maximum or minimum) distance measurement. The overall performance may be summarized with second-order moment statistics, which yields an intuitive shape distance in millimeters and also allows for simple and robust statistical hypothesis testing. This symmetric error function could also be applied in a contour agreement paradigm where a reference standard does not exist and non-symmetric error functions are problematic.

**Conclusion:** As compared to other available evaluation methods, the proposed statistical approach is not only simple to implement and but also reflects the segmentation performance locally and globally in an intuitive and consistent way.

**Clinical Relevance/Application:** The presented method can be used to present the difference between the segmented results and the reference standard in a statistical way.

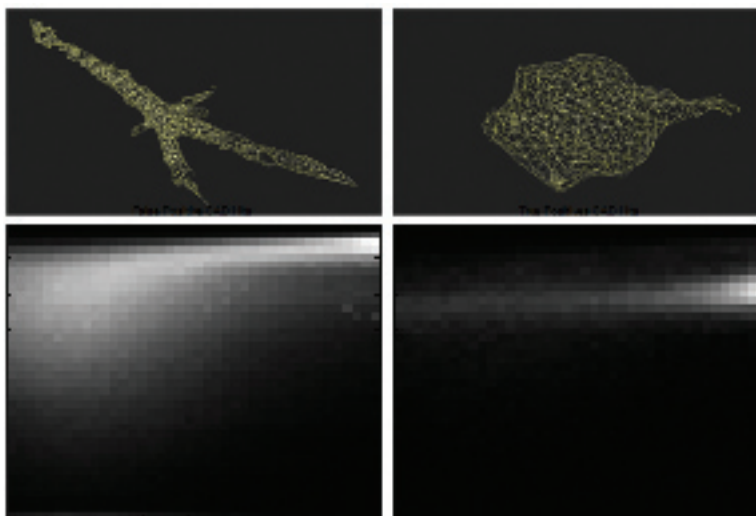
**REFERENCES/FUNDING SOURCE**  
NIH grant R01 CA109089.

## GSAP (Geometric Shape Analysis without Parameters): A Lung Nodule CAD (Computer Aided Detection) False Positive Reduction Algorithm which uses a Novel Non-parametric Shape Analysis Approach

ARPIT AGGARWAL, DAVID A OLSEN, JUSTUS E ROOS, GEOFFREY D RUBIN, SANDY NAPEL, DAVID S PAIK  
DEPARTMENT OF RADIOLOGY

**Purpose:** For a given CAD algorithm, achieving higher sensitivity occurs concurrently with an increase in FP (false positive) rate. The purpose of this work was to develop an algorithm to re-rank lung nodule CAD detections so that false positives decrease in rank relative to TPs (true positives) for an overall improvement in performance.

**Method and Materials:** We have designed GSAP to segment the relevant local shape features and then create a non-parametric shape signature that distinguishes between lung nodules and typical CAD false positives. A support vector machine is used to create a new ranking of CAD locations. For evaluation, the method was given our previously published SNO CAD algorithm's detections from 20 chest CT scans containing a total of 290 non-calcified nodules (187 nodules being  $\geq 3$  mm in size). 20-fold cross-validation was performed on all 290 nodules to assess the FP reduction algorithm.



*Model (top row) and shape signature (bottom row) of typical false positive (left) and true positive nodule (right).*

**Results:** The algorithm achieved an area under the ROC curve value of 0.99 in classifying all of SNO CAD's output. In particular we were able to achieve a specificity of 89.3% at 97.3% sensitivity for nodules of all sizes detected by SNO CAD. Overall detection performance improved from 696.0 FP/patient to 8.2 FP/patient while maintaining the sensitivity at 76.2%.

**Conclusion:** Our novel shape analysis algorithm was able to dramatically improve the performance of an existing CAD algorithm by successfully downgrading false positives relative to actual lung nodules.

CAD algorithms will gain utility when they can maintain low FP rates at high sensitivity and GSAP takes a major step in this direction by reducing ranks of FP detections.

### REFERENCES/FUNDING SOURCE

"Lung Nodule CAD False Positive Reduction Using a Novel Non-parametric Shape Analysis Approach in Chest Ct."  
NIH grant R01 CA109089..

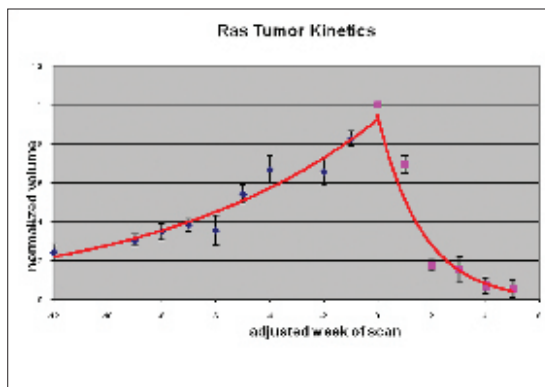


## Methodology to Characterize Lung Cancer Growth and Response to Targeted Therapy Using Quantitative Analysis of Small Animal Imaging

H. JILL LIN<sup>1</sup>, PHUOC T. TRAN<sup>2</sup>, SHRADHA BUDHIRAJA<sup>1,3</sup>, PAVEN K. BENDAPUDI<sup>2</sup>, DEAN W. FELSHER<sup>2</sup>, DAVID S. PAIK<sup>1</sup>  
DEPARTMENTS OF RADIOLOGY<sup>1</sup>, MEDICINE<sup>2</sup>, AND COMPUTER SCIENCE<sup>3</sup>

With the availability of small animal imaging techniques it is possible to track tumor growth and response to targeted therapy serially. Using different conditional transgenic models of murine lung cancer we hypothesized that statistical models could be constructed from quantitation of tumor growth and following oncogene-inactivated regression.

Two conditional transgenic lung tumor prone mouse cohorts were studied. These tumors were tracked using non-invasive serial microCT technique. In order to quantify tumor progression and regression, segmentation of lung tumor nodules in three-dimensions was performed on the microCT images using the level set segmentation algorithms that are based on the concept of active snakes implemented in ITK\_Snap. Tumor volumes were then computed from the segmentation, normalized with respect to its own largest volume and used for the analysis of the temporal changes in lung tumors. Statistical models of tumor behavior were constructed by fitting exponential curves to the growth and regression volumes separately for each tumor. Doubling time and regression half-lives were calculated.



Imaging-derived growth kinetics of oncogene dependent tumor growth and regression.

Our data suggests that tumor behavior can be modeled with exponential functions regardless of the oncogene used to induce tumors. The R2 values of the exponential curves for each data-set ranged between 0.92-0.95 for tumor growth and regression for two separate oncogenic pathways. In addition, quantitating and modeling these separate oncogene-dependent tumor cohorts allowed us to find novel difference in tumor behavior not apparent otherwise.

Oncogene-dependent tumor growth and regression following oncogene-inactivation can be modeled well by quantitation of serial microCT imaging data. The R2 values indicate that the complex biology of oncogene-dependent tumor growth and regression follows an exponential function.

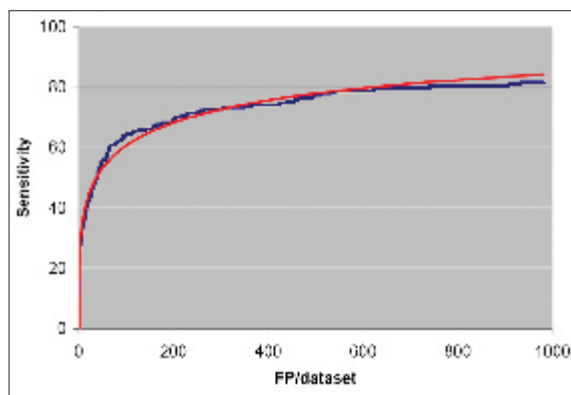
REFERENCES/FUNDING SOURCE  
NIH grant P50 CA114747 and NIH grant R25 CA118681.

## A Novel Parametric Free-response ROC (FROC) Methodology

DAVID S PAIK, DAVID A OLSEN, JUSTUS E ROOS, GEOFFREY D RUBIN  
DEPARTMENT OF RADIOLOGY

Purpose: While ROC analysis is desirable from an outcomes analysis perspective, FROC analysis can be better suited for detailed analysis of detection/classification and has greater statistically power. While ROC analysis is a mature field, FROC analysis has remained problematic, especially with regard to parametric modeling. The purpose of this work was to develop a novel parametric model for FROC analysis that does not rely on the same assumptions as current FROC models such as alternative FROC (AFROC) or initial detection and candidate analysis (IDCA).

Method and Materials: Whereas AFROC and IDCA rely on the Bunch transform between ROC space and FROC space, our model makes no attempt to transform to ROC space but rather to create a fully FROC parametric model in its own right. The parametric model has 2 free parameters just as does the binormal ROC model. These two parameters are direct indicators of overall accuracy and balance between early (low false positives) lesion detections and late (high false positives) detections.



Example CAD output FROC curve (blue) and parametric model fit (red).

Results: We have developed an alternative axis system that is analogous to normal deviate space for ROC, where parametric curves are transformed to straight lines. We have also developed a statistically robust method for dealing with censored data (i.e., lesions undetected by a reader or CAD) using methods similar to those used in Kaplan Meier analysis. Finally, we have developed a maximum likelihood estimator based on the method of scoring. Application of this methodology to various CAD outputs leads to extremely good fitting.

Conclusion: We have developed a novel FROC parametric model that does

not rely on the Bunch transformation that treats FROC curves as first-class citizens rather than as modified ROC curves. This statistical model will enable better statistical studies involving lesion detection and characterization that cannot be achieved using conventional ROC analysis.

REFERENCES/FUNDING SOURCE

A parametric model of FROC curves using reliability theory, in preparation.

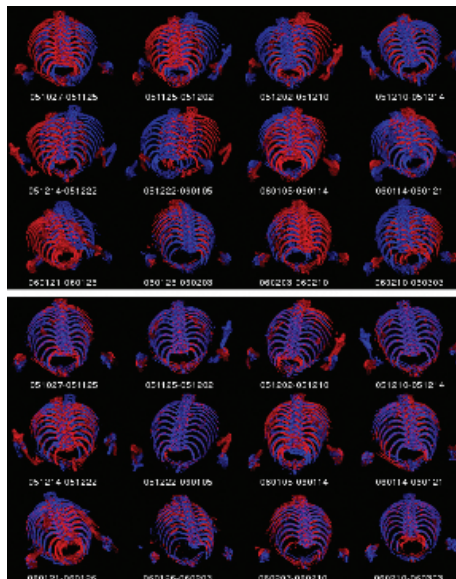


## A Segmentation and Registration Framework for Serial 3D Images of Mice

GUANGLEI XIONG<sup>1,2</sup>, SHRADHA BUDHIRAJA<sup>2,3</sup>, JILL LIN<sup>2</sup>, DEAN FELSHER<sup>4</sup>, PAVAN BENDAPUD<sup>4</sup>, DAVID PAIK<sup>2</sup>  
DEPARTMENTS OF BIOMEDICAL INFORMATICS<sup>1</sup>, RADIOLOGY<sup>2</sup>, COMPUTER SCIENCE<sup>3</sup>, AND MEDICINE<sup>4</sup>

Recent advances in genomics and proteomics have led us better understanding many human diseases and improving their diagnosis and treatment. Mice are the mammalian model well suited for the study of many human diseases. Recent advances in small animal imaging allow us to non-invasively track anatomical and physiological changes over a long period of time. In a high-throughput setting, manual evaluation of large image datasets generated is tedious, time-consuming and is difficult to obtain objective and reproducible interpretations. Therefore, automatic and quantitative analysis is desired. This study is carried out as part of efforts to characterize oncogene-induced tumors in a transgenic mouse lung cancer model. Segmentation and registration of serial 3D images are prerequisites to establish correspondences and measure tumor changes quantitatively. Traditionally, analysis was done manually. Herein, we propose a novel framework for automating this task. To our knowledge, this is the first application of segmentation and registration for serial 3D images of small animal.

The mouse body is extracted at every time point by segmentation using grayscale mathematical morphology. Then, a pairwise rigid registration is applied to address postural (position and orientation)



A full image set before (top) and after registration (bottom). For the purpose visualization of the results, only the bones are shown. Note the registration is done on whole volumes.

changes between consecutive time points. In order to capture the anatomical and physiological changes, pairwise non-rigid registration based on “Demons” algorithm is followed. The correspondences can be constructed from the obtained rigid transform and deformation field. A full serial 3D image set of mice are presented to demonstrate our approach (see the figure). Clearly, the mice images at consecutive time points align well after registration. To evaluate the results statistically, five identical points inside the mouse body from the consecutive time points are selected and compared before and after registration. A paired sample t-test shows significant improvements of mice alignment ( $p < 0.0001$ ).

The results from our implementation of this framework are demonstrated. With successful segmentation and registration, a number of applications, such as track lung tumors automatically and quantitatively, become possible. We believe our approach is generic enough to be applied to other applications by replacing the components with other similar and specialized methods. Our future direction

is to build a more user-friendly interface for this framework and test our approach on more data and applications.

### REFERENCES/FUNDING SOURCE

NIH grant P50 CA114747

## Quantitative Evaluation of the Lung Segmentation in CT Scans Obtained by the Adaptive Border Marching Algorithm

JIANTAO PU, GEOFFREY D RUBIN, SANDY NAPEL, JUSTUS E ROOS, CHIN A YI, DAVID S PAIK  
DEPARTMENT OF RADIOLOGY

**Purpose:** In computer-aided detection of lung nodules, automatic lung segmentation is widely used to narrow the search space and eliminate non-lung false positive detections. Our objective is to evaluate the lung segmentation performance of the Adaptive Border Marching Algorithm (ABMA), which aims to include juxtaleural nodules while minimizing oversegmentation in other regions, by comparing it against a manually drawn gold standard.

**Method and Materials:** To evaluate the lung segmentation performance, the experiments in this paper evaluated: (1) percentage of re-inclusion of juxtaleural nodules, and (2) per-voxel oversegmentation and undersegmentation ratios. Whether a juxtaleural nodule was correctly included or not was determined by a radiologist to see whether there is any obvious concavity along the lung boundary. To measure the fitting between the lung surfaces obtained by ABMA and the lung surfaces in the reference standard, we computed the distribution of the shortest Euclidean distances between the points from the segmentation result and the reference standard for both over- and under-segmentation. 20 MDCT chest scans were used for testing where nodule location and lung borders were determined by three radiologists.

**Results:** The mean number of lung surface points per case was 501,891. 100% of juxtaleural nodules were included following segmentation. The mean oversegmentation rate was 0.43%, and the mean undersegmentation was 1.63%. For undersegmentation, the 95th percentile distance was less than 2 mm; the 80th percentile was 0.0 mm and the maximum error was 34 mm. For oversegmentation, the 95th percentile was less than 1mm; the 80th percentile was 0.0 mm and the maximum error was 5 mm. The majority of undersegmentation error was concentrated in the hila and in one case due to substantial consolidation.

**Conclusion:** The ABMA can achieve a well-segmented lung boundary, thereby reducing CAD execution time and FPs, without exclusion of juxtaleural nodules.

**Clinical Relevance/Application:** The ABMA method can include all juxtaleural in our datasets with minimal over- or under-segmentation, thus acting as a robust pre-cursor to computer-aided detection of lung nodules.

### REFERENCES/FUNDING SOURCE

NIH grant R01 CA109089.

## Simulating the Health Insurance Program (HIP) Screening Mammography Trial of New York

RAY S. LIN<sup>1</sup>, BRONISLAVA M. SIGAL<sup>2</sup>, AND SYLVIA K. PLEVITIS<sup>2</sup>  
DEPARTMENTS OF <sup>1</sup>BIOMEDICAL INFORMATICS AND <sup>2</sup>RADIOLOGY,

The randomized controlled trial conducted by Health Insurance Program (HIP) of Greater New York demonstrated a breast cancer mortality reduction of approximately 24% due to screening mammography. We simulated this trial to further validate our natural history model of breast cancer.

We simulated the study and control arms of the HIP Trial with one million subjects in each arm. Subjects in the study group were offered four annual screening examinations after entry while subjects in the control group were recommended to undergo usual care. We randomly selected two-third of the subjects in the study group to participate in screenings in order to account for screening refusers in the HIP trial. Different screening schedule patterns were also simulated in proportion to the patterns observed in the HIP trial. The annual incidence rates were input based on the incidence observed in the HIP control group. Parameters for NHM model for stage progression and clinical detection were estimated based on SEER. We assume the median doubling time is half year and the median tumor diameter detected at screening is 16 mm.

Our model matches the actual incidence rates in the HIP study group within 95% confidence intervals. The detection rates at each screening in the simulations were slightly lower than the observed rates whereas the incidence rates of interval detected cases were slightly higher than the observed rates. Comparing tumor size and stage distribution at detection against the HIP trial, the simulations showed smaller tumors but matched the stage. In general, mortality and survival rates in both the study and the control groups matched the HIP trial within 95% confidence intervals.

Next, we will use our natural history model of breast cancer to estimate the effect of screening and the use of hormone replacement therapy on breast cancer incidence and mortality.

REFERENCES/FUNDING SOURCE  
NIH CISNET grant (U01CA088248)

## Identification of the Gene Regulatory Program Governing Transformation of Follicular Lymphoma to Diffuse Large B Cell Lymphomas

ANDREW J. GENTLES<sup>1</sup>, SU-IN LEE<sup>2</sup>, DAPHNE KOLLER<sup>2</sup>, SYLVIA K. PLEVITIS<sup>1</sup>  
DEPARTMENTS OF <sup>1</sup>RADIOLOGY AND <sup>2</sup>COMPUTER SCIENCE

Follicular lymphoma (FL) is an indolent malignancy of human germinal center B-cells that frequently undergoes neoplastic transformation to diffuse large B-cell lymphoma (DLBCL), with poor subsequent prognosis. Accompanying changes in gene expression are heterogeneous, and often conflicting. The Koller Lab developed a novel machine learning algorithm that identifies “modules” of co-regulated genes that are predictive of specific phenotype groups within a set of expression experiments. We applied the method to analyze a large set of FL/DLBCL microarrays, and identified ~30 modules of genes, which are highly associated with FL vs. DLBCL phenotypes. Many modules are enriched for specific GO processes, including ones associated with metabolism and immune system signaling. Two of the modules identified genes particularly relevant to transformation. One included downstream activation of the PAX5 transcription factor, which is central to establishment and maintenance of B-cell differentiation. The other implicated activation of STAT5 through the IL15 signaling pathway, which currently being targeted in flow cytometry analysis of signaling changes in FL/DLBCL transformation.

In order to reconstruct the regulatory program controlling module expression, it is necessary to provide a list of putative transcriptional regulators. We have constructed a set based on the following categories:

1) 2600 Transcription factors (TFs), assembled from Entrez Gene and a TF-specific microarray developed at the University of Washington; 2) RNA degradation and modification factors; 3) Chromatin modification factors; 4) Signaling pathways. We collated genes related to signaling pathways from the KEGG, Biocarta, and IPA pathway databases. In total we have assembled a list of ~5500 potential regulators which we are using to infer the regulatory program governing expression of the modules noted above.

We are currently using this list of putative regulators to generate gene regulatory programs controlling modules. This type of analysis has never before been performed in human data, being previously limited to yeast and mouse. Our work will provide the first application to human transcriptional networks. We will validate our results by evaluating our predicted regulatory modules and programs on independent datasets existing in the literature. Based on modifications in specific signaling pathways, we further aim to generate specific experimentally testable hypotheses about transformation that can be experimentally tested.

REFERENCES/FUNDING SOURCE  
ICBP NIH U56 CA112973.

## Statistical Modeling to Identify Biomarkers Differentially Expressed Among Responders Versus Non-responders Following Prostate Cancer Treatment

BABAK SHAHBABA<sup>1,2</sup>, ROBERT TIBSHIRANI<sup>2</sup>, PARAG MALLICK<sup>3</sup>, SYLVIA PLEVITIS<sup>1</sup>  
DEPARTMENTS OF <sup>1</sup>RADIOLOGY, <sup>2</sup>HEALTH RESEARCH AND POLICY, STANFORD UNIVERSITY  
AND <sup>3</sup>DEPARTMENT OF BIOCHEMISTRY, UCLA CEDARS-SINAI

We are developing novel statistical methods to analyze mass spectrometry data for the purpose of identifying biomarkers (i.e., protein/peptides) in the blood from cancer patients that predict treatment response. Our analysis supports the work of experimental molecular biologists in the Stanford Center for Cancer Nanotechnology Excellence whose aim is to identify and monitor biomarkers in the blood that predict response to getfinib (aka, Iressa) in prostate cancer patients. We provide the biologists a small subset of biomarkers (out of thousands of potential candidates) on which the tracking of response treatment could be performed most accurately.

Our current analysis is focused on an experiment designed by our biological collaborators, whereby A431 cells that respond to treatment and those that do not respond are analyzed by mass spectroscopy for peptides/proteins in three components: on the cell surface, intercellular, and secreted. Our methodological approach for choosing the biomarkers that are most differently expressed between responders and non-responders relies on a Bayesian framework whereby inferences are performed based on posterior predictive probabilities. In this approach,

we measure the amount of change in the posterior predictive probability of observed data (i.e., the abundance of a specific biomarker) from one experimental outcome to another (i.e., responders vs. non-responders). When a biomarker is significantly associated with the treatment, this probability is expected to change drastically under different conditions. The more significant a biomarker is, the larger the magnitude of this change. In this framework, selecting a subset of biomarkers is regarded as a decision theory problem. We have been applying our analysis to the datasets being provided by our collaborators and currently interpreting the results.

Once we have identified key biomarkers predictive of treatment response, we will extend our approach so that we can also identify the signaling pathways that behave differently between responders and non-responders.

REFERENCES/FUNDING SOURCE  
NCI U54 CCNE-TR .

## Conserved Boolean Relationships in Global Gene Expression

DEBASHIS SAHOO<sup>1</sup>, ANDREW GENTLES<sup>2</sup>, SYLVIA PLEVITIS<sup>2</sup>, DAVID DILL<sup>1</sup>  
DEPARTMENTS OF <sup>1</sup>COMPUTER SCIENCE AND <sup>2</sup>RADIOLOGY

We have discovered a large network of highly conserved Boolean relationships between gene expression levels. When each gene is assigned a threshold between “low” and “high” values of expression, we find many types of conserved relationships between gene pairs: (1) Genes A and B have an “equivalent” relationship when each gene is almost always high or low when the other is. (2) The genes have an “opposite” relationship if gene A is low when gene B is high and vice versa. These relationships hold approximately when the expression levels of the two genes are correlated or anti-correlated, but the relationships also hold for genes with similar behavior even when the relationship is far from linear. (3) In addition, we find asymmetric relationships, such as “if gene A is high, gene B is almost always high.” Such a relationship is asymmetric because it says nothing about the correspondence of the genes when gene A is low.

We have begun analyzing large amounts of publicly available microarray expression data to discover Boolean relationships between gene expression levels that conserved over a large variety of cancers, tissue types, disease conditions, and even across different species. As of this time, we have downloaded raw ex-

pression data from almost 16,000 Affymetrix arrays of various kinds, including over 14,000 human arrays. Our analysis has found over 86 million relationships between pairs of genes that held over 4,787 Affymetrix U133 plus 2.0 human microarrays, which have over 47,000 probesets. We searched for orthologous genes that have consistent behavior on human, mouse, and Drosophila arrays and found over 28,000 such relationships.

Identifying these conserved Boolean relationships should have several advantages, including providing new insights into robust regulatory relationships among genes, and differentiating between malignant phenotypes based on relationships between several genes. We are now in the process of exploring these networks, comparing the relationships with known biological relationships, analyzing sets of genes that are related to progression in lymphoma, and consulting with molecular biologists who are expert on certain groups of genes.

REFERENCES/FUNDING SOURCE  
ICBP NIH U56 CA112973



## Cross-species Mouse-human Comparison of Transformation of Lymphoma to More Aggressive Phenotypes

PAVAN BACHIREDDY<sup>1</sup>, JAN VAN RIGGELEN<sup>1</sup>, ANDREW J. GENTLES<sup>2</sup>, SYLVIA K. PLEVITIS<sup>2</sup>, DEAN W. FELSHER<sup>1</sup>  
DEPARTMENTS OF <sup>1</sup>MEDICINE/ONCOLOGY AND <sup>2</sup>RADIOLOGY

We hypothesize that cross-species comparison between human follicular lymphoma (FL) to diffuse large B-cell lymphoma (DLBCL) transformation and transgenic mouse MYC-driven primary/relapse tumors will elucidate mechanisms underlying the cancer transformation process. We performed a microarray analysis comparing the transformation of human follicular lymphoma to diffuse large B-cell lymphoma, with transformation of primary to relapsed T-cell lymphomas in a MYC-driven mouse transgenic model. We identified a small subset of genes that show the same pattern of changes in gene expression in both human and mouse transformation processes. 22 genes were up-regulated upon transformation, while 11 were down-regulated. Surprisingly, 22 these 33 genes are highly connected with each other. Using Ingenuity Pathway Analysis, these 22 genes were found to be associated with IL15 signaling, resulting in possible up-regulation of the FOS oncogene. FOS is associated with neoplastic transformation in a variety of cancers, and our cross-species comparison suggests a central mechanistic role for it in transformation of lymphomas to more aggressive types.

We are currently generating an additional 12 paired primary/relapse mouse samples from which mRNA has been extracted for gene expression microarray analysis to supplement our initial analysis. The microarray data is currently being generated on these new mouse samples and will be available imminently. These new samples of paired primary/relapse tumors resulted from a variety of experimental background including FVB and SCID immuno-compromised mice. These data will allow us to further characterize changes in gene expression relevant to the transformation process, and increase the statistical significance of our results. We will validate our results using real-time TaqMan PCR which can simultaneously interrogate several hundred target genes.

REFERENCES/FUNDING SOURCE  
ICBP NIH U56 CA112973.

## Microarray Analysis of Transcriptional Programs in MYC-dependent Tumor Cells During Progressive MYC Inactivation

CATHY SHACHAF<sup>1</sup>, ANDREW J. GENTLES<sup>2</sup>, DEBASHIS SAHOO<sup>3</sup>, SYLVIA K. PLEVITIS<sup>2</sup>, DEAN W. FELSHER<sup>1</sup>  
DEPARTMENTS OF <sup>1</sup>MEDICINE/ONCOLOGY, <sup>2</sup>RADIOLOGY, AND <sup>3</sup>COMPUTER SCIENCE

We have quantitatively probed the mouse MYC system through systematic variation of Myc expression.

For this analysis, we performed an experiment to determine if in MYC-dependent mouse T cell lymphomas. We used the mouse “Tet-system” to regulate MYC expression by titrating doxycycline in a lymphoma-derived cell line that requires maintenance of a transgenic Myc product to maintain its neoplastic phenotype. mRNA was extracted after regulating MYC levels for 24 hours and microarray gene expression data was generated to show how varying levels of MYC can induce different transcriptional programs.

Our computational analysis of the gene expression data identified a Myc threshold, below which the tumor cells die. We found critical changes in gene expression that occurred at or near the threshold level of MYC expression, and mapped these changes to cellular pathways and processes. The G1/S and G2/M cell cycle checkpoint pathways, and Death receptor/apoptosis signaling were highly implicated when MYC levels approached threshold levels of expression. We further analyzed changes in gene expression using a specifically-designed algorithm StepMiner that we developed to identify statistically significant binary shifts (steps) in gene expression. We found that 1573 array

probes showed a discrete increase in expression, and 2348 a discrete decrease, during the titration series. By characterizing the changes in gene expression that occurred “above MYC threshold”, “at MYC threshold”, “below MYC threshold” and “much below MYC threshold” we identified specific pathways implicated in the regression of tumorigenic phenotype during MYC inactivation. Detailed analysis of changes in pathways suggested a balance between MYC-stimulated proliferation, and apoptosis. Below MYC threshold, there is a decisive shift in gene expression profile in cells towards apoptosis and cell death, with re-establishment of cell cycle checkpoint activity. As a consequence, expression of transcription factors necessary for S-phase gene activation (E2F1, DP1) dropped at the MYC threshold. Thus by regulating MYC levels we were able to define and characterize expression profiles that impact the biological program of tumor cells.

REFERENCES/FUNDING SOURCE  
ICBP NIH U56 CA112973.

## Modeling the Effect of Prophylactic Oophorectomy on the Natural History of Breast Cancer among BRCA1/2 Mutation Carriers

PLEVRITIS SK<sup>1</sup>, SIGAL BM<sup>1</sup>, KURIAN AW<sup>2</sup>, DEPARTMENTS OF <sup>1</sup>RADIOLOGY AND <sup>2</sup>MEDICINE

Because of the significantly elevated risks of breast (BC) and ovarian (OC) cancer BRCA1/2 mutation carriers frequently recommended to undergo such invasive interventions as bilateral prophylactic mastectomy (PM) and prophylactic oophorectomy (PO). Unlike PM which is viewed as physical intervention not affecting disease progression, PO is considered to cause systemic changes which could affect natural history of the tumor. Our goal is to estimate the effect of PO on the natural history of breast cancer in order to estimate the impact of PO performed at different ages on life expectancy.

For PM it is assumed that if BC is not found at or before the time of PM woman has 90% chance of being cured and 10% chance of having the same BC history as without PM. For PO, we assumed that reported age-specific breast cancer incidence in BRCA1/2 mutation carriers represent incidence for the mixed population of women 30% of which underwent PO at age 45 that resulted in 50% BC risk reduction and 70% of those who chose not to undergo the procedure. We back calculated breast cancer incidence for women not undergoing PO. We also consider the effect of PO on all-cause mortality. We estimate that

PO at age 40 reduces life expectancy by 0.4 years due to an elevated risk of dying from cardiovascular disease and osteoporotic hip fracture to causes of death.

Two approaches are currently under investigation to model effect of PO on the natural history of breast cancer. Under the first approach we assume that undergoing PO before menopause results in slowing down of some of the tumors and curing others independently of the tumor natural history without PO. The second, simpler, approach is cure/non cure one; all tumors with onset between the age of PO and the age at menopause are cured. The second approach is producing results most consistent with the data, but we are still in a process of investigating the benefits and drawbacks of both approaches. This work should reveal a better understanding on the effect of hormone levels on the natural history of breast cancer, thus has implications for risk-reducing strategies and treatment.

### REFERENCES/FUNDING SOURCE

NCI U01CA088248 and Stanford Comprehensive Cancer Center

## On Relating Growth Rate, Stage Transitions, and Size at Symptomatic Detection for Different Models of the Natural History of Breast Cancer

BRONISLAVA M. SIGAL AND SYLVIA K. PLEVRITIS  
DEPARTMENT RADIOLOGY

Among US women, breast cancer is the most frequently diagnosed cancer and the second leading cause of cancer death. Screening for early detection of breast cancer promises to reduce breast cancer mortality. To estimate the benefit of current and new screening technologies, we compare screening outcomes predicted from four different stochastic models of the natural history of breast cancer.

The main assumptions of each model concern the tumor growth pattern, the tumor size at symptomatic detection and size of the tumor at transitions to advanced stages, such as metastases to the lymph nodes and distant organs. The main differences among the models are related to the assumptions on the stage transitions. Corresponding hazard functions for the four models are as follows: proportional to the tumor volume, tumor volume plus term independent of volume. Further term proportional to the derivative of the tumor volume was added. For the fourth model hazard is assumed to be proportional to the derivative of the function of the tumor volume. All models are fitted to the data on tumor size and stage from SEER database for the time period preceding dissemination of screening mammography. Models fits to the data are quite similar.

We mainly focused on comparison of the models growth rate properties, such as relationships between stage at symptomatic detection and tumor growth rate, which are not explicitly entered into models formulations. As expected, simulation studies showed that all four models predict different stage shifts.

Because natural history models of cancers are increasingly being used to estimate the impact of cancer control programs on the population, the criterion for model selection should not be simply datafit, but also a careful evaluation of the model predictions. Our four model produce similar fit to the data on unscreened population could have very different growth rate properties and varying screening outcomes. Our next step is to simulate existing screening trials with each of the four models and choose the model that most closely reproduces known screening outcomes.

### REFERENCES/FUNDING SOURCE

NIH/NCI CISNET grant (U01CA088248).

## A Natural History Model of Lung Cancer Applied to Simulating the Mayo Lung Project Screening Trial

MAKSIM PASHKEVICH, BRONISLAVA SIGAL, SYLVIA PLEVITIS, DEPARTMENT OF RADIOLOGY

Lung cancer is the leading cause of cancer-related death in the U.S. Screening high-risk individuals for lung cancer with Computed Tomography (CT) is currently being evaluated as a means to reduce lung cancer mortality. Understanding the natural history of lung cancer can help to assess the possible benefits of CT screening, as well as optimize screening schedules by population risk.

We developed a parametric stochastic model of the natural history of lung cancer that is based on biologically plausible assumptions and provides a reasonable fit to the data from the Mayo Lung Project (MLP), which was a randomized controlled trial of lung cancer screening by chest radiography and sputum cytology. The model assumes the exponential tumor growth, gamma distribution of the inverse tumor growth rate, symptomatic detection dependent on tumor size and stage, and size-driven metastatic progression mechanism. To obtain the complete likelihood estimator of the model parameters that accounts for detection type and includes censored cases and missing tumor sizes, we also model the cancer incidence and x-ray detection mechanism. We present joint estimates of model parameters, separately for non-small cell and small cell lung cancer types.

For non-small cell lung cancer, we estimate that the hazard of symptomatic detection is 12.8 times higher for tumors with clinically detectable metastases than for tumors without clinically detectable metastases and the median diameter at the onset of clinically detectable metastases is 4.1 cm. When simulating the MLP, we estimate that after seven years from trial randomization the mortality rate in the intervention arm was about 11% lower than in the control arm. Even though the MLP reported no mortality reduction due to screening, the MLP findings had a very wide 95% confidence interval. Due to the small size of the MLP trial, our finding of a 11% mortality reduction is consistent with the trial results. Also, if the control group did not receive an initial screening examination, we estimate a 16% mortality reduction due to chest radiography.

Our current work deals with extending the obtained results to address the mortality benefit and cost-effectiveness of screening for lung cancer with computed tomography.

REFERENCES/FUNDING SOURCE  
NIH/NCI R01 CA105366.

## The Impact of Screening Mammography on Age-Specific Trends in U.S. Breast Cancer Mortality

STEPHANIE L. BAILEY, BRONISLAVA SIGAL AND SYLVIA PLEVITIS, DEPARTMENT OF RADIOLOGY

We developed a simulation model that predicts U.S. breast cancer mortality trends from 1975 to 2000 and quantifies the impact of screening mammography on the overall age-adjusted trends. The primary objective of this work was to evaluate the impact of screening different age groups on the age-specific trends in breast cancer mortality.

We modified our existing Monte-Carlo simulation model wherein individual women undergo varying screening schedules and treatment regimes consistent with national trends and long-term outcomes are predicted. We extended the model to incorporate age-specific mammographic detection thresholds and tumor doubling times. We estimated the tumor doubling times by calibrating to the Surveillance, Epidemiology, and End Results (SEER) incidence trends. We estimated the age-specific mammographic detection thresholds by calibrating to both SEER incidence trends and data on screened tumor sizes provided by the Breast Cancer Surveillance Consortium (BCSC). We computed the contribution from screening mammography and adjuvant therapy on breast cancer mortality in the year 2000 for different age groups. The contribution of screening relative to adjuvant therapy increased with age.

If women ages 40-49 years were not screened, there would have been a 5.5% and 4.9% increase in mortality among women ages 40-49 years and ages 50-59 years at death, respectively. If women ages 50-59 years were not screened, there would have been a 10.2% and 8.1% increase in mortality among women ages 50-59 years and ages 60-69 years at death, respectively. If women ages 60-69 years were not screened, there would have been a 9.4% and 9.1% increase in mortality among women ages 60-69 years and ages 70-79 years at death, respectively.

Screening women above age 50 provided the largest breast cancer mortality reduction. This result was expected since younger women have a lower rate of screening, lowered sensitivity to mammography and faster tumor volume doubling times. However, an analysis based on life years saved may provide a different result for the magnitude of the benefit attributable to screening varying age groups.

REFERENCES/FUNDING SOURCE  
NIH/NCI Postdoctoral Fellowship in Advanced Techniques for Cancer Imaging; NIH/NCI CISNET grant (U01CA088248).

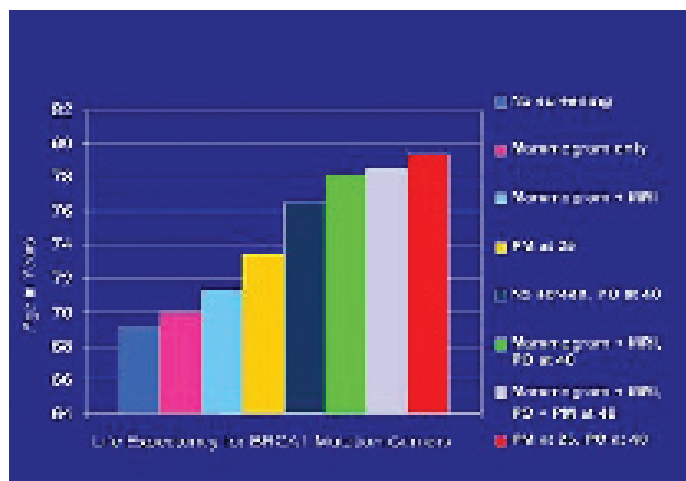


# A Clinical Decision Support Tool for BRCA1/2 Mutation Carriers Choosing Between Prophylactic Surgery and Breast Magnetic Resonance Imaging-Based Screening

ALLISON W. KURIAN<sup>1,2</sup>, BRONISLAVA M. SIGAL<sup>3</sup>, AND SYLVIA K. PLEVITIS<sup>3</sup>  
DEPARTMENTS OF <sup>1</sup>MEDICINE, <sup>2</sup>HEALTH RESEARCH AND POLICY, <sup>3</sup>RADIOLOGY

Women with deleterious mutations in the BRCA1/2 cancer susceptibility genes inherit lifetime risks of 45-65% for breast, and 11-39% for ovarian cancer; cancer risk management strategies involve earlier, more frequent, and more invasive interventions than in the general population. Prophylactic oophorectomy (PO) confers an 80-95% reduction in ovarian cancer risk, and approximately a 50% reduction in breast cancer risk for pre-menopausal women. Prophylactic mastectomy (PM) reduces breast cancer risk by 90-95%, but may have significant psychosocial side effects and a high incidence of complications. Intensive breast screening with mammography and magnetic resonance imaging (MRI) is an emerging alternative to PM for genetically predisposed women; however, breast MRI is associated with a high false-positive rate, and no associated mortality benefit has yet been demonstrated. Women with BRCA1/2 mutations must therefore choose between very different risk management approaches, when neither choice is free from significant side-effects, or supported by the highest level of evidence. We are performing a model-based decision support tool that estimates the life expectancy under various breast cancer risk management strategies for BRCA1/2 mutation carriers, including PM, MRI-based breast screening, and PO undertaken at different ages.

For the present analysis, we are using this model to assess the life expectancy of female BRCA1 and BRCA2 mutation carriers ages 25-



Comparison of life expectancy for a 25-year-old female BRCA1 mutation carrier under different risk-reduction strategies, including prophylactic mastectomy (PM), prophylactic oophorectomy (PO), screening mammogram, and magnetic resonance imaging (MRI)

69, under protocols of screening with annual mammography only compared to screening with annual mammography and MRI. We are evaluating the impact on life expectancy of adding PM and PO to each of these screening regimens. We are also computing life expectancy under scenarios of no screening, but PM at age 25 and PO at age 40, the ages at which clinical guidelines recommend initiating interventions to manage high cancer risks in BRCA1/2 mutation carriers. Initial results for a BRCA1 mutation carrier are presented in Figure 1; there is a notable effect of oophorectomy at age 40 on life expectancy.

Preliminary results suggest a strong beneficial effect of premenopausal oophorectomy on the

life expectancy of female BRCA mutation carriers. Revisions of the decision analytic model are ongoing, and final results are pending. Future work will include evaluating the tool among BRCA1/2 mutation carriers and then extending it to other groups of women at increased breast cancer risk, and other risk-reducing interventions.

## REFERENCES/FUNDING SOURCE

NIH R01 CA829040, U01 CA088248, R01 CA66785, the California Breast Cancer Research Program (11FB-0051), and Stanford Cancer Center 2007 Developmental Research Award in Population Sciences.

## T1 Oxymetry on High Grade Brain Tumor with Antiangiogenic Therapy

YI-SHAN YANG, JUNG-JIIN HSU, GARY GLOVER, SAMIRA GUCCIONE, DEPARTMENT OF RADIOLOGY

Glioblastoma multiforme (GBM) is a highly vascular malignant brain tumor. The tumor vasculature in GBM expresses the integrin  $\alpha v\beta 3$  in abundance. We have developed a targeted nanoparticle that can bind to this integrin and deliver therapeutic agents directly to these tumors. By complexing a suicide gene (mutated Raf gene (NP-ATP $\mu$ -Raf)) to this nanoparticle, we have successfully treated orthotopic rat brain tumor models. This gene disrupts the VEGF and FGF mediated signaling pathways that result in endothelial cell apoptosis. Significant tumor regression and long term survival have been observed on the rat RT2 and C6 tumor models. Because this approach destroys tumor vessels, we expect a drop in the oxygenation of the tumor in response to treatment and would like to follow the time course of changes that occur after treatment using *in vivo* MRI techniques.

Molecular oxygen (O<sub>2</sub>) is paramagnetic. Its presence in the tissue changes the longitudinal relaxation rate R<sub>1</sub> of hydrogen NMR. R<sub>1</sub> exhibits a linear relationship with the partial pressure of O<sub>2</sub> (pO<sub>2</sub>). Thus we can determine  $\Delta(pO_2)$  by measuring  $\Delta R_1$ . Recently, a fast T<sub>1</sub> mapping method was developed which can obtain a multi-slice T<sub>1</sub> map in just a few seconds, making dynamic mapping along a time course feasible (by definition  $R_1 = 1/T_1$ ). It is shown that this method can quantify the oxygenation change in the human brain between the resting and functionally activated states in a motor-visual task.

The purpose of these studies was to further develop this T<sub>1</sub> mapping for small-animal oxymetry and to perform measurement to investigate how the oxygen level is altered with the treatment of our anti-angiogenic nanoparticle as compared to untreated controls. RT2 (Rat glioma cell line) cells were implanted intracranially in male Fisher Rats. They were divided to two groups. Treated groups (Group 1) received the therapeutic nanoparticles. Control groups (Group 2) received saline. Another control group (Group 3) consisted of normal animals without tumor or treatment. T<sub>2</sub>-weighted MR is performed to obtain the tumor size. T<sub>1</sub> mapping oxymetry is then performed to evaluate the oxygenation at different stages of tumor progression.

Preliminary data from normal rat brains (Group 3) indicated that R<sub>1</sub> is sensitive to inhalation of 100% pure oxygen. The gas input contained two cycles of 6-min room air and 6-min pure oxygen. The observed  $\Delta(pO_2)$  could reach as much as 100 mmHg within each cycle. While our result is in agreement with other published, invasive oxymetry methods, we are currently developing our technique for better magnetic field homogeneity and higher image resolution and will extend this methodology to brain tumor bearing models.

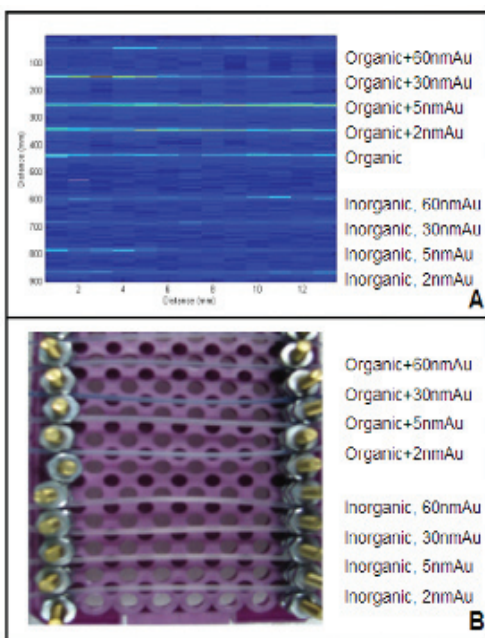
REFERENCES/FUNDING SOURCE  
Goldhirsh Foundation

## Development of Contrast Agents for Photoacoustic Tomography

YI-SHAN YANG<sup>1</sup>, SRIKANT VAITHILINGAM<sup>2</sup>, TE-JEN MA<sup>3</sup>, ÖMER ORAKLAN<sup>2</sup>, BUTRUS T. KHURI-YAKUB<sup>2</sup>, SAMIRA GUCCIONE<sup>1</sup>  
DEPARTMENTS OF <sup>1</sup>RADIOLOGY, <sup>2</sup>EDWARD L. GINTON LABORATORY AND <sup>3</sup>MECHANICAL ENGINEERING

Clinical imaging has asserted it's increasingly important role in clinical applications such as drug development, preventive care, early detection of disease, response to therapy, and monitoring of recurrence of pathologies. Photoacoustic tomography (PAT) is a new area of development in imaging technologies. PAT is a multi-modality imaging technique that utilizes non-ionizing energy to obtain both structural and functional information. This technology combines the advantages of high spatial resolution in ultrasound and the sensitivity of optical imaging. A critically underdeveloped area in PAT is development of contrast agents for this technology. In our lab, we have proposed, synthesized, and characterized several classes of PAT contrast agents. These classes broadly include organic, inorganic, and composite materials, and can be spherical or rod shaped.

*In vitro* and *in vivo* signal evaluation and image reconstruction using these broad classes of agents will provide the fundamental knowledge



on making PAT contrast agents and their signature signal characteristic. Additionally we will optimize the contrast agents with and without molecular targeting for *in vivo* use. Our goal in this project is the development of contrast agents for early detection of breast cancer, liver lesions, and unstable plaque.

(A) PAT image of vessel phantom filled with PAT contrast agents. (B) Photograph of phantom filled with PAT contrast agents. For both (A) and (B), the top group of samples are organic based composite with different sizes of gold. The bottom 4 samples are inorganic based gold particle. Signal intensity varies based on chemical composition of the agent.

REFERENCES/FUNDING SOURCE  
Canon Inc.

## Platforms for Synthesis of $^{18}\text{F}$ -labeled Probes for Molecular imaging Using PET

CHRISTOPHER CAIRES AND SAMIRA GUCCIONE  
DEPARTMENT OF RADIOLOGY

We are working on the development of new methods to attach  $^{18}\text{F}$  radiotracers to biologically relevant molecules for molecular imaging using positron emission tomography (PET). Current method for labeling molecules with  $^{18}\text{F}$  for PET imaging is not suitable for many biologically relevant molecules of interest, such as proteins. For example, the synthesis of FDG, the most common PET probe, involves procedures requiring very high temperatures, and anhydrous conditions. These conditions will denature many proteins of interest. In addition, the yield for FDG synthesis is poor. We are developing mediators for transferring the  $^{18}\text{F}$  label to proteins under mild conditions and good yields. These  $^{18}\text{F}$  radiotracers are unique because they can be “clicked” onto any protein or antibody. Once “clicked”

on, they can be used to image numerous diseases including cancer and inflammation. For example, if we want to image breast cancer, we can “click” our radiotracer onto Herceptin (a breast cancer antibody) and then inject into a patient to look for Her2 positive cancer cells. Our research has focused primarily on the synthesis (chemistry) of the radiotracers. We have identified some lead candidates and are now conducting experiments in small animals. Our long term goal is to translate this research into the clinic for molecular imaging of a broad spectrum of diseases in patients.

## Temperature Sensitive Liposomes for Local Drug Delivery Using Focused Ultrasound

MALIKA LARABI, MARK MACKANOS, RAJESH SHINDE, CHRIS CONTAG, SAMIRA GUCCIONE  
DEPARTMENT OF RADIOLOGY

Local delivery of therapeutic drugs will increase drug concentration at the site of treatment for maximum efficacy, and reduce systemic drug exposure. We have developed temperature sensitive stable liposomes that release their drug content upon local heating using focused ultrasound. These heat sensitive liposomes accumulate in the liver and can be used to deliver chemotherapy to liver lesions locally. Additionally, through specific molecular targeting, we can bind these liposomes to other sites of disease for local drug delivery. As an initial evaluation, luciferin was encapsulated in the liposome to provide release characteristics

after heating. The release profile upon heating was obtained in the presence of serum in vitro. We are conducting preliminary in vivo studies. The long-term goal of this project is to use focused ultrasound to heat and release chemotherapy to tumor lesions using targeted, heat-sensitive liposomes. In addition, other applications such as local release of antibodies in deep wounds or after surgery will be evaluated.

REFERENCES/FUNDING SOURCE  
Start up funds

## Toxicity Profile for Vascular Targeted Nanoparticles

MALIKA LARABI, SAMIRA GUCCIONE  
DEPARTMENT OF RADIOLOGY

The main focus of research in our laboratory has been the use of integrins expressed on pathologic vessels to deliver targeted contrast agents and therapies locally to the diseased site. Nanoparticles with ligands that bind the integrin  $\alpha_v\beta_3$  have been synthesized in our lab and used to deliver chemo, radiation or genes to the site of diseased vessels. We have extensively tested this approach with extremely promising results using animal models of melanoma, colon cancer, and primary brain tumors. This project report is a continuation of previous reports on this research topic from our laboratory. For clinical translation, toxicity studies are underway. We have evaluated kidney, and liver function. Electrolyte, metabolic, and cellular components of the blood has also

been analyzed in one species (rat). There are no toxic side effects at 6 times therapeutic dose. Additionally, no adverse reaction has been observed in vitro when adding the nanoparticles to human blood. With these promising results, we are proceeding towards the goal of completing the toxicity studies required for clinical translation.

REFERENCES/FUNDING SOURCE  
Start up funds

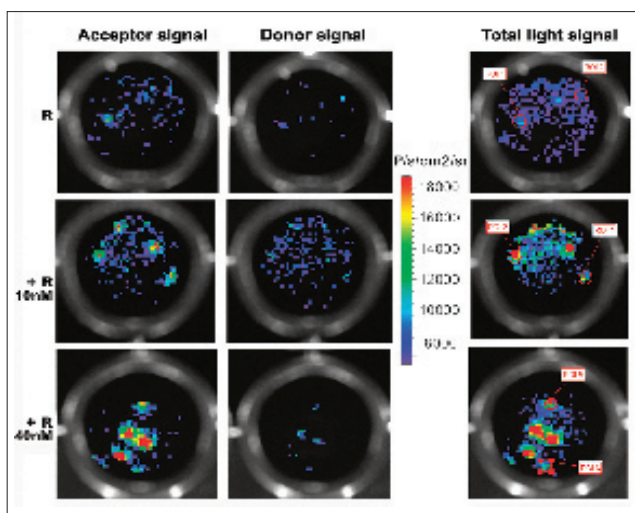


## Noninvasive Monitoring of In Vivo Protein Functions from Single Cells Using Bioluminescence Resonance Energy Transfer

ABHIJIT DE<sup>1</sup> AND SANJIV SAM GAMBHIR<sup>1,2</sup>

DEPARTMENTS OF <sup>1</sup>RADIOLOGY (MIPS) AND <sup>2</sup>BIOENGINEERING (BIO-X PROGRAM)

Here we report the significant advancements achieved as an imaging-based drug screening protocol as a measure of in vivo protein function directly from single living cells by using this vector. Imaging cellular events from single cell is an important component for the evaluation of true drug response. Previously, we reported construction of a new BRET vector utilizing a photon efficient mutant Renilla luciferase (Rluc8) donor in combination with a GFP2 acceptor. Luminescent spectral imaging by adding coelenterazine400a substrate to HT1080 cells stably over-expressing the GFP2-RLUC8 fusion show that the total light output from individual cells can be spectrally resolved and yield photon values of  $2.5 \pm 0.3 \times 10^4$  and  $0.6 \pm 0.1 \times 10^4$  photon/s/cm<sup>2</sup>/sr using the GFP2 and RLUC filter respectively. Single cell status was confirmed by allowing these cells to grow in culture until they divide. As one cell divide into two cells by 22h the average acceptor and donor photon yields are  $7.1 \pm 0.5 \times 10^4$  and  $1.3 \pm 0.9 \times 10^4$  photon/s/cm<sup>2</sup>/sr respectively. During



A 96-well plate containing a few stably selected HT1080 cells expressing the GFP2-FRB-FKBP12-RLUC8 fusion were subjected to different doses of rapamycin as marked and imaged using a CCD camera 4 h after plating. Individual cells were below detectable threshold with the substrate concentration (0.5  $\mu$ g/well) and the CCD integration time (1 min) used. With increasing drug concentration, as the interacting partners dimerize, the BRET partners come in closer proximity, leading to a higher BRET signal and thus enabling detection of BRET-specific GFP signal from individual cells. Pseudocolor scale bar represents the average luminescence photon output.

this study, a pCMV-GFP2-Rluc8 based single vector sensor construct was made by incorporating the gene sequences of two mTOR pathway proteins. Small molecule rapamycin drug efficacy was tested in HT1080 cells stably over-expressing the pCMV-GFP2-FRB-FKBP12-RLUC8 fusion. In the absence of small molecule rapamycin, FRB and FKBP12 domains do not interact, therefore the acceptor and donor moieties are well separated resulting in background signal only. With increasing rapamycin concentrations, as the two domains interact, conformational changes in the fusion protein bring the acceptor and donor moieties in closer proximity allowing detection of BRET specific GFP2 signal. These results signify that the GFP2-Rluc8 BRET vector can be used for rapid screening and evaluation of true drug response from single live cells.

### REFERENCES/FUNDING SOURCE

NIH grant 5R01 CA82214 and NCI P50 CA114747, NCI U54 CA119367, and NCI SAIRP.

## A Diverse Panel of Polypeptide Libraries for the Rapid Design and Engineering of New Molecular Imaging Agents

FRANK V. COCHRAN<sup>2</sup> AND SANJIV SAM GAMBHIR<sup>1,2</sup>

DEPARTMENTS OF <sup>1</sup>RADIOLOGY (MIPS AND BIO-X PROGRAM) AND <sup>2</sup>BIOENGINEERING

Development of new targeting agents is a central goal in molecular imaging. The ability to rapidly identify high-affinity ( $K_d \sim 1$  nM or better) binders to desired protein targets enhances the speed of developing novel molecular imaging agents. We report a diverse panel of new polypeptide libraries for use in yeast surface display for the discovery and engineering of target-specific peptide-based molecular imaging agents. We describe a robust strategy that incorporates rational design, directed evolution, and biophysical characterization for the discovery and optimization of high-affinity target binders with suitable pharmacokinetic profiles. These efforts are guided by structural and mechanistic insight of target recognition, and allow intelligent fine-tuning of targeting agents for the imaging application of interest. Peptide and small protein scaffolds offer several advantages over traditional antibody technology. The smaller size relative to antibodies permits facile production by the highly optimized methods of solid phase synthesis, better blood-pool clearance for high target to background ratios, and better tumor penetration. We have produced soluble ovarian cancer protein

targets in mammalian and insect cell expression systems for screening of these libraries by fluorescence activated cell sorting (FACS). FACS avoids many potential artifacts of surface-immobilized target screens and allows more rigorous and quantitative means to optimize the binding affinity. Libraries of  $\sim 10^6 - 10^8$  mutants were produced by error-prone PCR with nucleotide analogs and assembly PCR with degenerate nucleotides. Enrichment of high affinity binders is achieved after several rounds of sorting. Alternatively, these libraries are panned against cell monolayers using newly developed assays in order to recapitulate the natural target environment. Validation of engineered polypeptides decoupled from the yeast surface is performed in cell culture assays and small animal models. This work provides a molecular toolkit that will translate into clinical applications for the improved diagnosis, management, and treatment of human malignancies.

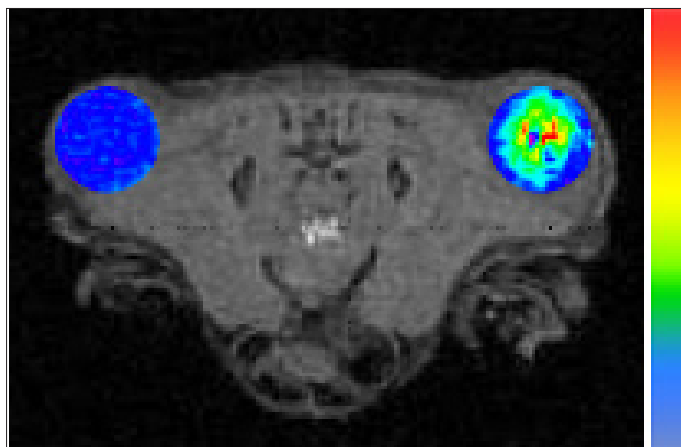
### REFERENCES/FUNDING SOURCE

Canary Foundation.

## Magnetotactic Bacteria as a Potential MRI Contrast Agent

MICHAEL BENOIT<sup>1</sup>, DIRK MAYER<sup>2</sup>, YORAM BARAK<sup>1</sup>, IAN CHEN<sup>3</sup>, WEI HU<sup>4</sup>, SHAY KEREN<sup>2</sup>, S.S. GAMBHIR<sup>2,3</sup>, A.C. MATIN<sup>1</sup>  
 DEPARTMENTS OF <sup>1</sup>MICROBIOLOGY & IMMUNOLOGY, <sup>2</sup>RADIOLOGY, <sup>3</sup>BIOENGINEERING (BIO-X PROGRAM), AND  
<sup>4</sup>MATERIALS SCIENCE & ENGINEERING

Magnetotactic bacteria occur naturally and produce chains of magnetite particles, which allow them to align along the Earth's geomagnetic field lines. The magnetite particles are similar to existing iron oxide particles used extensively as contrast agents for MRI enhancement. Due to the microaerophilic nature of magnetotactic bacteria, we reasoned that they may preferentially colonize cancerous tumors, enabling their visualization in vivo using MRI. Although certain bacteria have been known to preferentially colonize cancerous tumors for over 50 years, only recent advances in our understanding of, and ability to manipulate bacteria, have led to a renewed interest in their use for treating cancer. Here we report that *Magnetospirillum magnetotacticum* (AMB1) provide suitable contrast for in vivo imaging in nu/nu mice bearing 293T subcutaneous tumors. A T1 weighted positive contrast signal was achieved using as low as  $5 \times 10^8$  cells injected intratumorally (IT). This number of cells corresponds to approximately 0.015 mg Fe/kg of body weight, which is an order of magnitude less than the recommended dosage for FERIDEX



MRI of mouse one day post intratumoral injection of AMB1 cells (right) or medium only (left)

I.V. (0.56 mg Fe/kg of body weight). One day post injection, the signal was enhanced 2.5-fold (figure, right ROI) compared to control tumors injected with medium only (figure, left ROI), and a clear signal was still visible 7 days post injection. Determining the propensity of magnetotactic bacteria to colonize solid tumors in mice after intravenous (IV) injection is currently underway. Thus far, no significant immune response was detected in the infected mice compared to controls, indicating the potential "safety" of using AMB1 in vivo. Based on these observations we envision a bacterial, viral or

mammalian agent that can specifically target tumors and be visualized by MRI. Furthermore, the same agent could conceivably be altered to deliver therapies, such as reductive prodrug converting enzymes, thus providing a single tool for detecting and treating cancer.

REFERENCES/FUNDING SOURCE  
 NIH grant RR09784

## Combinatorial Complexity in the hsp90-p23 Reporter Protein Complementation Assay

CESAR A. RODRIGUEZ<sup>1</sup>, ANDREW LIPKIN<sup>1</sup>, CARMEL CHAN<sup>1</sup>, SANJIV S. GAMBHIR<sup>1,2</sup>  
<sup>1</sup>DEPARTMENTS OF RADIOLOGY (MIPS) AND <sup>2</sup>BIOENGINEERING (BIO-X PROGRAM)

**Purpose:** This work is a computational analysis of the interactions between hsp90, p23, and bioluminescent fusion versions of hsp90 and p23 (hsp90-rluc and p23-rluc) at the cellular scale. The bioluminescent fusion proteins are part of the hsp90-p23 reporter protein complementation assay under development in the Multimodality Molecular Imaging Laboratory at Stanford University. The assay consists of using bioluminescent imaging for indirect monitoring of in vivo protein-protein interactions. Ansamycin antibiotics which target the hsp90-p23 interaction are being evaluated using the assay.

**Methods:** The analysis consists of formal descriptions of assumptions, construction of a protein-protein interaction graph using a depth-first search algorithm, and evaluation of the network's dynamics with a system of ordinary differential equations. Hypotheses are formally stated for experimental verification. The final model consists of four protein monomer concentrations and six rate constants. We also formulated a preliminary model for protein production consisting of a system of ordinary differential equations that includes a decreasing Hill function.

**Results:** Four protein complexes and 6 protein-protein interactions are expected in the interactions between hsp90 and p23; 25 complexes and 49 interactions between hsp90, p23, hsp90-rluc, p23-rluc. Seven complexes are expected to provide bioluminescent signal. The tetrameric complexes predominate as the monomer concentrations increase. The protein production model demonstrates negative feedback dynamics that can lead to decreased levels of hsp90 with increasing levels of hsp90-rluc.

**Conclusions:** Hsp90, p23, hsp90-rluc, and p23-rluc interactions demonstrate combinatorial complexity. Complexes predominate as the monomer concentrations increase. Hsp90-rluc production may perturb the production of the endogenous hsp90. The computational analysis complements the image-based investigation of hsp90-p23 interactions and the evaluation of therapeutic agents that target the interaction.

REFERENCES/FUNDING SOURCE  
 Presented at the Joint Molecular Imaging Conference, 2007.  
 NIH-National Library of Medicine.

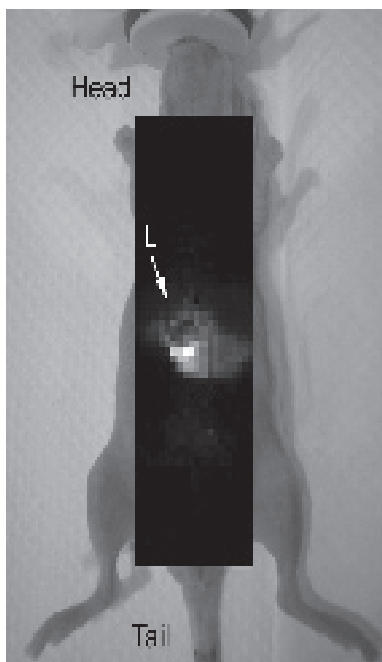
## Noninvasive Molecular Imaging of Small Living Subjects Using Raman Spectroscopy and Raman Nanoparticles

SHAY KEREN<sup>1</sup>, CRISTINA ZAVALA<sup>1</sup>, ZHEN CHENG<sup>1</sup>, OLIVIER GHEYSSENS, SANJIV SAM GAMBHIR<sup>1,2</sup>

DEPARTMENTS OF <sup>1</sup>RADIOLOGY (MIPS) AND <sup>2</sup>BIOENGINEERING (BIO-X PROGRAM)

Raman optical spectroscopy is a powerful diagnostic tool capable of identifying molecular fingerprints based on Raman scattering. However, the inherently weak magnitude of Raman scattering has limited its use in biomedical imaging in the past. This limitation is overcome using the recently developed surface enhanced Raman scattering (SERS) nanoparticles that have a very high Raman scattering cross-section. We present here, for the first time, noninvasive molecular imaging in living subjects using Raman spectroscopy and SERS nanoparticles.

Glass-encapsulated SERS nanoparticles (Oxonica Inc., Menlo Park, CA) composed of a gold core, Raman active molecular layer and glass coating, were used as molecular imaging agents for in vivo Raman spectroscopy. These nanoparticles are characterized by high multiplexing capability, NIR excitation and emission wavelength, physical robustness and relatively small size which make them ideal probes for small animal imaging. A Raman imaging setup based on the Renishaw in via Raman microscope (Renishaw plc, New Mills, UK), equipped with 785nm laser, was adapted for small animal imaging. We characterized the imaging system by testing its sensitivity (8.125 pM subcutaneously), linearity ( $R^2=0.99$ ) and reproducibility



*A: Bright field of hESCs (100X); B: GFP+ hESCs (400X); C: Beating area of EBs (100X); D: Bioluminescence signal increased with cell number; E: In vivo cardiac BLI imaging of hESC-CM*

(COV=3.1%). We demonstrated the multiplexing capability of Raman spectroscopy for live animal imaging of SERS nanoparticles by subcutaneously injecting two types of SERS nanoparticles with different Raman signatures into a mouse and distinguishing the relative concentration of each particle. Pharmacokinetics (n=6) and deep-tissue imaging of SERS nanoparticles accumulated in the liver was accomplished by raster scan over the mouse body, as shown in the figure below. This work sets the groundwork for an entirely new way of imaging small animals with potential for high multiplexing in order to monitor multiple biological events.

### REFERENCES/FUNDING SOURCE

This work was funded in part by NCI CCNE U54 CA119367, and ICMIC P50 CA114747.

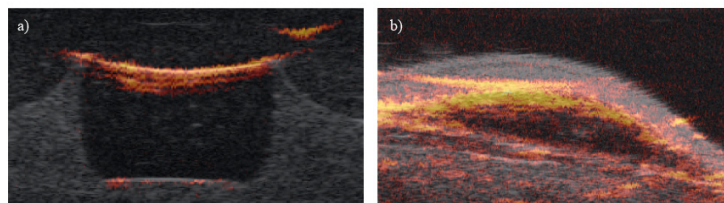


## Photoacoustic Tomography with High Resolution Small Animal Ultrasound System

SHAY KEREN<sup>1</sup>, ADAM DE LA ZERDA<sup>1,3</sup>, JELENA LEVI<sup>1</sup>, SRIKANT VAITHILINGAM<sup>3</sup>, OMER ORALKAN<sup>3</sup>, PIERRE KHURI-YAKUB<sup>3</sup>, SANJIV SAM GAMBHIR<sup>1,2</sup>  
DEPARTMENTS OF <sup>1</sup>RADIOLOGY (MIPS), AND <sup>2</sup>BIOENGINEERING (BIO-X PROGRAM), <sup>3</sup>ELECTRICAL ENGINEERING

Photoacoustic tomography is a novel molecular imaging modality with optical contrast agent specificity and high ultrasound resolution. While recent publications involve complicated construction from the ground up of dedicated photoacoustic instrumentation, we report the adaptation of the only high-end commercially available small animal ultrasound imaging system, Vevo-770 (VisualSonics), for photoacoustic functional imaging of living subjects.

The Vevo-770 system is equipped with a scanning head focused ultrasound transducer allowing noninvasive structural imaging with up to 40  $\mu$ m resolution, power Doppler detection and 3D visualization tools. In order to adapt the Vevo-770 for photoacoustic imaging several measures had to be taken including working in a receive-only mode, synchronization with a laser source and image processing adjustments. A high-power tunable Optical Parametric Oscillator laser, SureLight III OPO (Continuum Lasers) with 665-1000nm wavelength tunability,



Photoacoustic and pulse-echo superimposed image of 50  $\mu$ M ICG inclusion a), and subcutaneously injected to mouse b).

5nsec pulse duration and 10Hz repetition rate was used as an excitation light source.

In order to evaluate the performance of the Vevo-770 in the photoacoustic mode, a series of phantoms were built and imaged. To mimic the acoustical and optical properties of tissues, the phantoms were made from water(98%),

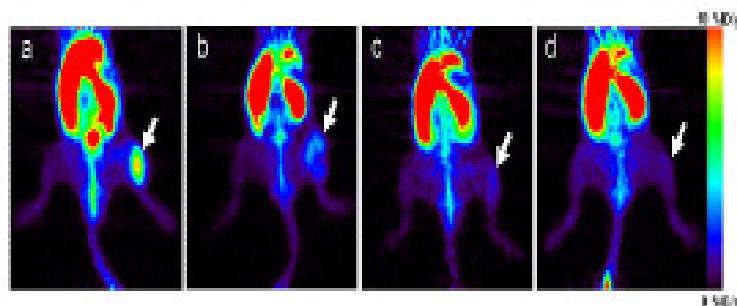
agarose(1%), Liposyn(1%). Sensitivity and linearity of the system were assessed by imaging a phantom containing inclusions of the photoacoustic contrast agent, Indocyanine Green (ICG), with varying concentrations. Depth of detection was evaluated by implanting ICG inclusions at different depths in a phantom. Finally, we demonstrated noninvasive photoacoustic imaging in small animals.

The Vevo-770 small animal ultrasound system adapted to perform combined pulse-echo and photoacoustic imaging, as seen in the figure, shows promising results. This work demonstrates high performance and robust photoacoustic molecular imaging in a system that can be readily employed by many laboratories.

## Assessment of Therapeutic Angiogenesis in Murine Hindlimb Ischemia Using Cu-labeled Vascular Endothelial Growth Factor-121 PET

JÜRGEN K. WILLMANN<sup>1</sup>, KAI CHEN<sup>1</sup>, HUI WANG<sup>1</sup>, RAMASAMY PAULMURUGAN<sup>1</sup>, MARK ROLLINS<sup>2</sup>, WEIBO CAI<sup>1</sup>, DAVID WANG<sup>1</sup>, IAN Y. CHEN<sup>1</sup>, AMELIE M. LUTZ<sup>1</sup>, OLIVIER GHEYSSENS<sup>1</sup>, MARTIN RODRIGUEZ-PORCEL<sup>1</sup>, XIAOYUAN CHEN<sup>1</sup>, SANJIV S. GAMBHIR<sup>1,3</sup>  
DEPARTMENTS OF <sup>1</sup>RADIOLOGY (MIPS) AND <sup>3</sup>BIOENGINEERING (BIO-X), STANFORD UNIVERSITY,  
<sup>2</sup>ANESTHESIA & PERIOPERATIVE CARE, UCSF

Vascular endothelial growth factor-121 (VEGF<sub>121</sub>), an angiogenic protein secreted in response to hypoxic stress in therapeutic angiogenesis, binds to VEGF receptors (VEGFR) overexpressed on vessels of ischemic tissue. The purpose of this study was to evaluate <sup>64</sup>Cu-VEGF<sub>121</sub> PET for non-invasive spatial and quantitative monitoring of VEGFR expression in a murine model of hindlimb ischemia with and without treadmill exercise training. <sup>64</sup>Cu-labeled VEGF<sub>121</sub> and VEGF<sub>Mutant</sub> were tested for VEGFR2 binding specificity in cell culture. Mice (n=46) underwent unilateral ligation of the femoral artery and postoperative tissue ischemia was assessed with laser Doppler imaging. Longitudinal VEGFR2 expression in exercised and non-exercised mice was visualized by <sup>64</sup>Cu-VEGF<sub>121</sub>-PET at postoperative day 8, 15, 22, and 29 and correlated with postmortem gamma counting. Hindlimb muscle tissue was excised for immunohistochemistry and western blotting. Compared with VEGF<sub>Mutant</sub>, VEGF<sub>121</sub> showed specific binding to VEGFR2. Perfusion in ischemic hindlimbs fell to 9% of contralateral hindlimb on postoperative day 1 and recovered to 82% on day 29. <sup>64</sup>Cu-VEGF<sub>121</sub> uptake in ischemic hindlimb significantly



Serial <sup>64</sup>Cu-VEGF<sub>121</sub> uptake in mice at (a) day 8, (b) day 15, (c) day 22, and (d) day 29 after left femoral arterial ligation. <sup>64</sup>Cu-VEGF<sub>121</sub> uptake (as expressed as %ID/g) in the left ischemic hindlimb muscle tissue (arrows) at different time points after surgery can be seen.

( $P < .001$ ) increased from a control level of 0.61 %ID/g to 1.62 %ID/g at postoperative day 8 (Figure), gradually decreased over the following 3 weeks (day 29, 0.59 %ID/g) and correlated with gamma counting ( $R^2 = 0.99$ ). Compared with non-exercised mice, <sup>64</sup>Cu-VEGF<sub>121</sub> uptake was significantly increased ( $P < .03$ ) in exercised mice and correlated with VEGFR2 levels on western blotting ( $R^2 = 0.76$ ). Ischemic hindlimb tissue stained positive for VEGFR2.

In conclusion, <sup>64</sup>Cu-VEGF<sub>121</sub> PET allows a longitudinal spatial and quantitative monitoring of VEGFR2 expression in murine hindlimb ischemia and visualizes the effects of stimulated therapeutic angiogenesis after treadmill exercise training. This study sets the groundwork for eventual translation of this approach for monitoring of therapeutic angiogenesis in patients.

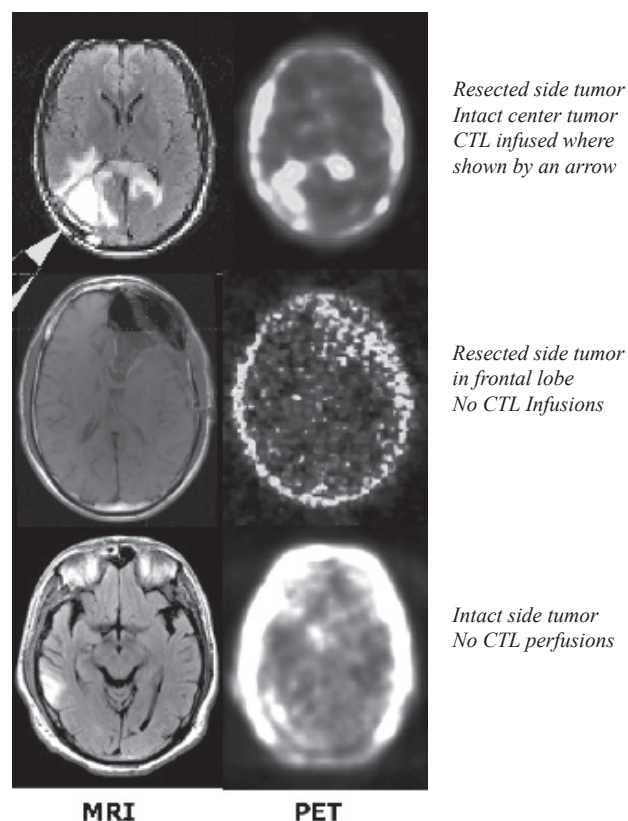
### REFERENCES/FUNDING SOURCE

The Swiss Foundation of Medical-Biological Grants (JKW), Novartis Research Foundation (JKW), Swiss Society of Radiology (JKW), NCI SAIRP, NHLBI 1 R01 HL078632, and NCI ICMIC CA114747 P50.

## [<sup>18</sup>F]FHBG PET Imaging of T Cell Homing in Patients with Gliomas

SHAHRIAR S. YAGHOUBI<sup>1</sup>, MICHAEL C. JENSEN<sup>4</sup>, YINGBING WANG<sup>3</sup>, ERIK MITRA,  
SHRADHA BUDHIRAJA, NAGICHETTIAR SATYAMURTHY<sup>5</sup>, MOHAMMAD NAMAVARI<sup>1</sup>, FREDERICK T CHIN<sup>1</sup>,  
MURUGESSAN SUBBARAYAN<sup>1</sup>, ANDREI IAGARU<sup>1</sup>, DAVID PAIK<sup>1</sup>, JOHANNES CZERNIN<sup>5</sup>, SANJIV S. GAMBHIR<sup>1,2</sup>  
DEPARTMENTS OF <sup>1</sup>RADIOLOGY (MIPS AND BIO-X PROGRAMS), <sup>2</sup>BIOENGINEERING, AND <sup>3</sup>MEDICINE, STANFORD UNIVERSITY  
<sup>4</sup>DIVISION OF CANCER IMMUNOTHERAPEUTICS & TUMOR IMMUNOLOGY, HOPE NATIONAL MEDICAL CENTER, DUARTE, CA,  
<sup>5</sup>MOLECULAR AND MEDICAL PHARMACOLOGY/NUCLEAR MEDICINE, UCLA, LOS ANGELES, CA

Noninvasive imaging of cell trafficking should allow early assessment of efficacy and side effects of adoptive cellular immunotherapy in cancer patients. Under a FDA authorized IND (61,880), we have imaged the biodistribution of the positron emission tomography (PET) reporter probe, 9-[4-[<sup>18</sup>F]fluoro-3-(hydroxymethyl)butyl]guanine ([<sup>18</sup>F]FHBG) in three groups of glioma patients (two hours after < 7 mCi intravenous). The imaged patients either had intact tumors, their tumors had been surgically removed, or had been infused autologous cytolytic T lymphocyte (CTL) clones (12 sessions, 107 to 108 cells each session) at the site of surgically removed recurrent tumor. The CTLs expressed Herpes Simplex virus type 1 thymidine kinase (HSV1-tk) PET reporter gene (confirmed by Ganciclovir sensitivity and tritiated Penciclovir uptake assays) and IL-13 zetakine. CD8<sup>+</sup> CTL infiltration into the tumors was confirmed by biopsy. The Figure illustrates brain PET and MRI images, indicating higher activities at tumor or resection sites. The Table lists the mean [<sup>18</sup>F]FHBG SUV ratios of tumor over brain background, meninges, heart and liver. These data suggest that [<sup>18</sup>F]FHBG, which cannot cross the blood brain barrier, can perfuse into glioma tumors and resection sites and may be detecting the HSV1-tk expressing CTLs. These studies also provided further evidence that [<sup>18</sup>F]FHBG administration in humans is safe. To our knowledge, this is the first study of directly imaging PET reporter gene expressing infused therapeutic cells in patients with PET-CT. In future studies, patients receiving autologous CTLs will be imaged before and after cell infusions, providing an ideal negative control for statistical analysis.



Images compare FHBG accumulation in the brains of the 3 groups of patients studied.

### REFERENCES/FUNDING SOURCE

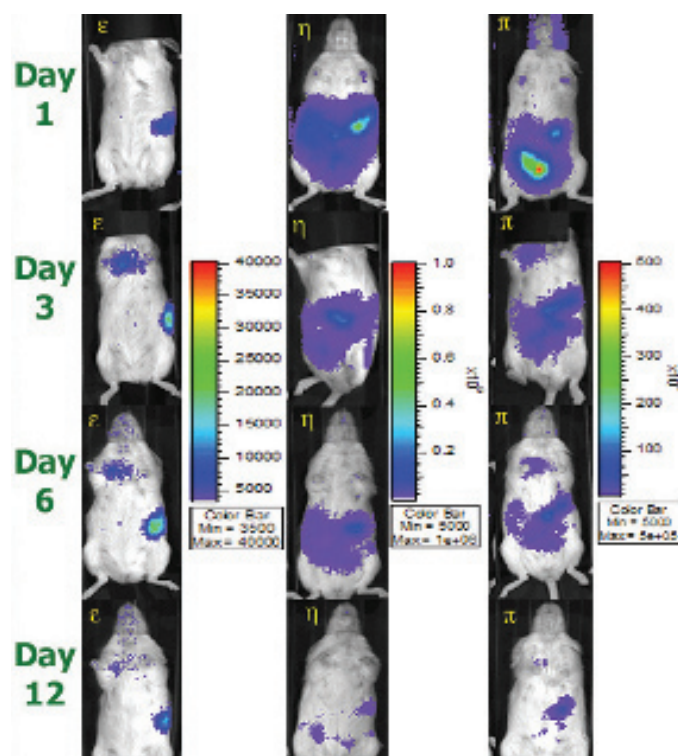
Yaghoubi SS, Couto MA, Chen C, Polavaram L, Cui G, Sen L, Gambhir SS. "Pre-Clinical Safety Evaluation of <sup>18</sup>F-FHBG: A PET Reporter Probe for Imaging Herpes Simplex Virus Type 1 Thymidine Kinase (HSV1-tk) or Mutant HSV1-sr39tk's Expression." *The Journal of Nuclear Medicine* 47(4): 706-715 (2006).  
Yaghoubi S, Barrio JR, Dahlbom M, Iyer M, Namavari M, Satyamurthy N, Goldman R, Herschman HR, Phelps ME, Gambhir SS. "Human Pharmacokinetic and Dosimetry Studies of [<sup>18</sup>F]FHBG, A Reporter Probe for Imaging Herpes Simplex Virus Thymidine Kinase (HSV1-tk) Reporter Gene Expression." *Journal of Nuclear Medicine* 42(8):1225-1234 (2001).  
Yaghoubi SS and Gambhir SS. "PET imaging of herpes simplex virus type 1 thymidine kinase (HSV1-tk) or mutant HSV1-sr39tk reporter gene expression in mice and humans using [<sup>18</sup>F]FHBG." *Nature Protocols* 1(6): 3069-3075 (2007).

## Bioluminescent Reporter Gene Based Imaging of Bone Marrow Derived Dendritic Cell Trafficking in Various Mouse Models

SHAHRIAR S YAGHOUBI<sup>1</sup>, REMI J CREUSOT<sup>2</sup>, C G FATHMAN<sup>2</sup>, SANJIV S GAMBHIR<sup>1,3</sup>

DEPARTMENTS OF RADIOLOGY (MIPS), <sup>2</sup>MEDICINE (CLINICAL IMMUNOLOGY) AND <sup>3</sup>BIOENGINEERING (BIO-X PROGRAM)

Preclinical adoptive immunotherapy studies with dendritic cells (DC) in murine models of autoimmune diseases show significant potential. We have monitored the homing patterns of Firefly luciferase (Fluc) expressing DCs in diabetic (NOD), arthritic (SKG) and normal FVB mice by bioluminescence imaging and post-mortem tissue distribution assays. DCs were generated from the bone marrow cells of Fluc transgenic mice of the above strains in the presence of IL-4 and GM-CSF. Five million DCs were injected intravenously (IV), intraperitoneally (IP) or subcutaneously (SC), and then scanned with a bioluminescence imaging CCD camera for up to 12 days. Three mice per group were also sacrificed each imaging day and important tissues were harvested and homogenized for Fluc activity assays. The figure illustrates the bioluminescence images of Fluc DC (5 million cells) injected FVB mice 10 minutes after injecting 3 mg D-Luciferin. Ex vivo biodistribution assay results indicated that IV injected DCs homed preferentially to spleen and pancreatic lymph nodes (PLN) and initially also to the lungs. IP injected DCs homed with high specificity to PLN and were also found to a lesser extent in lumbar and mesenteric lymph nodes, spleen and pancreas. In preliminary studies, subcutaneously injected DCs homed more efficiently to inguinal and pancreatic lymph nodes. These route-dependent organ DC accumulations did not differ between animal models in terms of biodistribution pattern, but differences were observed in kinetics. The preferential PLN homing of the DCs highlights their potential for targeted adoptive cellular therapy of type 1 diabetes. This is the most thorough analysis of DC trafficking reported in mouse models of autoimmune diseases.



Biodistribution of bone marrow derived dendritic cells expressing the Fluc reporter gene in FVB mouse strain, illustrated by bioluminescence imaging.

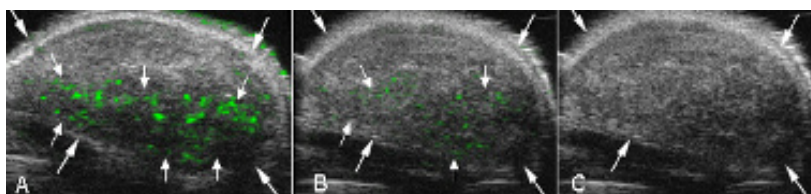


# Ultrasonic Imaging of Tumor Angiogenesis with Contrast Microbubbles Targeted to Vascular Endothelial Growth Factor Receptor Type 2 in Mice

JÜRGEN K. WILLMANN<sup>1</sup>, RAMASAMY PAULMURUGAN<sup>1</sup>, KAI CHEN<sup>1</sup>, OLIVIER GHEYSEN<sup>1</sup>, MARTIN RODRIGUEZ-PORCE<sup>1</sup>, AMELIE M. LUTZ<sup>1</sup>, IAN Y CHEN<sup>1</sup>, XIAOYUAN CHEN<sup>1</sup>, SANJIV S GAMBHIR<sup>1,2</sup>,  
DEPARTMENTS OF <sup>1</sup>RADIOLOGY (MIPS AND BIO-X PROGRAMS) AND <sup>2</sup>BIOENGINEERING

Vascular endothelial growth factor receptor type 2 (VEGFR2) is one of the major regulators of tumor angiogenesis and activation of the VEGF/VEGFR axis result in endothelial cell survival, mitogenesis, migration, differentiation, and vascular permeability. The purpose of this study was to prospectively evaluate contrast-enhanced ultrasound with microbubbles targeted to VEGFR2 for imaging tumor angiogenesis in

murine tumor models. An image-enhancing ultrasound contrast agent, consisting of encapsulated gaseous microbubbles, was developed specifically to bind VEGFR2 (using anti-VEGFR2 antibodies and biotin-streptavidin interaction) which is up-regulated on endothelial cells of tumor vessels. VEGFR2-targeted microbubbles (MBVEGFR2) and control microbubbles (isotype-matched control IgG-labeled microbubbles and non-labeled microbubbles) were tested for binding specificity on cells expressing VEGFR2 (mouse angiosarcoma SVR cells) and control cells (mouse skeletal myoblasts C2C12 cells). Expression of mouse VEGFR2 in cell culture cells was tested by immunocytochemistry and western blotting. In vivo, contrast-enhanced ultrasound imaging with MBVEGFR2 and control microbubbles was performed in 28 tumor-bearing nude mice (mouse angiosarcoma, n=18; rat malignant glioma, n=10). In cell culture, adherence of MBVEGFR2 on SVR cells (2.1 microbubbles/SVR cell) was significantly higher than adherence of con-



Transverse ultrasound images of murine subcutaneous malignant glioma tumor (white large arrows). Signal intensity (color coded in green, small arrows) after intravenous administration of microbubbles labeled with anti-VEGFR2 antibodies (A) is higher compared with microbubbles labeled with isotope-matched- (B) and non-labeled (C) microbubbles.

trol microbubbles (0.01-0.1 microbubbles/SVR cell;  $P < .0001$ ) and significantly more MBVEGFR2 attached to SVR cells than to C2C12 cells (0.15 microbubbles/C2C12 cell;  $P < .0001$ ). In vivo, contrast-enhanced ultrasound imaging showed significantly higher average video intensity when using MBVEGFR2 com-

pared with control microbubbles for both angiosarcoma ( $P < .0001$ ) and malignant glioma ( $P < .0002$ ) tumors (Figure). Immunohistochemistry confirmed VEGFR2 expression on vascular endothelial cells of both tumor types. In conclusion, ultrasonic imaging with contrast microbubbles targeted to VEGFR2 allows noninvasive visualization of VEGFR2 expression in tumor vessels in mice.

## REFERENCES/FUNDING SOURCE

Willmann JK, Paulmurugan R, Chen K, Gheysens O, Rodriguez-Porcel M, Lutz AM, Chen I, Chen S, Gambhir SS. Ultrasonic Imaging of Tumor Angiogenesis with Contrast Microbubbles Targeted to Vascular Endothelial Growth Factor Receptor Type 2 in Mice. *Radiology*.2007 (in press)  
Swiss Foundation of Medical-Biological Grants (JKW), Novartis Research Foundation (JKW), Swiss Society of Radiology (JKW), NCI SAIRP, NHLBI 1 R01 HL078632, NCI ICMIC CA114747 P50.

# Orthotopic Brain Tumor Imaging with <sup>18</sup>F-2-Fluorodeoxyisobutanol (<sup>18</sup>F-FDS)

ZI-BO LI<sup>1</sup>, ZHANHONG WU<sup>1</sup>, QIZHEN CAO<sup>1</sup>, DAVID W. DICK<sup>1</sup>, JEFFREY R. TSENG<sup>1</sup>, SANJIV S. GAMBHIR<sup>1,2</sup>, XIAOYUAN CHEN<sup>1</sup>  
DEPARTMENTS OF <sup>1</sup>RADIOLOGY (MIPS AND BIO-X PROGRAMS), AND <sup>2</sup>BIOENGINEERING

**Abstract:** <sup>18</sup>F-2-Fluorodeoxyglucose (<sup>18</sup>F-FDG) is the most commonly used positron emission tomography (PET) tracer for oncologic and neurological imaging applications. However, the high background in normal brain tissue limits its application for detecting tumor or inflammation in the gray matter but not in white matter. In this study, we synthesized <sup>18</sup>F-2-fluorodeoxyisobutanol (<sup>18</sup>F-FDS) and examined the superiority of <sup>18</sup>F-FDS to <sup>18</sup>F-FDG in imaging orthotopic brain tumor models and an ear inflammation model in mice.

**Methods:** <sup>18</sup>F-FDS was synthesized by reduction of <sup>18</sup>F-FDG using NaBH<sub>4</sub>. Cell uptake and efflux experiments were performed to evaluate the metabolic pathway of <sup>18</sup>F-FDS in cell culture. <sup>18</sup>F-FDS small animal PET imaging was then performed on tumor and inflammation models, and the results were compared with those obtained from <sup>18</sup>F-FDG-PET.

**Results:** <sup>18</sup>F-FDS was obtained from <sup>18</sup>F-FDG with an  $81 \pm 4\%$  yield in 30 min. Despite low cellular uptake in cell culture, <sup>18</sup>F-FDS had good tumor uptake and contrast in the subcutaneous U87MG tumor

model (4.54 %ID/g uptake at 30 min postinjection (p.i.) with tumor/muscle ratio equal to 2.7). Minimal uptake in the normal mouse brain facilitated good tumor contrast in both U87MG and GL-26 orthotopic tumor models. <sup>18</sup>F-FDG was unable to delineate the lesions from normal brain tissue. Both <sup>18</sup>F-FDG and <sup>18</sup>F-FDS had increased uptake in the inflamed foci of the TPA induced acute inflammation model.

**Conclusion:** <sup>18</sup>F-FDS can be easily obtained from <sup>18</sup>F-FDG for imaging brain tumor imaging. The very rapid distribution in the body and the high clearance from blood are most likely due to an extravascular distribution.

## REFERENCES/FUNDING SOURCE

NIH/NIBIB R21 EB001785, NCI R21 CA102123, NCI ICMIC P50 CA114747, NCI CCNE U54 CA119367, and R24 CA93862, Department of Defense (DOD) W81XWH-04-1-0697, W81XWH-06-1-0665, W81XWH-06-1-0042, and DAMD17-03-1-0143. We also thank the cyclotron team at the Stanford University for <sup>18</sup>F-FDG production.

## PET-CT Fly-through Virtual Bronchoscopy: A Model for Systematic Investigation of 3D Visualization

YERUSHALMI D<sup>1,2</sup>, QUON A<sup>1</sup>, FAHRIG R<sup>1</sup>, PELC NJ<sup>1,2</sup>, FANN JI<sup>3</sup>, GAMBHIR SS<sup>1,2</sup>,  
DEPARTMENTS OF <sup>1</sup>RADIOLOGY (MIPS), <sup>2</sup>BIOENGINEERING (BIO-X), <sup>3</sup>CARDIOTHORACIC SURGERY,

**Objectives:** Virtual bronchoscopy using FDG PET-CT is a promising tool relevant to diagnostics, treatment planning, and interventional guidance. In order to realize the clinical utility of this modality, a more thorough understanding of quantitative limitations is required. Here we present a physical model for investigating 3D visualization of endoluminal lesions of the airways using virtual PET-CT bronchoscopy and demonstrate the application of this model for studying the sensitivity for detection of lesions of different sizes, locations, and activity. **Methods:** An anatomically accurate plastinated porcine heart-lung phantom was used to simulate the airways and peripheral structures.

Capsules of various sizes between 4-10mm were designed and filled with physiologically relevant levels (1-5  $\mu$ Ci) of Fluorine-18 activity and were introduced into the trachea using a flexible bronchoscope and placed at locations along the bronchial tree. PET and CT images were acquired sequentially on a GE Discovery LS PET-CT scanner and reconstructed at 2.5mm and 5mm using the filtered-backprojection and OSEM algorithms respectively. PET and CT images were visualized



*Volume Rendered PET-CT Fusion Image alongside plastinated heart lung phantom. This figure shows the phantom that was used in this study.*

as a virtual bronchoscopy and as a volume-rendered fly-around image using GE Volume Viewer Plus, a commercial software tool. Fly-around perspective images clearly show focal tracer activity with respect to anatomical landmarks. **Conclusions:** The anatomical airway model described is a powerful tool for systematic investigation of 3D fly-through virtual bronchoscopy and fly-around visualization for PET-CT images. Future work may simulate more realistic conditions including background activity, variation in lesion morphology, as well as lesions located in regions peripheral or adjacent to the airways.

### REFERENCES/FUNDING SOURCE

Academy of Molecular Imaging, March 2006 (Abstract). The authors would like to thank Rakesh Mullick of GE Medical Systems for help rendering the fly-through images. Phantom development was supported by the Whitaker Foundation. This research was supported in part by NIH ICMIC P50 CA114747 and a Student Fellowship funded by the Education and Research Foundation for the Society of Nuclear Medicine.

## <sup>18</sup>F-Labeled BBN-RGD Heterodimer for Prostate Cancer

ZI-BO LI, ZHANHONG WU, KAI CHEN, EUN-KYOUNG RYU, AND XIAOYUAN CHEN  
DEPARTMENT OF RADIOLOGY (MIPS AND BIO-X PROGRAMS)

**Abstract:** Cyclic RGD peptides and bombesin (BBN) analogs have been radiolabeled for imaging integrin  $\alpha v \beta 3$  and gastrin-releasing peptide (GRP) receptor (GRPR) expression in various cancer types. However, tracers derived from monomeric RGD and BBN suffer from relatively low tumor accumulation and retention as well as unfavorable in vivo kinetics. In this study we developed a <sup>18</sup>F-labeled BBN-RGD heterodimer for positron emission tomography (PET) imaging of PC-3 tumor xenografted mice.

**Methods:** BBN hetero-dimer (BBN-RGD) was synthesized from bombesin(7-14) and c(RGDyK) through a glutamate linker. BBN-RGD peptide was then labeled with <sup>18</sup>F via the N-succinimidyl-4-<sup>18</sup>F-fluorobenzoate (<sup>18</sup>F-SFB) prosthetic group. The integrin and GRPR receptor binding characteristics of the heterodimeric peptide tracer <sup>18</sup>F-FB-BBN-RGD was evaluated in vitro by cell binding assay and in vivo by quantitative microPET imaging studies.

**Results:** FB-BBN-RGD had comparable  $\alpha v \beta 3$  integrin binding affinity with c(RGDyK) and comparable GRPR binding affinity with BBN(7-14). <sup>18</sup>F-FB-BBN-RGD had significantly higher tumor uptake ( $3.8 \pm 0.3\%$ ID/g) compared with monomeric RGD ( $1.9 \pm 0.2\%$ ID/g) and monomeric bombesin ( $1.1 \pm 0.2\%$ ID/g) peptide tracer analogs. The

receptor specificity of <sup>18</sup>F-FB-BBN-RGD in vivo was confirmed by effective blocking of the uptake in PC-3 tumor, which is both integrin and GRPR positive (partially blocked by either BBN or RGD alone but completely inhibited by RGD/BBN combination). Unlike <sup>18</sup>F-FB-BBN and <sup>18</sup>F-FB-RGD, which were mainly excreted through the hepatobiliary route, <sup>18</sup>F-FB-BBN-RGD had predominant renal clearance, resulting in high quality images.

**Conclusion:** Dual integrin  $\alpha v \beta 3$  and GRPR recognition showed significantly improved tumor targeting efficacy and pharmacokinetics compared with <sup>18</sup>F-labeled RGD and BBN analogs. The same heterodimeric ligand design may also be applicable to other receptor systems.

### REFERENCES/FUNDING SOURCE

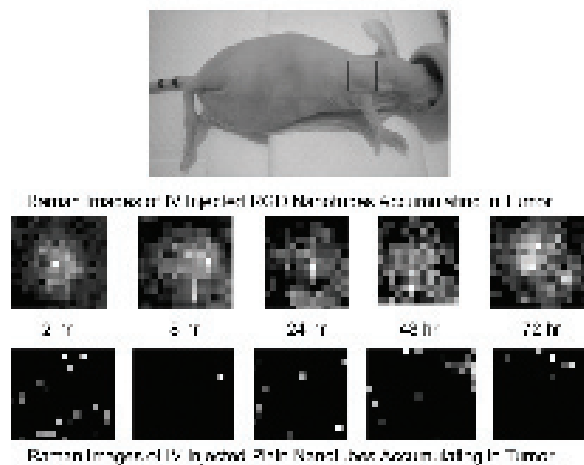
This work was supported in part by National Cancer Institute (NCI) (R21 CA102123, ICMIC P50 CA114747, CCNE U54 CA119367, and SARIP R24 CA93862), Department of Defense (DOD) (W81XWH-04-1-0697, W81XWH-06-1-0665, W81XWH-06-1-0042, DAMD17-03-1-0143, and BC061781), and a Dean's Fellowship (to ZL) from the Stanford University.

## Use of Non-invasive Raman Spectroscopy in Living Mice for Evaluation of Tumor Targeting with Carbon Nanotubes

C. ZAVALA<sup>1</sup>, S. KEREN<sup>1</sup>, Z. CHENG<sup>1</sup>, M. SCHIPPER<sup>1</sup>, X. CHEN<sup>3</sup>, Z. LIU<sup>2</sup>, H. DAI<sup>2</sup>, S.S. GAMBHIR<sup>1</sup>

<sup>1</sup>DEPARTMENTS OF RADIOLOGY (MIPS AND BIO-X PROGRAMS) AND <sup>2</sup>CHEMISTRY

In this project we used a Raman imaging system under development in our lab, in conjunction with single walled nanotubes (SWNTs), to produce deep tissue molecular images in living mice. We imaged mice using Raman scattering of light without the need to otherwise modify SWNTs. In addition, we demonstrated the ability of this optimized Raman instrument to localize SWNTs conjugated with RGD peptide in a U87MG xenograft model for in-vivo tumor targeting evaluation. Six female nude mice were inoculated with 20 million U87MG cells subcutaneously near right shoulder. Two weeks later, mice were divided into two groups. The first group (experimental) received a tail-vein injection of SWNTs conjugated with RGD. The second group (control) received SWNTs without RGD. Immediately after injection, in-vivo Raman imaging commenced to evaluate arrival of SWNTs in tumor. Raman spectra and mapping were acquired at 2, 8, 24, 48, and 72 hours of liver, tumor and contralateral shoulder. Mice were sacrificed at 72 hours, and tumor was excised for Raman mapping. Pharmacokinetics of SWNTs in tumor showed constant accu-



*Digital photograph of tumor bearing mouse depicting tumor area scanned with Raman spectroscopy (black box). The top panel depicts Raman tumor maps from a mouse receiving RGD nanotubes at various time points post injection. The bottom panel depicts Raman tumor maps from a different mouse receiving plain nanotubes at various time points post injection. Black pixels represent no Raman signal, and white pixels represent maximum Raman signal inherent of nanotubes. Notice how the top panel of tumor maps from the mouse that received RGD nanotubes shows a continued accumulation of nanotubes in the tumor area over 72 hours, as opposed to the bottom panel which shows no defined accumulation of nanotubes in the tumor area of a mouse that received plain nanotubes.*

mulation of RGD nanotubes for the first 30 minutes as opposed to plain nanotubes which showed initial accumulation followed by a rapid decrease. Raman spectra acquired from living mice receiving RGD nanotubes revealed a significant increase ( $p < 0.05$ ) in SWNT accumulation in the tumor compared to tumors of mice receiving non-targeted nanotubes at all time points. This data correlated well with ex-vivo Raman mapping of control mice which showed little to no accumulation in tumors. These results have significant implications toward developing a highly sensitive non-invasive preclinical Raman imaging modality as well as implementing various preexisting Raman nanoparticles for tumor targeting and multiplexing imaging capabilities.

### REFERENCES/FUNDING SOURCE

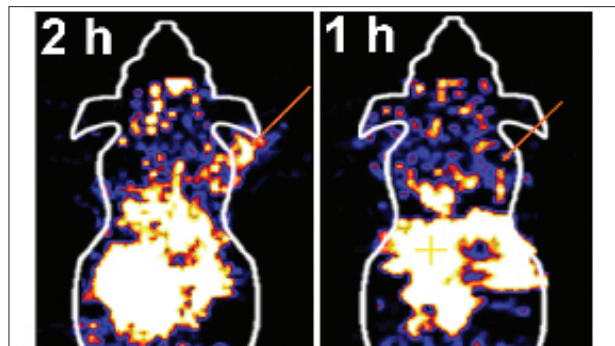
NIH Training grant T32 CA09695-15 Advanced Techniques for Cancer Imaging.



## MicroPET Imaging of HER2 Expression Using $^{64}\text{Cu}$ Labeled Synthetic Affibody Molecules

Z. CHENG<sup>1</sup>, O. PADILLA DE JESUS<sup>2</sup>, A. DE 1, J. WEBSTER<sup>2</sup>, O. GHEYSENS<sup>1</sup>, J. LEVI<sup>1</sup>, M. NAMAVARI<sup>1</sup>, S. WANG<sup>1</sup>, R. ZHANG<sup>2</sup>, J. HOERNER<sup>2</sup>, H. GRADE<sup>2</sup>, F. A. SYUD<sup>2</sup>, S. S. GAMBHIR<sup>1</sup>, DEPARTMENT OF <sup>1</sup>RADIOLOGY (MIPS AND BIO-X PROGRAMS) STANFORD UNIVERSITY AND <sup>2</sup>GLOBAL RESEARCH, GENERAL ELECTRIC COMPANY

Development of molecular probes based on novel engineered protein constructs is under active investigation due to the great potential of this generalizable strategy for imaging a variety of cell surface tumor targets. HER2-binding Affibody molecules are such engineered proteins and have been radiolabeled with different radioisotopes for targeting HER2 positive tumors. In this report,  $^{64}\text{Cu}$  labeled HER2-binding Affibody proteins were prepared and their ability to image HER2 expression in living mice using microPET were evaluated. The commercially available anti-HER2 Affibody molecule in monomeric ( $Z_{\text{HER2}}$ ) and dimeric ( $(Z_{\text{HER2}})_2$ ) forms were site-specifically modified with a prepared maleimide-functionalized chelator 1, 4, 7, 10-tetraazacyclododecane-1, 4, 7-tris(acetic acid)-10-acetate mono (N-ethylmaleimide amide) (Mal-DOTA). The resulting DOTA-Affibody conjugates were radiolabeled with  $^{64}\text{Cu}$ , and evaluated in cultured cells and nude mice bearing subcutaneous SKOV3 tumors.  $^{64}\text{Cu}$  labeled DOTA- $Z_{\text{HER2}}$  and DOTA- $(Z_{\text{HER2}})_2$  was prepared in high radiochemical purity (>98%) and specific activity (over 24 MBq/nmol). Cell uptake studies revealed that both probes specifically accumulated



Decay corrected coronal microPET images of nude mice bearing SKOV3 tumor. Images were acquired 1 h after tail vein injection of  $^{64}\text{Cu}$ -DOTA- $Z_{\text{HER2}}$  without (left image) or with (right image) pre-injection of 500  $\mu\text{g}$  Herceptin. Arrows indicate the location of tumors.

in SKOV3 cells. Biodistribution experiments showed that tumor uptake values of  $^{64}\text{Cu}$  labeled DOTA- $Z_{\text{HER2}}$  and DOTA- $(Z_{\text{HER2}})_2$  were  $6.12 \pm 1.44$  %ID/g and  $1.46 \pm 0.50$  %ID/g, respectively, in nude mice (N=3) bearing SKOV3 xenografts at 4 h post-injection. Moreover,  $^{64}\text{Cu}$ -DOTA- $Z_{\text{HER2}}$  exhibited significantly higher tumor/muscle and tumor/blood ratios than that of  $^{64}\text{Cu}$ -DOTA- $(Z_{\text{HER2}})_2$  at all the times examined in this study. MicroPET imaging of  $^{64}\text{Cu}$ -DOTA- $Z_{\text{HER2}}$  in SKOV3 tumor mice clearly showed good tumor localization. The tumor

uptake of  $^{64}\text{Cu}$ -DOTA- $Z_{\text{HER2}}$  could also be inhibited with a pre-injection of HER2 binding antibody, Herceptin. This study demonstrates that  $^{64}\text{Cu}$  labeled  $Z_{\text{HER2}}$  is a promising molecular probe for imaging HER2 receptor expression in living mice. Affibody molecules against other targets are also under investigation and hold promise as a generalizable imaging strategy.

## Activity Based Probe for MicroPET Imaging of Cysteine Cathepsins

MIN-KYUNG SO<sup>1</sup>, CHENJIE XU<sup>1</sup>, Z. CHENG<sup>1</sup>, G. BLUM<sup>2</sup>, O. GHEYSENS<sup>1</sup>, M. BOGYO<sup>2</sup>, S. S. GAMBHIR<sup>1</sup>  
DEPARTMENTS OF <sup>1</sup>RADIOLOGY (MIPS AND BIO-X PROGRAMS) AND <sup>2</sup>PATHOLOGY

Cysteine cathepsins have been reported to be actively involved in tumor progression, invasion and metastasis. Currently radionuclide imaging agents are not available for these important tumor biomarkers. Fluorescent activity based probes (ABPs) can selectively form a covalent bond with the active-site presented on the target protease. Our research goals are to develop radiolabeled ABPs for imaging cathepsins activity in tumors in living animals. One of the protease labeling functionalities, acyloxymethyl ketone (AOMK) was used as a scaffold for development of PET radionuclides labeled ABPs. 1,4,7,10-tetraazacyclododecane-1,4,7,10-tetraacetic acid conjugated AOMK analog [Z-FK(DOTA)-AOMK] was synthesized and it was radiolabeled with  $^{64}\text{Cu}$ . The biodistribution and microPET imaging of the probe were investigated in nude mice (N=3) bearing subcutaneous tumors.  $^{64}\text{Cu}$ -Z-FK(DOTA)-AOMK was synthesized in high radiochemical purity (>95%) and spe-

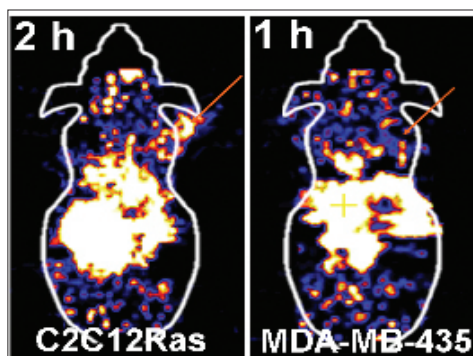


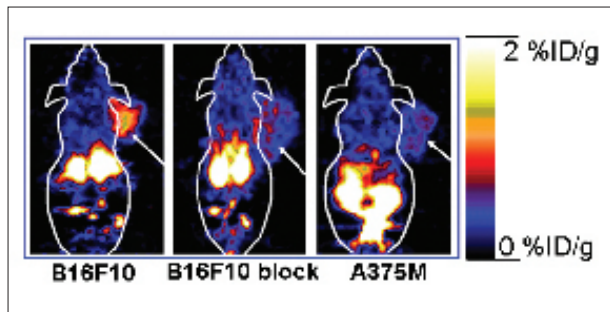
Figure: Coronal microPET images of a mouse bearing C2C12/Ras tumor (left) or MDA-MB-435 breast cancer (right) at different time after tail vein injection of  $^{64}\text{Cu}$ -Z-FK(DOTA)-AOMK. Arrows indicate location of tumors.

cific activity (over 17.8 MBq/nmol at the end of synthesis). Labeling of whole C2C12/Ras cell expressing high levels of cathepsins and MDA-MB-435 cell with a relatively low cathepsins expression confirmed that  $^{64}\text{Cu}$ -Z-FK(DOTA)-AOMK can specifically form a stable covalent linkage with cysteine cathepsins. Biodistribution experiments showed that tumor uptake values and tumor to background ratios of  $^{64}\text{Cu}$ -Z-FK(DOTA)-AOMK in a C2C12/Ras tumor were much higher than in a MDA-MB-435 tumor. MicroPET imaging studies further demonstrated that the C2C12/Ras tumor could be clearly visualized with good tumor to contralateral background contrast at 2 and 24 h post-injection. In contrast, low tumor uptake and poor tumor to normal tissue contrast in MDA-MB-435 tumor was observed. This study, for the first time, developed and validated a PET probe for cysteine cathepsins targeted tumor imaging.

## Evaluation of $^{18}\text{F}$ -Labeled-Alpha-Melanocyte Stimulating Hormone Analog for Melanocortin 1 Receptor Imaging

Z. CHENG, L. ZHANG, E. GRAVES, Z. XIONG, M. DANDEKAR, X. CHEN, S. S. GAMBHIR  
DEPARTMENT OF RADIOLOGY AND MOLECULAR IMAGING PROGRAM AT STANFORD

Fluorine-18 labeled small synthetic peptides have emerged as attractive probes for imaging various molecular targets with positron emission tomography (PET). The alpha-melanocyte-stimulating hormone receptor ( $\alpha$ -MSH receptor, MC1R) is over-expressed in most murine and human melanomas. It is a promising molecular target for both melanoma diagnosis and therapy. However,  $^{18}\text{F}$  compounds have not been successfully developed for imaging MC1R. An  $\alpha$ -MSH analog, NAPamide, was radiolabeled with *N*-succinimidyl-4- $^{18}\text{F}$ fluorobenzoate ( $^{18}\text{F}$ SFB). The resulting radiopeptide was evaluated as a potential molecular probe for microPET imaging of melanoma and MC1R expression in melanoma xenografted mouse models. The binding affinity of  $^{19}\text{F}$ SFB conjugated NAPamide,  $^{19}\text{F}$ FB-NAPamide was determined to be  $7.2 \pm 1.2$  nM using B16F10 cells and  $^{125}\text{I}$ -(Tyr2)-[Nle,4D-Phe7]- $\alpha$ -MSH [125I-(Tyr2)-NDP] as a radioligand. The biodistribution of  $^{18}\text{F}$ FB-NAPamide was then investigated in C57BL/6



Decay corrected coronal microPET images of C57 mouse bearing B16F10 tumor (left and middle images) and Fox Chase Scid mouse bearing A375M tumor (right images). Arrows indicate the location of tumors.

mice (N=3) bearing subcutaneous murine B16F10 melanoma tumors with high expression of MC1Rs and Fox Chase Scid mice (N=3) bearing human A375M melanoma with a relatively low number of MC1R receptors. Biodistribution experiments showed that tumor uptake values of  $^{18}\text{F}$ FB-NAPamide were  $1.19 \pm 0.11$  and  $0.46 \pm 0.11$  %ID/g, in B16F10 and A375M xenografted melanoma at 1 h post-injection, respectively ( $P < 0.05$ ). Furthermore, the B16F10 tumor uptake was significantly inhibited by co-injection with excess  $\alpha$ -MSH peptide ( $P < 0.05$ ), indicating that  $^{18}\text{F}$ FB-NAPamide specifically recognizes the MC1R in living mice. MicroPET

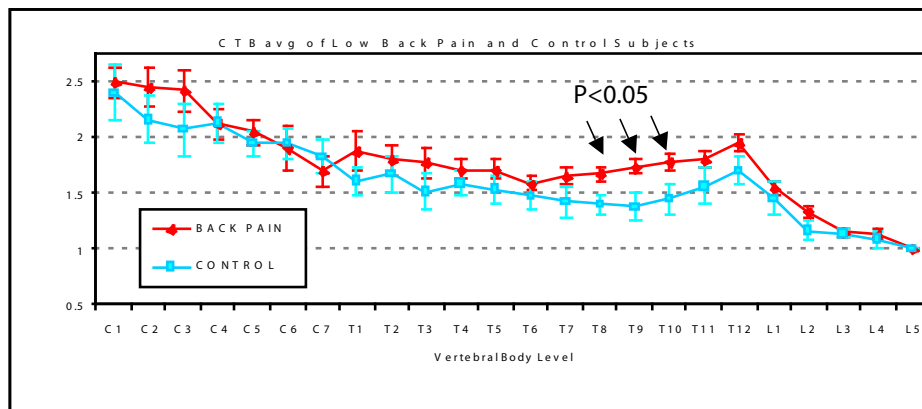
imaging of  $^{18}\text{F}$ FB-NAPamide in mice bearing B16F10 and A375M tumors at 1 h after tail vein injection revealed good B16F10 tumor-to-background contrast, while low A375M tumor-to-background ratios.  $^{18}\text{F}$ FB-NAPamide is a promising molecular probe for  $\alpha$ -MSH receptor positive melanoma PET imaging and warrants further study.

## Increased $^{18}\text{F}$ -FDG Uptake is Observed Within the Spinal Canal in Low Back Pain Patients

BRIAN KIM, ERIK MITTRA, HARPREET DHATT, BAO DO, EDWARD GRAVES, SANDIP BISWAL  
DEPARTMENT OF RADIOLOGY AND MOLECULAR IMAGING PROGRAM AT STANFORD

**Purpose:** Understanding spinal cord and cauda equina glucose metabolism may provide insight into causes or manifestations of low back pain. We have retrospectively characterized the distribution of 2-deoxy-2- $^{18}\text{F}$ -fluoro-D-glucose ( $^{18}\text{F}$ -FDG) within the entire length of the spinal canal in subjects with and without low back pain using whole body PET/CT.

**Method:** IRB approval was attained. A retrospective review of 14 negative whole body  $^{18}\text{F}$ -FDG PET/CT studies with non-CNS cancers was performed. Seven of the subjects had described 'low back pain' (LBP) and 7 subjects (control) described 'no pain' on their entrance questionnaire. Using the transaxial CT to define the spinal canal, fixed-dimension oval region of interests (ROIs) were placed within the canal and excluded the bony elements of the spine. PET ROI measurements (SUVavg) were obtained at every slice of the study C1 to S1. Transaxial measurements at L5, where minimal neural tissue is present, served as an internal control. For each vertebral level, mean SUVavg was calculated. For comparative analysis, we defined the canal-to-background (CTBavg) ratio as canal mean SUVavg:L5 SUVavg. Data was analyzed using RT Image analysis software and Student t-tests. Significance is  $p < 0.05$ .



**Results:** The mean L5 SUVavg was 0.75 and 0.82 for LBP and control patients which was not statistically different ( $p < 0.38$ ). Significantly higher mean CTBavg values were observed at vertebral levels T8, T9 and T10 in LBP subjects over controls (1.66, 1.73 and 1.78 versus 1.39, 1.37 and 1.44;  $p < 0.033$ , 0.020 and 0.048, respectively).

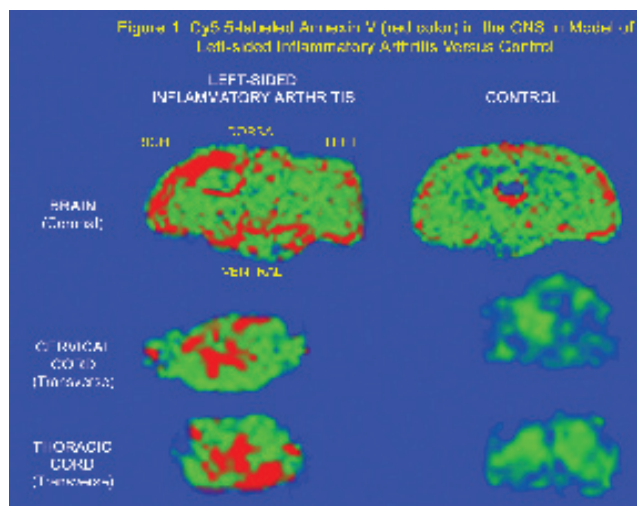
**Conclusion:** Increased  $^{18}\text{F}$ -FDG uptake is observed in the distal thoracic spinal canal in subjects describing low back pain. Increased neurosensory and neuromotor activity in the spinal cord at these levels related to LBP may explain this observation.

## Subjects Suffering from Inflammatory Arthritis Demonstrate Increased Cy5.5-labeled Annexin V Uptake in the Central Nervous System

SANDIP BISWAL<sup>1</sup>, DANYE CHENG<sup>1</sup>, ZOIA LEVASHOVA<sup>1</sup>, JONATHAN F. TAIT<sup>3</sup>, JEAN-LUC VANDERHEYDEN<sup>2</sup>, FRANCIS BLANKENBERG<sup>1</sup>,  
DEPARTMENT OF RADIOLOGY, (MIPS), STANFORD UNIVERSITY SCHOOL OF MEDICINE,  
<sup>2</sup>GE HEALTHCARE, <sup>3</sup>UNIVERSITY OF WASHINGTON, SEATTLE

**Objective:** During significant metabolic stress, cells 'express' phosphatidylserine (PS) to the outer leaflet of the cell membrane bilayer. Annexin V, a 35kD protein that binds to PS, can be utilized as an imaging agent to study cellular stress in subjects with pain. The purpose of this project is to develop objective methods for the detection and localization of pain-related activation of the CNS using labeled Annexin V.

**Methods:** Approval for the project was attained by our institute's IACUC. An animal model of monoarticular arthritis created by intradermal injection of 20ul of Complete Freund's Adjuvant in the left forepaw and 50ul in the left hindpaw of 5 month old Swiss-Webster mice. Inflammation on the paw proceeded for the next 72 hours. Under isoflurane anesthesia, the animals were injected intravenously with 5ug Cy5.5-labeled Annexin V. After a one-hour incubation period with the tracer, animals were simultaneously sacrificed and perfused



*Phosphorimages of representative thick sections from the central nervous system obtained from an animal with left-sided inflammatory arthritis and control animal after systemic injection of Cy5.5-labeled Annexin V. Positive signal (red color) indicates binding of Cy5.5-labeled Annexin V increased of 5 to 9-fold over background (green color) ( $p < 0.036$ ) in animals with left-sided inflammatory arthritis. Arthritic animals also showed focal increases throughout the CNS particularly in the right side of the brain, dorsal horn of the cervical cord as well as other regions of cord.*

with phosphate buffered saline. The central nervous system including the entire brain and spinal cord were harvested. Fluorescence imaging of the specimens was performed using CRi's Maestro and Molecular Dynamic's Typhoon. Image analysis was performed using Image J.

**Results:** Binding of Cy5.5-labeled Annexin V increased of 5 to 9-fold over background ( $p < 0.036$ ) in animals with left-sided inflammatory arthritis. Experimental animals also showed focal increases throughout the CNS particularly in the right side of the brain, dorsal horn of the cervical cord as well as other regions of cord (Fig). In contrast, control animals had minimal uptake of Cy5.5-labeled Annexin V.

**Conclusion:** Annexin V is a promising tracer for objectively demonstrating the activation of pain-related sensorineural pathway in the spinal cord and brain.

## microPET Imaging of Urokinase-type Plasminogen Activator Receptor Expression Using a <sup>64</sup>Cu-Labeled Linear Peptide Antagonist

ZI-BO LI<sup>1</sup>, GANG NIU<sup>1</sup>, HUI WANG<sup>1</sup>, LINA HE<sup>1</sup>, MICHAEL PLOUG<sup>2</sup> AND XIAOYUAN CHEN<sup>1</sup>  
DEPARTMENTS OF <sup>1</sup>RADIOLOGY (MIPS AND BIO-X PROGRAMS) STANFORD UNIVERSITY SCHOOL OF MEDICINE, STANFORD, CALIFORNIA  
AND <sup>2</sup>RIGSHOSPITALET COPENHAGEN BIOCENTER, COPENHAGEN, DENMARK

**Abstract:** Malignant tumors are capable of degrading the surrounding extracellular matrix (ECM), resulting in local invasion or metastasis. Urokinase-type plasminogen activator (uPA) and its cell surface receptor (uPAR) are central molecules in one of the major protease systems involved in ECM degradation. In this study we developed a <sup>64</sup>Cu-labeled uPAR-binding peptide for PET imaging of uPAR expression in vivo. **Methods:** The uPAR-binding peptide antagonist AE105 (D-Cha-F-s-r-Y-L-W-S), developed by combinatorial chemistry, was conjugated with DOTA and then labeled with <sup>64</sup>Cu for microPET imaging of mice bearing U87MG human glioblastoma (uPAR positive) and MDA-MB-435 human breast cancer (uPAR negative) tumors in the presence and absence of non-radiolabeled AE105. As a control, <sup>64</sup>Cu-labeled AE105-mut (D-Cha-F-s-r-Y-L-E-S) that does not bind to uPAR was also used. **Results:** Surface Plasmon Resonance measurement indicates that DOTA conjugation at the N-terminus of AE105 has little effect on the binding kinetics for its interaction with immobilized uPAR. MicroPET imaging revealed rapid and high tumor radioactivity accumulation of <sup>64</sup>Cu-DOTA-AE105 in uPAR positive U87MG tumors ( $10.1 \pm 0.86$

%ID/g at 4.5 h,  $n=3$ ) but not in uPAR negative MDA-MB-435 tumors ( $1.2 \pm 0.3$  %ID/g at 4.5 h,  $n=3$ ). <sup>64</sup>Cu-DOTA-AE105mut by replacing the Trp (W) with Glu (E) abolished the receptor binding in vitro and had only background tumor uptake in vivo. The uPAR receptor specificity of <sup>64</sup>Cu-DOTA-AE105 was further confirmed by effective blocking of tumor uptake in the presence of AE105. **Conclusion:** Successful demonstration of the ability of <sup>64</sup>Cu labeled uPAR specific probe to visualize uPAR expression in vivo may allow for clinical translation of this class of radiopharmaceuticals for cancer detection, patient stratification for uPA/uPAR system based cancer therapy, and for monitoring anti-uPAR treatment efficacy.

### REFERENCES/FUNDING SOURCE

NIBIB R21 EB001785, NCI R21 CA102123, NCI P50 CA114747, NCI U54 CA119367, NCI R24 CA93862, Department of Defense (DOD) (W81XWH-04-1-0697, W81XWH-06-1-0665, W81XWH-06-1-0042, and DAMD17-03-1-0143), Dean's fellowship from Stanford University (to Zi-Bo Li).



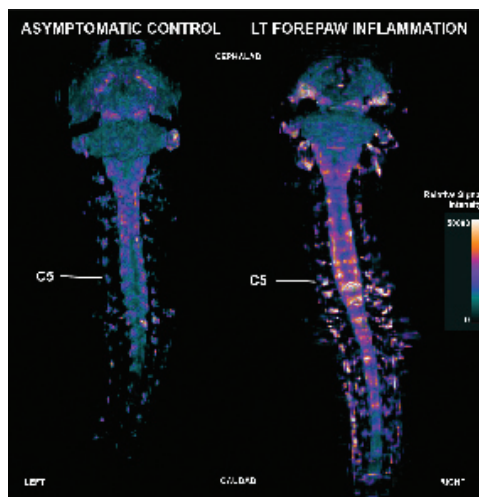
# Validation of Manganese-Enhanced Magnetic Resonance Imaging (MEMRI) as a Method to Detect Changes in the Spinal Cord Following Painful Stimuli

SHEEN-WOO LEE<sup>1</sup>, EDWARD GRAVES<sup>2</sup>, TAE JOO JEON<sup>1</sup>, SANG HOON LEE<sup>1</sup>, GARRY E. GOLD<sup>1</sup>, SANDIP BISWAL<sup>1</sup>

<sup>1</sup>DEPARTMENTS OF RADIOLOGY (MIPS) AND <sup>2</sup>RADIATION ONCOLOGY

**Purpose:** Manganese-enhanced MRI (MEMRI) exploits Mn<sup>2+</sup> ion's ability to act as a surrogate marker for calcium and powerful T1 shortening effect. Mn<sup>2+</sup> enters active neuronal cells through voltage-gated calcium channels. We validate MEMRI for detection of active areas in the spinal cord related to nociception by producing quantitative T1 maps and by ex vivo measurements of manganese.

**Methods:** A model of painful inflammation was created by injection of Complete Freund's Adjuvant into the forepaw of Sprague-Dawley rats (N=12). Twenty four hours after the systemic injection of manganese chloride (30mM), the spinal cords of the living animals were scanned in a 3T MRI. Gradient echo images were taken for anatomical analysis of the spinal cord. T1 measurements were performed using 8 different inversion times in sagittal inversion-recovery T1-weighted fast spin-echo sequence. Using CMIR\_Image analysis software, ROIs were placed on spinal cord to quantify the degree of manganese enhancement. T1 measurements were adjusted accord-



Three-dimensional maximum intensity projection (dorsal projection) obtained from axial T1-weighted manganese-enhanced magnetic resonance imaging (MEMRI) of the central nervous and nearby dorsal root ganglia (DRG) from a rat with forepaw pain and a control rat. In the subject with pain, the dorsal aspect of the cervical cord and DRGs particularly from levels C4 through C7 show increased signal intensity compared to the control

ing to administered dose, animal weight and background levels. Mn<sup>2+</sup> content of the harvested cord was measured by inductive coupled plasma (ICP). The data were analyzed with Student t-test on an Excel spreadsheet.

**Results:** There was increased signal intensity particularly along the dorsal aspect of the cervical cord of pain subject group compared to the control animal on MEMRI (Figure). The corrected T1 value of the cervical cord in the pain group was less than the control (22.83±3.74 vs 23.49±2.33 respectively, p<0.05). ICP data showed that the cervical cord Mn was higher in the pain group than the control (38.6±9.21 vs 24.0±5.30, p<0.05).

**Conclusion:** The result suggests that the MEMRI is a promising modality for showing the pain-activated sensorineural pathway in the spinal cord channels. We validate MEMRI for detection of active areas in the spinal cord related to nociception by producing quantitative T1 maps and by ex vivo measurements of manganese.

## PET Reporter Probes to Monitor $\beta$ -cells in Transgenic Mice Expressing a Triple Fusion Reporter Gene

JULIA RASOOLY<sup>3</sup>, ANKIT GARG<sup>1</sup>, HOA DANG<sup>2</sup>, PRITHA RAY<sup>3</sup>, FRED CHIN<sup>3</sup>, MOHAMMAD NAMAVARI<sup>3</sup>, DANIEL KAUFMAN<sup>2</sup>, SAM GAMBHIR<sup>1,3</sup>

DEPARTMENTS OF <sup>1</sup>BIOENGINEERING (BIO-X PROGRAM), <sup>3</sup>RADIOLOGY (MIPS), STANFORD UNIVERSITY, STANFORD CA AND

<sup>2</sup>MOLECULAR AND MEDICAL PHARMACOLOGY, UNIVERSITY OF CALIFORNIA, LOS ANGELES, CA,

A non-invasive method to monitor the insulin-producing  $\beta$ -cells of the pancreas in mice would enable assessment of  $\beta$ -cell mass during of the development of murine type I and type II diabetes and aid in the development of interventional therapies.

C57BL6 mice (n=7) that carry a transgene consisting of a mouse insulin promoter driving the expression of a triple fusion (MIP-TF mice) of firefly luciferase-egfp-truncated HSV1-sr39thymidine kinase reporter genes were imaged with microPET, microCT, and a cooled CCD camera. These mice express the trifusion reporter in the  $\beta$ -cells of the pancreas. Heretofore, it has not been possible to image the mouse pancreas with microPET due to its small size and its proximity to the probe excretion pathways. Here, we assessed the ability to image the  $\beta$ -cells of the MIP-TF mice using 1) 9-(4-[<sup>18</sup>F]fluoro-3-hydroxymethylbutyl)guanine (FHBG) and imaging at late time points post-probe injection, and 2) using 2'-deoxy-2'-[<sup>18</sup>F]fluoro-5-ethyl-1-b-D-arabinofuranosyluracil (FEAU).

At a 5 hour time-point post-injection, [<sup>18</sup>F]FEAU achieved a higher mean signal accumulation in the pancreas than [<sup>18</sup>F]FHBG: [<sup>18</sup>F]FEAU was 2.79±0.80 %ID/g and [<sup>18</sup>F]FHBG was 1.18±0.94%ID/g (p=0.01). In comparison to [<sup>18</sup>F]FHBG, which showed

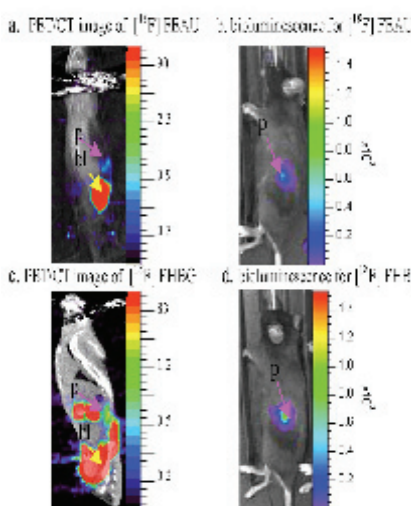


Figure. (a) coronal [<sup>18</sup>F]FEAU PET/CT image and (b) bioluminescence image of the same mouse. (c) coronal [<sup>18</sup>F]FHBG PET/CT image and (d) bioluminescence image of the same mouse. In most [<sup>18</sup>F]FHBG images, spillover signals from probe excretion pathways blurred the pancreas signal. In all images, 'p' arrows denote areas of pancreas and 'bl' arrows denote bladder.

2007 AMI/SMI Conference in Providence, RI

a mean signal accumulation in the lower GI of 2.97±4.95%ID/g and in the liver of 2.61±3.57%ID/g, [<sup>18</sup>F]FEAU displayed predominantly renal clearance and showed a gastrointestinal signal of 1.07±0.71%ID/g (p=0.0003) and liver signal of 0.94±0.63%ID/g (p=0.005). Our results suggest that [<sup>18</sup>F]FEAU may be a promising PET radiotracer for non-invasive quantitative assessment of type II diabetes in C57BL6 MIP-TF mice that are fed a high fat diet, and of type I diabetes in non-obese diabetic (NOD) mice. TF-expressing islets are also useful for microPET studies of islet survival after transplantation.

### REFERENCES/FUNDING SOURCE

NCI ICMI P50 CA 114747, NCI R01 CA082214, National Academies Ford Foundation.

## The Presence of Relatively Small Number of Mesenchymal Stem Cells Promotes Accelerated Growth in Osteosarcoma Tumor Xenografts

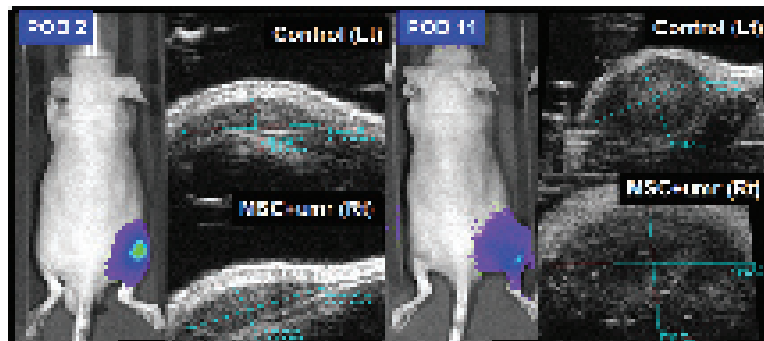
TAE JOO JEON<sup>1</sup>, SHEEN-WOO LEE<sup>2</sup> AND SANDIP BISWAL<sup>1</sup>

DEPARTMENT OF <sup>1</sup>RADIOLOGY (MIPS), STANFORD UNIVERSITY, STANFORD, CALIFORNIA  
AND <sup>2</sup>POCHON CHA UNIVERSITY, SUNGNAM, KOREA.

**Purpose:** In the presence of cancer cells, normal progenitor cells are recruited to form supportive stromal elements for tumor growth. Using bioluminescence (BLI) and ultrasound (USI), we wanted to determine whether the addition of mesenchymal stem cells (MSCs) promotes osteosarcoma tumor xenograft growth.

**Methods:** Animal studies were approved by our institute's IACUC. A mixture of cells containing 2x10<sup>6</sup> umr osteosarcoma cells and 25% or 5% reporter Firefly luciferase-expressing MSCs were suspended in Matrigel® and then xenografted onto the rear flanks of nude mice (N=10). As a control, 2x10<sup>6</sup> umr cells in Matrigel® only were grafted on the contralateral side. Serial in vivo bioluminescence images were obtained by a Xenogen IVIS 200 every three days for 16 days to monitor the presence of reporter MSCs. Tumor volume was obtained using a Visualsonics Vevo 770 high resolution ultrasound. Microsoft Excel Spreadsheets and Student t-tests were utilized for statistical analysis. Significance is p<0.05.

**Results:** Xenografts containing a mixture of umr cells and reporter MSCs showed significantly more rapid growth compared to the umr control xenograft from the 3rd day of inoculation (p<0.0128). On day



*Serial bioluminescence (BLI) and ultrasound (US) images obtained from a single mouse containing two tumor xenografts, one on the left flank (Lt) containing osteosarcoma (umr) cells only and the other located on the right (Rt) flank containing umr cells mixed with Firefly luciferase-expressing adipose-derived mesenchymal stem cells (MSCs). As measured by US, the size of the xenografts enlarged faster over time in the xenografts supplemented by MSCs. Positive BLI signal was observed on post-operative day (POD) 2 in the MSC-containing xenograft, suggesting presence and survival of the reporter MSCs. However, by the POD 11, BLI signal decreased substantially suggesting some loss of MSCs or perhaps gene silencing.*

xenograft containing MSCs ('umr + MSCs') grew larger in size than the xenografts containing osteosarcoma cells alone ('umr').

**Conclusion:** Despite their rapid attrition, the presence of a small population of MSCs within the tumor mass contribute to rapid osteosarcoma tumor growth. The results underscore the importance of understanding the role of normal adult stem cells in the developing neoplasm.

9, measured tumor volumes of umr-MSC mixture vs. control tumor were 56.72 ± 24.12 mm<sup>3</sup> and 19.18 ± 10.56 mm<sup>3</sup>, respectively. BLI showed persistence of reporter MSCs during the duration of the experiment, albeit in lower levels (5.7 to 8.3%) than the early post-inoculation period. While preliminary comparisons indicate no significant difference in tumor growth rate between 25% and ~5% MSC-containing xenografts, both MSC-containing xenografts grow faster than control xenografts. The accompanying figure shows ultrasound (US) images of how the osteosarcoma

## PET Imaging of Angiogenesis Formation in Teratoma from Human Embryonic Stem Cells

FENG CAO, ZIBO LI, KAI CHEN, HUI WANG, WEIBO CAI, XIAOYUAN CHEN, JOSEPH C.WU  
DEPARTMENT OF RADIOLOGY AND MOLECULAR IMAGING PROGRAM AT STANFORD

**Objectives:** Teratoma formation can be a serious drawback after transplantation of human embryonic stem cells (hESCs) for cell or tissue regenerative purposes. Here we investigated the angiogenic process within teratomas derived from hESCs in vivo by positron emission tomography (PET) imaging of  $\alpha v\beta 3$  integrin using the  $^{64}\text{Cu}$ -labeled DOTA-RGD tetramer  $^{64}\text{Cu}$ -DOTA-E{E[c(RGDyK)]<sub>2</sub>}<sub>2</sub>.

**Methods:** Federally approved hESCs (H9 line) were stably transduced to express firefly luciferase and enhanced green fluorescence protein (Fluc-eGFP) for bioluminescence imaging (BLI) and FACS, respectively. Adult nude mice (n=10) were injected subcutaneously with  $2 \times 10^6$  of undifferentiated hESCs. Longitudinal BLI and microPET imaging with  $^{18}\text{F}$ -FDG and  $^{64}\text{Cu}$ -DOTA-E{E[c(RGDyK)]<sub>2</sub>}<sub>2</sub> were performed.

**Results:** Eight weeks following transplantation, all of the hESCs grafts evolved into teratomas as confirmed by longitudinal BLI. MicroPET imaging revealed specific and prominent uptake of  $^{64}\text{Cu}$ -DOTA-E{E[c(RGDyK)]<sub>2</sub>}<sub>2</sub> in vascularized teratoma compared with control human ovarian carcinoma cell line (2008 line) tumor with low

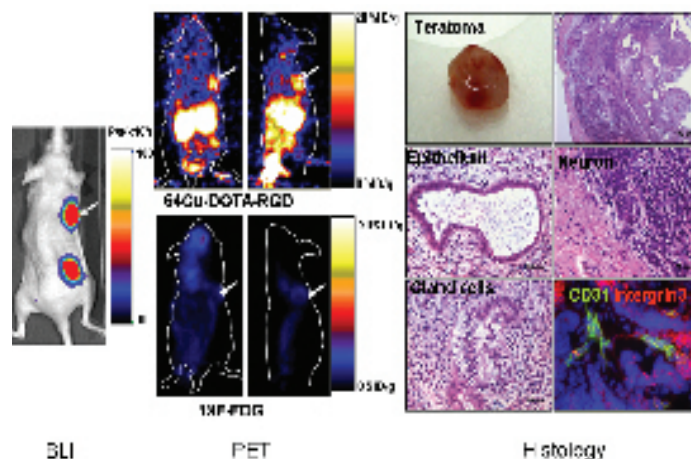


*Figure: PET imaging of angiogenesis formation in hESC-derived teratomas. (Left) BLI shows robust Fluc signal 8 weeks after subcutaneous transplantation of  $2 \times 10^6$  hESCs. (Middle) MicroPET imaging demonstrates robust uptake of  $^{64}\text{Cu}$ -DOTA-E{E[c(RGDyK)]<sub>2</sub>}<sub>2</sub> (binds to integrin receptor) but low uptake of  $^{18}\text{F}$ -FDG (metabolic activity) within hESC-derived teratoma. (Right) H&E show presence of all 3 germ layers within the teratoma. Immunofluorescence stains positive for integrin  $\beta 3$  (red) and CD31 (green) within the teratoma, consistent with the in vivo PET imaging data of angiogenesis.*

intergrin expression ( $10.1 \pm 3.4$  vs.  $1.4 \pm 1.2$  %ID/g;  $P < 0.01$ ). Interestingly, hESC-derived teratomas had low uptake of  $^{18}\text{F}$ -FDG ( $0.6 \pm 0.2$  vs  $0.4 \pm 0.3$  %ID/g in background at week 8,  $p = \text{NS}$ ) (Figure 1). Histology of the teratoma showed proper differentiation into all three germ layers. Immunofluorescence staining of CD31 and  $\alpha v\beta 3$  integrin revealed significantly higher expression compared to human ovarian carcinoma cell line confirming the in vivo imaging results ( $P < 0.05$ ). Finally, the cells dissociated from teratoma also showed higher uptake and retention of  $^{64}\text{Cu}$ -DOTA-E{E[c(RGDyK)]<sub>2</sub>}<sub>2</sub> compared with 2008 cell line ( $P < 0.05$ ).

**Conclusions:** We successfully demonstrated the ability of  $^{64}\text{Cu}$ -DOTA-E{E[c(RGDyK)]<sub>2</sub>}<sub>2</sub>

to visualize integrin expression during teratoma formation in vivo. This tracer may have clinical applicability for monitoring tumorigenicity after hESC transplantation in the future.

### REFERENCES/FUNDING SOURCE

American Heart Association (FC).

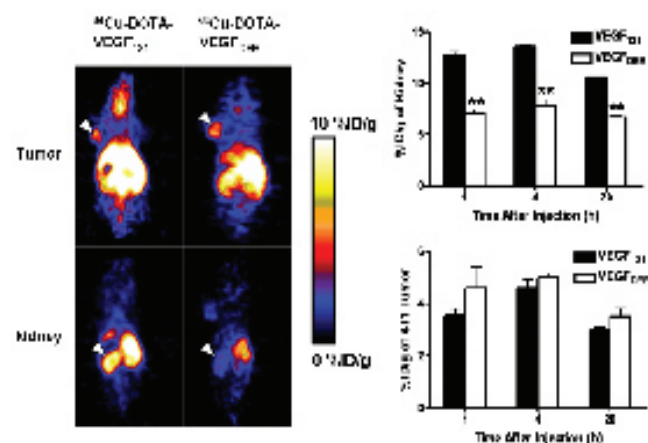


## A VEGF Receptor-2 Specific PET Tracer Based on VEGF121 Mutant

HUI WANG, WEIBO CAI, KAI CHEN, ZI-BO LI, AMIR KASHEFI, LINA HE, AND XIAOYUAN CHEN  
DEPARTMENT OF RADIOLOGY (MIPS AND BIO-X PROGRAMS)

**Objective:** The high renal uptake of  $^{64}\text{Cu}$ -labeled VEGF<sub>121</sub> is a major concern in microPET imaging for VEGFRs expression. The unfavorable dosimetry prompts us to develop VEGFR2 specific mutants. **Methods:** Three VEGF<sub>121</sub> mutants were generated by DNA recombinant. The proteins were purified and conjugated with DOTA. The binding affinity to VEGFRs and their VEGFR2 phosphorylation function were evaluated in vitro. The DOTA conjugates of VEGF<sub>121</sub> and mutants were then labeled with  $^{64}\text{Cu}$  and their biodistribution was compared using 4T1 tumor-bearing mice by microPET imaging. Blocking experiments and ex vivo histopathology was carried out to confirm the in vivo results.

**Results:** The VEGF<sub>121</sub> and three mutants were successfully purified and DOTA conjugated. The cell binding assay results demonstrated one D63AE64AE67A mutant has 26-fold decrease binding affinity to VEGF1 without compromising VEGFR2 binding compared with VEGF121.



Representative figures demonstrated VEGFDEE mutant has 2-fold lower kidney uptake without compromising its tumor targeting effect as compared with VEGF121.

MicroPET imaging revealed that both  $^{64}\text{Cu}$ -DOTA-VEGF121 and  $^{64}\text{Cu}$ -DOTA-D63AE64AE67A were rapidly, specifically accumulated in 4T1 tumors. In contrast, the kidney uptake of  $^{64}\text{Cu}$ -DOTA-D63AE64AE67A showed 1.5-fold decrease compared with  $^{64}\text{Cu}$ -DOTA-VEGF<sub>121</sub>. Blocking experiments confirmed the VEGFR specificity of  $^{64}\text{Cu}$ -DOTA-D63AE64AE67A. Immunofluorescence staining showed kidney expressed both VEGFRs in high level, whereas 4T1 tumor expressed VEGFR2 only.

**Conclusion:** Successful demonstration of the ability of  $^{64}\text{Cu}$ -DOTA-D63AE64AE67A to visualize VEGFR2 expression specifically

in vivo with decreased kidney uptake may allow for clinical translation of this radiopharmaceutical for imaging tumor angiogenesis and as a targeted delivery vehicle for VEGFR-targeted cancer therapy.

### REFERENCES/FUNDING SOURCE

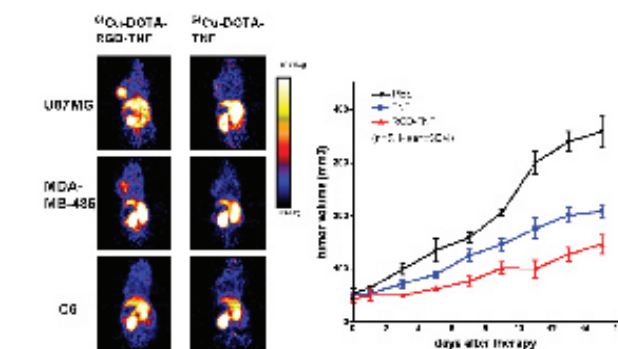
EJNMMI DOI 10.1007/s00259-007-0524-0, in press

## Efficient in vivo Tumor Targeting of a RGD-TNF Fusion Protein

HUI WANG, KAI CHEN, WEIBO CAI, ZI-BO LI, LINA HE, AND XIAOYUAN CHEN  
DEPARTMENT OF RADIOLOGY (MIPS AND BIO-X PROGRAMS)

**Objectives:** The clinical use of tumor necrosis factor alpha (TNF- $\alpha$ ) as an anti-cancer drug is limited to local treatments because of its dose-limiting systemic toxicity. Our objective of this study is to improve the anti-tumor therapeutic index of TNF by targeted delivery of TNF to integrin  $\alpha\text{v}\beta 3$  positive tumor site. **Methods:** RGD-TNF fusion protein was conjugated with DOTA for  $^{64}\text{Cu}$  labeling. The cytotoxicity and integrin  $\alpha\text{v}\beta 3$  binding affinity of RGD-TNF, and its DOTA conjugate were evaluated in vitro. The in vivo tumor targeting efficacy and pharmacokinetics of  $^{64}\text{Cu}$ -DOTA-RGD-TNF and  $^{64}\text{Cu}$ -DOTA-TNF were compared using 3 tumor models with high, medium and low integrin  $\alpha\text{v}\beta 3$  expression level. Prove-of-principle therapy was carried out to test the anti-tumor effect of RGD-TNF in integrin  $\alpha\text{v}\beta 3$  positive tumor model.

**Results:** RGD-TNF fully retained its cytotoxicity and showed cell killing effect independent of integrin  $\alpha\text{v}\beta 3$  expression level in vitro. Cell binding assay demonstrated that RGD-TNF specifically bind to integrin  $\alpha\text{v}\beta 3$ -positive cells. Quantitative microPET imaging studies revealed that tumor uptake of  $^{64}\text{Cu}$ -DOTA-RGD-TNF correlated well with integrin  $\alpha\text{v}\beta 3$  density: U87MG ( $8.11 \pm 0.88$  %ID/g) > MDA-



A: representative figures demonstrated integrin  $\alpha\text{v}\beta 3$  depended tumor accumulation of  $^{64}\text{Cu}$ -DOTA-RGD-TNF; B: RGD-TNF showed enhanced anti-tumor effect in integrin  $\alpha\text{v}\beta 3$  positive MDA-MB-435 tumor model compared with TNF.

MB-435 ( $4.39 \pm 0.65$  %ID/g) > C6 ( $1.93 \pm 0.56$  %ID/g). In contrast,  $^{64}\text{Cu}$ -DOTA-TNF showed similar background level uptake in all three tumor models. Successful blocking of the tumor uptake of  $^{64}\text{Cu}$ -DOTA-RGD-TNF by RGD-peptide further confirmed the integrin  $\alpha\text{v}\beta 3$  specificity of  $^{64}\text{Cu}$ -DOTA-RGD-TNF in vivo. Therapeutic studies at a dose of 1.25mg/kg on nude mice bearing established ( $\sim 75\text{mm}^3$ ) human breast MDA-MB-435 xenograft tumors demonstrated potent tumor suppression compared with TNF.

**Conclusions:** RGD-TNF fusion protein combining features that potentially allow a high degree of integrin  $\alpha\text{v}\beta 3$  selective action may be translated into clinical use for integrin  $\alpha\text{v}\beta 3$  positive cancer therapy.

### REFERENCES/FUNDING SOURCE

NCI R21 CA102123, P50 CA114747, R24 CA93862, U54 CA119367, Department of Defense (DOD) (W81XWH-04-1-0697, W81XWH-06-1-0665, W81XWH-06-1-0042, DAMD17-03-1-0143, BC061781), and a Benedict Cassen Postdoctoral Fellowship from the Education and Research Foundation of the Society of Nuclear Medicine (W.Cai).

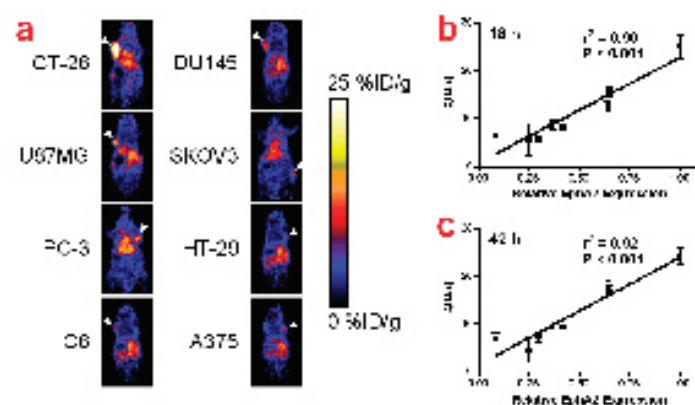
# Quantitative PET Imaging of EphA2 Expression in Tumor-bearing Mice

WEIBO CAI, ALIREZA EBRAHIMNEJAD, KAI CHEN, QIZHEN CAO, ZI-BO LI, DAVID A. TICE, AND XIAOYUAN CHEN  
DEPARTMENT OF RADIOLOGY AND MOLECULAR IMAGING PROGRAM AT STANFORD

**Objectives:** EphA2 receptor tyrosine kinase is overexpressed in a wide variety of tumors. High EphA2 expression has been correlated with increased metastatic potential and poor patient survival in several cancer types. To date, in vivo imaging of EphA2 has not been investigated.

**Methods:** We labeled 1C1, a humanized monoclonal antibody (mAb) against both human and murine EphA2, with  $^{64}\text{Cu}$  through chelating agent 1,4,7,10-tetraazacyclododecaneN,N',N'',N'''-tetraacetic acid (DOTA) and carried out positron emission tomography (PET) imaging in eight tumor models at multiple time points post-injection of  $^{64}\text{Cu}$ -DOTA-1C1. The tumor uptake quantified from microPET imaging was correlated with the relative EphA2 expression level measured by Western blot.

**Results:** The radiolabeling yield was  $88.9 \pm 9.5\%$  ( $n = 7$ ) and the specific activity of  $^{64}\text{Cu}$ -DOTA-1C1 was  $1.3 \pm 0.1$  GBq/mg of 1C1 mAb. The 1C1 mAb retained antigen-binding affinity/specificity after DOTA conjugation as measured by FACS analysis.  $^{64}\text{Cu}$ -DOTA-1C1 uptake in EphA2-positive CT-26 tumors was as high as  $25.1 \pm 2.5\%$  ID/g ( $n = 3$ ) at 18 h post-injection.  $^{64}\text{Cu}$ -DOTA-IgG, an isotype-matched con-



a. MicroPET images of tumor-bearing mice at 18 h after injection of  $^{64}\text{Cu}$ -DOTA-1C1 ( $n = 3$  per tumor type). Arrowheads indicate tumors.

b. Correlation of relative tumor tissue EphA2 expression (measured by Western blot) and the average %ID/g values of tumor  $^{64}\text{Cu}$ -DOTA-1C1 uptake (measured by PET) at 18 h post-injection.

c. Correlation of relative tumor tissue EphA2 expression and the average %ID/g values of tumor  $^{64}\text{Cu}$ -DOTA-1C1 uptake at 42 h post-injection

trol, exhibited minimal non-specific uptake in all eight tumors. In vivo EphA2 specificity of  $^{64}\text{Cu}$ -DOTA-1C1 was confirmed by successful blocking of CT-26 tumor uptake by unlabeled 1C1. Most importantly, the tumor uptake (%ID/g) obtained from PET imaging had excellent linear correlation with the relative tumor tissue EphA2 expression level measured by Western blot, where  $r^2$  equals 0.90 and 0.92 at 18 and 42 h post-injection, respectively.

**Conclusions:** The tumor uptake of  $^{64}\text{Cu}$ -DOTA-1C1 measured by microPET imaging reflects tumor EphA2 expression level in vivo. This is the first report of quantitative radioimmuno PET imaging of EphA2 in living subjects. Future clinical investigation of  $^{64}\text{Cu}$ -DOTA-1C1 is warranted.

## REFERENCES/FUNDING SOURCE

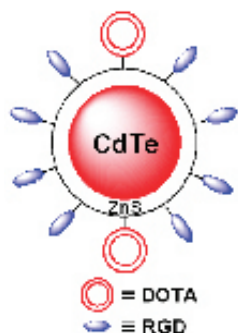
MedImmune, Inc., National Cancer Institute (NCI) (R21 CA102123, P50 CA114747, U54 CA119367, and R24 CA93862), Department of Defense (DOD) (W81XWH-04-1-0697, W81XWH-06-1-0665, W81XWH-06-1-0042, and DAMD17-03-1-0143), and a Benedict Cassen Postdoctoral Fellowship from the Education and Research Foundation of the Society of Nuclear Medicine (to W. Cai).

## Dual Functional Quantum Dot-Based Probe for Near-Infrared Fluorescence and Positron Emission Tomography Imaging of Cancer

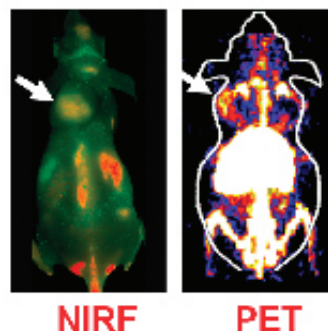
WEIBO CAI, KAI CHEN, ZI-BO LI, SANJIV S. GAMBHIR, AND XIAOYUAN CHEN  
DEPARTMENT OF RADIOLOGY (MIPS AND BIO-X PROGRAMS)

**Objectives:** In vivo imaging of quantum dots (QDs) are mostly qualitative or semi-quantitative. Development of dual modality near-infrared fluorescence (NIRF)/positron emission tomography (PET) probe may allow accurate assessment of the pharmacokinetics and tumor targeting efficacy of QDs. **Methods:** QD705 (705 nm emission) were labeled with RGD peptides (for targeting integrin  $\alpha_v\beta_3$ ) and DOTA chelator (for PET imaging after  $^{64}\text{Cu}$ -labeling). PET/NIRF imaging, tissue homogenate fluorescence measurement, and immunofluorescence staining were performed using U87MG tumor-bearing mice.

**Results:** There are about 90 RGD peptides per QD particle. DOTA-QD-RGD exhibited integrin  $\alpha_v\beta_3$ -specific binding in cell culture. The U87MG tumor uptake of  $^{64}\text{Cu}$ -DOTA-QD was less than 1 %ID/g at all time points examined while the uptake of  $^{64}\text{Cu}$ -DOTA-QD-RGD was significantly higher. PET, ex vivo NIRF imaging, and tissue homogenate fluorescence measurement gave the liver-, spleen-, and kidney-to-muscle ratios of about 100:1, 40:1, and 1:1, respectively. The U87MG tumor-to-muscle ratio is about 3:1 and 1:1 for DOTA-QD-RGD and DOTA-QD, respectively. Excellent linear correlation was



*A dual functional probe for positron emission tomography and near-infrared fluorescence imaging of tumor vasculature.*



found between the results measured by in vivo PET and ex vivo NIRF imaging/tissue homogenate fluorescence ( $r^2 = 0.93$ ). Tumor vasculature staining revealed that DOTA-QD-RGD targets mainly the tumor vasculature via RGD-integrin  $\alpha_v\beta_3$  interaction with little extravasation.

**Conclusions:** We quantitatively evaluated the tumor targeting efficacy of dual functional QD-based probes using NIRF and PET imaging. Noninvasive PET imaging provides a robust measure of the probe distribution in vivo. This dual functional probe

can give sufficient tumor contrast at much lower concentration than that required for in vivo NIRF imaging, thus significantly reducing toxicity. It also overcomes the tissue penetration limitation of NIRF imaging, allowing for quantitative targeted imaging in deep tissue.

### REFERENCES/FUNDING SOURCE

National Cancer Institute (NCI) (R21 CA102123, P50 CA114747, U54 CA119367, and R24 CA93862), Department of Defense (DOD) (W81XWH-04-1-0697, W81XWH-06-1-0665, W81XWH-06-1-0042, and DAMD17-03-1-0143), and a Benedict Cassen Postdoctoral Fellowship from the Education and Research Foundation of the Society of Nuclear Medicine (to W. Cai).



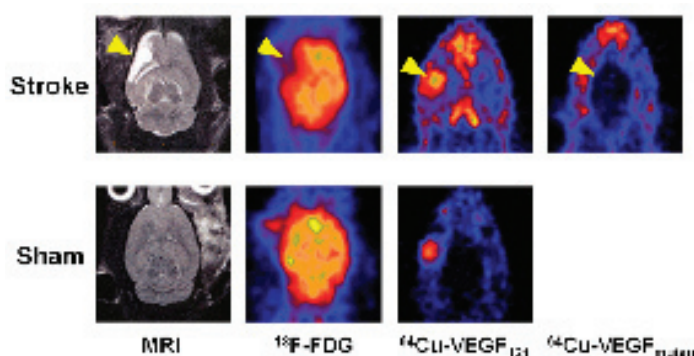
## PET Imaging of VEGFR Expression in Stroke

WEIBO CAI, RAPHAEL GUZMAN, KAI CHEN, ANDREW R. HSU, TONYA BLISS, GUOHUA SUN, HUI WANG,  
LINA HE, ZI-BO LI, ANNE-LISE D. MAAG, NOBUTAKA HORI, GARY K. STEINBERG, XIAOYUAN CHEN  
DEPARTMENT OF RADIOLOGY (MIPS AND BIO-X PROGRAMS)

**Objective:** Vascular endothelial growth factor (VEGF) and VEGF receptors (VEGFRs) play important roles during neurovascular repair after stroke. In this study, we evaluated the kinetics of VEGFR expression during post-stroke angiogenesis in a rat model.

**Methods:** In Sprague-Dawley rats, stroke was created by permanent occlusion of the distal middle cerebral artery (dMCAo). The rats were subjected to MRI and PET scans before surgery and at 2, 9, 16, 23 days after surgery. Several tracers were used for PET, namely  $^{18}\text{F}$ -FDG (to measure the metabolic activity of the brain),  $^{64}\text{Cu}$ -DOTA-VEGF<sub>121</sub> (previously validated for imaging VEGFR expression), and  $^{64}\text{Cu}$ -DOTA-VEGFmutant (with much lower VEGFR binding affinity than VEGF<sub>121</sub>). Ex vivo immunofluorescence staining was carried out on frozen brain sections to assess VEGFR expression and vessel density (CD31) at different days after stroke. Autoradiography using  $^{125}\text{I}$ -VEGF<sub>165</sub> on frozen stroke brain tissue was also carried out to validate the in vivo imaging results.

**Results:** The stroke in the rat brain was confirmed by T2-weighted MRI and  $^{18}\text{F}$ -FDG PET. The stroke size based on MRI was relatively stable over time while the size of “cold spot” in  $^{18}\text{F}$ -FDG PET varied to a certain extent, likely due to inflammation.  $^{64}\text{Cu}$ -DOTA-VEGF<sub>121</sub> uptake in the stroke area peaked at about 10 days after surgery, indicating



MRI and  $^{18}\text{F}$ -FDG PET confirmed the stroke in the rat brain (arrowheads).  $^{64}\text{Cu}$ -labeled VEGF<sub>121</sub> had intense uptake in the stroke area at day 10.  $^{64}\text{Cu}$ -labeled VEGFmutant had no appreciable uptake in the stroke area. Note there is also significant uptake of  $^{64}\text{Cu}$ -labeled VEGF<sub>121</sub> in the surgical wound.

neovascularization as confirmed by ex vivo histology. VEGFR specificity of  $^{64}\text{Cu}$ -DOTA-VEGF<sub>121</sub> uptake was confirmed by significantly lower uptake of  $^{64}\text{Cu}$ -DOTA-VEGFmutant in vivo and intense  $^{125}\text{I}$ -VEGF<sub>165</sub> uptake ex vivo in the stroke area. No appreciable uptake of  $^{64}\text{Cu}$ -DOTA-VEGF<sub>121</sub> was observed in the brain of sham operated rats, although the uptake in the surgical wound was obvious.

**Conclusions:** For the first time, we successfully evaluated the VEGFR expression kinetics noninvasively in a stroke rat model.

Monitoring VEGFR expression in vivo after stroke is clinically relevant and may be translated into the clinic to determine the right timing for stroke therapy and to monitor the therapeutic efficacy by imaging post-stroke angiogenesis.

### REFERENCES/FUNDING SOURCE

National Cancer Institute (NCI) (R21 CA102123, P50 CA114747, U54 CA119367, and R24 CA93862), Department of Defense (DOD) (W81XWH-04-1-0697, W81XWH-06-1-0665, W81XWH-06-1-0042, and DAMD17-03-1-0143), and a Benedict Cassen Postdoctoral Fellowship from the Education and Research Foundation of the Society of Nuclear Medicine (to W. Cai).

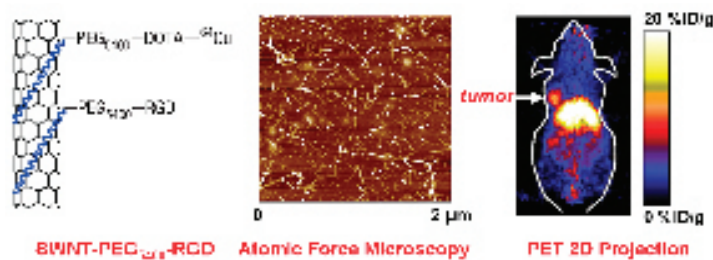
# PET Imaging and Efficient Tumor Targeting of Labeled Single-Walled Carbon Nanotubes

WEIBO CAI<sup>1</sup>, ZHUANG LIU<sup>1</sup>, LINA HE<sup>1</sup>, HONGJIE DAI<sup>2</sup>, XIAOYUAN CHEN<sup>1</sup>  
DEPARTMENTS OF <sup>1</sup>RADIOLOGY (MIPS AND BIO-X PROGRAMS) AND <sup>2</sup>CHEMISTRY

**Objectives:** Single-walled carbon nanotubes (SWNTs), with strong absorbance in the near-infrared (NIR) window, have been used for cancer cell killing by NIR radiation induced heating. In this study we evaluated the in vivo pharmacokinetics and tumor targeting efficacy of RGD peptide (potent integrin  $\alpha\beta_3$  antagonist) labeled biocompatible SWNTs.

**Methods:** SWNTs (100-300 nm long) with different length poly(ethylene glycol) (PEG, MW 2,000 or 5,000 Da) coating were labeled with both cyclic RGD peptide (for targeting integrin  $\alpha\beta_3$ ) and DOTA (for PET imaging after <sup>64</sup>Cu complexation). The number of DOTA chelators and RGD peptides per SWNT was measured by isotope dilution method. Biodistribution studies and ex vivo Raman spectroscopic measurements was carried out to confirm the PET results.

**Results:** The SWNTs were quite stable in vivo and well PEGylated SWNTs exhibited relatively long blood circulation and low uptake by the reticuloendothelial system. Efficient targeting of integrin  $\alpha\beta_3$ -positive U87MG human glioblastoma tumor was achieved with SWNTs functionalized by RGD peptides. A high tumor accumulation of up to 15%ID/g is attributed to the multivalent effect of SWNTs. Integrin



Single-walled carbon nanotube (SWNT) as a nanoplatfrom for in vivo tumor targeting and imaging

$\alpha\beta_3$ -negative tumor and SWNTs labeled with DOTA only were used as controls and both showed very low level tumor uptake (< 5%ID/g) due to passive targeting, confirming the integrin  $\alpha\beta_3$  specificity of RGD peptide labeled SWNTs. The Raman signatures of SWNTs provided direct evidence of the presence of SWNT in the targeted tumor tissue, confirming the PET imaging results.

**Conclusions:** For the first time, we demonstrated in vivo targeted tumor imaging using radio-labeled SWNTs. These and the lack of toxic effects warrant SWNTs for future in vivo applications which may open up exciting new venues for nanoparticle-based targeted drug delivery and cancer therapy.

## FUNDING SOURCE:

National Cancer Institute (NCI) (R21 CA102123, P50 CA114747, U54 CA119367, and R24 CA93862), Department of Defense (DOD) (W81XWH-04-1-0697, W81XWH-06-1-0665, W81XWH-06-1-0042, and DAMD17-03-1-0143), and a Benedict Cassen Postdoctoral Fellowship from the Education and Research Foundation of the Society of Nuclear Medicine (to W. Cai).

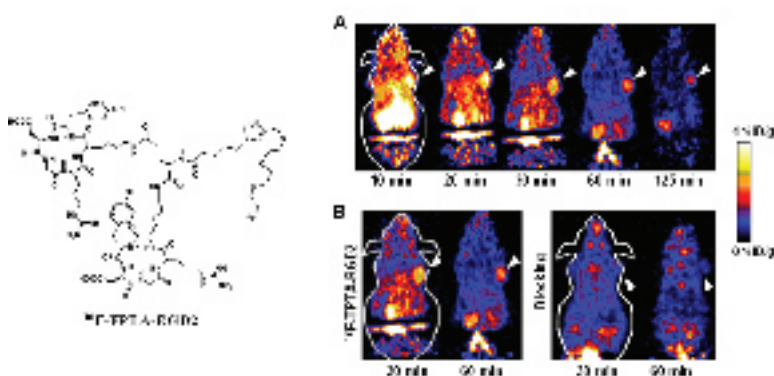
# Click Chemistry for $^{18}\text{F}$ -Labeling of RGD Peptides and microPET Imaging of Tumor $\alpha\text{v}\beta 3$ Integrin Expression

ZI-BO LI, ZHANHONG WU, KAI CHEN, FREDERICK T. CHIN AND XIAOYUAN CHEN  
DEPARTMENT OF RADIOLOGY (MIPS AND BIO-X PROGRAMS)

The cell adhesion molecule integrin  $\alpha\text{v}\beta 3$  plays a key role in tumor angiogenesis and metastasis. A series of  $^{18}\text{F}$ -labeled RGD peptides have been developed for PET of integrin expression based on primary amine-reactive prosthetic groups. In this study we report the use of the Cu(I)-catalyzed Huisgen cycloaddition, also known as ‘click reaction’, to label RGD peptides with  $^{18}\text{F}$  by forming 1,2,3-triazoles.

**Methods:** Nucleophilic fluorination of a toluenesulfonic alkyne provided  $^{18}\text{F}$ -alkyne in high yield, which was then reacted with an RGD azide. The  $^{18}\text{F}$ -labeled peptide was subjected to microPET studies in murine xenograft models. Metabolic stability of the newly synthesized tracer was also analyzed.

**Results:** The  $^{18}\text{F}$ -alkyne was purified by HPLC and prepared in 30 min (non-decay-corrected yield:  $65.0 \pm 1.9\%$ ) starting from the azeotropically-dried  $^{18}\text{F}$ -fluoride. Dimeric RGD azide was coupled with the  $^{18}\text{F}$ -alkyne to afford the coupled product in high yield (non-decay-corrected yield:  $52.0 \pm 8.3\%$ ) within 45 min including HPLC-purification. The overall synthesis was completed in 110 min and resulted in a 26.9 % radiochemical yield (non-decay-corrected) with an estimated spe-



Structure of  $^{18}\text{F}$ -fluoro-PEG-triazole-E(RGDyK) $_2$  ( $^{18}\text{F}$ -FPTA-RGD2) and coronal microPET images of U87MG tumor-bearing mice.

cific activity of 100-150 TBq/mmol. Murine microPET experiments showed good tumor uptake ( $2.1 \pm 0.4\%$  ID/g at 1 h postinjection (p.i.)) with rapid renal and hepatic clearance of  $^{18}\text{F}$ -fluoro-PEG-triazoles-RGD2 ( $^{18}\text{F}$ -FPTA-RGD2) in a subcutaneous U87MG glioblastoma xenograft model (kidney:  $2.7 \pm 0.8\%$  ID/g, liver:  $1.9 \pm 0.4\%$  ID/g).

**Conclusion:** The new tracer  $^{18}\text{F}$ -FPTA-RGD2 was synthesized with high radiochemical yield and high specific activity. This

tracer exhibited good tumor-targeting efficacy, relatively good metabolic stability, and favorable in vivo pharmacokinetics. This new  $^{18}\text{F}$  labeling method based on ‘click reaction’ will also be useful for radio-labeling of other biomolecules with azide group in high yield.

## REFERENCES/FUNDING SOURCE

NCI (R21 CA102123, ICMIC P50 CA114747, CCNE U54 CA119367, and SARIP R24 CA93862), Department of Defense (DOD) (W81XWH-04-1-0697, W81XWH-06-1-0665, W81XWH-06-1-0042, DAMD17-03-1-0143, and BC061781), and a Dean’s Fellowship (to ZL) from the Stanford University.

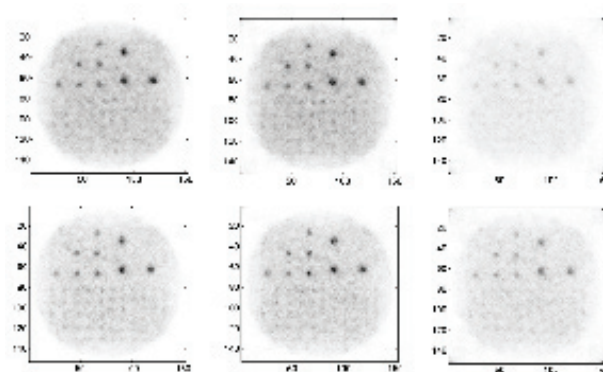


## Bayesian Estimator for Angle Recovery: Event Classification and Reconstruction in Positron Emission Tomography

ANGELA M K FOUDRAY, CRAIG S LEVIN

DEPARTMENT OF RADIOLOGY AND MOLECULAR IMAGING PROGRAM AT STANFORD

PET at the highest level is an inverse problem: reconstruct the location of the emission (biological function) from detected photons. Ideally, we would like to directly measure an annihilation photon's incident direction on the detector. In the developed algorithm, Bayesian Estimation for Angle Recovery (BEAR), we utilized the increased information gathered from localizing interactions in the detector from single photons and developed a Bayesian estimator for a photon's incident direction. Probability distribution functions (PDFs) were filled using a center of mass (COM) reference space, which had the following computational advantages: (1) a significant reduction in the size of the data in measurement space, making further manipulation and searches faster (2) the construction of COM space does not depend on measurement location, it takes advantage of measurement symmetries, and data can be added to the training set without knowledge and recalculation of prior training data, (3) calculation of posterior probability map is fully parallelizable, it can scale to any number of processors. These PDFs were used to estimate the point spread function (PSF) in incident angle space for (i) algorithm assessment and (ii) to provide probability selection criteria for classification. The algorithm calculates both the incident theta and phi angle, with ~16 degrees RMS in both orthogonal angle spaces, limiting the incoming direc-



*This image shows contrast improvement in the BEAR filtered images (bottom) versus the unfiltered images (top), for 0.1, 1 and 5 mCi acquisitions.*

tion to the interior of a narrow cone.

Having information about the characteristics of an incoming photon could allow a higher degree of certainty about how that detected photon (and ultimately event) should be used, if at all. Benefits of having direction and energy information about a photon incident on the detectors include: more precise event typing (Singles, Randoms, Scatters, Multiples, Trues) for 1) filters, 2) reclamation of previously unusable events and 3) for LOR assignment (event positioning).

Feature size did not improve using the BEAR algorithm as an angle filter, but the contrast ratio improved 40% on average for the three noise cases analyzed (0.1, 1, 5 mCi total activity which produced unfiltered images with a Random percentage of total events acquired of 1%, 18% and 50%, respectively).

### REFERENCES/FUNDING SOURCE

This work was partially funded by the PEO International for the Scholar Award received by AMKFoudray. The MaxEnt organization for full sponsorship to attend and present this work at the 27th International MaxEnt Workshop. This work was also supported in part by the following grants: NIH-National Cancer Institute R21 CA098691, NIH-NIBIB R21/R33 EB003283, and NIH-NCI CA119056.

## Noise Performance of PSAPD PET Detector Multiplexing Circuits

FRANCES W.Y. LAU<sup>1</sup>, PETER D. OLCOTT<sup>2</sup>, MARK A. HOROWITZ<sup>1</sup>, CRAIG S. LEVIN<sup>3</sup>  
DEPARTMENTS OF <sup>1</sup>ELECTRICAL ENGINEERING, <sup>2</sup>BIOENGINEERING, AND <sup>3</sup>RADIOLOGY (MIPS)

We are designing a position sensitive avalanche photodiode (PSAPD)-based 1mm3 resolution PET (Positron Emission Tomography) system with thousands of readout channels. Multiplexing of the PSAPDs reduces the density of the readout circuit board, thus simplifying the system design. However, due to the leakage current of the PSAPDs, multiplexing may significantly degrade the signal-to-noise ratio (SNR), reducing spatial, temporal, and energy resolution. We used SPICE simulations to study the noise performance of two front-end multiplexing circuit configurations, shown in Fig 1: a) multiplexing with differential preamplifiers and b) multiplexing with single-ended preamplifiers, and compared their performance to the case without multiplexing.

With the novel differential multiplexing technique, four PSAPDs can be multiplexed with less than a 0.2dB decrease in the SNR for energy measurements. When multiplexing with single-ended preamplifiers, two PSAPDs can be multiplexed with only a 0.1dB decrease in the SNR for energy measurements if energy is measured from the common termi-

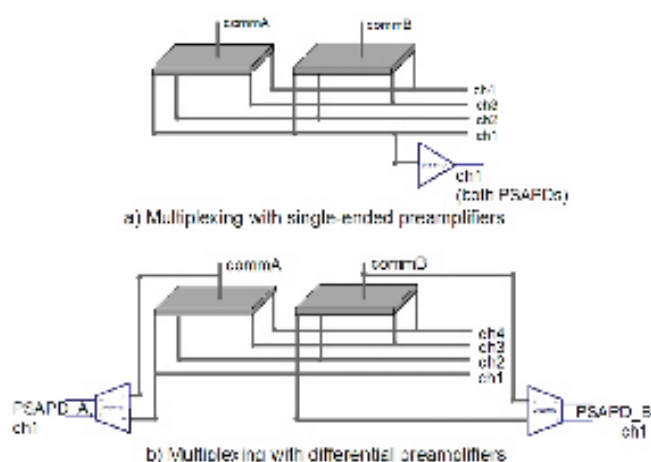


Fig 1. Multiplexing architectures. Note: Only the preamplifiers for channel 1 are shown for clarity. Spatial channels (ch 1-4) are used to calculate position of interaction

nal of the PSAPD. For both cases, if time is measured from the same terminal as the terminal used for energy measurements, then we also expect little degradation in time resolution.

We are currently studying spatial resolution by analyzing interactions that are not at the center, but preliminary analyses indicate that the differential architecture is beneficial. We are also verifying our simulation results experimentally and investigating the limit to the multiplexing.

In conclusion, the differential multiplexing scheme is superior to the single-ended approach because four PSAPDs can be multiplexed without significantly degrading the energy and time resolution. The size and complexity of our system will be

constrained by the number of channels on the board, not chip size, so the dramatic reduction in the number of channels facilitated by this novel differential multiplexing approach will be a significant advantage.

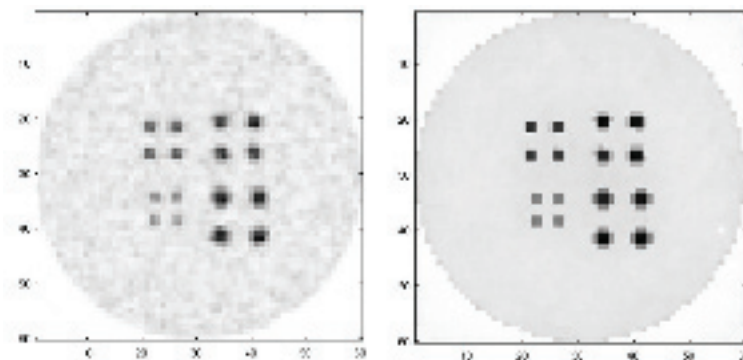
REFERENCES/FUNDING SOURCE  
NIH grants R01CA119056 and NIH-EB003283

# PET Image Reconstruction with a Bayesian Projector for Multi-Electronic Collimation Schemes

GARRY CHINN AND CRAIG S. LEVIN

DEPARTMENT OF RADIOLOGY AND MOLECULAR IMAGING PROGRAM AT STANFORD

We evaluated a new image reconstruction algorithm using a Bayesian projector for multi-collimation PET systems. We are developing a PET system using high spatial and energy resolution 3-D detectors made from cadmium zinc telluride with cross-strip anodes and cathodes. This PET system can collimate photon pairs by coincidence timing and can collimate single photons by the kinematics of Compton scatter within the detector (Compton collimation). Compton collimation of single photons can dramatically increase overall photon sensitivity by making use of events that are discarded by conventional PET systems. However, single photon events offer lower spatial resolution than coincidence measurements. Previously, we showed that conventional maximum likelihood reconstruction by the list-mode ordered subset expectation-maximization (OS-EM) algorithm for these “multi-collimation” data sets yields no measurable improvement over images reconstructed using high-resolution collimation alone. We also studied a Bayesian projector function with non-uniform emission probability along the line of



*Images of a cylindrical phantom with 1, 1.25, 1.5 and 1.75 mm spheres spaced by twice the diameter are shown for reconstruction using (left) only coincidence photons and (right) coincidence and Compton collimation photons. The cylinder is 7.5 cm high and 3 cm in diameter. A total of 500  $\mu$ Ci of activity was placed in the phantom with a total simulated scan time of 2.5 min. A total of 10 million coincidence events and 11 million Compton collimation events were recorded. Adding Compton collimation photons improved the signal-to-noise ratio of coincidence photons by 20-600% in the spheres and by 1000% in the background cylinder*

response weighted by an image prior generated from the low-resolution (Compton collimation) channel, to reconstruct the high-resolution (coincidence) channel. In this work, we investigated a novel approach using priors generated by reconstructing images from the high-spatial resolution coincidence data followed by post-reconstruction smoothing with a new spatially varying 3-D filter function. The 3D OS-EM algorithm was used with the prior-weighted Compton collimated single photon data and the conventional (unweighted) projector to reconstruct the coincidence photon data. For 1 to 1.75 mm

diameter spheres placed in a warm cylinder with a 10:1 concentration ratio, we showed that this approach could improve the signal-to-noise in the background ten-fold and 20% or better in the spheres with equal or better sphere-to-cylinder contrast and no loss in spatial resolution.

## REFERENCES/FUNDING SOURCE

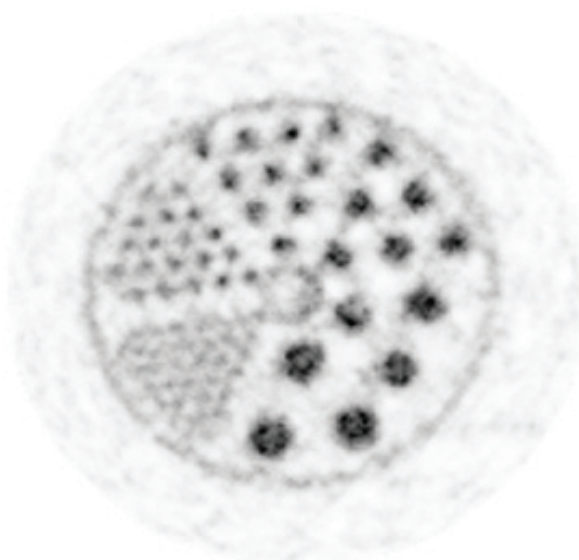
This work was partially funded by NIH R01CA120474 and California Breast Cancer Research Program 12IB-0092.



## Fully 3D List-Mode OSEM for High-Resolution PET with Graphics Processing Units

GUILLEM PRATX<sup>1,2</sup>, GARRY CHINN<sup>2</sup>, P OLCOTT<sup>2</sup>, CRAIG LEVIN<sup>2</sup>  
 DEPARTMENTS OF <sup>1</sup>ELECTRICAL ENGINEERING, AND <sup>2</sup>RADIOLOGY (MIPS)

The amount of information generated by PET is increasing rapidly, driven by (1) the finer sampling by smaller detector elements and (2) the increased number of physical quantities measured and recorded with the new generation of PET detector technology (arrival time, time-of-flight, energy, depth-of-interaction, incident photon angle, etc.). In this context, reconstructing directly from the raw list-mode data has proved to be particularly appealing and useful to deal with the parameter complexity as well as sparseness of the data. This reconstruction problem lends itself naturally to a maximum-likelihood formulation. List-mode approaches have been successfully used in several applications in which the sparseness of the data is important. An issue often reported with list-mode algorithms is the tremendous amount of computation required since each recorded event requires multiple individual back-and-forward line projections. We therefore investigated the use of the new generation of graphics processing units (GPUs) to drastically accelerate the line projection operations and im-



*Hot rod phantom (110  $\mu$ Ci – 20 min scan) reconstructed with list-mode 3D OSEM (96 updates) using a GeForce 7900 GTX GPU.*

plement a fully-3D list-mode ordered-subsets expectation-maximization (OSEM). A desirable characteristic of our approach is that it facilitates a straightforward implementation of resolution-blurring kernels that represent an accurate detector tube-of-response. We showed that the GPU implementation is 50 times faster but as accurate as its CPU counterpart, and that the incorporation of a shift-invariant resolution-blurring model lead to a reduction in the noise without loss of resolution. Ultra-high resolution PET systems for pre-clinical imaging is the current focus of our efforts. Image reconstruction for PET systems that measure the time-of-flight is going to be the next application for our technique.

## REFERENCES/FUNDING SOURCE

NIH R01CA119056, NIH R33 EB00328, NIH R01CA120474, CBCRP 12IB-0092, Stanford Bio-X, NVIDIA.

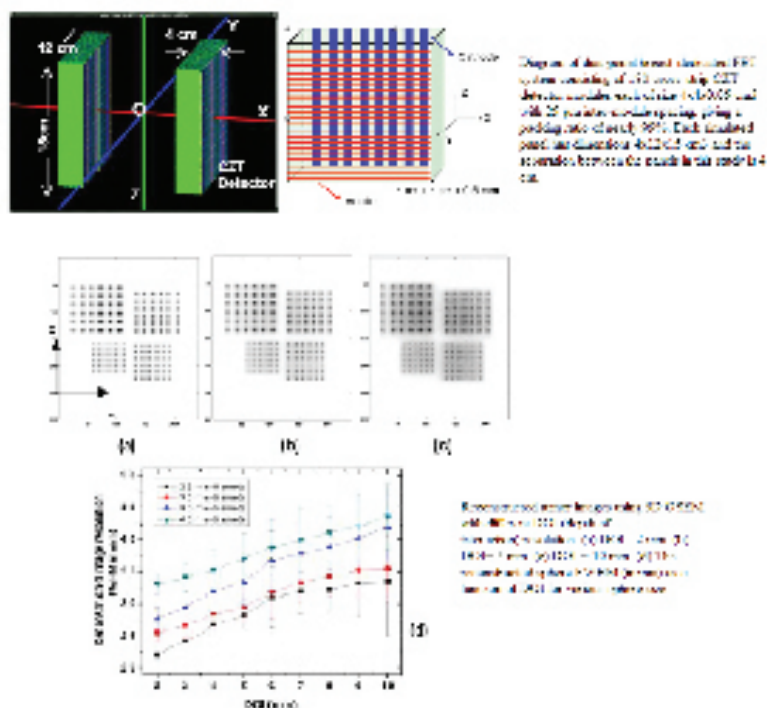
# Performance Study of a High Resolution CZT-based PET Camera for Breast Imaging

HAO PENG, PETER D OLCOTT, GUILLEM PRATX, ANGELA M K FOUDRAY, GARRY CHINN, CRAIG S LEVIN  
DEPARTMENT OF RADIOLOGY AND MOLECULAR IMAGING PROGRAM AT STANFORD

We are developing a dual-panel cadmium zinc telluride (CZT) detector PET system dedicated to breast imaging, which consists of two 4 cm thick 12x15 cm<sup>2</sup> area CZT panels with adjustable separation. The performance of the proposed CZT dual panel PET system was investigated using Monte-Carlo simulation. This project focuses on the predicated system performance that exploits CZT's superior energy resolution ( $<2\%$  at 511 keV), high photon sensitivity, and uniform 1 mm spatial resolution throughout field-of-view (FOV). The design uses 4-cm thick edge-on 3D positioning CZT detectors with a cross-strip electrode readout scheme. We expect that the system can achieve  $\sim 32\%$  coincidence photon sensitivity for a point source at the center and 4 cm panel separation, and for a simplified breast phantom surrounded by heart and torso compartments, the noise-equivalent-count (NEC) of system is expected to be  $\sim 42,000$  cts/sec under the optimum configuration ( $\sim 5\%$  energy window and  $\sim 8$  ns time window) for 200  $\mu$ Ci activity in the breast phantom. Images of spherical sources of various diameters are going to be reconstructed using a list mode 3D OSEM algorithm. The depth of interaction (DOI), spatial resolution, and image quality are being investigated before we build the real system.

## REFERENCES/FUNDING SOURCE

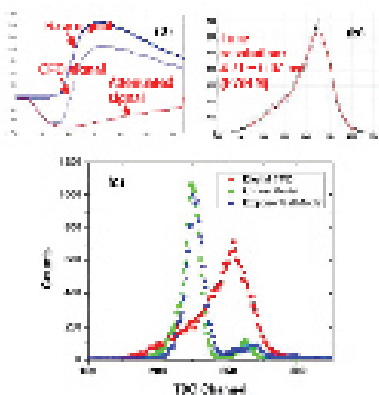
This work was supported in part by grants R01CA120474 from NIH and 12IB-0092 from California Breast Cancer Research Program.



## Evaluation of a Fully Digital Data Acquisition for PET Systems

HAO PENG, PETER D OLCOTT, ANGELA M K FOUDRAY, CRAIG S LEVIN.  
DEPARTMENT OF RADIOLOGY AND MOLECULAR IMAGING PROGRAM AT STANFORD

Most existing PET/SPECT scanner data acquisition systems are implemented based on analog subsystems with discrete circuits or application specific integrated circuits (ASIC). This solution yields cost effective results in dedicated systems but offers little flexibility and upgradeability. Currently, advances in field-programmable gate arrays (FPGA) allow a larger part of analog circuits to be replaced by digital logic. We are prototyping a high-resolution position-sensitive APD (PSAPD) based PET system, using a fully digital data acquisition system with free-running analog-to-digital converters (ADC) and FPGA logic. Numerical algorithms for digital shaping and digital timing pickup were tested and the results were compared to those obtained by using analog NIM modules for a LSO/PSAPD detector module with 1 mm LSO crystals. Compared to analog processing circuits,



the digital system exhibits comparable energy resolution and crystal peak-to-valley ratio in the flood source position map. A significant improvement in the coincidence time resolution was found using a digital CFD (4.71 $\pm$ 0.07 ns FWHM) over the analog counterpart (8.67 $\pm$ 0.10 ns). These improvements may be attributed to the better noise and linearity performance

Timing performance of digital and analog systems for PET.

	FWHM (ns)	FWHM (ns)
Timing resolution	4.71 $\pm$ 0.07	8.67 $\pm$ 0.10
Energy resolution	1.12 $\pm$ 0.07	1.12 $\pm$ 0.07
Coincidence resolution	4.71 $\pm$ 0.07	8.67 $\pm$ 0.10
Timing resolution	4.71 $\pm$ 0.07	8.67 $\pm$ 0.10

of the digital system. A linear time interpolation model provides the best time resolution (1.72 $\pm$ 0.07 ns). This will help us implement the data acquisition system for our dedicated breast PET system.

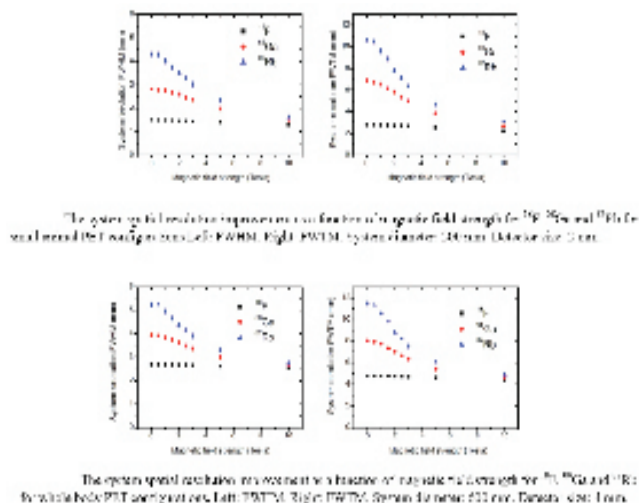
### REFERENCES/FUNDING SOURCE

This work was supported in part by grants R01CA120474 from NIH and 12IB-0092 from California Breast Cancer Research Program

## Study of Potential PET Spatial Resolution Improvement in PET/MRI Dual Modality Systems

HAO PENG AND CRAIG S LEVIN.  
DEPARTMENT OF RADIOLOGY AND MOLECULAR IMAGING PROGRAM AT STANFORD

This paper reports the effects of a static magnetic field on the PET spatial resolution in a combined PET/MRI system. Combining PET and MRI enables spatio-temporal correlation of anatomical/functional information. If successful, this combined information may facilitate the study of molecular-based disease and provide more effective patient management. PET spatial resolution is mainly determined by three factors: positron diffusion range, system diameter and photon detector size. MRI can improve the PET resolution by reducing the positron diffusion range in the lateral direction (orthogonal to the static magnetic field), which is most significant for high-energy positron isotopes such as  $^{64}\text{Cu}$ ,  $^{124}\text{I}$ ,  $^{68}\text{Ga}$  and  $^{82}\text{Rb}$ . This study investigated the PET resolution improvement for both whole-body PET and small animal PET systems using Monte-Carlo simulation for three isotopes ( $^{18}\text{F}$ ,  $^{68}\text{Ga}$  and  $^{82}\text{Rb}$ ). The resolution was studied as a function of magnetic field strength from 0 up to 10 T. For both systems, the resolution improvement is insignificant for  $^{18}\text{F}$  but very significant for  $^{68}\text{Ga}$  (47.2%) and  $^{82}\text{Rb}$  (61.7%) at 10 T. The results show that PET/MRI may facilitate the evaluation of new highenergy positron-based pharmaceuticals due to the PET lateral resolution improvement.





## GRAY: Photon Ray Tracer for PET Applications

PETER D. OLCOTT<sup>1,2</sup>, SAMUEL R. BUSS<sup>2</sup>, GUILLEM PRATX<sup>1,3</sup>, FREZGHIE HABTE<sup>1</sup>, CHRIS K. SRAMEK<sup>4</sup>, CRAIG S. LEVIN<sup>1</sup>

<sup>1</sup>RADIOLOGY (MIPS), <sup>2</sup>BIO-ENGINEERING, <sup>3</sup>ELECTRICAL ENGINEERING, <sup>4</sup>APPLIED PHYSICS

GRAY (High Energy Photon Ray Tracer) is a Monte-Carlo ray-driven high energy photon transport engine for mainly PET and SPECT applications that supports complex mesh based primitives for source distributions, phantom shapes, and detector geometries. Monte-Carlo modeling is critical for system design evaluation and image reconstruction development. Ray tracing is a technique used in computer graphics to render scenes with realistic light properties. We adapted an open source ray tracing engine to support the physical properties of high energy photon transport. The main project goal of GRAY is to provide a means to import advanced geometrical mesh primitives from graphical CAD programs to create animated vectorial based phantoms and complex detector geometries while preserving physical accuracy and efficient runtime. These phantoms will be able to model complex moving objects targeted towards developing novel image reconstruction algorithms for cardiac, respiratory, and tracer kinetic modeling. Traditionally, complex geometrical



Complete path from source geometry through image reconstruction: Detailed 3-D CAD modeling of a rat phantom (LEFT), import of the vector geometry into GRAY to generate a simulated scan in a small animal box PET scanner (MIDDLE), a volumetric visualization of a reconstruction of the rat using a fully 3-D OSEM image reconstruction (RIGHT). The rat phantom has two cold spheres added to the eyes to create a hole in the phantom.

phantoms were simulated using a series of discrete voxelized sources that represent the activity source distributions and attenuation media. By using rejection testing, constructive solid geometry can create primitives that are combined using Boolean operations to create complex phantoms. The high energy photon physics modeling of GRAY has been validated against GATE for both runtime performance and accuracy.

GRAY runs an order of magnitude faster than GATE with improved geometric modeling capabilities for detectors and sources. To highlight the capabilities of GRAY, a complex mesh phantom of a rat was filled with uniform activity, placed in a high resolution 1mm<sup>3</sup> small animal box PET scanner, simulated with GRAY, and reconstructed using list-mode 3-D OSEM reconstruction.

### REFERENCES/FUNDING SOURCE

This work was supported in part by grants R01CA120474 from NIH and 12IB-0092 from California Breast Cancer Research Program.

## Evaluation of a New Readout ASIC for a 1 mm Resolution PET System Based Upon Position Sensitive Avalanche Photodiodes

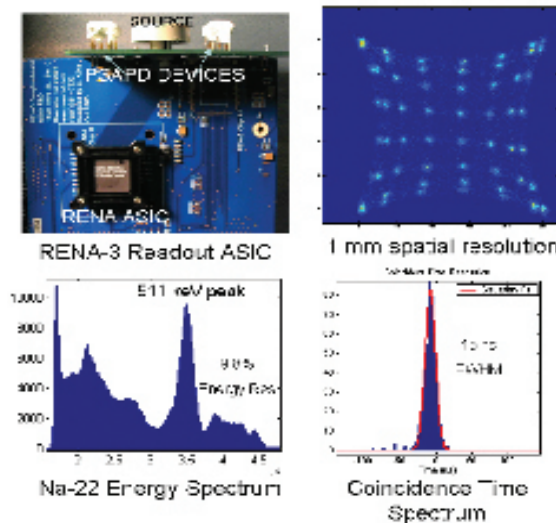
P. D. OLCOTT<sup>1,2</sup>, C. S. LEVIN<sup>1</sup>, V. B. CAJIBE<sup>2</sup>, M. CLAJUS, T. O. TUMER<sup>3</sup> AND A. VOLKOVSKI<sup>4</sup>

DEPARTMENTS: <sup>1</sup>RADIOLOGY (MIPS) <sup>2</sup>BIOENGINEERING, <sup>3</sup>ELECTRICAL ENGINEERING, <sup>4</sup>APPLIED PHYSICS

**Objectives :** Position sensitive avalanche photodiodes (PSAPD) [1] are becoming increasingly a practical replacement for photomultiplier tubes and facilitate the development of 1 mm resolution PET systems that are capable of recording the 3D photon interaction coordinates [2]. A key bottleneck in the development of 1 mm resolution positioning detectors are the development of ASICs that can readout hundreds to thousands of detector channels [3].

**Methods :** NOVA R&D, Inc has developed a 36-channel fully asynchronous charge sensitive readout ASIC known as RENA-3 [4], for high sensitivity, low noise readout of semiconductor detectors. We coupled two 8x8 mm PSAPD devices with 1mm thick LSO sheet crystals and 1 mm<sup>3</sup> pixellated LSO arrays to a RENA-3 chip. Using a 10 uCi Na-22 point source, we analyzed coincident 511 keV photon data acquired with the RENA-3 acquisition system.

**Results :** Initial experiments show that the RENA-3 ASIC can resolve a 7x7 array of 1 mm<sup>3</sup> LSO scintillation crystals coupled to



Two PSAPD Devices are setup for a Na-22 coincidence experiment and readout using a RENA-3 data acquisition system. A 7x7 array of 1x1x1 mm<sup>3</sup> crystals are resolved, with excellent energy spectra and adequate time resolution.

PSAPD detectors operated in coincidence with <13% FWHM energy resolution and ≤12 ns (17 ns paired) FWHM time resolution. Readout board optimizations will likely produce significant time resolution improvements.

**Conclusions :** First results indicate that a highly integrated readout ASIC for a compact 3D positioning PET detector based upon 1 mm LSO crystals coupled to avalanche photodiodes can realize 1 mm spatial resolution with <13% FWHM energy resolution and ≤12 ns FWHM time resolution. Further optimizations are underway to improve the time resolution.

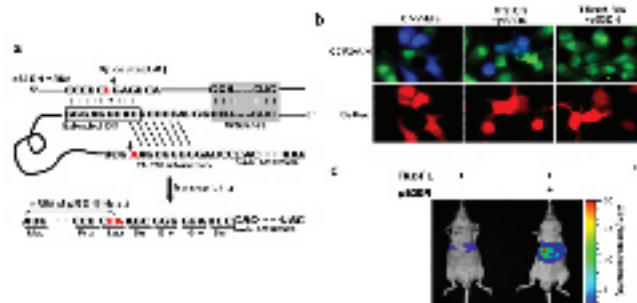
### REFERENCES/FUNDING SOURCE

NIH NIBIB R33 EB003283, NCI R21 CA098691, NCI R01 CA119056, OTTCCAT GT60615 (NOVA R&D, Inc). Olcott, Peter D; Levin, Craig S; Cajibe, Victoria B; Clajus, Martin; Tumer, Tumay O; Volkovskii, Alexander, "Evaluation of a new readout ASIC for a 1 mm resolution PET system based upon position sensitive avalanche photodiodes", SNM 2007, Washington DC.

## Ribozyme-Mediated Imaging of mRNA in Living Animals

MIN-KYUNG SO, GAYATRI GOWRISHANKAR, SUMITAKA HASEGAWA, JIANGHONG RAO  
DEPARTMENT OF RADIOLOGY AND MOLECULAR IMAGING PROGRAM AT STANFORD

In vivo imaging of a specific mRNA target has remained a challenge due to the small copy number of mRNA targets per cell. We present here a new approach to image mRNA in vivo based on group I introns Tetrahymena thermophila ribozyme. Tetrahymena ribozymes constitute a class of catalytic RNA molecules, capable of catalyzing cis- and trans-splicing reactions. We designed plasmid constructs containing the trans-splicing ribozyme, an engineered reporter mRNA, and an antisense sequence against an mRNA target. These constructs were able to bind the mRNA target and produce a fusion mRNA that could be translated into functional reporter enzymes. Two different reporters have been exploited to image the mRNA of a dominantly negative p53 (p53DN) gene: beta-lactamase for single living cell imaging and firefly luciferase for whole living mice. Analyses of the splicing reaction products confirmed that these constructs were able to target and image mRNA targets in vivo. For a transiently transfected construct, spliced products could be seen from the RT-PCR as early as 24 hrs after transfection, and splicing-dependant luciferase activity began to increase at 48 hrs and maximized around 72 hrs. A  $9.5 \pm 1.9$  fold difference was observed between tumors with and without the p53DN mRNA 24hrs following the tumor implant (72 hrs after transfection). In summary, we have shown here the first example of imaging ribozyme-mediated trans-splicing activity in living animals. This splicing-dependant reporter assay may be applied to directly image endogenous mRNAs, especially over-expressed tumor-specific mRNAs in living subjects.



*Ribozyme-mediated imaging of the p53DN mRNA with the ribozyme reporters. (a) Schematic diagram of the ribozyme reporter (TRz-Bla) targeting the p53DN mRNA. Arrows indicate the 5' splice site (U41) on the p53DN mRNA and the 3' splice site on the ribozyme reporter. Shaded area downstream of the 5' splice site marks the 200 nt antisense. Boxed 9 nucleotides are extended IGS. The G-U wobble base-pair at the 5' splice site is indicated by a black dot (\*). Oblique lines indicate the 7 bp P1-P10 interaction. (b) Fluorescence microscopy images of COS7 cells transfected with indicated constructs and stained with CCF2/AM at 72 h post-transfection. Upper panel shows an overlay of frames captured at 530 nm (green emission) and 460 nm (blue emission), and lower panel shows the DsRed positive cells (emission at 605 nm). (c) Systemic delivery of the ribozyme-firefly luciferase reporter (TRz-FL) into living mice. Bioluminescent signal in mice 24hrs after they had been injected intravenously with the TRz-FL and the p53DN target mRNA (p53DN) or an empty vector, using the hydrodynamic method of delivery.*

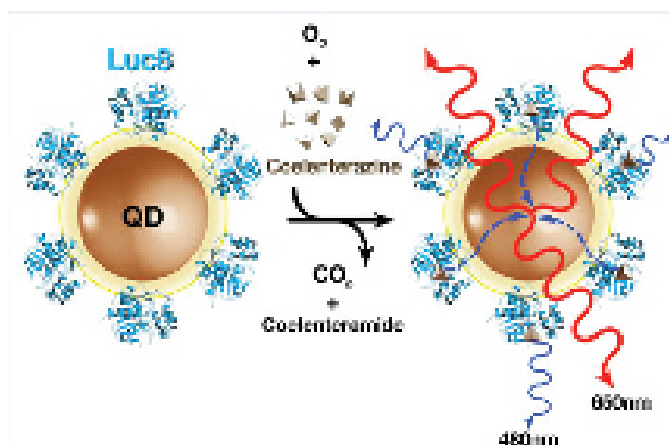
### REFERENCES/FUNDING SOURCE

Burroughs Wellcome Fund, ICMIC@Stanford, and BRCP Idea Award.

## Bioluminescent Quantum Dot Conjugates as Nanosensors and Imaging Probes

JIANGHONG RAO, MIN-KYUNG SO, CHENJIE XU, ANDREAS LOENING, YAN ZHANG, SANJIV S. GAMBHIR  
DEPARTMENT OF RADIOLOGY AND MOLECULAR IMAGING PROGRAM AT STANFORD

Semiconductor quantum dots (QDs) offers attractive optical properties as fluorescence probes for biological imaging and detection. QDs can luminesce fluoresce also transfer fluorescence resonance energy (FRET) to organic fluorophores, and have been applied to design FRET-based nanosensors for small molecule analytes and for enzyme activity. Here we will present a different type of QD conjugate that can fluoresce via bioluminescence resonance energy transfer (BRET). We have developed several methods to conjugate QDs to a mutant of the bioluminescent protein Renilla luciferase (Rluc8) covalently and non-covalently. The formation of the conjugate results in an energy transfer phenomenon between Rluc8 (as the donor) and QDs (as the acceptor) — bioluminescence resonance energy transfer (BRET). We have characterized the QD-BRET conjugates in vitro and in vivo; the BRET ratio varied with the conjugation methods and conditions, and can be as high as 2.30. We have applied to this QD-BRET system to design QD nanosensors for the detection of small ions like  $Mg^{2+}$  and for enzyme function like pro-



*Design of the BRET-QD conjugate and the BRET-QD catalytic reaction. Each quantum dot (QD) may have several copies of the enzyme (Luc8) covalently linked to the surface, as shown above. Exposure to the luciferase substrate, coelenterazine, causes the emission of light of peak wavelength 480 nm from the luciferase molecule. Because the quantum dot is closely linked to the luciferase molecule, the energy from this reaction couples non-radiatively to the quantum dot acceptor (shown by the arrows with dotted lines). In this example, the quantum dot emits light in the red to near-infrared regions (655 nm).*

for imaging biological events at deep tissues in small living animals.

REFERENCES/FUNDING SOURCE  
Burroughs Wellcome Fund, and CCNE.

tease. The QD conjugates were injected into a nude mouse and gave strong BRET emissions. The long wavelength BRET emissions were more easily detected, especially in deep tissues. Cells labeled with bioluminescent QDs were readily imaged in the lungs after i.v. injection, but were not detectable with fluorescence imaging. We also examined the possibility of multiplexed bioluminescence imaging in vitro and in the living mouse with QDs. Since these QD conjugates can emit light without external illumination, thus the issue of high fluorescent background strong autofluorescence background with fluorescence imaging is avoided. These unique features of BRET-based QDs should open many new avenues for QD-based nanosensor design and imaging in living subjects, especially





# PUBLICATIONS AND PRESENTATIONS

YEARS ON THE CUTTING EDGE



## PEER-REVIEWED PRESENTATIONS AT SCIENTIFIC MEETINGS

**ISMRM 2007**  
**15<sup>th</sup> Scientific Meeting**  
**Berlin, Germany, May 2007**

Aksoy M, Liu C, Moseley M, Bammer R. The effect of navigator resolution on registration accuracy in rigid head motion correction.

Aksoy M, Liu C, Bammer R. Rigid head motion correction for DTI using non-linear conjugate gradient.

Aksoy M, Liu C, Bammer R. Tensor estimation for DTI using non-linear conjugate gradient.

Balchandani P, Spielman D. Fat suppression for 1H MRSI at 7T using a spectrally selective adiabatic inversion pulse.

Balchandani P, Spielman D, Pauly JM. Interleaved narrow-band adiabatic spatial-spectral pulse sequence for 1H MRSI at 7T.

Barral JK, Lustig M, Tikov N, Nishimura DG. RF pulse design for FLASE.

Barral JK, Wu HH, Gold GE, Pelc NJ, Pauly JM, Nishimura DJ. Accurate reconstruction in PR-MRI despite truncated data.

Chen J, Bouley D, van den Bosch M, Sommer G, Butts Pauly K. Evaluation of chronic cryo prostate lesions by diffusion-weighted MRI.

Faranesh AZ, Yankeelov TE. Incorporation of a vascular term into a reference region model for the analysis of DCE-MRI data.

Gilson WD, Hofmann LV, Kedziorek, S Shah, Korosoglou JW, Bulte M, Stuber, Kraitchman DL. Positive contrast MRI demonstrates retention of mesenchymal stem cell therapy administered intramuscularly in ischemic skeletal muscle.

Gold G, Bangerter N, Saroswiecki E, Han E, Gurney P, Wright G, Hargreaves BA. In vivo T2, T1 $\rho$ , and sodium imaging of articular cartilage at 3.0T: initial experience.

Gold G, Busse R, Stevens K, Han E, Brau A, Beatty P, Chen C, Joshi S, Chang S, Beaulieu C. Isotropic MRI of the knee at 1.5T with 3D-FSE-XETA (extended echo train acquisition).

Granlund KL, Hargreaves BA. Linear off-resonance correction for partial-k-space 3D spiral imaging.

Gu M, Spielman DM. Robust water and lipid suppression using multiple dualband frequency-selective RF pulses for 1H spectroscopic imaging at 3T.

Han M, Daniel BL, Hargreaves BA. Accelerated bilateral DCE 3D spiral breast imaging using TSENSE and partial fourier methods.

Han M, Daniel BL, Hargreaves BA. Rapid DCE breast MRI using TSENSE accelerated 3D spiral imaging.

Hargreaves BA, Bangerter NK, Staroswiecki E, Daniel BL. Sodium and proton breast MRI.

Hargreaves BA, Han M, Alley MT, Beatty PJ, Brau AS, Daniel BL. Clinical bilateral breast MRI at Stanford.

Holdsworth SJ, Bammer R, Newbould RD, Skare S. Benchmarking SAP-EPI and PROPELLER for diffusion imaging.

Holdsworth SJ, Bammer R, Newbould RD, Skare S. In vivo assessment of canine prostate thermal ablations with magnetization transfer imaging.

Hope TA, Alley MT, Miller DC, Herfkens RJ. Cardiovascular flow quantification.

Hu Y, Glover GH. 3D spiral technique for high resolution fMRI.

Jong KL, Horst KC, Ikeda DM, van den Bosch M, Pal S, Herfkens RJ, Daniel BL, Dirbas FM. Characteristic breast MRI findings after accelerated partial breast irradiation.

Josan S, Pauly J, Butts Pauly K, Bruce Daniel BL. Inverted double half RF for ultrashort T2 imaging.

Kwong A, Klifa C, Lo G, van den Bosch M, Daniel BL, Nola Hylton N, Ikeda DM. MRI of the breast: quantification of breast density and background enhancement in healthy volunteers.

Les AS, Draney MT, Tedesco MM, Park J, Herfkens RJ, Dalman RL, Taylor CA. Hemodynamics in abdominal aortic aneurysms during rest and simulated exercise.

Lew C, Alley M, Spielman D, Bammer R, Chan F. Autocalibrated phase-contrast imaging.

Liu C, Bammer R, Moseley ME. Parallel imaging reconstruction for arbitrary trajectories using k-space sparse matrices (kSPA).

Liu C, Hu Y, Lu J, Glover GH, Moseley ME. 3D kSPA for high spatial and high temporal resolution fMRI.

Liu C, Moseley ME. 3D kSPA image reconstruction for undersampled arbitrary trajectories.

Lu W, Gold GE, Yu H, Hargreaves BA. Multi-resolution non-iterative field map estimation for water and fat separation.

Lu W, Reeder SB, Daniel BL, Hargreaves BA. Chemical shift correction in bipolar multi-echo sequences for water and fat separation.

Mayer D, Spielman DM, Bammer R. Fast parallel spiral chemical shift imaging at 3 tesla using iterative SENSE reconstruction.

Mayer D, Spielman DM. Fast 1H missing-pulse SSFP chemical shift imaging of the human brain at 7 tesla.

Mayer D, Zahr NM, Sullivan EV, Pfefferbaum A. In vivo metabolite differences between the basal ganglia and cerebellum of the rat brain detected with proton MRS at 3T.

Mazin SR, Pelc NJ. A fast 3D reconstruction algorithm for inverse-geometry CT based on an exact PET rebinning algorithm.

Newbould RD, Gold G, Bammer R. Simultaneous T1, T2, PD, and B1 mapping with dual angle IR-bSSFP (DAIRy-bSSFP).

Newbould RD, Skare S, Albers G, Gold G, Bammer R. Simultaneous T2 and T2\* dynamic susceptibility contrast perfusion imaging using a multi-echo parallel imaging approach.

Nordell A, Bammer R, Skare S. Image based ghost correction for oblique imaging

Nordell A, Bammer R, Skare S. Major speed-up of Nyquist ghost correction in ramp-sampled EPI.

Pisani LJ, Bammer R, Glover G. Time-variable filtering of spiral acquisitions for outer volume suppression.



Rieke V, Hargreaves BA, Butts Pauly K. PRF shift thermometry using multiple-acquisition phase-cycled balanced SSFP.

Schmiedeskamp H, Newbould RD, Glover GH, Pruessmann KP, Bammer R. Improvements in parallel imaging accelerated fMRI.

Schmiedeskamp H, Pisani LJ, Lui C, Law C, Pruessmann KP, Glover GH, Bammer R. Distortion reduction for spiral-fMRI: comparison of iterative and non-iterative parallel imaging reconstruction algorithms.

Schulte T, Müller-Oehring EM, Mayer D, Vinco S, Pfefferbau MA, Sullivan EV. Neural correlates of attentional control of conflict processing: fMRI evidence from a Stroop match-to-sample task.

Sherbondy A, Blemker S, Arnold E, Napel S, Delp S, Gold G. Measuring human gastrocnemius pennation angle utilizing most likely pathway distributions in diffusion tensor imaging.

Skare S, Balchandani P, Newbould RD, Bammer R. Adiabatic refocusing pulses in 3T and 7T diffusion imaging.

Skare S, Newbould RD, Bammer R. Continuous 2D GRAPPA kernel for propeller trajectories.

Skare S, Newbould RD, Bammer R. GRAPPA estimations

using undersampled propeller trajectories.

Thomason M, Glover GH, FIRST BIRN. Controlled inspiration depth reduces variance in breath-holding induced BOLD signal.

Tran DN, Fleischmann D, Rakshe T, Roos JE, Rosenberg J, Straka M, Napel S. Femoropopliteal artery centerline interpolation using contralateral shape.

Tran DN, Fleischmann D, Rakshe T, Roos JE, Rosenberg J, Straka M, Napel S. MRI-detected breast lesions less than 5 mm in size: variables that influence the likelihood of malignancy.

van den Bosch M, Liu EH, Josan S, Butts Pauly K, Bouley DM, Daniel BL. Ice ball imaging during cryoablation of canine prostates: contrast-enhanced MRI provides most accurate delineation of the acute necrotic zone.

Zahr NM, Mayer D, Sullivan EV, Pfefferbaum A. Differential effects of age on tissue water-referenced proton metabolites in basal ganglia, pons, and cerebellum using an MRS sequence optimized for glutamate detection.

Zhang J, Lu C, Moseley M. 3D self-navigated interleaved spiral (3D-SNAILS) for DWI.

## RSNA 2006 92nd Scientific Assembly and Annual Meeting Chicago, IL, November 2006

Chuyeshov G, Kukuk M, Napel S. Localizing a guidewire in three dimensions during endovascular interventions using single-view fluoroscopy and a stereo roadmap: method and feasibility study.

Fleischmann D. Thoracic aortic aneurysms: from annulus to hiatus.

Gold GE, Busse RF, Stevens KJ, Han E, Brau AC, Beatty P. Isotropic MRI of the musculoskeletal system with 3D-FSE-XETA (extended echo train acquisition).

Goldberg SA, Fleischmann D, Wexler L, Friedberg MK, Perry SB, Feinstein JA, Chan FP. Cardiac CT angiography for the characterization of coronary anomalies in infants and young children.

Goldberg SA, Fleischmann D, Wexler L, Perry SB, Feinstein JA, Chan FP. Noninvasive assessment of pulmonary vein stenosis in young children using cardiac-gated CT.

Hellinger JC, Chan FP, Fleischmann D, Rubin GD. Pediatric upper extremity multidetector-row CT angiography: clinical experience in 24 patients.

Iagaru A, Malini V, Mittra ES, Quon A, Ikeda DM, Daniel BL. 18F FDG PET/CT evaluation of patients with breast cancer.

Iagaru A, Mittra ES, Rodriguez C, Le QTX, Gambhir SS, Quon A. 18F FDG PET/CT evaluation of nasopharyngeal carcinoma patients: what is the definition of whole body scanning?

Iagaru A, Quon A, Goris ML, Gambhir SS, McDougall

IR. 18F FDG PET/CT evaluation of osseous and soft tissue sarcomas.

Iagaru A, Quon A, Johnson D, Goris ML, McDougall IR, Gambhir SS. 18F FDG PET/CT in the management of melanoma.

Iagaru A, Rodriguez C, El-Maghraby T, Quon A, Gambhir SS, McDougall R. 18F FDG PET/CT evaluation of patients with cervical carcinoma.

Kim BS, Harpreet S, Dhatt HS, Mittra ES, Bao H, Do BH, Graves EE, Biswal S. A difference in the pattern of 18F-FDG uptake is observed within the spinal canal in low back pain patients.

Kukuk M, Arakawa H, Marks MP, Do HM, Napel S. Rotational roadmapping: a contrast- and time-efficient navigation technique based on a single acquisition of multiple views.

Kukuk M, Rosenberg J, Napel S. Co-visualization of stereoscopic and monoscopic images for instrument navigation in the interventional room.

Lee SW, Graves EE, Jeon TJ, Lee SH, Gold GE, Biswal S. Manganese-enhanced magnetic resonance imaging (MEMRI) detects changes in the spinal cord following painful stimuli.

Mittra ES, Iagaru A, Fischbein NJ, Le QTX, Gambhir SS, Quon A. 18F-FDG PET/CT in evaluation of patients with nasopharyngeal carcinoma.

Olsen DA, Paik DS, Roos JE, Napel S, Rubin GD. External validity of cross-validation on computer-aided detection (CAD) of lung nodules enabled by the LIDC dataset.

Olsen DA, Roos JE, Paik DS, Napel S, Rubin GD. Influence of lung nodule characteristics on computer-aided detection (CAD) based on the Lung Imaging Database Consortium (LIDC) CT dataset.

Paik DS, Olsen DA, Roos JE, Rubin GD. A novel parametric free-response ROC (FROC) methodology.

Paik DS, Roos JE, Liu EG, Rubin GD. Modes of failure in radiologist interpretation of CT lung nodule CAD.

Paulson EK, Durham N, Boll DT, Durham MD, Pelc NJ. Technical aspects of dual energy imaging.

Pu J, Rubin GD, Roos JE, Paik DS. Correcting under-segmentation of juxtapleural lung nodules in chest CT.

Rakshe T, Fleischmann D, Rosenberg J, Roos JE, Napel S. Error prediction and performance evaluation of a principal component analysis (PCA)-based algorithm for reconstructing missing segments of vascular centerlines in lower extremity CT angiography (CTA).

Rakshe T, Fleischmann D, Rosenberg JK, Roos JE, Napel S. Statistical evaluation of a principal component analysis (PCA)-based algorithm for reconstructing centerlines in missing vascular segments in CT angiography (CTA).

Rubesova E, Vance CJ, Bammer S, Dutta S, Barth RA. Three-dimensional MR imaging volumetric measurements of the normal fetal colon.

Rubin GD, Roos JE. Potential equalization of radiologists' diagnostic performance with the use of computer-aided detection (CAD) as a second reader in lung nodule detection on chest CT.

Rubin GD. Vascular interventional keynote speaker: advances in CTA.

Shi R, Beaulieu CF, Rosenberg JK, Shin LK, Mogensen MA, Freeman C, Joshi AJ, Pankhudi P, Napel S. Transparent rendering of intraluminal contrast for 3D polyp visualization in CT colonography.

Stevens K, Busse R, Beehler C, Han E, Bra Au, Beatty P, Beaulieu C, Gold G. Isotropic MRI of the ankle at 3.0T with 3D-FSE-xeta (extended echo train acquisition).

Sun S, Rubin GD, Zhuge F, Napel S. Lung nodule registration using a semi-rigid model and a knowledge-enhanced simulated annealing optimizer.

Sundaram P, Beaulieu CF, Napel S. A curvature scale-space approach to computer-aided detection (CAD) of polyps in CT colonography (CTC).

Sundaram P, Beaulieu CF, Yee J, Olcott EW, Napel S. A pilot study evaluating the efficiency of "patch view": a new paradigm for reviewing the output of a computer-aided polyp detection method.

Tran D, Fleischmann D, Rakshe T, Roos JE, Rosenberg JK, Napel S. Peripheral CT angiography (CTA): can contralateral shape information be used to interpolate occluded femoro-popliteal arterial centerlines?

Tran DN, Fleischmann D, Rakshe T, Roos JE, Rosenberg J, Napel S. Lower extremity CT angiography (CTA): can contralateral shape information be used to interpolate occluded femoro-popliteal arterial centerlines in patients with peripheral arterial occlusive disease (PAOD)?

van den Bosch M, Daniel BL, Dirbas FM, Ikeda DM. MRI Detected breast lesions of 5 mm or less in size: variables that

influence the likelihood of malignancy.

van den Bosch MA, Kuo W, Miller C, Dake MD, Mitchell RS, Sze D. Intentional coverage of the left subclavian artery during endovascular repair of complicated type B aortic dissections increases the risk of type IA endoleaks.

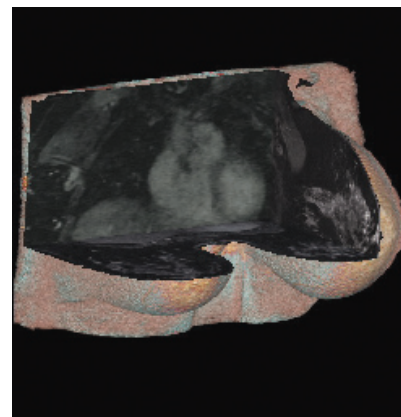
Wang ZJ, Yeh BM, Joe BN, Coakley FV, Busse R, Zaharchuk G. MR imaging measurement of urine oxygen tension in vivo using T1 relaxivity: a feasibility study.

Willmann JK, Chen K, Rollins M, Wang DS, Chen X, Gambhir SS. Molecular imaging of therapeutic angiogenesis in murine hindlimb ischemia using PET and <sup>64</sup>Cu-labeled vascular endothelial growth factor121.

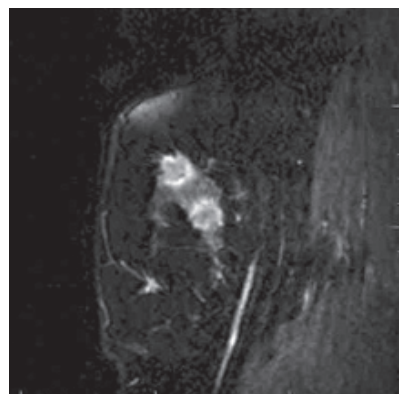
Willmann JK, Paulmurugan R, Chen K, Gheysens O, Chen X, Gambhir SS. Ultrasonic imaging of tumor angiogenesis with contrast microbubbles targeted to vascular endothelial growth factor receptor type 2 in mice.

Yi CA, Olsen DA, Roos JE, Paik DS, Napel S, Rubin GD. Characteristics of true positive (TP) lung nodules detected by computer-aided detection (CAD) but subsequently rejected by radiologists on chest MDCT scans.

## BREAST IMAGING NOW.....2007



## BREAST IMAGING THEN.....1992



## SNM

### 54th Annual Meeting

### Washington DC, June 2-6, 2007

Berman D, Ziffer J, Gambhir DD, Sandler M, Groshar D, Dickman D, Sharir T, Nagler M, Ben-Haim S, Shlomo BH. D-SPECT: A novel camera for high speed quantitative molecular imaging: initial clinical results.

Blankenberg FG, Levashova Z, Backer M, Backer J. PET imaging of angiogenesis with scVEGF-DOTA-PEG-Cu-64.

Cai W, Chen K, He L, Cao Q, Koong A, Chen X. Quantitative PET of EGFR expression in living mice using <sup>64</sup>Cu-labeled anti-EGFR mAb cetuximab.

Cai W, Ebrahimnejad A, Chen K, Cao Q, Li ZB, Tice DA, Chen X. Quantitative radioimmunoPET of EphA2 in xenograft-bearing mice.

Cai W, Liu Z, He L, Nakayama N, Chen K, Sun X, Chen X, Dai H. PET imaging and highly efficient tumor targeting of labeled single-walled carbon nanotubes in mice.

Cao Q, Cai W, Li ZB, Chen K, He L, Li HC, Hui M, Chen X. PET of acute and chronic inflammation in living mice.

Cao Q, He L, Niu G, Li HC, Hui M, Chen X. Multimodality imaging to monitor IL-18bp-Fc-IL-1ra fusion protein treatment of breast cancer lung metastasis.

Cao Q, Li ZB, Wu Z, He L, Neamati N, Chen X. Evaluating anti-tumor effect of a dimeric RGD peptide-paclitaxel conjugate on breast cancer.

Chinn G, Foudray A, Zhang J, Levin C. Image reconstruction strategy for a 1 mm resolution dual-panel breast-dedicated PET system that measures photon interaction depth.

Iagaru A, Masamed R, Quan V, Singer P, Conti P. Detection of occult papillary thyroid cancer with F-18 FDG PET/CT.

Kalinyak J, Iagaru A, McDougall IR. F-18 FDG PET/CT detection of thyroid cancer.

Li ZB, Cai W, Cao Q, Chen K, Wu Z, He L, Chen X. <sup>64</sup>Cu-labeled tetrameric and octameric RGD peptides for microPET imaging of tumor  $\alpha v \beta 3$  integrin expression.

Li ZB, Niu G, He L, Chen X. MicroPET imaging of urokinase-type plasminogen activator receptor (uPAR) expression using <sup>64</sup>Cu-labeled uPAR-binding peptides.

Li ZB, Wu Z, He L, Chin FT, Chen X. "Click" labeling of RGD peptide with <sup>18</sup>F and microPET imaging of  $\alpha v \beta 3$  integrin expression.

Niu G, Li Z, Wang H, He L, Xing L, Chen X. MicroPET imaging of urokinase-type plasminogen activator receptor expression using <sup>64</sup>Cu-labeled cyclo[19,31[D-Cys19]uPA19-31.

Patton J, Sandler M, Berman D, Vallabhajosula S, Dickman S, Gambhir SS, Nagler M, Ben Haim S. D-SPECT: A new solid state camera for high speed molecular imaging.

Pratx G, Olcott P, Chinn G, Levin C. Accelerated list-mode 3D-OSEM reconstruction for PET on a graphics processing unit.

Sherbondy AJ, Dougherty R, Ben-Shachar M, Cheung SH, Napel S, Wandell BA. Identifying the most likely white matter pathways between two brain regions.

Sigg D, Iagaru A, Levin C, Quon A. Partial volume correction of PET/CT derived SUV values in lung nodules.

Vasanawala M, Iagaru A, Rosenberg J, Famir S, Segal G.

Renal cell carcinoma: can F-18 FDG PET be a useful tool?

Wang H, Cai W, Li ZB, He L, Chen X. Efficient in vivo tumor targeting of a RGD-TNF fusion protein.

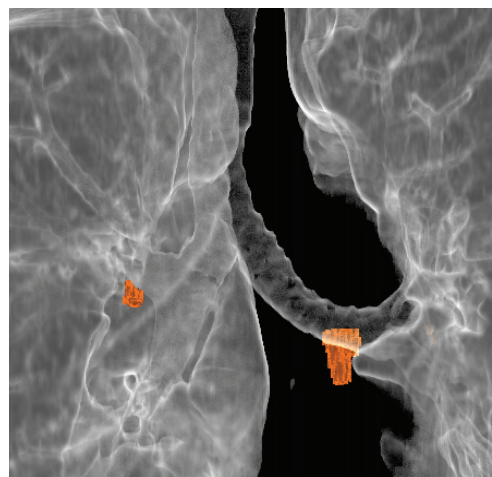
Wu Z, Li ZB, Cai W, He L, Chin FT, Li F, Chen X. <sup>18</sup>F-labeled mini-PEG spacers RGD dimer (<sup>18</sup>F-FPRGD2): synthesis and microPET imaging of  $\alpha v \beta 3$  integrin expression.

Wu Z, Li ZB, Cai W, He L, Chin FT, Li F, Chen X. MicroPET imaging of tumor  $\alpha v \beta 3$  integrin expression using <sup>18</sup>F-labeled PEGylated tetrameric RGD peptide (<sup>18</sup>F-FPRGD4).

Xie X, Cao F, Lin S, Dutta S, Brown M, Matthewson S, Chungfat N, Gambhir SS, Wang E, Wu J. Proteomic analysis of the effects of reporter genes used for imaging stem cell transplant.

Zhao Y, Kuge Y, Zhao S, Inubushi M, Morita K, Strauss HW, Blankenberg FG, Tamaki N. Comparison of <sup>99m</sup>Tc-annexin A5 with <sup>18</sup>F-FDG for the detection of atherosclerosis in ApoE<sup>-/-</sup> mice.

Zhao Y, Kuge Y, Zhao S, Inubushi M, Morita K, Strauss HW, Blankenberg FG, Tamaki N. Effects of long-term cholesterol feeding on aortic accumulation of <sup>18</sup>F-FDG and <sup>99m</sup>Tc-annexin A5 in ApoE<sup>-/-</sup> and normal mice.



2005 NUCLEAR MEDICINE IMAGE OF THE YEAR



## SMI Annual Meeting

Benoit M, Mayer D, Barak Y, Chen I, Hu W, Keren S, Gambhir SS, Matin AC Magnetotactic bacteria as a potential MRI contrast agent.

Biswal S, Cheng D, Levashova Z, Tait JF, Vanderheyden JL, Blankenberg F. Subjects suffering from inflammatory arthritis demonstrate increased Cy5.5-labeled annexin V uptake in the central nervous system.

Cai W, Chen K, Li ZB, Gambhir SS, Chen X. Dual functional quantum dot-based probe for near-infrared fluorescence and positron emission tomography imaging of cancer.

Cai W, Ebrahimnejad A, Chen K, Cao Q, Li ZB, Tice DA, Chen X. Quantitative PET imaging of EphA2 expression in tumor-bearing mice.

Cai W, Guzman R, Chen K, Hsu AR, Bliss T, Sun G, Wang H, He L, Li ZB, Maag AD, Hori N, Steinberg GK, Chen X. PET imaging of VEGFR expression in stroke.

Cao F, Li Z, Chen K, Wang H, Cai W, Chen X, Wu JC. PET imaging of angiogenesis formation in teratoma from human embryonic stem cells.

Chan CT, Paulmurugan R, Gheysens OS, Kim J, Mazitschek R, Chiosis G, Stuart SL, Gambhir SS. High-throughput screening of novel kinase inhibitors and imaging phosphorylation events in living subjects using a novel split luciferase complementation system.

Cheng Z, De Jesus OP, De A, Webster J, Gheysens O, Levi J, Namavari M, Wang S, Zhang R, Hoerner J, Grade H, Syud FA, Gambhir SS. MicroPET imaging of HER2 expression using Cu labeled synthetic affibody molecules.

Cheng Z, Blum G, Gheysens O, Bogoy M, Gambhir SS. Activity based probe for microPET imaging of cysteine cathepsins.

Cochran F, Ray P, Lutz AM, Gambhir SS. Early detection and imaging of ovarian cancer with peptides identified by surface display technology that target vascular smooth muscle growth-promoting factor (VSGP/F-spondin).

Cochran FV, Gambhir SS. A diverse panel of polypeptide libraries for the rapid design and engineering of new molecular imaging agents.

Doyle TC, Sheikh AY, Sheikh MK, Cao F, Yang PC, Robbins RC, Wu JC. A comparison between spectral and time domain imaging systems for imaging quantum dots in small living animals.

Girard-Hughes E. [18F]FHBG PET imaging of T cell homing in patients with gliomas.

Keren S, de la Zerda A, Levi J, Vaithilingam S, Oralkan O, Khuri-Yakub P, Gambhir SS. Photoacoustic tomography with high resolution small animal ultrasound system.

Keren S, Zavaleta C, Chen Z, Gheysens O, Gambhir SS. Noninvasive molecular imaging of small living subjects using raman spectroscopy and raman nanoparticles.

Kim B, Mittra E, Dhatt H, Do B, Graves E, Biswal S. Increased 18F-FDG uptake is observed within the spinal canal in low back pain patients.

Li ZB, Niu G, Wang H, He L, Ploug M, Chen X. MicroPET imaging of urokinase-type plasminogen activator receptor expression using a Cu-labeled linear peptide antagonist.

Li ZB, Wu Z, Cao Q, Dick DW, Tseng JR, Gambhir SS, Chen X. Orthotopic brain tumor imaging with F-2-Fluorodeoxyribose (F-FDS).

Li ZB, Wu Z, Chen K, Chin FT, Chen X. Click chemistry for F-labeling of RGD peptides and microPET imaging of tumor integrin expression.

Li ZB, Wu Z, Chen K, Ryu EK, Chen X. F-labeled BBN-RGD heterodimer for prostate cancer.

Peng H, Levin CS. Study of potential PET spatial resolution improvement in PET/MRI dual modality systems.

Peng H, Olcott PD, Foudray AMK, Levin CS. Evaluation of a fully digital data acquisition system for PET systems.

Peng H, Olcott PD, Pratz G, Foudray AMK, Chinn G, Levin CS. Performance study of a high resolution CZT-based PET camera for breast imaging.

Pratz G, Chinn G, Olcott P, Levin CS. Fast fully-3D list-mode OSEM for high-resolution PET using PC graphics hardware.

Rodriguez CA, Lipkin A, Gambhir SS. Combinatorial complexity in the hsp90-p23 reporter protein complementation assay.

Willmann JK, Chen K, Wang H, Paulmurugan R, Rollins M, Cai W, Wang D, Chen IY, Lutz AM, Gheysens O, Rodriguez-Porcel M, Chen X, Gambhir SS. Assessment of therapeutic angiogenesis in murine hindlimb ischemia using Cu-labeled vascular endothelial growth factor-121 PET.

Willmann JK, Paulmurugan R, Chen K, Gheysens O, Rodriguez-Porcel M, Lutz AM, Chen IY, Chen X, Gambhir SS. Ultrasonic imaging of tumor angiogenesis with contrast microbubbles targeted to vascular endothelial growth factor receptor type 2 in mice.

Xiong G, Budhiraja S, Lin J, Felsher D, Bendapudi P, Paik D. A segmentation and registration framework for serial 3D images of mice.

Yaghoubi SS, Remi J, Creusot RJ, Fathman CG, Gambhir SS. Bioluminescent reporter gene based imaging of bone marrow derived dendritic cell trafficking in various mouse models.

Yerushalmi D, Quon A, Fahrig R, Pelc NJ, Fann JJ, Gambhir SS. PET-CT fly-through virtual bronchoscopy lesion quantification and amplification; parameters affecting 3D visualization.

Zavaleta C, Keren S, Cheng Z, Schipper M, Chen X, Liu Z, Dai H, Gambhir SS. Use of non-invasive raman spectroscopy in living mice for evaluation of tumor targeting with carbon nanotubes.

## OTHER SCIENTIFIC MEETING PRESENTATIONS

Alam R, Dixit V, Kang H, Fisher M, Li Z-B, Chen X, Juliano R. Delivery of anionic antisense oligonucleotides via bivalent RGD ligands. Gordon Research Conference: Nucleosides, Nucleotides & Oligonucleotides; July 2007; Newport, RI.

Barth RA. MRI of fetal anomalies, challenging pediatric cases. 4th Joint Conference: International Symposium on State-of-the-Art Imaging in Barcelona; July 5-7, 2007; Dubrovnik, Croatia.

Cai W, Chen K, Mohamedali KA, Cao Q, Gambhir SS, Rosenblum MG, Chen X. Positron emission tomography imaging of VEGFR expression in solid tumors by <sup>64</sup>Cu-DOTA-VEGF121. 98th AACR Annual Meeting; April 2007; Los Angeles, CA.

Cosby KM, Hofmann LV, Kedziorek D, Gilson WD, Barnett BP, Huang G, Arepally A, Bulte JW, Kraitchman D. Innovation in Intervention Session of the 56th Annual Scientific Session of American College of Cardiology (ACC); March 24, 2007; New Orleans.

Cosby M, Hofmann LV, Barnett BP, Kedziorek DA, Gilson WD, Korosoglou G, Huang G, Bulte JW, Kraitchman DL. A novel radio-opaque barium/alginate microencapsulation technique for allogeneic mesenchymal stem cell delivery and localization. Sept. 18, 2006.

Fazel S, Mallidi HR, Lee R.S, Sheehan MP, Liang D, Herfkens R, Mitchell S, Miller C. The aortopathy of bicuspid aortic valve disease has distinctive patterns and usually involves the transverse aortic arch. 33rd Annual Meeting of the Western Thoracic Surgical Association; June 27-30, 2007; Santa Ana Pueblo, NM.

Fleischmann D, Straka M, Scherthaner R, Varchola A, Roos J, Tran D, Rakshe T, Bernhard M, Solcany V, Napel S, Lammer J, Gröller E, Sramek M. AngioVis II: from science to practice of lower extremity CTA visualization. Invited exhibit, European Congress of Radiology; March 2007; Vienna, Austria.

Fleischmann D. Injecting contrast with ever faster scanners. European Congress of Radiology (ECR), 2007; Vienna, Austria.

Gilbertson-Dahdal D, Dutta S, Barth RA, Varich L. Three newborns with malrotation and midgut volvulus mimicking duodenal atresia on plain film. Postgraduate Course and Annual Meeting of the Society of Pediatric Radiology; April 17-21, 2007; Miami, FL.

Gold G, Busse R, Stevens K, Han E, Brau A, Beatty P, Beaulieu C. Isotropic MRI with 3D-FSE-XETA (extended echo train acquisition). Proceedings of the Society of Computed Body Tomography and Magnetic Resonance; March 2007.

Han S, Iagaru A, Zhu HJ, Goris ML. 90Y-Ibritumomab (Zevalin) in the management of refractory non-Hodgkin's lymphoma. British Nuclear Medicine Society Autumn Meeting; Sept. 4-5, 2006; Cambridge, UK.

Helm E, Babyn P, Newman B. Thoracic manifestations of sickle cell disease in children. 50th Annual Meeting of the Society of Pediatric Radiology; April 2007; Miami, FL.

Hofmann LV. Catheter-directed thrombolysis: how I do it. Society of Interventional Radiology Multimodality Symposium; October 18, 2006; Washington DC.

Hofmann LV. [Workshop]. Endograft update AVIR. 31st Annual Scientific Meeting of the Society of Interventional Radiology; April 1, 2006; Toronto Ontario, Canada.

Hofmann LV. [Workshop]. Venous thrombolysis. 31st Annual Scientific Meeting of the Society of Interventional Radiology. April 1, 2006; Toronto Ontario, Canada.

Hofmann LV. Isolated thrombolysis workshop. Society of Interventional Radiology Multimodality Symposium; Oct. 18, 2006; Washington DC.

Hofmann LV. Thrombolytic therapy for arterial disease. 32nd Annual Scientific Meeting; March 5, 2007; Seattle, WA.

Hsu AR, Cai W, Veeravagu A, Chen K, Mohamedali KA, Vogel H, Hou LC, Tse VCK, Rosenblum MG, Chen X. Multimodality molecular imaging of glioblastoma growth inhibition using the vascular-targeting fusion toxin VEGF121/rGel. 98th AACR Annual Meeting; April 2007; Los Angeles, CA.

Huisman T, Ghassemi M, Gomez A, Willi U, Hintz S, Ringertz H, Barth RA. European-American multi-center comparison of plain films frequency in neonatology. Postgraduate Course and Annual Meeting of the European Society of Paediatric Radiology. June 3-7, 2007; Barcelona, Spain.

Huynh LT, Krasnokutsky M, Vertinsky AT, Rooks VJ, Barnes PD. Fetal MR imaging of brain, head & neck, and spine abnormalities. Poster presentation: American Society of Neuroradiology/American Society of Pediatric Neuroradiology; June 13, 2007; Chicago IL.

Iagaru A, Quan V, Jadvar H, Conti PS. Sentinel lymph node scintigraphy and 18F FDG PET/CT in the management of breast cancer. ACNP Annual Meeting; Feb 15-18, 2007; San Antonio, TX.

Iagaru A, Wang Y, Mari C, Rodriguez CA, Quon A, Goris ML, Gambhir SS. 18F FDG PET/CT prediction of response to chemotherapy in lymphoma: when is the optimal time for the first re-evaluation scan? ACNP Annual Meeting; Feb 15-18, 2007; San Antonio, TX.

Ikeda D. MRI lexicon: what should be improved? magnetic resonance imaging and accelerated partial breast irradiation. Fourth International Congress on MR Mammography; Sept. 25-30, 2006; Jena, Germany.

Ikeda, D. Preoperative needle localizations and core biopsy in breast imaging clinical practice. IEEE, 2006 Nuclear Science Symposium, Medical Imaging Conference and 15th International Room Temperature Semiconductor Detector Workshop; Oct. 29-Nov 4, 2006; San Diego, CA.

Kedziorek DA, Hofmann LV, Gilson W, Bulte JWM, Kraitchman DL. Monitoring of mesenchymal stem cell arteriogenesis therapy in a rabbit hindlimb ischemia model. Society of Molecular Imaging Annual Meeting. Sept. 2, 2006.

Kedziorek DA, Gilson WD, Blush E, Cosby K, Soto VA, Bulte JWM, Hofmann LV, Kraitchman DL. Mesenchymal stem cell therapy in a rabbit hindlimb ischemia model. The 56th Scientific Session of the American College of Cardiology; March 26, 2007; New Orleans, LA.

## OTHER SCIENTIFIC MEETING PRESENTATIONS

Krasnokutsky M, Barnes P. Cerebral venous thrombosis: a mimic of nonaccidental injury. Accepted for Scientific Paper Session. Society for Pediatric Radiology; April 18, 2007; Miami FL.

Krasnokutsky M, Barnes P. Spinal cord injury without radiographic abnormality (SCIWORA)--a mimic of nonaccidental injury. Scientific Paper Session. Society for Pediatric Radiology. April 20, 2007; Miami FL.

Krasnokutsky M, Barnes P. Spinal cord injury without radiographic abnormality (SCIWORA)--a mimic of nonaccidental injury. Scientific Paper Session. American Society of Neuroradiology/American Society of Pediatric Neuroradiology. June 13, 2007; Chicago IL.

Kuo W. Retrieval of the difficult Günther-Tulip IVC filter: snare over guide wire loop technique. Society of Interventional Radiology 31st Annual Scientific Meeting. Abstract No. 345; March 1-6, 2007; Seattle, WA.

Les AS, Cheng CP, Draney M, Blomme MT, Figuerora CA, LaDisa JF, Park JM, Herfkens RJ, Dalman RL, Taylor CA. Hemodynamics in abdominal aortic aneurysms during rest and simulated exercise. Proceedings of the ASME 2007 Summer Bioengineering Conference; June 20-24, 2007; Keystone, CO.

Lewis S, Jagaru A, Quon A, Kamaya A. Artifacts and pitfalls on 18F FDG PET/CT. ARRS Annual Meeting; May 6-11, 2007; Orlando, FL.

McDougall IR. Controversies in the management of thyroid cancer: thyroglobulin positive/iodine negative patients. Society of Nuclear Medicine Meeting; June 2007; Washington DC.

McDougall IR. Thyroid cancer. IVth Stanford Medical Symposium; April 6th, 2007; Stanford, CA.

McDougall IR. Treatment of thyroid cancer with I-131. guidelines and controversies. Northern California Chapter, Society of Nuclear Medicine; Feb 2007; Oakland CA.

Padmanabhan P, Biswal S. A new imaging approach for calcium dependent calmodulin activation in cells. Oral presentation at the Academy of Molecular Imaging Annual Conference; 2006; Orlando, FL.

Padmanabhan P, Ramasamy P, Gambhir SS, Biswal S. Peptide linkers are not necessarily needed for efficient non-invasive fluorescence-bioluminescence reporter bi-fusion for imaging in living mice. Poster presentation at the Academy of Molecular Imaging Annual Conference; 2006; Orlando, FL.

Padmanabhan P, Ramasamy P, Gambhir SS, Biswal S. Simultaneous non-invasive imaging of estrogen receptor ligand induced homodimerization and gene transactivation in living mice. Oral presentation at the Academy of Molecular Imaging Annual Conference; 2006; Orlando, FL.

Rubesova E, Chueh J, Hintz SR, Dutta S, Barth RA. Third trimester fetal MRI: can we replace postnatal imaging? Postgraduate Course and Annual Meeting of the Society of Pediatric Radiology; April 17-21, 2007; Miami, FL.

Rubesova E, Rosenberg J, Hoggard E, Chawla S, Gomez A, Ullberg U, Huisman T, Ghassemi M, Willi U, Hintz S, Ringertz H, Barth R. European-American multicenter comparison of plain films frequency in neonatology, ESPR 44 Annual Meeting; 2007; Barcelona.

Shi R, Napel S, Rosenberg JK, Shin LK, Freeman C, Mogensen MA, Joshi AJ, Pankhudi P, Beaulieu CF. Transparent rendering of intraluminal contrast for 3D polyp visualization in CT colonography. 7th International Symposium on Virtual Colonoscopy, Boston University; 2006; Boston, MA.

Shin LK, Hargreaves BA, Brau ACS, Banerjee S, Napel S, Jeffrey Jr. RB, Beaulieu CF, Herfkens RJ. MR colonography at 3T using autocalibrating reconstruction for Cartesian (ARC) sampling--initial experience. 7th International Symposium on Virtual Colonoscopy, Boston University; 2006; Boston, MA.

Sundaram P, Beaulieu CF, Napel S. Colon polyp detection using smoothed shape operators. 7th International Symposium for Virtual Colonoscopy; Nov. 2006; Boston, MA.

Tran DN, Roos JE, Straka M, Sandner D, Razavi H, Chang M, Pelc N, Napel S, Fleischmann D. Promises and limitations of dual-energy CT in lower extremity CT angiography. Society of Computed Body Tomography/Magnetic Resonance; March 2007; Orlando, FL.

Vasanawala SS, Barth RA, Ganguly A, Fahrig R, Rieke V, Daniel B, Kennedy WA. MRI Voiding cystography in the evaluation of vesicoureteral reflux. Postgraduate Course and Annual Meeting of the Society of Pediatric Radiology. April 17-21, 2007; Miami, FL.

Wootton-Gorges SL, Buonocore MH, Kuppermann N, Marcin JP, Barnes PD, Neely EK, et al. Cerebral proton MRS in children with diabetic ketoacidosis. Scientific Paper Session. Society for Pediatric Radiology; April 18, 2007; Miami FL.

Zilber S, Epstein N, Lee SW, Larsen M, Ma T, Smith RL, Biswal S, Goodman SB. Mouse femoral intramedullary model: technique and microCT scan validation. Poster presentation at the 53rd Annual Meeting of Orthopedic Research Society; 2007; San Diego, CA.

Zilber S, Lee SW, Smith RL, Biswal S, Goodman SB. In vivo QCT and PET scanning of the murine femur containing PMMA particles. Poster presentation at the 53rd Annual Meeting of Orthopedic Research Society; 2007; San Diego, CA.



## PUBLISHED PAPERS

- Bangerter NK, Hargreaves BA, Gold GE, Stucker DT, Nishimura DG. Fluid-attenuated inversion-recovery SSFP imaging. *J Magn Reson Imaging*. 2006 Dec;24(6):1426-31.
- Budoff MJ, Achenbach S, Blumenthal RS, Carr JJ, Goldin JG, Greenland P, Guerci AD, Lima JA, Rader DJ, Rubin GD, Shaw LJ, Wiegers SE. Assessment of coronary artery disease by cardiac computed tomography: a scientific statement from the American Heart Association Committee on Cardiovascular Imaging and Intervention, Council on Cardiovascular Radiology and Intervention, and Committee on Cardiac Imaging, Council on Clinical Cardiology. *Circulation*. 2006;114:1761-1791.
- Caffarelli AD, Banovac F, Cheung SC, Fleischmann D, Mitchell RS. Unusual case of later thoracic stent graft failure after cardioversion. *Ann Thorac Surg*. 2006 May;81(5):1875-7.
- Cao F, Drukker M, Lin S, Sheikh AY, Xie X, Li Z, Connolly AJ, Weissman IL, Wu JC. Molecular imaging of embryonic stem cell misbehavior and suicide gene ablation. *Cloning Stem Cells*. 2007 Spring;9(1):107-17.
- Chang GY, Cao F, Krishnan M, Huang M, Li Z, Xie X, Sheikh AY, Hoyt G, Robbins RC, Hsiai T, Schneider MD, Wu JC. Positron emission tomography imaging of conditional gene activation in the heart. *J Mol Cell Cardiol*. 2007 Jul;43(1):18-26.
- Chang GY, Xie X, Wu JC. Overview of stem cells and imaging modalities for cardiovascular diseases. *J Nucl Cardiol*. 2006 Jul;13(4):554-69.
- Cheng CP, Wilson NM, Hallett RL, Herfkens RJ, Taylor CA. In vivo MR angiographic quantification of axial and twisting deformations of the superficial femoral artery resulting from maximum hip and knee flexion. *J Vasc Interv Radiol*. 2006;17(6):979-87.
- Chinn G, Foudray AM, Zhang J, Levin CS. Image reconstruction strategy for a 1m resolution dual-panel breast-dedicated PET system that measures photon interaction depth. *Journal of Nuclear Medicine*. 2006;47(1):182P.
- Deckers RH, van Gelderen P, Ries M, Barrett O, Duyn JH, Ikonomidou VN, Fukunaga M, Glover GH, de Zwart JA. An adaptive filter for suppression of cardiac and respiratory noise in MRI time-series data. *NeuroImage*. 2006;33:1072-1081.
- Dey J, Napel S. Targeted 2D/3D registration using ray normalization and a hybrid optimizer. *Medical Physics*. 2006;33(12):4730-4738.
- Do BH, Mari C, Biswal S, Kalinyack J, Gambhir SS. Diagnosis of aseptic deep venous thrombosis of the upper extremity in a cancer patient using fluorine-18 fluorodeoxyglucose positron emission tomography/computerized tomography (FDG PET/CT): a case report. *Ann Nuc Med*. 20(2):151-5.
- Fahrig R, Dixon R, Payne T, Morin RL, Ganguly A, Strobel N. Dose and image quality for a cone-beam C-arm CT system. *Medical Physics*. 2006 Dec;33(12):4541-4550.
- Fleischmann D, Hallett RL, Rubin FD. CT angiography of peripheral arterial disease. *J Vasc Interv Radiol*. 2006;17:3-26.
- Fleischmann D, Lammer J. Peripheral CT angiography for interventional treatment planning. *Europ. Radiol*. 2006;(16S):58-64.
- Foudray AMK, Habte F, Chinn G, Zhang J, Levin CS. Count rate studies of a box-shaped PET breast imaging system comprised of position sensitive avalanche photodiodes utilizing Monte Carlo simulation. *Physica Medica*. 2006;XXI(suppl 1):64-67.
- Foudray AMK, Habte F, Levin CS, Olcott PD. Positioning annihilation photon interactions in a thin LSO crystal sheet with a position-sensitive avalanche photodiodes. *IEEE Transactions on Nuclear Science*. 2006 Oct;53-5(pt 1):2549-2556.
- Fredricson M, Moore W, Biswal S. Sacral stress fractures: MRI not always definitive for early stage injuries. *Am J Sports Med*. 35(5):835-9. Epub 2007 Jan 29.
- Friedman L, Glover GH. Reducing inter-scanner variability of activation in a multi-center fMRI study: controlling for signal-to-fluctuation-noise-ratio (SFNR) differences. *NeuroImage*. 2006;32:1656-1668.
- Friedman L, Glover GH. Report on a multicenter fMRI quality assurance protocol. *JMRI*. 2006;23:827-839.
- Friedman L, Glover GH, Kranz D, Magnotta V. FIRST BIRN. Reducing scanner-to-scanner variability of activation in a multi-center fMRI study: role of smoothness equalization. *NeuroImage*. 2006;32:1656-68.
- Fuller S, Reeder S, Shimakawa A, Yu H, Johnson J, Beaulieu C, Gold G. Iterative decomposition of water and fat with echo asymmetry and least-squares estimation (IDEAL) FSE imaging of the ankle: initial clinical experience. *Am J Roentgenol*. 2006 Dec;187(6):1442-7.
- Fuller SB, Reeder S, Shimakawa A, Yu H, Johnson, BeaGaab N, Gabrieli JD, Glover GH. Assessing the influence of scanner background noise on auditory processing I. an fMRI study comparing three experimental designs with varying degrees of scanner noise. *Human Brain Mapping*. 2007;28:703-20.
- Gaab N, Gabrieli JD, Glover GH. Assessing the influence of scanner background noise on auditory processing II: an fMRI study comparing auditory processing in the absence and presence of recorded scanner noise using a sparse design. *Human Brain Mapping*. 2007;28:721-32.
- Gold GE, Hargreaves BA, Reeder SB, Block WF, Vasanawala SS, Kornaat PR, Bammer R, Newbould R, Beaulieu CF. Balanced SSFP imaging of the musculoskeletal system. *JMRI*. 2007 Feb;25:270-8.
- Gold GE, Reeder SB, Yu H, Kornaat P, Shimakawa AS, Johnson JW, Beaulieu CB, Brittain JH. Articular cartilage of the knee: rapid 3D MR imaging at 3.0T with IDEAL balanced steady-state free precession—initial experience. *Radiology*. 2006 Aug;240(2):546-551.
- Graves EE, Quon A, Loo BW Jr. RT\_image: an open-source tool for investigating PET in radiation oncology. *Technol Cancer Res Treat*. 2007 Apr;6(2):111-21.
- Habte F, Olcott PD, Levin CS, Foudray AM. Prototype parallel readout system for position sensitive PMT based gamma-ray imaging systems. *IEEE Transactions on Nuclear Science*. 2007;54-1(1):60-65.
- Habte F, Foudray AMK, Olcott PD, Levin CS. Effects of system geometry and other physical factors on photon sensitivity of high resolution positron emission tomography. *Physics in Medicine and Biology*. 2007;52:3753-3772.
- Habte F, Levin CS. Study of a new geometry for whole body clinical PET systems using Monte Carlo simulation. *Journal of Nuclear Medicine*. 2006;47(1):394P.

- Haddad F, Perez M, Fleischmann D, Valantine H, Hunt SA. Giant coronary aneurysms in heart transplantation: an unusual presentation of cardiac allograft vasculopathy. *J Heart Lung Transplant*. 2006;25:1367-1370.
- Hargreaves BA, Cunningham CH, Han M, Pauly JM, Lee JH, Daniel BL. New aspects on pulse sequence design for breast MRI. *Eur. Radiol*. 2006 Sep;16(suppl 5):E35-E37.
- Hargreaves BA, Cunningham CH, Pauly JM, Daniel BL. Independent phase modulation for efficient dual-band 3D imaging. *Magn Reson Med*. 2007 Apr;57(4):798-802.
- Hellinger JC, Fleischmann D, Cheung S, Rubin GD. Indirect upper extremity (UE) multidetector-row computed tomography (MDCT) venography: initial technical experience. *European Radiology*. 2006;15(suppl 1);348.
- Hellinger JC, Quon A, Rubin GD, Fleischmann D, Herfkens R. PET-CT angiography: technique and clinical application. *European Radiology*. 2006;15(suppl 1);428-429
- Hendel RC, Patel MR, Kramer CM, Poon M, Hendel RC, Carr JC, Gerstad NA, Gillam LD, Hodgson JM, Kim RJ, Kramer CM, Lesser JR, Martin ET, Messer JV, Redberg RF, Rubin GD, Rumsfeld JS, Taylor AJ, Weigold WG, Woodard PK, Brindis RG, Hendel RC, Douglas PS, Peterson ED, Wolk MJ, Allen JM, Patel MR. ACCF/ACR/SCCT/SCMR/ASNC/NASCI/SCAI/SIR 2006 appropriateness criteria for cardiac computed tomography and cardiac magnetic resonance imaging: a report of the American College of Cardiology Foundation Quality Strategic Directions Committee Appropriateness Criteria Working Group, American College of Radiology, Society of Cardiovascular Computed Tomography, Society for Cardiovascular Magnetic Resonance, American Society of Nuclear Cardiology, North American Society for Cardiac Imaging, Society for Cardiovascular Angiography and Interventions, and Society of Interventional Radiology. *J Am Coll Cardiol*. 2006;48:1475-1497.
- Hoefl F, Ueno T, Reiss A, Meyler A, Whitfield-Gabrieli S, Glover GH, Keller TA, Kobayashi N, Mazaika P, Just MA, Gabrieli JDE. Prediction of children's reading skills using behavioral functional and structural neuroimaging measures. *Behavioral Neuroscience*. 2007;121:602-613.
- Hsu JJ, Glover GH. Rapid MRI method for mapping the longitudinal relaxation time. *JMR*. 2006;181:98-106.
- Hu YL, Glover GH. Partial k-space acquisition method for improved SNR efficiency and temporal resolution in 3D fMRI. *Magn Reson Med*. 2006;55:1106-1113.
- Iagaru A, McDougall IR. F-FDG PET/CT demonstration of an adrenal metastasis in a patient with anaplastic thyroid cancer. *Clinical Nuclear Medicine*. 2007;32:13-15.
- Iagaru A, Quon A, Johnson D, Gambhir SS, McDougall IR. 2-Deoxy-2-[F-18]fluoro-D-glucose positron emission tomography/computed tomography in the management of melanoma. *Mol Imaging Biol*. 2007 Jan-Feb;9(1):50-7.
- Iagaru A, Quon A, McDougall IR, Gambhir SS. F-18 FDG PET/CT evaluation of osseous and soft tissue sarcomas. *Clin Nucl Med*. 2006 Dec;31(12):754-60.
- Iagaru A, Quon A. Advances in metabolic imaging for surgical oncology. *Surg Oncol Clin N Am*. 2007 Apr;16(2):273-92.
- Iagaru A, Quon A, McDougall IR. Merkel cell carcinoma: is there a role for 2-Deoxy-2-[F-18]fluoro-D-glucose-positron emission tomography/computed tomography? *Molecular Imaging and Biology*. 2006;8:212-217.
- Ikeda DM. Mainstream breast cancer radiology perspective. *Physics Medica*. 2007 Jun;XXI(suppl 1): 4-6.
- Iribarren C, Husson G, Go AS, Lo JC, Fair JM, Rubin GD, Hlatky MA, Fortmann SP. Plasma leptin levels and coronary artery calcification in older adults. *J Clin Endocrinol Metab*. 2007;92:729-732.
- Kamaya A, Quon A, Jeffrey RB. Sonography of the abnormal parathyroid gland. *Ultrasound Q*. 2006 Dec;22(4):253-62. Review.
- Kobayashi C, Glover GH, Temple E. Children's and adults' neural bases of verbal and nonverbal 'theory of mind.' *Neuropsychologia*. 2007 Apr 8;45:1522-1532.
- Kuo WT, Bostaph AS, Loh CT, Frisoli JK, Kee ST. Retrieval of trapped Günther Tulip inferior vena cava filters: snare over guidewire loop technique. *Journal of Vascular and Interventional Radiology*. 2006 Nov;17:845-1849.
- Lauritsch G, Boese J, Wigstroom L, Pruemmer M, Fahrig R. Temporal resolution in cardiac C-arm CT in the presence of variable heart rate. 9th Int. Meeting on Fully 3D Image Reconstruction in Radiology and Nuclear Medicine. 2007:358-361.
- Lee RS, Fazel S, Schwarze U, Fleischmann D, Berry GJ, Liang D, Miller DC, Mitchell RS. Rapid aneurysmal degeneration of a Stanford type B aortic dissection in a patient with Loeys-Dietz syndrome. *J Thorac Cardiovasc Surg*. 2007;134:242-243.
- Levin CS, Habte F, Foudray AMK, Chang J, Chinn G. Impact of high energy resolution detectors on the performance of a PET system dedicated to breast cancer imaging. *Physica Medica*. 2006;XXI(suppl 1):28-34.
- Lew CD, Alley MT, Bammer R, Spielman DM, Chan FP. Peak velocity and flow quantification validation for sensitivity-encoded phase-contrast MR imaging. *Acad Radiol*. 2007 Mar;14:3:258-69.
- Loo BW Jr., Draney MT, Sivanandan R, Ruehm SG, Pawlicki T, Xing L, Herfkens RJ, Le QT. Indirect MR lymphangiography of the head and neck using conventional gadolinium contrast: a pilot study in humans. *Int J Radiat Onc Bio Phys*. 2006; 66(2):462-8.
- Marsden AL, Vignon-Clementel IE, Chan FP, Feinstein JA, Taylor CA. Effects of exercise and respiration on hemodynamic efficiency in CFD simulations of the total cavopulmonary connection. *Annals of Biomedical Engineering*. 2007 Feb;35(2): 250-63.
- Mayer D, Dreher W, Leibfritz D, Spielman DM, RF refocused echoes of J-coupled spin systems: effects on RARE-based spectroscopic imaging. *Magn Reson Med*. 2007 Apr 24;57(5):967-971
- Mayer D, Levin YS, Hurd RE, Glover GH, Spielman DM. Fast metabolic imaging of systems with sparse spectra: application for hyperpolarized (13)C imaging. *Magn Reson Med*. 2006 Oct;56(4):932-7
- Minn YA, Fisher PG, Barnes PD, Dahl GV. A syndrome of irreversible leukoencephalopathy following pediatric allogeneic

bone marrow transplantation. *Pediatr Blood & Cancer*. 2007;203:7-13.

Niederkoeh R, McDougall IR. Reproducibility of whole-body <sup>131</sup>I scan, serum thyrotropin and stimulated thyroglobulin values in patients studied twice after injection of recombinant human thyrotropin. *European Journal Nuclear Medicine and Molecular Imaging*. 2007;34:363-367.

Niederkoeh RD, Quon A. No apparent alteration of F-18 FDG biodistribution when injected shortly after insulin glargine. *Clin Nucl Med*. 2007 Apr;32(4):302-3.

Padmanabhan P, Ray P, Ramasamy P, Hoffman AR, Gambhir SS, \*Biswal S, \*Ulaner GA. Non-destructive imaging of human telomerase reverse transcriptase (hTERT) promoter activity using a tri-modality fusion reporter construct. *J Nuc Med*. 2006;47:270-277. \*Co-corresponding authors.

Patel DA, Chang ST, Goodman KA, Quon A, Thorndyke B, Gambhir SS, McMillan A, Loo BW Jr, Koong AC. Impact of integrated PET/CT on variability of target volume delineation in rectal cancer. *Technol Cancer Res Treat*. 2007 Feb;6(1):31-6.

Pisani L; Bammer R; Glover GH. Restricted field of view magnetic resonance imaging of a dynamic time series. *Magn Reson Med*. 2007;57:297-307.

Plevritis SK, Kurian AW, Sigal BM, Daniel BL, Ikeda DM, Stockdale FE, Garber AM. Cost-effectiveness of screening BRCA1/2 mutation carriers with breast magnetic resonance imaging. *JAMA*. 2006 May 24;295(20):2374-84.

Po J, Margolis DJ, Cunningham CH, Herfkens RJ, Ikeda DM, Daniel BL. Water-selective special-spatial contrast-enhanced breast MRI for cancer detection in patients with extra capsular and injected silicone. *Magn Reson Imaging*. 2006 Dec;24(10):1363-7.

Prümmer M, Wigstrom L, Hornegger J, Boese J, Lauritsch G, Strobel N, Fahrig R. Cardiac C-arm CT: efficient motion correction for 4D-FBP. Institute of Pattern Recognition, FA University Erlangen-Nuremberg. Nuclear Science Symposium Conference Record. 2006 Oct:2620-2628

Prümmer M, Wigstroem L, Fahrig R, Lauritsch G, Hornegger J. Cardiac C-Arm CT: SNR enhancement by combining multiple retrospectively motion corrected FDK-like reconstructions. In: Horsch, Alexander, Deserno, Thomas M, Handels, Heinz, eds. *Bildverarbeitung für die Medizin*. Berlin, Germany: Springer; 2007:222-226.

Prümmer M, Fahrig R, Wigström L, Boese J, Lauritsch G, Strobel N, Hornegger J. Cardiac C-arm CT: 4D non-model based heart motion estimation and its application. *Proceedings of the SPIE*. 2007;6510:651015.

Quon A, Fischbein NJ, McDougall IR, Le QT, Loo BW Jr, Pinto H, Kaplan MJ. Clinical role of <sup>18</sup>F-FDG PET/CT in the management of squamous cell carcinoma of the head and neck and thyroid carcinoma. *J Nucl Med*. 2007 Jan;48(suppl 1):58S-67S. Review.

Quon A, Napel S, Beaulieu CF, Gambhir SS. 'Flying through' and 'flying around' a PET/CT scan: pilot study and development of 3D integrated <sup>18</sup>F-FDG PET/CT for virtual bronchoscopy and colonoscopy. *J Nuclear Med*. 2006;47:1081-87.

Rakow-Penner R, Bruce Daniel, Huanzhou Yu, Sawyer-Glover A, Glover GH. Relaxation times of breast tissue at 1.5T

and 3T using IDEAL. *J. Magn Reson Imag*. 2006;23:87-91.

Rakshe T, Fleischmann D, Rosenberg J, Roos JE, Napel S. Knowledge-based interpolation of curves: application to femoropopliteal arterial centerline restoration. *Med Image Analysis*. 2007;11:157-16.

Rand T, Basile A, Cejna M, Fleischmann D, et al. PTA versus carbofilm-coated stents in infrapopliteal arteries: pilot study. *Cardiovasc Intervent Radiol*. 2006; 29:29-38.

Reeder SB, McKenzie CA, Pineda AR, Yu H, Shimakawa A, Brau AC, Hargreaves BA, Gold GE, Brittain JH. Water-fat separation with IDEAL gradient-echo imaging. *J Magn Reson Imaging*. 2007 Mar;25(3):644-52.

Reeder SB, Yu H, Johnson J, Shimakawa A, Brittain JH, Pelc NJ, Beaulieu CF, Gold GE. T1 and T2 weighted fast spin-echo imaging of the brachial plexus and cervical spine with IDEAL water-fat separation. *JMRI*. 2006 Oct;24:825-32.

Roos JE, Fleischmann D, Köchl A, Rakshe T, Straka M, Napoli A, Kanitsar A, Sramek A, Gröller. Multipath curved planar reformation of the peripheral arterial tree in CT angiography. *Radiology*. 2007;244:281-290.

Samiian L, Daniel B, Wapnir L. Resolution of hypoalbuminemia after excision of malignant phyllodes tumor. *Clin Breast Cancer*. 2006 Dec;7(5):411-2.

Segal JB, Streiff MB, Hofmann LV, Thornton K, Bass EB. Management of venous thromboembolism: a systematic review for a practice guideline. *Annals of Internal Medicine*. 2007 Feb;146(3):211-22.

Sheikh AY, Lin SA, Cao F, Cao YA, van der Bogt KE, Chu P, Chang CP, Contag CH, Robbins RC, Wu JC. Molecular imaging of bone marrow mononuclear cell homing and engraftment in ischemic myocardium. *Stem Cells*. 2007 Jul 12. Epub ahead of print.

Shi R, Schraedley-Desmond P, Napel S, Olcott E, Jeffrey, Jr., RB, Yee J, Zalis ME, Margolis D, Paik DS, Sherbondy A, Sundaram P, Beaulieu CF. CT colonography: influence of 3D viewing and features of polyp candidates on interpretation using computer aided detection. *Radiology*. 2006;239(3):768-776.

Sommer G, Bouley D, Frisoli J, Pierce L, Sandner-Porkristl D, Fahrig R. Determination of three-dimensional zonal renal volumes using contrast-enhanced CT. *JCAT*. 2007;31(2):209-213.

Strouse PH, Newman B, Afshani E. CT of tracheal agenesis. *Pediatr Radiol*. 2006 Sep;36(9):920-6.

Sun S, Rubin GD, Paik D, Steiner RM, Zhuge F, Napel S. Registration of lung nodules using a semi-rigid model: method and preliminary results. *Med Phys*. 2007;34:613-626.

Swijnenburg RJ, van der Bogt KE, Sheikh AY, Cao F, Wu JC. Clinical hurdles for the transplantation of cardiomyocytes derived from human embryonic stem cells: role of molecular imaging. *Curr Opin Biotechnol*. 2007 Feb;18(1):38-45.

Taira AV, Herfkens RJ, Gambhir SS, Quon A. Detection of bone metastases: assessment of integrated FDG PET/CT imaging. *Radiology*. 2007 Apr;243(1):204-11.

Tang BT, Cheng CP, Draney MT, Wilson NM, Tsao PS, Herfkens RJ, Taylor CA. Abdominal aortic hemodynamics in young healthy adults at rest and during lower limb exercise: quantification using image-based computer modeling. *Am J*



Physiol Heart Circ Physiol. 2006;291(2):H668-76. Epub 2006 Apr 7.

Thomason ME, Foland LC, Glover GH. Calibration of BOLD fMRI using breath-holding reduces group variance during a cognitive task. *Human Brain Mapping*. 2007;28:59-68.

Tsukiji M, Nguyen P, Narayan G, Hellinger J, Chan F, Herfkens R, Pauly JM, McConnell MV, Yang PC. Peri-infarct ischemia determined by cardiovascular magnetic resonance evaluation of myocardial viability and stress perfusion predicts future cardiovascular events in patients with severe ischemic cardiomyopathy. *J Cardiovasc Magn Reson*. 2006;8(6):773-9.

van den Bosch MA, Daniel BL, Pal S, Nowels KW, Birdwell RL, Jeffrey SS, Ikeda DM. MRI-guided needle localization of suspicious breast lesions: results of a freehand technique. *Eur Radiol*. 2006 Aug;16(8):1811-7.

van den Bosch MA, Sze DY, Hofmann LV. Clinical presentation: fibromuscular dysplasia. *Amer J Kidney Diseases*. 2007;49(5):xliii-xliv.

van der Bogt KE, Swijnenburg RJ, Cao F, Wu JC. Molecular imaging of human embryonic stem cells: keeping an eye on differentiation, tumorigenicity and immunogenicity. *Cell Cycle*. 2006 Dec;5(23):2748-52. Epub 2006 Dec 1.

Vasanawala MS, Wang Y, Quon A, Gambhir SS. F-18 fluorodeoxyglucose PET/CT as an imaging tool for staging and restaging cutaneous angiosarcoma of the scalp. *Clin Nucl Med*. 2006 Sep;31(9):534-7.

Vigen KK, Jarrard J, Rieke V, Frisoli J, Daniel BL, Butts K. In vivo porcine liver radiofrequency ablation with simultaneous MR temperature imaging. *J Magn Reson Imaging*. 2006 Apr;23(4):578-84.

Wen Z, Fahrig R, Conolly, Pelc NJ. Investigation of electron trajectories of a Sn x-ray tube in magnetic fields of MR scanners. *Medical Physics*. 2007;34(6):2048-2058.

Wen Z, Pelc NJ, Nelson WR, Fahrig R. Study of increased radiation when an X-ray tube is placed in a strong magnetic field. *Medical Physics*. 2007;33(2):408-418.

Wootton-Gorges SL, Buonocore MH, Kupperman N, Marcin JP, Barnes PD, Neely EK, DiCarlo J, McCarthy T, Glaser NS. Cerebral proton magnetic spectroscopy in children with diabetic ketoacidosis. *Am J Neuroradiol*. 2007;28:895-899.

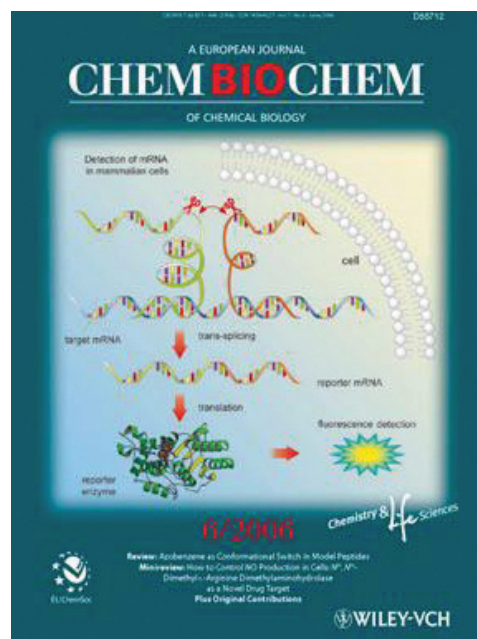
Wu JC, Bengel FM, Gambhir SS. Cardiovascular molecular imaging. *Radiology*. 2007 Aug;244(2):337-55.

Wu JC, Cao F, Dutta S, Xie X, Kim E, Chungfat N, Gambhir S, Mathewson S, Connolly AJ, Brown M, Wang EW. Proteomic analysis of reporter genes for molecular imaging of transplanted embryonic stem cells. *Proteomics*. 2006 Dec;6(23):6234-49.

Yeung JJ, Kim HJ, Abbruzzese TA, Vignon-Clementel IE, Draney-Blomme MT, Yeung KK, Perkash I, Herfkens RJ, Taylor CA, Dalman R. Aortoiliac hemodynamic and morphologic adaptation to chronic spinal cord injury. *J Vasc Surg*. 2006;(44):1254-1265.

Zilber S, Epstein N, Lee SW, Larsen M, Ma T, Smith RL, Biswal S, Goodman SB. Mouse femoral intramedullary injection

model: technique and microCT scan validation. Accepted for Publication. *J Biomed Mater Res B Appl Biomater*. 2007 Jun 11; Epub ahead of print.



## BOOK CHAPTERS

Hsu AR, Chen X. Biomedical applications of quantum dot semiconductor nanoparticles. In: Nalwa HS, ed. *Encyclopedia of nanoscience and nanotechnology*.

McDougall IR. Management of thyroid cancer and related nodular disease. Springer; 2006.

McDougall IR. *Thyroid Cancer in Clinical Practice*. Springer; 2007.

Newman B, Effmann E. Lung masses. In: Slovis T, ed. *Caffey's pediatric diagnostic imaging*. 11th edition. Philadelphia, Pennsylvania: Elsevier Inc.; 2007. In press.

Towbin A, Newman B. Syndromes and chromosomal disorders and the heart. In: Slovis T, ed. *Caffey's pediatric diagnostic imaging*. 11th edition. Philadelphia, Pennsylvania: Elsevier Inc.; 2007. In press.

Towbin A, Newman B. Systemic diseases affecting the heart. In: Slovis T, ed. *Caffey's pediatric diagnostic imaging*. 11th edition. Philadelphia, Pennsylvania: Elsevier Inc.; 2007. In press.

## PAPERS SUBMITTED OR IN PRESS

Balchandani P, Spielman D. Fat suppression for 1H MRSI at 7T using spectrally selective adiabatic inversion recovery. Submitted to Magn Res Med. 2007 June.

Balchandani P, Pauly J, Spielman D. Interleaved narrow-band PRESS sequence with adiabatic spatial-spectral refocusing pulses for 1H MRSI at 7T. Submitted to Magn Res Med. 2007 May.

Balchandani P, Pauly J, Spielman D. Slice-selective tunable-flip adiabatic low peak-power excitation (STABLE) pulse. Submitted to Magn Res Med. 2007 May.

Barnes PD, Krasnokutsky M. Imaging of the central nervous system in suspected or alleged nonaccidental injury, including the mimics. *Topics in Magnetic Resonance Imaging*. 2007 Jul. In press.

Barnes PD. Imaging of the developing brain. *Topics in Magnetic Resonance Imaging*. 2007 Jul. In press.

Biswal S, Resnick D, Gambhir SS. Molecular imaging review series: integration of molecular imaging into your musculoskeletal imaging practice. *Radiology*. 2006. In press.

Brindis RG, Kramer CM, Poon M, Rubin GD. Reply. *J Am Coll Cardiol*. 2007;49:1751-1752. In press.

Freeman C, Rieke V, Fahrig R, Ganguly A, Daniel B. The performance of a "truly" hybrid X-Ray/MR for combining hysterosalpingogram and MRI in infertility patients: our initial experience. *AJR Am J Roentgenol*. In press.

Friedman L, Stern H, Brown GG, Mathalon DH, Turner J, Glover GH, Gollub RL, Lauriello J, Lim KO, Cannon T, Greve DN, Bockholt HJ, Belger A, Mueller B, Doty MJ, He J, Wells W, Smyth P, Pieper S, Kim S, Kubicki M, Vangel M, Potkin SG. Test-retest and between-site reliability in a multicenter fMRI study. *Hum Brain Mapp*. 2007. In press.

Ganguly A, Gold G, Butts K, Mayer D, Moseley M, Pelc NJ, Fahrig R. Quantitative evaluation of the relaxivity effects of iodine on Gd-DTPA signal for MR arthrography. *Journal of Magnetic Resonance Imaging*. In press.

Geraghty P, van den Bosch MA, Spielman DM, Hunjan S, Daniel BL, Birdwell RL, Fong KJ, Stables LA, Zakhour M, Herfkens RJ, Ikeda DM. MRI and H MRS of the breast cancer: presence of choline is related to k21 value of the tumor in patients with invasive ductal carcinoma. Submitted to *European Radiology*.

Gold G, Busse R, Beehler C, Han E, Baru A, Beatty P, Beaulieu C. Isotropic MRI of the knee with 3D-FSE-xeta

(extended echo train acquisition)—initial experience in healthy volunteers. *AJR Amer J Roentgen*. 2007. In press.

Gold GE, Pappas GP, Blemker SS, Whalen ST, Campbell G, McAdams T, Beaulieu CF. Abduction and external rotation in shoulder impingement: an open MRI study on healthy volunteers. *Radiology*. 2006. In press.

Gu M, Spielman D. Robust water and lipid suppression using multiple optimized frequency selective pulses for 1H spectroscopic imaging at 3T. Submitted to Magn Res Med. 2007 Jun.

Habte F, Olcott PD, Foudray AMK, Levin CS, Zhang J, Chinn G. Simulation and measurement of gamma-ray and annihilation photon imaging detectors. *IEEE Transactions on Nuclear Science*. 2007. In press.

Hu YL, Glover GH. 3D spiral technique for high resolution fMRI. *MRM*. In press.

Hwang GL, Hofmann LV. The role of image-guided vascular intervention in therapeutic angiogenesis translational research. *Expert Review of Cardiovascular Therapy*. In press.

Keren S, Gheysens O, Levin CS, Gambhir SS. Characterization of a small animal time-domain fluorescence tomography imaging system. *IEEE Transactions on Medical Imaging*. 2007. In press.

Kim D, Gu M, Cunningham C, Chen A, Baumer F, Glenn O, Vigneron D, Spielman D, Barkovich A. Fast 3D 1H-MRSI of the pediatric brain with motor dysfunction. Submitted to *JMRI*. 2007.

Konukoglu E, Acar B, Beaulieu C, Napel S. HDF: heat diffusion fields for polyp detection in CT colonography. Submitted to *Signal Processing*. 2006.

Konukoglu E, Acar B, Paik DS, Beaulieu CF, Napel S. PELS: polyp enhancing level-set evolution of the colon wall. *IEEE Trans Med Imaging*. 2006. In press.

Konukoglu E, Acar B, Paik DS, Beaulieu CF, Napel S. PELS: polyp enhancing level-set evolution of the colon wall. *IEEE Transactions on Medical Imaging*. 2007 May. In press.

Kukuk M, Napel S. Rotational roadmapping: a new image-based navigation technique for the interventional room. *MICCAI* 2007. 2006 May. In press.

Kuo WT, Loh CT, Sze DY. Emergency percutaneous retrieval of a G2 filter after migration to the right ventricle. *Journal of Vascular and Interventional Radiology*. 2007. In press.

Lee SW, Greve JM, Leaffer D, Lollini L, Bailey P, Gold G, Biswal S. Early histological changes seen in a murine model of inflammatory arthritis (RA) can be detected with micro-computed tomography (microCT) and micro-magnetic resonance imaging (microMRI). Submitted to Radiology. 2007.

Lertvaranurak VR, Sage-el A, Quon A, Spielman D, Fischbein N, Atlas, SW Gambhir SS. 18F-FDG-positron emission tomography and 1H magnetic resonance spectroscopy in the differentiation of recurrent or residual gliomas versus radiation injury. Submitted to Radiology. 2007.

Levin Y, Mayer D, Yen YF, Hurd R, Spielman DM. Least-squared reconstruction algorithm for optimization of fast metabolic imaging as applied to hyperpolarized 13C. Magn. Res. Med. 2007. In press.

Lew C, Chan F, Spielman D, Alley M, Clayton D, Bammer R. SENSE phased-constrained reconstruction with iterative phase refinement. Magn, Res. Med. 2007. In press.

Meyer D, Spielman D, Bammer R. Fast parallel spiral chemical shift imaging at 3 Tesla using iterative SENSE reconstruction. Submitted to Magn Res Med. 2007.

Nau WH, Diederich CJ, Ross AB, Butts K, Rieke V, Bouley D, Gill H, Daniel B, Sommer G. Conformal heating of canine prostate using interstitial ultrasound applicators with MR thermal monitoring. Medical Physics. In press.

Nguyen JT, Peterson JS, Biswal S, Beaulieu CF, Fredericson M. Stress-related injuries about the lesser trochanter in long-distance runners. Submitted to AJR. 2007.

Olcott PD, Habte F, Levin CS, Foudray AMK. Performance characterization of a miniature, high sensitivity gamma-ray camera. IEEE Transactions on Nuclear Science. 2007. In press.

Padmanabhan P, Biswal S. A new imaging approach for calcium dependent calmodulin activation in cells. 2006. In press.

Padmanabhan P, Ramasamy P, Gambhir SS, Biswal S. Simultaneous non-invasive imaging of estrogen receptor ligand induced homodimerization and gene transactivation in living mice. 2007. In press.

Raman R, Raman B, Napel S, Rubin GD. Improved speed of bone removal in CT angiography (CTA) using automated targeted morphological separation: method and evaluation in CTA of lower extremity occlusive disease (LEOD). JCAT. 2007 Jun. In press.

Shi R, Napel S, Rosenberg JK, Shin LK, Freeman CB, Mogensen MA, Joshi AJ, Pankhudi P, Beaulieu CF. Transparent rendering of intraluminal contrast for 3D polyp visualization at CT colonography. JCAT. 2006 Dec. In press.

Stillman AE, Oudkerk M, Ackerman M, Becker CR, Buszman PE, de Feyter PJ, Hoffmann U, Keadey MT, Marano R, Lipton MJ, Raff GL, Reddy GP, Rees MR, Rubin GD, Schoepf UJ, Tarulli G, van Beek EJ. Use of multidetector computed tomography for the assessment of acute chest pain: a consensus statement of the North American Society of Cardiac Imaging and the European Society of Cardiac Radiology. Int J Cardiovasc Imaging. 2007 Jan. In press.

Sun S, Zhuge F, Rosenberg J, Rubin GD, Napel S. Learning-enhanced simulated annealing: method, evaluation, and application to lung nodule registration. International Journal

of Applied Intelligence. 2007 Mar. In press.

Sundaram, P, Zamorodian, AJ, Beaulieu CF, Napel S. Colon polyp detection using smoothed shape operators: preliminary results. Submitted to Medical Image Analysis. 2007 Feb.

Tatum G, Newman B, Ralphe C. Neonatal congestive heart failure due to a subclavian artery to subclavian vein fistula diagnosed by non-invasive procedures. Congenital Heart Disease. In press.

Thomason ME; Glover GH. Controlled inspiration depth reduces variance in breath-holding induced BOLD signal. NeuroImage. In press.

Tran DN, Fleischmann D, Rakshe T, Roos JE, Rosenberg J, Straka M, Napel S. Femoropopliteal artery centerline interpolation using contralateral shape. Medical Physics. 2007. In press.

van den Bosch M, Daniel BL, Rieke V, Butts RK, Kermit E, Jeffrey SS. MRI-guided radiofrequency ablation of breast cancer: Feasibility study in three patients. JMRI. In press.

Vertinsky AT, Barnes PD. Macrocephaly, increased intracranial pressure, and hydrocephalus. Topics in Magnetic Resonance Imaging. 2007 Jul. In press.



